



## AVERTISSEMENT

Ce document est le fruit d'un long travail approuvé par le jury de soutenance et mis à disposition de l'ensemble de la communauté universitaire élargie.

Il est soumis à la propriété intellectuelle de l'auteur. Ceci implique une obligation de citation et de référencement lors de l'utilisation de ce document.

D'autre part, toute contrefaçon, plagiat, reproduction illicite encourt une poursuite pénale.

Contact : [ddoc-theses-contact@univ-lorraine.fr](mailto:ddoc-theses-contact@univ-lorraine.fr)

## LIENS

Code de la Propriété Intellectuelle. articles L 122. 4

Code de la Propriété Intellectuelle. articles L 335.2- L 335.10

[http://www.cfcopies.com/V2/leg/leg\\_droi.php](http://www.cfcopies.com/V2/leg/leg_droi.php)

<http://www.culture.gouv.fr/culture/infos-pratiques/droits/protection.htm>

INSTITUT NATIONAL POLYTECHNIQUE DE LORRAINE

Institut Jean Lamour  
UMR 7198 CNRS - Nancy - Université - UPV - Metz  
Ecole Doctorale Énergie Mécanique et Matériaux

## DOCTORAT

en SCIENCE et INGÉNERIE des MATÉRIAUX et MÉTALLURGIE

présenté par

**Rafik ADDOU**

en vue d'obtenir le grade de

DOCTEUR DE L'INSTITUT NATIONAL POLYTECHNIQUE DE LORRAINE

---

**Surfaces d'alliages métalliques complexes :  
structure, propriétés et nanostructuration**

---

soutenu publiquement le  
**lundi 29 mars 2010**

devant le **JURY** composé de:

**Philippe Dumas**, *Professeur* - Président du jury  
**Marie-Geneviève Barthés-Labrousse**, *Directeur de Recherche* - Rapporteur  
**Marc de Boissieu**, *Directeur de Recherche* - Rapporteur  
**Bertrand Lenoir**, *Maître de conférences* - Examinateur  
**Oliver Gröning**, *Directeur scientifique* - Examinateur  
**Jean-Marie Dubois**, *Directeur de Recherche* - Directeur de thèse  
**Julian Ledieu**, *Chargé de Recherche* - Co-directeur de thèse

## ACKNOWLEDGEMENT

Experimental Physics is necessarily the result of team work, as such I would like to thank everybody who contributed to this thesis. Some people I would particularly like to mention:

I express my deep gratitude and sincere thanks to my supervisor Jean-Marie Dubois for agreeing to be the director of this thesis. He always showed a lot of genuine interest in this work through our meetings which I found very reassuring and encouraging.

My special thanks go to Julian Ledieu who has done much more than supervise my thesis. I learned many things with and from him. He helped me share his sense of humour, rigour and enthusiasm. Merci Julian!

I would like to thank Oliver Groening for having generously shared excellent and remarkable experience in surface science. Merci Oliver!

I would also like to express my gratitude to Vincent Fournée, who kept a watchful and trained eye on my thesis, and also for his reactivity and his patience.

The European Network of Excellence on “Complex Metallic Alloy”, Contract No. NMP3-CT-2005-500145 and the “Région Lorraine” are acknowledged for their financial support. My thanks go also to the european partners, Marc Heggen, Michael Feirebacher and Peter Gille for the growth of samples, Karsten Horn for hosting me in Berlin, Marian Krajčí and Jürgen Hafner for calculations.

I wish to thank all the members of the “Métallurgie et Surfaces” team of international renown, notably Emily Gaudry for calculations, Marie-Cécile de Weerd for growth of samples, Ajay Shukla and Thalia Deniozou for giving support to the experiments and analysis, Thomas, Sam and Seb for various discussions.

I would like to thank all the members in the “nanotech@surfaces” lab for the great working environment. Thanks go to Pierangelo Groening, the laboratory leader for sharing some of his vast knowledge on photoelectron spectroscopy, Pascal Ruffieux and Roland Widmer for numerous helpful discussions, Matthias Treier and Ruben Maeder for giving support to the experiments.

I do not forget the most formidable work of our secretaries which greatly facilitated our daily lives: Anne-Marie, Géraldine, Martine, Josette, Liliane, Laurence, Valérie & Nathalie, and Patricio and Francesco for solving my computer problem's.

And all the people: Houssaine, Dominique, Geneviève, Rahim, Zeineb, Diana, Béa, Mariya, Djam, Ana, Kamel, Kristina, Marta, Robert, David, Cédric, Roxane & Nadia... with whom, for one reason or the other, I have shared very good moments.

Last, but not least, I thank my family, specially my parents (Joudia & Mimoun) and my sisters (Hanan, Wissam & Sanae), for their non-stop support and incredible love, which is the most important of all. Chokrane :-)

“Un problème créé ne peut être résolu en réfléchissant de la même manière  
qu'il a été créé”

“A person who never made a mistake has never tried anything new”

*Albert Einstein*

À mes parents,

À Hanan,

À Wissam,

À Sanae.

# Contents

<b>1 Résumé en français</b>	<b>1</b>
1.1 Introduction . . . . .	1
1.1.1 Introduction Générale . . . . .	1
1.1.2 Le modèle structural des deux approximants étudiés . . .	6
1.1.3 Détails expérimentaux . . . . .	10
1.2 Etude structurale de la surface (100) du cristal $\text{Al}_{13}\text{Co}_4$ . . . . .	11
1.2.1 Préparation de la surface . . . . .	11
1.2.2 Identification structurale de la surface . . . . .	12
1.2.3 Densité d'états électroniques calculée et bande de valence	15
1.2.4 Images STM simulées . . . . .	16
1.2.5 Conclusions . . . . .	17
1.3 Etude structurale de la surface (010) du cristal T- $\text{Al}_3(\text{Mn, Pd})$ .	18
1.3.1 Préparation de la surface . . . . .	18
1.3.2 Structure atomique de la surface . . . . .	20
1.3.3 Structure électronique de la surface . . . . .	23
1.3.4 Conclusions . . . . .	24
1.4 Adsorption du Pb sur les cristaux d' $\text{Al}_{13}\text{Co}_4$ et de T- $\text{Al}_3(\text{Mn, Pd})$	25
1.4.1 Croissance du plomb sur la surface (100) du cristal $\text{Al}_{13}\text{Co}_4$	25
1.4.2 Croissance du plomb sur la surface (010) du cristal T- $\text{Al}_3(\text{Mn, Pd})$	29
1.4.3 Conclusions . . . . .	32
1.5 Caractérisation de l'adsorption de Cu sur la surface (100) du cristal $\text{Al}_{13}\text{Co}_4$ . . . . .	33
1.5.1 Adsorption du Cu à 300 K . . . . .	33
1.5.2 Adsorption du Cu pour une température inférieure ou égale à 573 K . . . . .	35
1.5.3 Conclusions . . . . .	37
1.6 Conclusions et perspectives . . . . .	38
<b>2 Introduction</b>	<b>40</b>
2.1 General presentation . . . . .	40
2.2 Complex metallic alloys systems . . . . .	43
2.2.1 Definition . . . . .	43
2.2.2 Quasiperiodicity and approximant phases . . . . .	43
2.2.3 Physical properties of CMAs . . . . .	49
2.2.4 Growth techniques . . . . .	51

2.3	Complex metallic alloys surfaces . . . . .	53
2.3.1	Generality on alloy surfaces and surface phenomena . . . . .	53
2.3.2	Surface structures of quasicrystals . . . . .	53
2.3.3	Surface structure of approximants . . . . .	57
2.4	Quasicrystalline surfaces as templates . . . . .	60
2.4.1	Adsorption sites and role of surface clusters . . . . .	60
2.4.2	Periodic overlayers . . . . .	62
2.4.3	Pseudomorphic overlayers . . . . .	64
2.4.4	Nanoislands with “magic heights” . . . . .	68
2.5	Conclusions . . . . .	70
<b>3</b>	<b>Investigation of the (100) surface of the Al<sub>13</sub>Co<sub>4</sub> crystal</b>	<b>72</b>
3.1	Introduction . . . . .	72
3.2	Model of the bulk structure . . . . .	73
3.3	Experimental details . . . . .	75
3.4	Experimental results . . . . .	76
3.4.1	Surface preparation . . . . .	76
3.4.2	Investigation of the surface structure . . . . .	77
3.4.3	Structural model of both surface terminations . . . . .	78
3.5	Electronic structure calculations . . . . .	82
3.5.1	Computational details . . . . .	83
3.5.2	Calculated DOS and experimental valence band . . . . .	84
3.5.3	Simulated STM images . . . . .	84
3.6	Discussion . . . . .	88
3.7	Conclusions . . . . .	90
<b>4</b>	<b>Structural Investigation of the (010) surface of the orthorhombic T-Al<sub>3</sub>(Mn, Pd) crystal</b>	<b>91</b>
4.1	Introduction . . . . .	91
4.2	Model of the bulk structure . . . . .	93
4.3	Experimental details . . . . .	95
4.4	Computational details . . . . .	95
4.5	Results . . . . .	96
4.5.1	Identification of the surface structure . . . . .	96
4.5.2	<i>Ab initio</i> determination of cleavage plane . . . . .	101
4.5.3	STM images from <i>ab initio</i> calculations . . . . .	103
4.5.4	Surface investigated by XPD measurements . . . . .	104
4.5.5	Electronic character of the surface . . . . .	106
4.6	Discussion . . . . .	111
4.7	Conclusions . . . . .	113
<b>5</b>	<b>Lead adsorption on orthorhombic Al<sub>13</sub>Co<sub>4</sub> and T-Al<sub>3</sub>(Mn, Pd)</b>	<b>114</b>
5.1	Introduction . . . . .	114
5.2	Experimental details . . . . .	116
5.3	Structural investigation of Pb adsorption on the Al <sub>13</sub> Co <sub>4</sub> (100) surface . . . . .	116

5.3.1	Deposition at 300 K . . . . .	116
5.3.2	Pb deposition at 573 K . . . . .	125
5.4	Structural investigation of Pb adsorption on the T-Al <sub>3</sub> (Mn, Pd) (010) surface . . . . .	127
5.4.1	Deposition at 300 K . . . . .	127
5.4.2	Deposition at 573 K . . . . .	132
5.5	Discussion . . . . .	134
5.6	Conclusions . . . . .	137
<b>6</b>	<b>Copper adsorption on the (100) surface of the Al<sub>13</sub>Co<sub>4</sub> crystal</b>	<b>138</b>
6.1	Introduction . . . . .	138
6.2	Structural Models: from $\beta$ - to $\gamma$ -phase . . . . .	140
6.3	Experimental details . . . . .	141
6.4	Experimental results . . . . .	142
6.4.1	The clean surface of the <i>p</i> -10 <i>f</i> Al <sub>13</sub> Co <sub>4</sub> crystal . . . . .	142
6.4.2	Investigation of Cu adsorption at 300 K . . . . .	144
6.4.3	Investigation of Cu adsorption up to 573 K . . . . .	152
6.5	Discussion . . . . .	163
6.6	Conclusions . . . . .	165
<b>7</b>	<b>Conclusions and perspectives</b>	<b>166</b>
<b>A</b>	<b>XPD and SSC methods</b>	<b>168</b>
A.1	X-ray Photoelectron Diffraction . . . . .	168
A.2	Single Scattering Cluster Simulations . . . . .	169
<b>Bibliography</b>		<b>172</b>

## List of abbreviations

1D	One Dimensional
2D	Two Dimensional
3D	Three Dimensional
$2-f$	Twofold
$3-f$	Threefold
$5-f$	Fivefold
$6-f$	Sixfold
$10-f$	Tenfold
p- $10-f$	pseudo-tenfold
AFM	Atomic Force Microscopy
CMA	Complex Metallic Alloy
CAE	Constant Analyzer Energy
DFT	Density Functional Theory
DOS	Density of States
DS	Doniach Šunjić
$E_F$	Fermi level
FF	Forward Focusing
FFT	Fast Fourier Transform
HR	High Resolution
LEED	Low Energy Electron Diffraction
ML	Monolayer
MLE	Monolayer Equivalent
PB	Pentagonal Bipyramid
QC	Quasi-periodic Crystal
SSC	Single Scattering Cluster
STM	Scanning Tunneling Microscopy
STS	Scanning Tunneling Spectroscopy
$T_1$	Termination 1
$T_2$	Termination 2
UHV	Ultra High Vacuum
UPS	Ultraviolet Photoelectron Spectroscopy
VT	Variable Temperature
XPS	X-ray Photoelectron Spectroscopy
XPD	X-ray Photoelectron Diffraction

# Chapter 1

## Résumé en français

### 1.1 Introduction

#### 1.1.1 Introduction Générale

Un cristal est défini par une maille primitive (unité élémentaire<sup>1</sup>) remplissant parfaitement l'espace sans recouvrement et sans laisser de vide. Ces unités se répartissent dans un cristal périodiquement suivant les noeuds d'un réseau, appelé **réseau de Bravais**. Ce réseau est défini par un ensemble infini de points discrets avec une structure et une orientation qui se répète dans l'espace. La périodicité génère des symétries de translation et de rotation laissant le réseau de Bravais invariant. Une *symétrie de rotation* est dite d'ordre- $n$  lorsqu'il y a invariance après une rotation de  $2\pi/n$  (où  $n = 2, 3, 4$  ou  $6$ ) [1]. La théorie des groupes de symétrie de translation en dimensions 3 montre l'inexistence d'un cristal possédant un axe de symétrie d'ordre-5 ( $n = 5$ ). Explicitement, cette symétrie est interdite car l'espace 2D (ou 3D) ne peut pas être rempli uniquement par des pentagones (ou des icosaèdres). Alors qu'il analysait par microscopie électronique à transmission la structure d'alliages binaires Al-Mn obtenus par solidification rapide, Dany Shechtman découvre en 1982 une phase cristalline (de composition Al<sub>86</sub>Mn<sub>14</sub>) possédant une symétrie icosaédrique, i.e. produisant un cliché de diffraction d'ordre-5 [2]. Il faudra attendre deux ans (1984) avant que cette découverte du cristal quasi-périodique<sup>2</sup> soit finalement publiée<sup>3</sup>. Cette découverte fut largement contestée, notamment par Linus Pauling, double prix Nobel. Suite à cette découverte, l'Union Internationale de Cristallographie *IUCr* [3] a publié une nouvelle définition du cristal en 1992, pour inclure celle du quasicristal. Ainsi, un cristal est défini comme **un solide possédant un spectre de diffraction essentiellement discret**. Un quasicristal est caractérisé par une maille infinie, par un ordre à grande distance et par des symétries interdites par la cristallographie "classique" (comme les

<sup>1</sup>Ces unités peuvent être décorées des atomes, des amas d'atomes, des molécules ou des ions, etc.

<sup>2</sup>Ou **quasicristal (QC)**.

<sup>3</sup>La publication est intitulée "*Metallic Phase with Long-Range Orientational Order and No Translational symmetry*" [2].

symétries de rotation d'ordre -5, -8, -10 ou -12). Comme les QC<sub>s</sub>, les approximants sont inclus dans la classe des alliages métalliques complexes (CMAs). Les approximants sont des intermétalliques cristallins possédant des motifs structuraux similaires et une composition proche de celle du quasicristal parent. D'une manière générale, les CMAs sont des matériaux dont la maille cristalline peut contenir plusieurs centaines, voire des milliers d'atomes [4]. Les quasicristaux représentent le cas limite où la maille est considérée comme infinie. L'intérieur de la maille des CMAs est constituée d'agrégats de taille nanométrique et de symétrie élevée. La complexité dans ces alliages réside notamment dans la difficulté de décrire exactement la position des atomes dans une maille "géante". Cette complexité structurale engendre des propriétés nouvelles et atypiques. Ces matériaux présentent souvent des compromis entre des propriétés qui s'excluent dans les alliages conventionnels. Ils sont envisagés pour un certain nombre d'applications technologiques dans des domaines aussi variés que les revêtements aux propriétés mécaniques exceptionnelles, les barrières thermiques, les matériaux thermoélectriques, le stockage de l'hydrogène ou encore la catalyse [5]. Les applications des alliages métalliques complexes font essentiellement appel aux propriétés de surface et il est donc nécessaire d'en étudier la structure et les propriétés.

Une des propriétés physiques qui caractérise plusieurs CMAs est la réduction de la densité des états (DOS) électroniques au niveau de Fermi  $E_F$ , connu comme le ***pseudo-gap*** [6–11]. Ce dernier est souvent mis en avant pour expliquer certaines propriétés atypiques des CMAs. Le *pseudo-gap* est produit lorsque la sphère de Fermi interagit avec la *pseudo-zone* de Jones. L'ouverture d'un *pseudo-gap* dans la densité d'états pourrait être expliquée par une combinaison entre le mécanisme de Hume-Rothery [12] et une hybridation *sp-d* en présence de métaux de transition, comme dans le cas des phases  $\gamma$ -Al<sub>4</sub>Cu<sub>9</sub> et  $\gamma$ -Cu<sub>5</sub>Zn<sub>8</sub> [13]. L'existence du *pseudo-gap* dans la DOS à  $E_F$  explique le comportement inhabituel de la résistivité  $\rho$  dans les CMAs. Ces alliages constitués essentiellement de métaux se comportent plutôt comme des semi-conducteurs [14]. La résistivité d'un quasicristal augmente lorsque la température baisse. La mesure de la résistivité électrique dans le quasicristal Al-Pd-Re à basse température atteint une valeur de près de  $2 \Omega.cm$ , soit environ  $10^8$  de fois supérieure à celle de l'Al qui reste l'élément chimique principal [15, 16]. Une autre propriété atypique des CMAs repose sur la conductivité thermique. Cette dernière vaut seulement  $2 W/m.K$  pour le quasicristal *i*-Al-Cu-Fe. Pour les métaux, la conductivité thermique est beaucoup plus grande. Elle est évaluée à  $170 W/m.K$  pour l'Al et à  $390 W/m.K$  pour le Cu [17, 18]. Enfin, plusieurs CMAs se distinguent par un coefficient de frottement et d'adhésion faible. Ces propriétés rendent ces surfaces particulièrement attrayantes pour leur utilisation sous forme de films minces ou de revêtements.

Le concept d'apéridicité existait bien avant la découverte des QC<sub>s</sub>. Par exemple, la séquence mathématique de Fibonacci peut être regardée comme la représentation d'un quasicristal unidimensionnel. Le pavage de Penrose quant à lui permet d'appréhender le concept d'apéridicité en 2D. Pour illustrer la

suite de Fibonacci, nous considérons deux segments; un court  $S$  (pour *Short*) et un long  $L$ . La séquence de Fibonacci est construite à partir des règles de substitution suivantes:  $S \rightarrow L$  et  $L \rightarrow LS$  (voir la table 2.2.2.1). Dans une série de Fibonacci, le rapport entre le nombre de segments  $L$  et le nombre des segments  $S$  converge vers le nombre d'or  $\tau$ :

$$\tau = \frac{1 + \sqrt{5}}{2} \approx 1.6180339\dots \quad (1.1)$$

Une autre façon pour représenter la série de Fibonacci est:

$$0, 1, 1, 2, 3, 5, 8, 13, 21, 34, 55, \dots \quad (1.2)$$

Au fur et à mesure de la construction de la suite, le rapport entre deux nombres successifs de cette série tend vers le nombre d'or. Un nombre  $f(n)$  de cette série est calculé en additionnant les deux nombres qui le précédent (cf.  $55 = 34+21$ ):

$$f(n) = f(n - 2) + f(n - 1) \quad (1.3)$$

Pas	Séquence	L/S	Ratio $\tau$
0	S	-	-
1	L	1/0	-
2	LS	1/1	1
3	LSL	2/1	2
4	LSLLS	3/2	1.5
5	LSLLSLSL	5/3	1.667
6	LSLLSLSLLSLLS	8/5	1.6
7	LSLLSLSLLSLLSLLSLLS	13/8	1.625
8	LSLLSLSLLSLLSLLSLLSLLSLLSLLS	21/13	1.615
n	$f(n) = f(n - 2) + f(n - 1)$	$N_L/N_S$	$\tau=1.61803$

Table 1.1: *Construction de la suite de Fibonacci et sa relation avec le nombre d'or  $\tau$ .  $N_L$  ( $N_S$ ) présente le nombre des segments  $L$  ( $S$ ). La fonction  $f(n)$  montre la méthode pour obtenir un nombre de la série de Fibonacci.*

Nous nous penchons à présent sur la construction du pavage de Penrose [19]. Le pavage est construit à partir de deux losanges élémentaires “fin” et “gro” possédant une arête de même longueur. Le premier losange possède un angle de  $36^\circ$  et le deuxième un angle de  $72^\circ$ . Les deux losanges sont assemblés suivant des règles spécifiques. Ces règles d’assemblage consistent à faire coïncider les flèches disposées sur les bords des losanges. Ce pavage bidimensionnel, bien que non-périodique, est parfaitement ordonné avec des motifs locaux qui se répètent plusieurs fois dans le plan (Fig.1.1(a)). La transformée de Fourier (Fig.1.1(b)) calculée à partir de cette structure montre une symétrie d’ordre-5 semblable au diagramme de diffraction mesuré par Shechtman *et al.* [2].

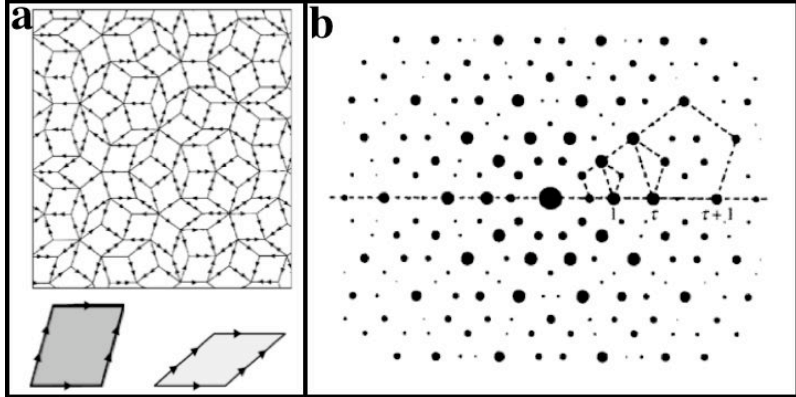


Figure 1.1: (a) Pavage de Penrose construit à partir des deux losanges “fin” (à droite) et “gros” (à gauche) en bas de la figure (a). (b) Diagramme de diffraction calculé à partir d’un pavage similaire à celui montré sur la figure (a).

D’une façon similaire, la structure du volume d’un quasicristal peut être interprétée par un pavage de Penrose tridimensionnel décoré par des agrégats suivant des règles d’assemblage très précises. Ces amas forment un pavage apériodique dans les quasicristaux parfaits et ils décorent une maille périodique dans les approximants. A titre d’illustration, la structure du quasicristal Al-Pd-Mn est décrite par deux types d’amas; l’agrégat de *pseudo-Mackay* PMI (**P**seudo **M**ackay **I**cosahe**d**ra) [20, 21] et celui de Bergman (B) [22]. Le PMI contient 51 atomes avec un diamètre de 9.6 Å. Il est constitué de: (i) un Mn entouré de 8 atomes décorant une partie des sommets d’un dodécaèdre, (ii) un icosaèdre intermédiaire de 12 atomes et (iii) un icosidodécaèdre externe de 30 atomes. L’agrégat de Bergman est constitué de deux couches concentriques et contient 33 atomes: (i) un icosaèdre de 13 atomes et (ii) un dodécaèdre de 20 atomes [23]. La structure du quasicristal se décrit alors dans l’espace à trois dimensions comme un arrangement hiérarchique de ces agrégats imbriqués.

Bien que le domaine des CMA ait atteint une certaine maturité, plusieurs questions concernant notamment les positions atomiques dans certaines phases apériodiques restent ouvertes. En surface, d’autres questions demeurent; les phénomènes de relaxation, de reconstruction de la surface, de ségrégation chimique sont-ils attendus sur les alliages métalliques complexes? Les propriétés présentes dans le massif sont-elles préservées en surface des échantillons? Les règles permettant de prédire la hauteur de coupe dans les quasicristaux pour générer les surfaces sont-elles identiques pour les approximants?

Pour tenter de répondre à certaines de ces questions, les surfaces des quasicristaux et plus récemment les surfaces des approximants ont été largement étudiées par plusieurs auteurs. La première surface quasicristalline caractérisée est la phase décagonale de l’Al-Cu-Co [24]. Depuis ces travaux, de nombreuses surfaces ont été analysées à l’aide de techniques expérimentales diverses mais aussi par des calculs *ab initio* de structure électronique: la surface d’ordre-2, -3 et -5 du quasicristal *i*-Al-Pd-Mn [25–41], la surface d’ordre-5 du quasicristal

*i*-Al-Cu-Fe [40, 42–46], la surface d'ordre-5 du quasicristal *i*-Al-Cu-Ru [47], la surface d'ordre-5 du quasicristal *i*-Ag-In-Yb [48] et la surface d'ordre-2 et -10 du quasicristal *d*-Al-Ni-Co [31, 35, 49–60]. Avant le début de cette thèse, seule la surface (010) d'ordre pseudo-10 de la phase  $\xi'$ -Al<sub>77.5</sub>Pd<sub>19</sub>Mn<sub>3.5</sub> avait été étudiée par Fournée *et al.* et Sharma *et al.* [61, 62]. Depuis ces travaux et parallèlement à cette thèse, plusieurs surfaces d'approximants ont été étudiées pour les composés  $Y$ -Al<sub>75.8</sub>Ni<sub>2.1</sub>Co<sub>22.1</sub>,  $\mu$ -Al<sub>4</sub>Mn et la phase  $\gamma$ -Al<sub>4</sub>Cu<sub>9</sub> dans le cadre du réseau CMA [63–65]. Ces études montrent que la surface après plusieurs cycles de préparation bombardement-recuit est comparable à certains plans du volume. Les plans denses et riches en Al sont préférentiellement sélectionnés comme terminaison de surface. Pour modéliser des systèmes apériodiques et effectuer des calculs *ab initio* exigeant une maille finie, les approximants très proches structurellement des QCs ont été introduits [31]. L'approximant représente aussi un état intermédiaire de complexité entre le cristal et le quasicristal. L'étude de ces matériaux peut apporter certaines réponses quant à l'influence d'une complexité structurale croissance sur les propriétés physico-chimiques des surfaces. Les deux échantillons utilisés dans cette thèse sont des approximants des quasicristaux décagonaux et possèdent une complexité structurale et une composition chimique différentes.

Mon travail de thèse a été effectué entre 2006-2009, à l'Institut Jean Lamour (IJL) de Nancy dans l'équipe 203 “Métallurgie et Surfaces”<sup>4</sup> en collaboration avec le laboratoire fédéral Suisse Empa-Thun dans l'équipe 127 “Nanotech@surfaces”<sup>5</sup>. Cette thèse entre dans le cadre du réseau européen d'excellence des alliages métalliques complexes CMA NoE<sup>6</sup>. Ce réseau regroupe 20 partenaires européens couvrant ainsi un large spectre d'expertises dans le domaine des alliages métalliques complexes. Les échantillons étudiés dans cette thèse proviennent essentiellement de nos collaborateurs à Jülich et München en Allemagne. Dans ce travail de thèse, nous étudierons la structure de la surface d'ordre-*pseudo*-10 de deux cristaux considérés comme approximants aux quasicristaux décagonaux [66–69]. Les deux surfaces caractérisées sont la surface (100) de l'alliage binaire d'Al<sub>13</sub>Co<sub>4</sub> [70] et la surface (010) de l'alliage ternaire T-Al<sub>3</sub>(Mn, Pd) [71]. Ensuite, ces deux surfaces seront utilisées comme substrats pour former des films minces métalliques. Plusieurs techniques expérimentales, des simulations numériques et des calculs *ab initio* sont utilisés pour réaliser cette étude. La structure atomique des surfaces propres et des films minces a été identifiée par microscopie à effet tunnel (STM)<sup>7</sup> et par diffraction des électrons lents (LEED)<sup>8</sup>. La structure électronique est mesurée par deux techniques de photoémission, la spectroscopie de photoélectrons X (XPS)<sup>9</sup> et

---

<sup>4</sup>Department CP2S, Institut Jean Lamour (UMR 7198 CNRS-Nancy-Université-UPV-Metz), Ecole Nationale des Mines, Parc de Saurupt, 54042 Nancy Cedex, France

<sup>5</sup>Empa, Swiss Federal Laboratories for Materials Testing and Research, nanotech @ surfaces Laboratory, Feuerwerkerstraße 39, CH-3602 Thun, Switzerland.

<sup>6</sup>Complex Metallic Alloys Network of Excellence

<sup>7</sup>Scanning Tunneling Microscopy

<sup>8</sup>Low Energy Electron Diffraction

<sup>9</sup>X-ray Photoelectron Spectroscopy

UV (UPS)<sup>10</sup>. La diffraction des photoélectrons X (XPD)<sup>11</sup> a été utilisée pour déterminer les arrangements atomiques des plans au voisinage de la surface. Les résultats XPD ont été interprétés en utilisant les modélisations SSC<sup>12</sup>. Des calculs *ab initio* ont été accomplis pour générer des images STM et la densité totale et partielle d'états électroniques.

### 1.1.2 Le modèle structural des deux approximants étudiés

Dans cette section, nous présentons le modèle structural des deux approximants étudiés. Les modèles des cristaux orthorhombiques d' $\text{Al}_{13}\text{Co}_4$  et de T- $\text{Al}_3(\text{Mn}, \text{Pd})$  sont donnés respectivement par Grin *et al.* [66] et par Klein *et al.* [68].

#### 1.1.2.1 Le modèle structural du cristal orthorhombique $\text{Al}_{13}\text{Co}_4$

L'alliage binaire  $\text{Al}_{13}\text{Co}_4$  est un approximant du quasicristal décagonal d'Al-Ni-Co [67, 72, 73]. Grin *et al.* ont mesuré la structure atomique dans le volume en utilisant les techniques de la diffraction des rayons *X* sur monocrystal et la diffraction de poudre [66]. Ce cristal orthorhombique (Symbole de Pearson: *oP102*) de composition  $\text{Al}_{76.5}\text{Co}_{23.5}$  appartient au groupe d'espace *Pmn2*<sub>1</sub>. Il possède 102 atomes par maille (78 atomes d'Al et 24 de Co) avec les paramètres de maille suivant [66, 74]:  $a = 8.158 \text{ \AA}$ ,  $b = 12.342 \text{ \AA}$  et  $c = 14.452 \text{ \AA}$ . La structure de ce cristal est semblable à celle d'autres CMAs comme les phases monocliniques  $\text{Al}_{13}\text{Fe}_4$  [75, 76] et  $\text{Al}_{13}\text{Co}_4$  [77], ainsi que les phases  $\epsilon\text{-Al}_3\text{Co}$  [72] et l' $\text{Al}_{13}(\text{Pd},\text{Fe})_4$  [78]. La structure de cet approximant est décrite le long de la direction [100] par deux types de plans: un plan plat *F* (pour *flat* en anglais) et un plan corrugé *P* (pour *puckered* en anglais). Ces plans sont empilés le long de l'axe *a*, suivant la séquence:  $F_{0.0}P_{0.25}F_{0.5}P_{0.75}$ , où les plans  $P_{0.25}$  et  $P_{0.75}$  sont en position miroir par rapport au plan  $F_{0.5}$ . La distance moyenne qui sépare deux de ces plans est de 2  $\text{\AA}$ . Le plan *F* contient 17 atomes d'Al et 8 de Co. Le plan *P* est plus riche en Al et plus dense que le plan *F*. Il contient 22 atomes d'Al et 4 atomes de Co. Dans le modèle de Grin, la structure ne contient pas de lacunes et tous les sites atomiques sont entièrement occupés par un seul élément.

Les plans empilés suivant l'axe *a* de ce cristal possèdent une symétrie d'ordre *pseudo-10*. En connectant les atomes de Co, la structure du plan *F* peut être décrite par un pavage formé de pentagones et de losanges. Les atomes d'Al du plan *F* décorent les pentagones de Co de deux façons distinctes; soit en formant un pentagone distordu à l'intérieur du pentagone de Co, soit en se positionnant au centre et au milieu des arêtes du pentagone de Co (Fig.1.2(a)). La connexion entre les pentagones du Co est complétée par

---

<sup>10</sup>Ultraviolet Photoelectron Spectroscopy

<sup>11</sup>X-ray Photoelectron Diffraction

<sup>12</sup>Single-Scattering Cluster

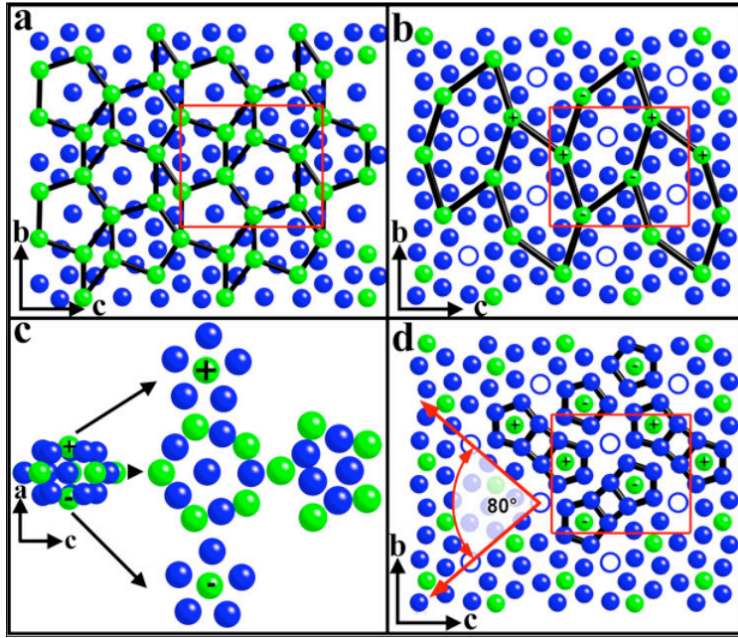


Figure 1.2: La structure du cristal d' $\text{Al}_{13}\text{Co}_4$  est représentée suivant la direction [100] [66]. Les sphères noires (bleues) correspondent aux atomes d'Al et les sphères grises (vertes) aux atomes du Co. Le rectangle indique la maille orthorhombique. (a) Pavage tracé sur le plan plat  $F$  composé par des pentagones et des losanges en connectant les atomes du Co. (b) Le pavage correspondant au plan corrugé  $P$  est composé par des hexagones étirés obtenus en connectant les atomes du Co. (c) Description de l'amas 3D appelé bi-pyramide pentagonale (PB): à gauche, une vue 3D de l'amas PB. Les signes (+) et (-) indiquent respectivement les atomes du Co, situés au-dessus et en dessous des pentagones d'Al; au milieu, nous retrouvons les 3 couches qui forment l'amas PB. Ce dernier est constitué d'un plan plat au centre (formé par un pentagone de Co et un pentagone centré d'Al) et de deux pentagones positionnés au sommet et à la base du PB; à droite, la couche de jonction qui relie les amas PB entre eux le long de la direction [100]. (d) Sur le plan corrugé  $P$ , chaque atome du Co est entouré par un pentagone d'Al formant le sommet ou la base du PB. Les atomes d'Al indiqués par des cercles n'appartiennent pas à l'agrégat PB, et sont intitulés atomes "ciments".

des losanges. Dans le plan  $P$ , la connexion entre les atomes de Co forme un pavage composé d'hexagones étirés (Fig.1.2(b)). Ces hexagones (de longueur d'arête égale à 6.5 Å) pointent dans deux directions. Chaque atome de Co est situé au centre d'un pentagone d'Al. Ces atomes de Co sont positionnés soit légèrement au-dessus ou soit en dessous des pentagones d'Al (position indiquée, respectivement, par (+) et (-) sur la Fig.1.2(b-d)). Le plan  $P$  peut être décrit également par deux types de motifs bi-pentagonaux (Fig.1.2(d)). La longueur des arêtes de ces pentagones individuels varie entre 2.66 et 3.05 Å. Les deux

types de bi-pentagones sont orientés l'un par rapport à l'autre avec un angle de  $80^\circ$ . Cette structure atomique est décrite le long de l'axe  $a$  par un empilement d'agrégats atomiques dit "bi-pyramide pentagonale" PB (pour *pentagonal bipyramid* en anglais) [67, 73, 79]. Cet amas tridimensionnel est composé par 23 atomes (dont 17 atomes d'Al et 6 du Co) et contient 3 couches, une couche équatoriale plate et deux couches corrugées (cap) en haut (+) et en bas (−) de l'amas. La connection entre les amas PB est effectuée par la couche de jonction présentée à droite de la Fig.1.2(c).

### 1.1.2.2 Le modèle structural de la phase T-Al<sub>3</sub>(Mn, Pd)

La phase orthorhombique T-Al<sub>3</sub>(Mn, Pd) est un approximant de la phase décagonale stable du quasicristal Al-Pd-Mn [81]. La structure atomique de cette phase a été déterminée par diffraction des rayons X sur un monocristal avec une composition Al<sub>72.3</sub>Pd<sub>3.2</sub>Mn<sub>24.5</sub> [68, 80]. Le groupe d'espace de ce cristal est *Pnma*, avec une maille composée par 156 atomes et de paramètres suivants:  $a = 14.717 \text{ \AA}$ ,  $b = 12.510 \text{ \AA}$  et  $c = 12.594 \text{ \AA}$ . Les plans atomiques le long de la direction [010] révèlent également une symétrie d'ordre *pseudo*-10.

D'après le modèle de Klein *et al.* [68], deux plans différents décrivent la structure atomique le long de la direction [010]; un plan plat  $F$  et un plan corrugé  $P$ . Ce dernier est divisé en deux sous-plans, à savoir  $P1$  et  $P2$ . Le plan  $F$  situé à  $y = 0.25$  est composé de 22 atomes par maille, avec 14 atomes d'Al et 8 atomes de Mn. La connexion entre les atomes de Mn dans ce plan forme un pavage composé de pentagones et de losanges (voir Fig.1.3(a)). Le plan corrugé  $P1$  situé à  $y \approx 0.38$  est composé de 12 atomes d'Al organisés suivant des chaînes pentagonales (voir Fig.1.3(b)). Les positions atomiques dans les plans  $P1$  et  $P2$  sont totalement occupés, tandis que certaines positions sont partagées avec des lacunes dans le plan  $F$ . Le plan  $P2$  situé à  $y \approx 0.43$  est composé de 16 atomes des trois éléments (Al, Pd et Mn), et quatre de ces sites atomiques (2 Al + 2 Mn) sont totalement occupés. Les 12 autres sites atomiques sont partiellement occupés, avec 10 sites décorés soit avec de l'Al soit avec du Mn, et les 2 autres sites sont partagés entre l'Al et le Pd. Le plan  $P2$  peut être décrit par des chaînes pentagonales en zigzag, où les pentagones sont formés par les sites mixtes d'Al/Mn et les atomes d'Al. Les sites de Mn totalement occupés forment une chaîne de zigzags dans ce plan (voir Fig.1.3(c)). La figure 1.3(d) montre une colonne d'amas icosaédriques qui décrivent la structure le long de l'axe  $b$  et centré autour du point  $x$  (voir Fig.1.3(a,b)). Le cluster est formé par un empilement de prismes ( $p$ ) et d'anti-prismes pentagonaux ( $a$ ) séparés par un atome individuel et suivant la séquence *apaapa*. L'empilement des plans le long de la direction [010] suit la séquence (voir Fig.1.3(e)):

$$P2P1FP1P2P2^*P1^*F^*P1^*P2^* \quad (1.4)$$

où les plans  $F(y = 0.25)$  et  $F^*(y = 0.75)$  sont des plans miroirs. Les plans  $P1^*$ ,  $P2^*$  et  $F^*$  sont tournés de  $\pi$  par rapport aux plans  $P1$ ,  $P2$  et  $F$ . La maille consiste ainsi en deux blocs de plans ( $P2P1FP1P2$ ) et

$(P2^*P1^*F^*P1^*P2^*)$ , chaque bloc ayant une épaisseur égale à  $b/2$ . L'espace de vide entre les deux blocs est de 1.75 Å. Les distances entre les différents plans sont  $d_{P1P2} = 0.625$  Å,  $d_{FP1} = 1.626$  Å et  $d_{FP2} = 2.251$  Å.

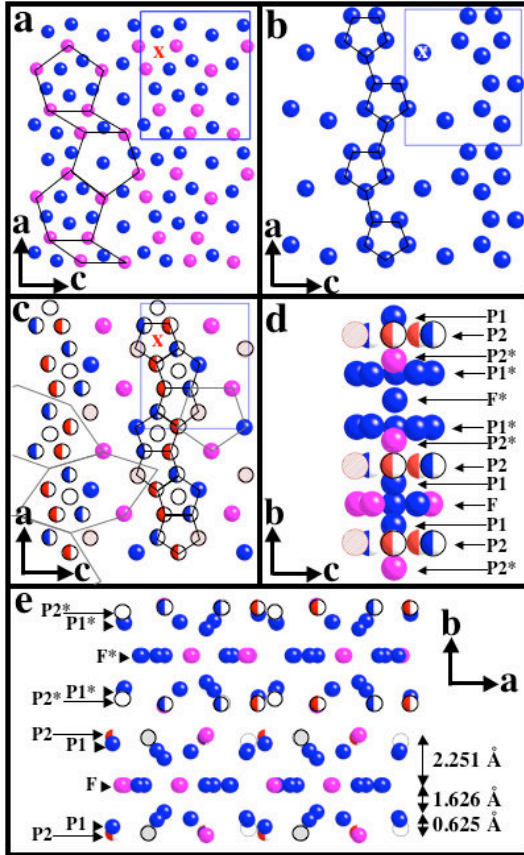


Figure 1.3: La structure du cristal  $T\text{-Al}_3(\text{Mn}, \text{Pd})$  est présentée suivant la direction [010] [68, 80]. Les atomes d'Al sont représentés par les sphères noires (bleues) et les atomes de Mn sont représentés par les sphères grises (roses). Les autres sites atomiques sont des sites mixtes. La maille orthorhomboïque est soulignée par un rectangle. (a) Représentation du plan plat  $F$ . (b) Représentation du plan corrugé  $P1$  composé uniquement d'atomes d'Al formant des chaînes pentagonales. (c) Représentation du plan corrugé  $P2$  composé par les 3 éléments Al, Pd, et Mn. Plusieurs positions sont occupées par deux éléments. Les sphères noires (bleues)-blanches correspondent aux sites mixtes Mn/Al (0.5/0.5), les sites occupés par le Mn/Al (0.3/0.7) sont représentés par les sphères grises (rouges)-blanches, les sites occupés par le Mn/Al (0.15/0.85) sont représentés par les sphères grisées et les sites occupées par le Pd/Al (0.625/0.375) sont présentés par les cercles vides. Les atomes de Mn s'organisent en zigzag et les autres sites forment une chaîne pentagonale. (d) Schéma de la colonne des clusters icosaèdriques centrée au point  $x$  marqué sur (a-c). (e) Représentation de l'empilement des plans perpendiculairement à l'axe  $b$ .

### 1.1.3 Détails expérimentaux

Dans ce travail, nous avons utilisé quatre échantillons, trois cristaux de l’Al<sub>13</sub>Co<sub>4</sub> produit à Jülich, Münich et à Nancy par la méthode Czochralski et un cristal de T-Al<sub>3</sub>(Mn, Pd) produit à Jülich par la méthode de flux. Après la croissance, la surface a été orientée par diffraction de Laue et coupée suivant la direction [100] pour le cristal d’Al<sub>13</sub>Co<sub>4</sub> et suivant la direction [010] pour le cristal de T-Al<sub>3</sub>(Mn, Pd). La surface a été polie mécaniquement par une pâte de diamant en diminuant la taille des grains jusqu’à 0.25  $\mu\text{m}$  et en utilisant du Syton® durant le cycle final. L’échantillon fixé sur une plaque de tantale est introduit ensuite dans la chambre ultra-vide (UHV), avec une pression de base de  $5 \times 10^{-11} \text{ mbar}$ . La préparation de la surface consiste en des cycles de bombardements ioniques d’Ar<sup>+</sup> et de recuits à la température appropriée. La surface (100) de l’échantillon Al<sub>13</sub>Co<sub>4</sub> a été préparée par un bombardement à 1.5  $kV$  (réduit progressivement à 1  $kV$ ) pour une durée de 20 minutes, suivi d’un recuit à des températures variant entre 1073 et 1173  $K$ . Les durées de recuit varient entre 40 minutes et 2 heures. La surface (010) de l’échantillon T-Al<sub>3</sub>(Mn, Pd) a été préparée par un bombardement à 2  $kV$  durant 30 minutes et un recuit à des températures qui varient entre 853 et 923  $K$  pendant une durée allant de 40 minutes à 2 heures. La température de l’échantillon est contrôlée par un pyromètre optique infrarouge avec une émissivité établie à 0.35, couplé à un thermocouple de type *K*. La composition chimique et la structure électronique de l’échantillon sont contrôlées par les techniques XPS et UPS. Le LEED est vérifié après chaque préparation de la surface. Les mesures STM ont été effectuées à température ambiante en utilisant un AFM/STM (VT-AFM) Omicron qui fonctionne à température variable. Les mesures XPD ont été effectuées séparément dans une autre chambre UHV (à l’Empa de Thun) en utilisant une source non-monochromatique de Mg K<sub>α</sub> (1253.6 eV) ou d’Al K<sub>α</sub> (1486.6 eV) et un analyseur d’électrons EA 125 HR qui fonctionne en mode énergie constante (CAE). La calibration du spectromètre a été effectuée en utilisant l’énergie de bande de l’Au 4f<sub>7/2</sub> qui vaut 83.8 eV. Avant d’effectuer les mesures XPD, la qualité de la surface est contrôlée par LEED et XPS.

Après caractérisation des structures atomiques des deux approximants, ces derniers ont été utilisés comme substrat pour des études d’adsorption. Avant chaque dépôt, la qualité et la structure de la surface sont contrôlées par LEED, STM et XPS. Le dépôt a été effectué à température ambiante en utilisant une cellule Omicron de type EFM3 (bombardement électronique d’un creuset), contrôlée en flux. Le taux de dépôt est calibré par STM en mesurant à 300  $K$  les aires recouvertes par les adsorbats sous la monocouche. Durant le dépôt, la pression de la chambre est de l’ordre de  $1 \times 10^{-10} \text{ mbar}$ . Le dépôt du Pb à haute température est accompli avec un substrat chauffé à 573  $K$  durant le dosage. Pour le dépôt du Cu à haute température, le substrat est chauffé à des températures qui varient entre 300 et 573  $K$ . Après le dosage, l’échantillon est maintenu à la température de dosage pendant 15 minutes.

## 1.2 Etude structurale de la surface (100) du cristal $\text{Al}_{13}\text{Co}_4$

Dans ce chapitre, nous rapportons notre étude détaillée de la surface (100) de la phase orthorhombique de l'alliage binaire d' $\text{Al}_{13}\text{Co}_4$ , en utilisant des techniques expérimentales et des calculs *ab initio*. Nous présentons pour la première fois une étude de la structure atomique et électronique de cette surface.

### 1.2.1 Préparation de la surface

Le cliché de LEED (Fig.1.4(a)) est composé de taches de diffraction fines arangées suivant une maille orthorhombique. Le rapport des paramètres de maille mesurés ( $\frac{c}{b} = 1.186$ ) sur le cliché de diffraction est similaire à celui donné par *Grin et al.* ( $\frac{c}{b} = 1.171$ ) [66]. La symétrie d'ordre *pseudo-10* du cliché est moins remarquable que celle mesurée sur d'autres approximants [61, 71]. Les clichés de LEED enregistrés pour les différentes conditions de préparation sont qualitativement identiques, mais la distribution de l'intensité des taches de diffraction varie d'une préparation à l'autre.

Les images STM enregistrées sur la surface (100) du cristal  $\text{Al}_{13}\text{Co}_4$ , montrent deux types de terminaison, libellées  $T1$  et  $T2$ . La présence de la terminaison  $T2$  dépend largement des conditions de préparation de la surface. Cependant,  $T1$  est toujours présente sur les différentes terrasses imagées (voir Fig.1.4(b-c)). Les marches observées sur les images possèdent une hauteur de  $4.2 \pm 0.2 \text{ \AA}$ , ce qui correspond à la moitié du paramètre de maille  $a$  ( $a/2 = 4.08 \text{ \AA}$ ). La hauteur moyenne qui sépare les deux terminaisons  $T1$  et  $T2$  est de  $2.2 \pm 0.2 \text{ \AA}$ . Cette valeur correspond à la distance qui sépare les plans  $F$  et  $P$  dans le modèle structural. La rugosité de  $T2$  est deux fois plus grande que celle de  $T1$  ( $Z_{rms}(T2) = 0.57$  et  $Z_{rms}(T1) = 0.30$ ).

Pour une température de recuit de  $1115 \text{ K}$  pendant  $1 \text{ h}$ , la terminaison  $T1$  domine les terrasses de largeur inférieure à  $20 \text{ nm}$  et la  $T2$  reste visible. Pour la même température de recuit et durant  $2 \text{ h}$ , la  $T2$  domine les terrasses et la  $T1$  est visible sur les bords de marche. En augmentant le temps de recuit de  $1$  à  $2$  heures, les terrasses deviennent plus larges et la terminaison  $T2$  apparaît sur ces terrasses (comparer Fig.1.4(b) et (c)). Une surface recuite à  $1165 \text{ K}$  indique une désorption de la  $T2$  laissant la  $T1$  comme une terminaison qui domine sur toutes les terrasses. La  $T2$  est désorbée complètement pour un recuit à  $1173 \text{ K}$  durant  $2 \text{ h}$ . À ce stade, la présence des lacunes sur la terminaison  $T1$  indiquent le début de l'évaporation de cette terminaison. Il est intéressant de mentionner que les bords de marche restent dépourvus de toute terminaison  $T2$ . Ce phénomène est très certainement une conséquence de mécanismes et de contraintes liés à la hauteur et au bord des marches (Fig.1.4(b-d)). Ces bords de marches sont similaires à ceux observés sur la surface d'ordre *pseudo-10* de la phase  $\xi'$ -Al-Pd-Mn. La rugosité et la diffusivité des marches sont qualitativement moins importantes ici que dans les surfaces quasicristallines [82].

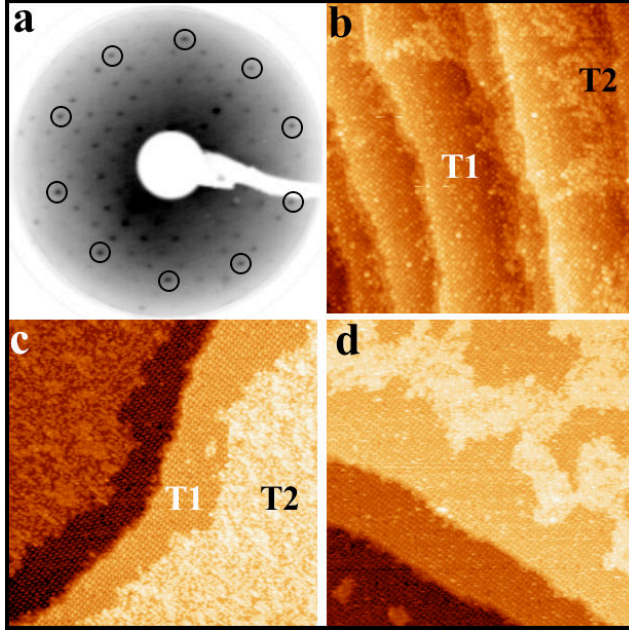


Figure 1.4: (a) Cliché LEED enregistré à 80 eV sur une surface recuite à 1103 K pendant 1 h. (b)-(d) Images STM ( $100 \times 100 \text{ nm}^2$ ) montrant l'évolution de la morphologie pour différentes températures et temps de recuit. (b)  $T = 1115 \text{ K}$  pour  $t = 1 \text{ h}$ , (c)  $T = 1115 \text{ K}$  pour  $t = 2 \text{ h}$ , et (d)  $T = 1165 \text{ K}$  pour  $t = 1 \text{ h}$ . Les deux types de terminaison sont indiqués par  $T1$  et  $T2$ .

### 1.2.2 Identification structurale de la surface

L'analyse des deux terminaisons  $T1$  et  $T2$  par LEED, STM et XPD ne montre aucune reconstruction latérale de la surface. Les spectres XPS confirment qu'il n'y a pas ségrégation chimique sur cette surface. La terminaison  $T1$  peut être décrite par des hexagones étirés et centrés. Chaque sommet d'un hexagone passe par le centre d'un motif de bi-pentagone (voir Fig.1.5(a)). Ces motifs bi-pentagonaux ressemblent à ceux de la Fig.1.2(d) qui décrivent le plan corrugué  $P$  dans le modèle structural. L'angle entre les hexagones sur deux terrasses successives est mesuré à  $80^\circ$ . La hauteur de marche est égale à  $a/2$ . La dimension des pentagones et de la maille de la terminaison  $T1$  sont cohérentes avec celles données par le plan  $P$  ( $x = 0.25$  ou  $x = 0.75$ ) du modèle structural. La transformée de Fourier (FFT) (insert de la Fig.1.5(b)) calculée à partir d'une région  $T1$  montre une structure orthorhombique avec des paramètres de maille ( $b = 12.6 \pm 0.3 \text{ \AA}$  et  $c = 14.5 \pm 0.1 \text{ \AA}$ ) similaires à ceux du modèle structural [66].

Sur une même terrasse, la structure de  $T1$  est constituée de motifs bi-pentagonaux qui pointent dans la même direction (Fig.1.5(a-b)). La structure observée à la surface de la  $T1$  peut être modélisée par 10 atomes d'Al et par 2 atomes de Co. Il est fréquent d'observer des jonctions entre motifs bi-pentagonaux que nous désignons atomes "ciment". Ces atomes "ciments"

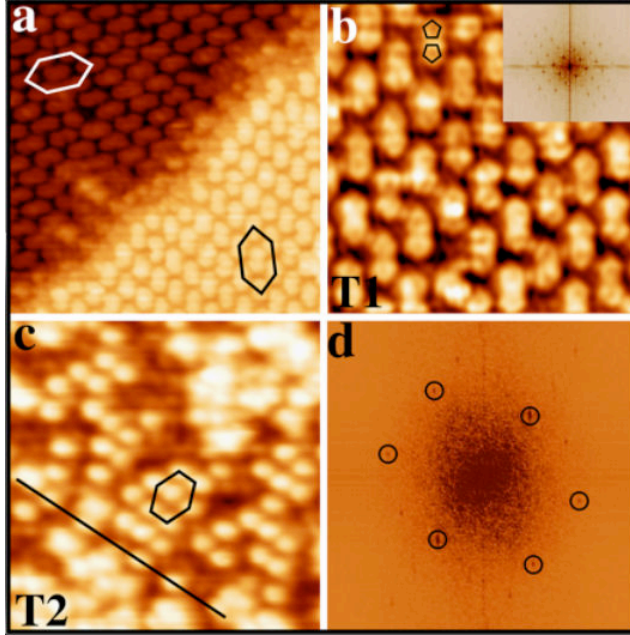


Figure 1.5: (a) Image STM ( $20 \times 20 \text{ nm}^2$ ) de haute résolution montrant deux terrasses successives. L'angle entre deux hexagones étirés est mesuré à  $80^\circ$  entre deux terrasses successives. (b) Image STM ( $10 \times 10 \text{ nm}^2$ ) de résolution atomique enregistrée sur la T1. Des motifs bi-pentagonaux sont indiqués sur l'image. Insert: FFT de la T1 de l'image (b). (c) Image STM ( $10 \times 10 \text{ nm}^2$ ) de résolution atomique enregistrée sur la T2. L'ordre observé sur la T2 est indiqué par la ligne et la forme hexagonale. (d) La FFT calculée à partir d'une région T2 ( $30 \times 50 \text{ nm}^2$ ) montre une structure orthorhombique avec 6 taches plus intenses (encerclées).

n'appartiennent pas à l'amas PB qui relie les motifs bi-pentagonaux. La région T2 de la surface (100) d' $\text{Al}_{13}\text{Co}_4$  est parfaitement ordonnée, comme indiqué sur l'image STM de résolution atomique (voir Fig.1.5(c)). Bien que la T2 soit incomplète, la FFT calculée à partir de cette région montre une structure bien ordonnée. Plusieurs analyses ont été réalisées sur la région T2 pour identifier sa structure atomique. Les positions et les arrangements atomiques de la T2 sont attribuées à des atomes d'Al du plan F du modèle structural. Ces atomes d'Al sont intitulés Al5, Al6, Al7 et Al8 dans le modèle proposé par Grin *et al.* [66]. Les 4 atomes d'Al forment une superstructure oblique qui définit la position des atomes de T2. La position des 4 atomes formant cette superstructure sont:  $(0, 0)$ ,  $(\frac{1}{2}, 0)$ ,  $(\frac{1}{4}, \frac{1}{2})$  et  $(\frac{3}{4}, \frac{1}{2})$ . Le cliché de diffraction calculé à partir de cette superstructure montre une structure orthorhombique avec 6 taches plus intenses autour du centre. Il est semblable à celui calculé à partir de la région T2.

Ces résultats montrent que les plans riches en Al sont sélectionnés à la surface. Etant donné l'absence de reconstruction ou de ségrégation chimique

à la surface, l'énergie libre du système est minimisée par l'exposition des plans atomiques ayant l'énergie de surface la plus faible. Pour la majorité des surfaces de CMAs étudiées jusqu'à présent, les terminaisons sont rapportées à des plans du modèle structural. Pour les CMAs à base d'Al, les surfaces se terminent par des plans denses et riches en Al, c'est-à-dire par l'élément possédant l'énergie de surface la plus faible. Ce critère de sélection des plans de surface est aussi vérifié sur la surface d'ordre *pseudo*-10 du cristal  $\text{Al}_{13}\text{Co}_4$ . Cette surface présente plusieurs similarités avec la surface d'ordre *pseudo*-10 de l'approximant  $\xi'$ -Al-Pd-Mn [61, 62]. Dans ces deux cas, une hauteur de marche unique (correspondant à la moitié du paramètre de maille) est mesurée en surface. Le cliché LEED est cohérent avec une symétrie d'ordre *pseudo*-10. Les deux terminaisons qui composent la surface (100)  $\text{Al}_{13}\text{Co}_4$  font références à des plans incomplets du modèle structural. La structure de la surface est interprétée par comparaison à l'amas élémentaire PB. Elle est décrite par un arrangement des PB coupés perpendiculairement au niveau des "cap" pour former les motifs bi-pentagonaux. L'existence de deux types de terminaisons montre que l'amas pourrait être découpé suivant le plan corrugé au niveau des "cap" pour former les bi-pentagones de la  $T_1$ , ou bien suivant le plan plat  $F$  pour former la structure de la terminaison  $T_2$ .

La surface a été analysée par diffraction des photoélectrons X pour déterminer la nature de la structure atomique des plans proches de la surface. Les mesures ont été réalisées sur la surface (100) d' $\text{Al}_{13}\text{Co}_4$ , pour les deux émetteurs suivants: Al 2s ( $E_{Kin} = 1370 \text{ eV}$ ) et Co 2p<sub>3/2</sub> ( $E_{Kin} = 708 \text{ eV}$ ) (Fig.1.6(a-b)). La répartition des taches de diffraction et leurs intensités respectives révèlent une symétrie décagonale maintenue en surface. Ces motifs décagonaux ressemblent à ceux obtenus sur la surface du quasicristal décagonal Al-Ni-Co [60].

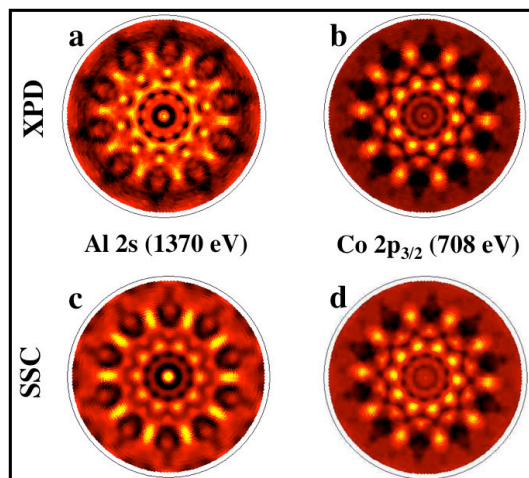


Figure 1.6: *Les motifs XPD expérimentaux mesurés sur la surface (100)  $\text{Al}_{13}\text{Co}_4$  pour les deux niveaux de cœur (a) Al 2s et (b) Co 2p<sub>3/2</sub>. Les motifs générés par la SSC pour les émissions (c) Al 2s et (d) Co 2p<sub>3/2</sub>.*

Ces résultats indiquent que les arrangements autour de l’Al et le Co dans les plans proches de la surface possèdent un ordre décagonal. Des simulations SSC (Single-Scattering Cluster) ont été effectuées pour les deux niveaux de coeur l’Al  $2s$  et le Co  $2p_{3/2}$  pour interpréter les motifs expérimentaux observés. Les motifs XPD ont été reproduits par les simulations SSC (Fig.1.6(c-d)). Cette similité dans les intensités et les positions montre que la structure du massif est conservée dans la région proche de la surface.

### 1.2.3 Densité d’états électroniques calculée et bande de valence

Des calculs de structure électronique *ab initio* ont été effectués pour déterminer la distribution de la densité des charges électroniques pour le cristal d’ $\text{Al}_{13}\text{Co}_4$ . La densité des états électroniques totale calculée pour le cristal orthorhombique  $\text{Al}_{13}\text{Co}_4$  (bas de la Fig.1.7) montre l’existence d’un pseudogap situé à gauche du niveau de Fermi ( $E_F = 0$ ). Le pic dominant dans la DOS totale est situé autour de  $2.0\text{ eV}$  en dessous du niveau de Fermi. Ce dernier est attribué à la contribution des états  $d$  des atomes de Co. Nos résultats sont en accord avec la DOS calculée à partir du cristal monoclinique  $m\text{-Al}_{13}\text{Co}_4$  [67]. Les expériences de photoémission UPS ont été réalisées pour déterminer la bande de valence de la surface (100) d’ $\text{Al}_{13}\text{Co}_4$ . Le spectre expérimental (haut de la Fig.1.7) est dominé par les états  $d$  de l’atome de Co dans la gamme d’énergie  $[-0.5, -2.5\text{ eV}]$  en dessous de l’énergie du niveau de Fermi. Le spectre calculé est en accord avec la bande de valence mesurée. Nous observons un décalage de  $0.5\text{ eV}$  entre le spectre expérimental et calculé. Le signal de la DOS totale observé au-dessus du niveau de Fermi est dû à la contribution des états  $s$  et  $p$  de l’Al. Expérimentalement, cette région pourrait être sondée par photoémission inverse.

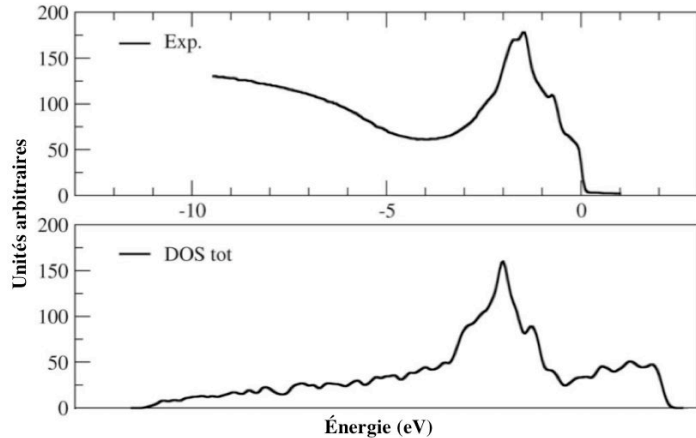


Figure 1.7: *Densité totale des états électroniques calculée pour le cristal d’ $\text{Al}_{13}\text{Co}_4$  (bas) comparée au spectre UPS mesurant la bande de valence (haut).*

### 1.2.4 Images STM simulées

Les images STM simulées issues des calculs *ab initio* ont permis de discriminer parmi les différentes terminaisons possibles à la surface. Quatre modèles de surface ont été testés afin d'obtenir le meilleur accord avec les images expérimentales. Les deux premiers correspondent aux plans complets  $P$  et  $F$ . Suivant la troncature perpendiculairement à la direction [100], le modèle  $P_m$  (ou  $F_m$ ) est formé en laissant comme terminaison de surface le plan  $P$  (ou le plan  $F$ ). Les deux autres modèles  $P_m^+$  et  $P_m^-$  contenant chacun 88 atomes (12 atomes d'Al et 2 atomes de Co ont été retirés du plan complet) sont issus

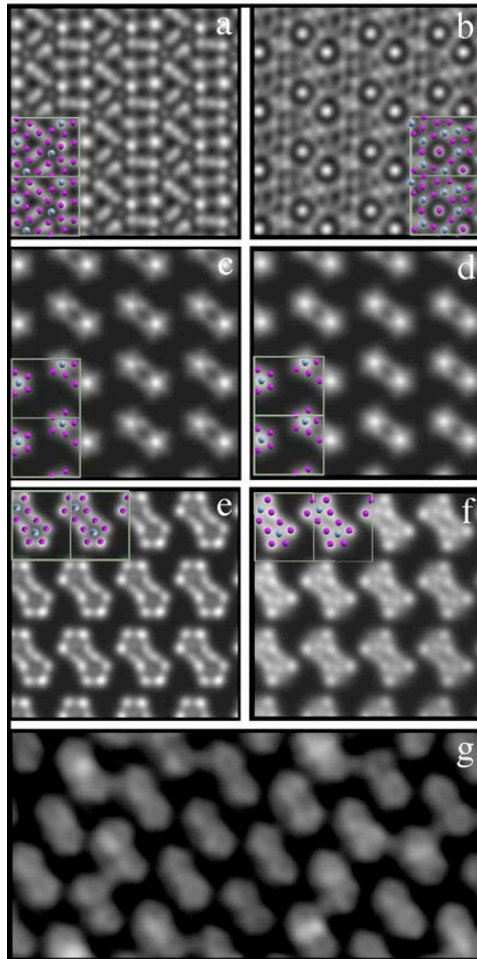


Figure 1.8: (a) *Images STM simulées* ( $5 \times 5 \text{ nm}^2$ ) ( $V_{bias} = -1.3 \text{ V}$ ) comparées à (g) l'*image STM expérimentale* ( $5 \times 10 \text{ nm}^2$ ,  $V_{bias} = -1.3 \text{ V}$ ,  $I = 0.08 \text{ nA}$ ). Les *images STM* sont simulées à partir du plan (a) corrugué  $P$  et (b) plat  $F$ . (c) et (d) correspondent respectivement à l'*image simulée non-relaxée et relaxée* du modèle  $P_m^+$ . (e) et (f) correspondent respectivement à l'*image simulée non-relaxée et relaxée* du modèle  $P_m^-$ . La structure cristallographique des plans est superposée sur les *images simulées*.

du modèle  $P_m$ . Le  $P_m^+$  est construit en préservant à la surface uniquement les motifs bi-pentagonaux formés par les bi-pentagones d'Al et les atomes de Co libellés (+) (sur les Figs.1.2(c-d)). Le quatrième modèle structural  $P_m^-$  est formé en conservant à la surface les bi-pentagones centrés par les atomes de Co libellés (-) situés légèrement en dessous du plan (sur les Figs.1.2(c-d)). L'influence de la relaxation du système sur les surfaces simulées a été testée sur les modèles  $P_m^+$  et  $P_m^-$  (voir les Figs.1.8(d) et (f)). Les images STM simulées à partir des surfaces relaxées ne montrent pas de différences importantes par rapport aux modèles non-relaxés.

La figure 1.8 présente les images STM simulées pour les différents modèles de surface  $P_m$ ,  $F_m^-$ ,  $P_m^+$ , et  $P_m^-$ . Les images STM simulées à partir des plans complets  $P$  ( $P_m$ ) et  $F$  ( $F_m$ ) (Fig.1.8(a-b)), ne présentent aucune ressemblance avec les images STM expérimentales (Fig.1.8(g)). Les figures 1.8(c-f) ont été simulées d'après les terminaisons de surface incomplètes présentées comme modèles  $P_m^+$  et  $P_m^-$ . Ces images simulées révèlent des motifs bi-pentagonaux alignés dans une même direction. Le fort contraste observé sur les images simulées à partir du modèle  $P_m^+$  est généré par les atomes du Co (+) au centre des bi-pentagones d'Al. Les deux images STM relaxées et non-relaxées ne ressemblent pas à l'image mesurée. Cependant, un meilleur accord est obtenu à ce stade pour le modèle  $P_m^-$  pour une surface relaxée ou pas. La différence entre le modèle relaxé et non-relaxé (Fig.1.8(e) et (f)) se situe au niveau du contraste dû à l'atome de Co (-), et au niveau des deux atomes d'Al situés aux extrémités des motifs bi-pentagonaux. Ces observations indiquent que la structure de la surface (100) d' $\text{Al}_{13}\text{Co}_4$  est incomplète, avec une désorption préférentielle d'une partie des atomes présents sur le plan  $P$  du volume.

### 1.2.5 Conclusions

Nous avons étudié la structure atomique de la surface (100) du cristal orthorhombique d' $\text{Al}_{13}\text{Co}_4$ . La topographie de la surface consiste en des terrasses et marches de hauteur  $a/2$ . Suivant les paramètres utilisés pour la préparation de la surface, deux terminaisons coexistent sur les terrasses atomiques. Les deux terminaisons sont corrélées aux plans incomplets présents dans le modèle structural [66]. Pour une température de recuit supérieure à 1173 K, une seule terminaison est préservée à la surface. Elle est attribuée au plan corrugé incomplet composé de 12 atomes. Les images STM simulées valident le modèle de surface proposé. Ce dernier consiste en un plan corrugé incomplet où seuls deux pentagones d'Al centrés par des atomes de Co situés légèrement en dessous du plan sont préservés.

## 1.3 Etude structurale de la surface (010) du cristal T-Al<sub>3</sub>(Mn, Pd)

Dans cette partie, nous présenterons l'étude de la surface (010) de la phase orthorhombique T-Al<sub>3</sub>(Mn, Pd). Les résultats obtenus seront comparés avec les modèles structuraux disponibles et les calculs théoriques.

### 1.3.1 Préparation de la surface

D'après le cliché de LEED (Fig.1.9), un recuit de l'échantillon à 863 K pendant 2 heures suffit pour obtenir une surface ordonnée. Bien que la structure de la surface soit orthorhombique, ce cliché de diffraction est dominé par dix taches plus intenses que les autres. L'anneau décagonal ainsi obtenu confirme la symétrie d'ordre *pseudo*-10 de cette surface T-Al<sub>3</sub>(Mn, Pd). Le rapport des dimensions de la maille orthorhombique ( $\frac{a}{c} \approx 1.18$ ) est similaire à celui donnée par Klein *et al.* ( $\frac{a}{c} = 1.17$ ) [68].

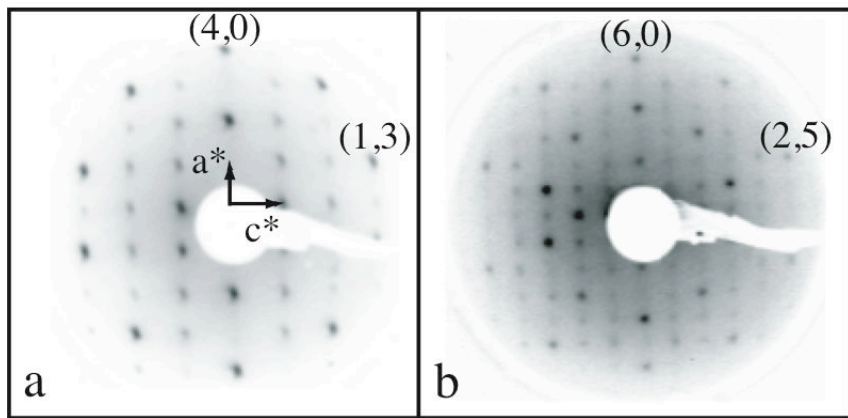


Figure 1.9: *Cliché de LEED enregistré sur la surface (010) du cristal orthorhombique T-Al<sub>3</sub>(Mn, Pd) à 25 eV (a) et 55.9 eV (b).*

A ce stage, les images STM présentent une topographie de surface composée de terrasses et de marches (Fig.1.10(a)). Les terrasses sont séparées par une hauteur de marche égale à  $6.3 \pm 0.3$  Å, ce qui correspond à la moitié du paramètre de maille *b* (*b*/2). Une hauteur de marche équivalente à la moitié du paramètre de maille *a* a été également mesurée sur d'autres surfaces d'approximants [62, 70, 83]. Une marche supplémentaire d'une hauteur égale à  $2.25 \pm 0.10$  est observée essentiellement sur des terrasses étroites (Fig.1.10(b)). Cette hauteur spécifique pourrait être corrélée aux distances inter-plans  $d_{FP2}$  (=2.251 Å) ou  $d_{P1^*P2}$  (=2.378 Å) du modèle structural. La largeur des terrasses varie entre 0.1 à 0.3  $\mu m$ . La rugosité des bords de marche s'avère plus prononcée ici que celle observée sur d'autres approximants (Al<sub>13</sub>Co<sub>4</sub> [70] et chapitre 3 et  $\xi'$ -Al-Pd-Mn [61]). La rugosité intrinsèque des terrasses ( $Z_{rms}$ ),

qui dépend de la taille de la région imagée et des conditions de balayage, varie de 0.1 à 0.2 Å. Les valeurs de  $Z_{rms}$  obtenues sur cette surface sont deux fois plus faibles que celles obtenues sur les surfaces quasicristallines. La FFT de la surface montre une structure orthorhombique avec des paramètres de maille identiques à ceux du modèle structural.

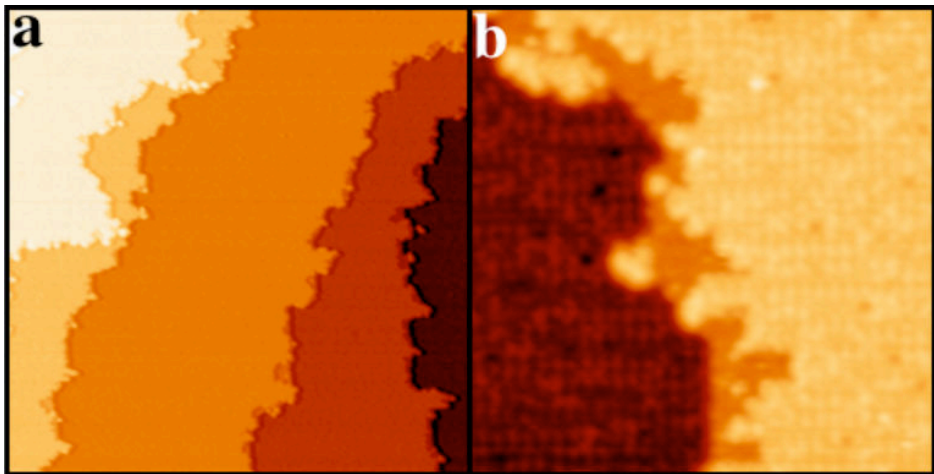


Figure 1.10: (a) Image STM ( $250 \times 250 \text{ nm}^2$ ) montrant la morphologie de la surface (010) du cristal  $T\text{-Al}_3(\text{Mn, Pd})$ . (b) Image STM ( $40 \times 40 \text{ nm}^2$ ) de haute résolution. La maille orthorhombique et une terrasse très étroite peuvent être distinguées.

Les images STM de résolution atomique enregistrées sur les différentes terrasses dévoilent un nombre conséquent d'imperfections structurales (Fig.1.11). La surface peut être décrite comme composée de zones d'intensités homogènes distribuées sur un réseau orthorhombique de manière irrégulière. En plus de ces imperfections, la dépendance en polarisation des images STM rend difficile l'identification de la structure atomique de la surface. Cette variation du contraste en fonction des paramètres de balayage a été vérifiée en comparant 4 images STM enregistrées pour différentes valeurs de tension sur la même région de la surface et à courant tunnel constant ( $I_t = 40 \text{ pA}$ ). Un courant tunnel plus important permet d'obtenir une résolution atomique. Les images STM obtenues en sondant les états inoccupés proches du niveau de Fermi ( $V_b = 0.8 \text{ V}$ ) montre une topographie dominée par des motifs larges et brillants, distribués d'une manière périodique. Lorsque nous sondons les états occupés (images STM mesurées pour une tension négative), la structure apparaît moins rugueuse et est dominée par des zigzags se propageant le long de la direction [100]. Les lacunes de surface sont systématiquement visibles indépendamment de la polarisation utilisée.

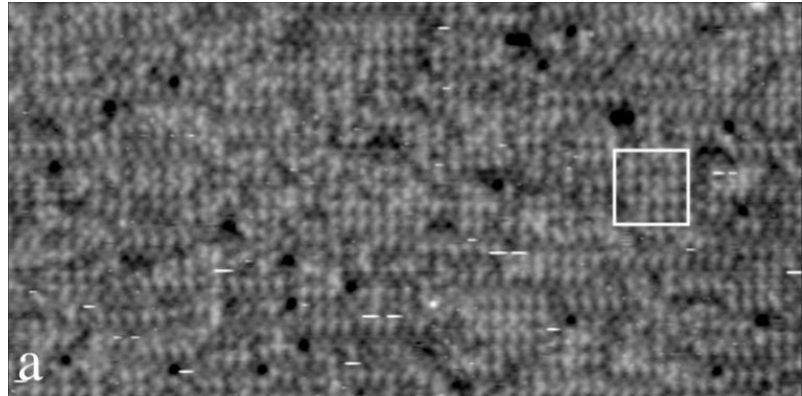


Figure 1.11: (a) Image STM ( $70 \times 35 \text{ nm}^2$ ) enregistrée sur une terrasse pour  $V_b = 2.0 \text{ V}$  et  $I_t = 0.06 \text{ nA}$ . Le rectangle blanc souligne une région de contraste homogène.

### 1.3.2 Structure atomique de la surface

#### 1.3.2.1 Images STM expérimentales

La figure 1.12 présente des images STM de résolution atomique obtenues sur la surface (010) de T-Al<sub>3</sub>(Mn, Pd) pour un courant tunnel élevé. Il existe une bonne correspondance entre les arrangements atomiques observés expérimentalement et ceux présents sur les plans corrugués  $P1$  et  $P2$  du modèle structural. En effet, les chaînes pentagonales se propageant le long de la direction [100] sur ces deux plans du volume sont aisément visibles sur la Fig.1.12(a). Cependant, aucun accord n'a pu être établi avec le plan plat  $F$ . Pour différencier les deux types de plans  $P$ , nous avons superposé sur l'image STM les deux structures possibles. Notre discrimination entre  $P1$  et  $P2$  repose sur la position des atomes situés entre les chaînes de pentagones. Dans un cas ( $P2$ ), les atomes isolés de Mn (encerclés sur la Fig.1.12(c-d)) sont alignés avec les arêtes communes des pentagones. Dans l'autre ( $P1$ ), l'alignement des atomes d'Al avec la chaîne pentagonale est différent. De par la cohérence avec les positions atomiques, nous concluons à une structure de surface terminée par le plan  $P2$  du modèle structural.

Les différences de contraste observées sur les images STM sont liées au désordre chimique intrinsèque à la structure du cristal et à une occupation mixte des sites de  $P2$ . Il est intéressant de noter que les lacunes présentes sur la Fig.1.12 sont comparables aux étoiles sombres (DS pour “dark star”) qui peuplent la surface d’ordre-5 du quasicristal  $i$ -Al-Pd-Mn. Ces DS sont produites par une décoration irrégulière de la première couche de l’amas de *pseudo*-Mackay [84]. Les dépressions présentes sur la surface de T-Al<sub>3</sub>(Mn, Pd) n’ont pas de correspondance dans le modèle structural. Cependant, elles sont créées par l’apparition d’une lacune sur les sites atomiques labellisés TM(5) dans le modèle de Klein [68]. Les positions TM(5) sont occupées soit par

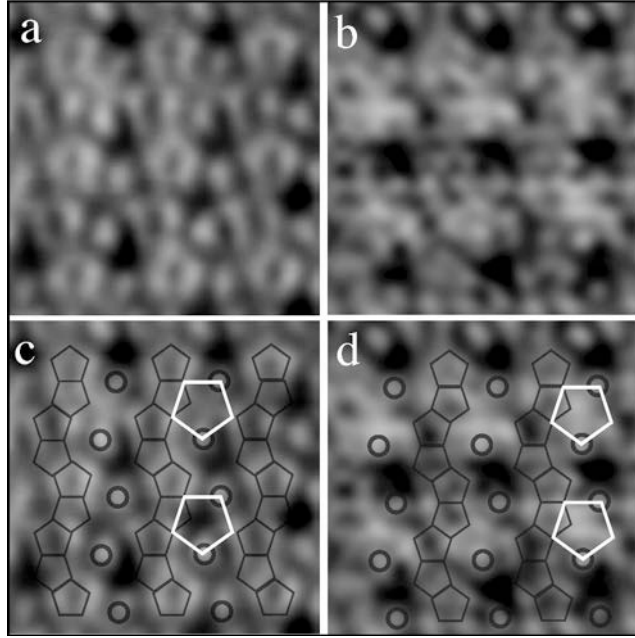


Figure 1.12: (a) Images STM ( $4 \times 4 \text{ nm}^2$ ) de résolution atomique (filtrées par transformée de Fourier rapide). (a) et (c) sont enregistrés à  $V_{bias} = -0.4 \text{ V}$  et  $I_t = 0.36 \text{ nA}$ . (b) et (d) sont enregistrées sur une autre région pour une polarisation de  $V_{bias} = 0.6 \text{ V}$  et  $I_t = 0.50 \text{ nA}$ . Un pavage décrivant la structure du plan P2 a été superposé aux deux images (c) et (d). Les chaînes pentagonales se propageant en zigzag le long de la direction [100] et les atomes individuels de Mn sont clairement distingués.

des atomes de Mn(0.15) soit par de l’Al(0.85). Elles sont localisées sur la Fig.1.12(c) à l’intérieur des grands pentagones blancs et à l’intérieur des étoiles sombres. Lorsque ces sites sont occupés, ils contribuent significativement à l’intensité de l’image STM, limitant la résolution des chaînes pentagonales (forte intensité à l’intérieur du pentagone blanc sur la Fig.1.12(d)). Cette désorption atomique sélective pourrait être expliquée par l’environnement local et l’occupation du site TM(5). Les deux plus proches voisins correspondent aux sites TM(1) et TM(3) avec des facteurs d’occupation respectivement de 0.3Mn-0.7Al et 0.5Mn-0.5Al. Suivant la décoration chimique des sites TM(1) et TM(3), l’interaction avec les atomes du site TM(5) (0.15Mn-0.85Al) devrait être considérablement différente (attractive/répulsive). De plus, une coordination réduite des atomes Mn/Al des sites TM(5) à la surface pourrait favoriser une telle désorption.

### 1.3.2.2 Images STM simulées

Pour identifier la structure de la surface, des images STM simulées du plan P2 ont été générées à partir de calculs *ab initio* des structures électroniques. La dépendance du contraste observée expérimentalement est reproduite sur les

images STM calculées à courant constant et pour deux valeurs de polarisation de la pointe STM;  $V_{bias} = -0.4 \text{ V}$  et  $V_{bias} = +0.4 \text{ V}$  correspondant respectivement aux états occupés et inoccupés autour du niveau de Fermi. Le contraste à l'intérieur du plus large pentagone (souligné en rouge sur la Fig.1.13) et des sites occupés par le Mn varie considérablement. Le désordre chimique associé à la structure réelle de la surface ne peut pas être pris en compte par les calculs qui demandent un seul élément par site. Cette restriction implique une comparaison simplement qualitative entre les images expérimentales et simulées. Les motifs principaux caractérisant les images STM expérimentales sont reproduits sur les images simulées (pentagones, lacunes). Les zones sombres (ou lacunes) sur la Fig.1.13 correspondent à l'emplacement des étoiles sombres de la Fig.1.12. La différence de forme s'explique ici par une occupation du site TM(5) par un atome de Mn dans les simulations.

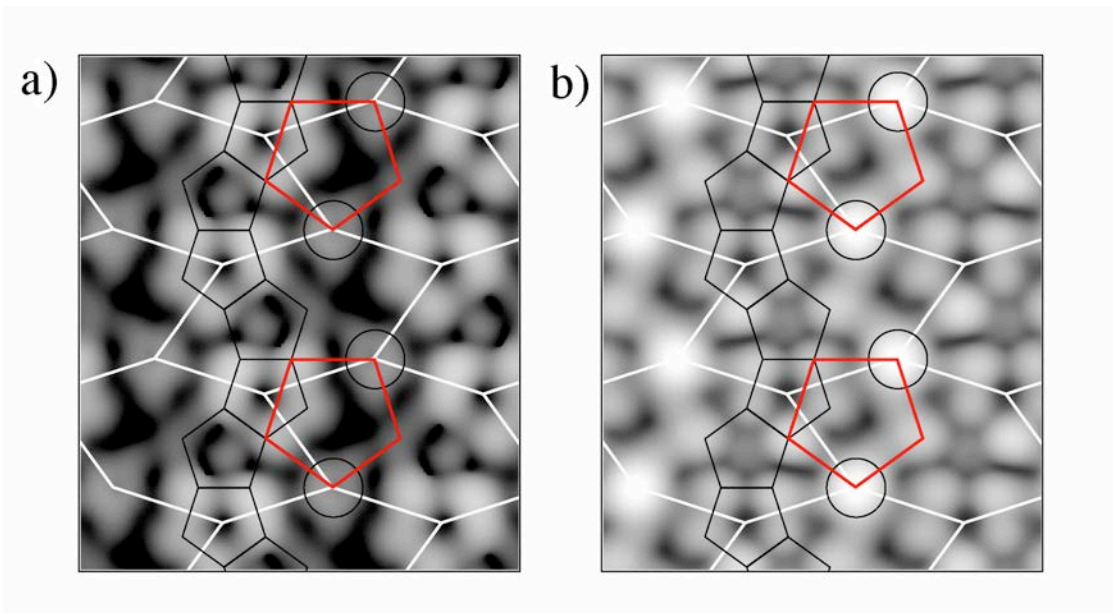


Figure 1.13: *Images STM simulées pour une surface terminée par un plan  $P2$  pour (a)  $V_b = -0.4 \text{ V}$  et pour (b)  $V_b = +0.4 \text{ V}$ . Les motifs caractérisant cette surface sont indiqués sur les deux images.*

Le long de l'axe  $b$ , la plus grande distance qui sépare deux plans consécutifs se situe entre les deux plans  $P2$  et  $P2^*$ . A l'aide de calculs DFT, il a été possible de déterminer la hauteur de coupe la plus favorable à travers le modèle, perpendiculairement à la direction [010]. L'application d'une contrainte de traction le long de l'axe (010) suivie d'une relaxation structurale démontre que le clivage s'effectue entre deux plans  $P2$  et  $P2^*$ . Dans le modèle structural, le plan  $P1$  est situé à  $0.625 \text{ \AA}$  sous le plan  $P2$ . Une combinaison des deux plans ( $P2 + P1$ ) produit une couche plus dense que le plan  $F$  et une concentration en Al plus élevée. En accord avec les précédents travaux sur les surfaces quasicristallines [42], le clivage du cristal se fait entre les plans les plus distants

le long de la direction [010], exposant ainsi à la surface les plans les plus denses, composés d'éléments à faible énergie de surface (riche en Al). Il n'est pas possible d'estimer la concentration des atomes d'Al ou des métaux de transition (Pd et Mn) à la surface du fait du désordre chimique intrinsèque à la structure du modèle et aux imperfections structurales observées à la surface. Cependant, l'analyse des spectres XPS ne montre aucune ségrégation chimique sur cette surface. Nos résultats indiquent également qu'il n'y a pas de reconstruction latérale de la surface (010) de la phase T-Al<sub>3</sub>(Mn, Pd).

### 1.3.2.3 Diffraction des photoélectrons X

La même surface a été étudiée par diffraction des photoélectrons X. Les résultats sont comparés avec les simulations SSC. Les motifs XPD ont été mesurés pour les trois émetteurs Al 2s, Pd 3d<sub>5/2</sub> et Mn 2p<sub>3/2</sub> en utilisant une source Al K<sub>α</sub> (1486.7 eV). Les images sont composées de plusieurs anneaux de 10 taches d'intensité équivalente. Ces motifs ont été parfaitement reproduits par nos simulations SSC. Ces simulations n'ont pas permis d'identifier la terminaison préférentielle à la surface. Cependant, ces résultats révèlent que la région proche de la surface possède localement une symétrie décagonale.

### 1.3.3 Structure électronique de la surface

Dans les quasicristaux et les alliages d'Al-Mn, les états *d* du Mn dominent la DOS totale autour du niveau de Fermi ( $E_F$ ). La structure électronique de ces alliages est caractérisée par une réduction de la DOS au niveau de  $E_F$  (*pseudo-gap*). L'analyse de la structure électronique de la surface (010) de la phase T-Al<sub>3</sub>(Mn, Pd) a été réalisée par les techniques de photoémission XPS et UPS. Les spectres sont comparés à ceux obtenus sur la surface d'ordre-5 du quasicristal *i*-Al-Pd-Mn et aux calculs *ab initio* de structure électronique. La comparaison entre les deux spectres expérimentaux d'UPS mesurés sur la phase T-Al<sub>3</sub>(Mn, Pd) et le quasicristal *i*-Al-Pd-Mn (Fig.1.14) montre une variation de l'intensité spectrale proche du niveau de Fermi plus rapide pour l'approximant que pour le quasicristal. En d'autres termes, le spectre de la bande de valence de la phase T-Al<sub>3</sub>(Mn, Pd) a un caractère plus métallique. Une concentration plus élevée des atomes de Mn dans cet alliage T-Al<sub>3</sub>(Mn, Pd) permet d'expliquer une contribution des états *d* du Mn plus importante dans la DOS totale. Cependant, la légère diminution de l'intensité spectrale entre le niveau de Fermi et -0.5 eV pourrait être expliquée par l'existence d'un *pseudo-gap* moins prononcé dans le cas de l'approximant que dans le quasicristal. Ces résultats ont été confrontés à des calculs *ab initio*. Ces derniers reproduisent les bandes de valence mesurées expérimentalement sur le quasicristal et l'approximant.

Une approche indirecte a été utilisée pour évaluer la DOS et la présence ou pas d'un *pseudo-gap* au  $E_F$ . Elle est basée sur l'étude de l'asymétrie du spectre de la raie du Mn 2p. Le paramètre d'asymétrie  $\alpha$  donné par la formule de

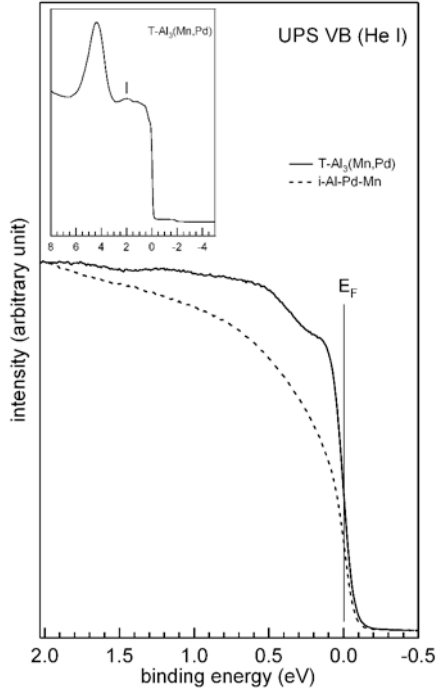


Figure 1.14: Spectre UPS proche du niveau de Fermi  $E_F$  du cristal  $T\text{-Al}_3(\text{Mn, Pd})$  (courbe continue) et le quasicristal  $i\text{-Al-Pd-Mn}$  (courbe pointillée).

Doniach-Šunjić [85] renseigne indirectement sur la DOS au  $E_F$ . Le *pseudo-gap* dans le quasicristal  $i\text{-Al-Pd-Mn}$  mène à un paramètre d'asymétrie  $\alpha$  entre 0.14 et 0.18, significativement plus bas que celui mesuré à 0.34 pour un métal Mn [86]. Pour la phase  $T\text{-Al}_3(\text{Mn, Pd})$ , nous avons mesuré un facteur d'asymétrie égal à  $\alpha = 0.200 \pm 0.013$ . Cette valeur confirme nos résultats précédents, à savoir que la phase  $T\text{-Al}_3(\text{Mn, Pd})$  semble plus métallique que le quasicristal parent et possède un *pseudo-gap* moins prononcé que ce dernier dû à une importante contribution des états  $d$  du Mn dans la DOS au  $E_F$ .

### 1.3.4 Conclusions

La structure atomique de la surface (010) du cristal orthorhombique  $T\text{-Al}_3(\text{Mn, Pd})$  a été étudiée par plusieurs techniques expérimentales et par des calculs *ab initio* de structure électronique. Le cliché de LEED et les motifs XPD confirment la symétrie d'ordre *pseudo-10* de cette surface. Pour une surface préparée à 923 K, les terrasses observées possèdent une très faible rugosité et sont séparées par une hauteur du marche égale à la moitié du paramètre maille ( $b/2$ ). Malgré les imperfections structurales qui caractérisent cette surface, nous avons pu corrélérer la structure atomique observée par STM aux plans corrugés présents dans le modèle structural [68]. La terminaison de la surface consiste en une combinaison du plan  $P2$  et du plan  $P1$  situé à 0.65 Å

en dessous de  $P2$ . La forte variation du contraste en fonction de la polarisation de la pointe STM est reproduite par les images STM simulées du plan  $P2$ . Les mesures de photoémission révèlent que cette phase cristalline est caractérisée par une densité d'états électroniques plus élevée au niveau de Fermi par rapport à celle mesurée sur la surface d'ordre 5 de la phase  $i$ -Al-Pd-Mn.

## 1.4 Adsorption du Pb sur les cristaux d' $\text{Al}_{13}\text{Co}_4$ et de T-Al<sub>3</sub>(Mn, Pd)

Dans cette partie, les deux surfaces précédemment caractérisées sont utilisées comme substrats pour des études d'adsorption atomique. Notre objectif est ici de former un film pseudomorphique constitué d'une seul élément. Une telle configuration devrait permettre d'établir l'importance de la complexité structurale, indépendamment de la complexité chimique, sur les propriétés physico-chimiques des CMA.

À l'équilibre thermodynamique, le mode de croissance couche par couche [87] est obtenu lorsque:

$$\Delta\gamma = \gamma_0 + \gamma_i - \gamma_s \leq 0 \quad (1.5)$$

où  $\gamma_0$  et  $\gamma_s$  sont, respectivement, les énergies libres de surface de l'adsorbat et du substrat et  $\gamma_i$  correspond à l'énergie libre de l'interface adsorbat-substrat. À ce stade, nous connaissons pas l'énergie de surface de l'adsorbat des deux approximants terminés par des plans riches en Al. Du fait de son énergie de surface plus faible que celles de l'Al(111) (favorisant ainsi une croissance couche par couche), le Pb apparaît comme un adsorbat approprié. Les deux échantillons utilisés présentent une complexité différente. L'alliage binaire  $\text{Al}_{13}\text{Co}_4$  possède une maille de 102 atomes où tous les sites atomiques sont entièrement occupés (voir section 1.1.2.1). La phase ternaire T-Al<sub>3</sub>(Mn, Pd) possède une maille de dimension plus importante (156 atomes) avec des sites atomiques qui sont entièrement occupés par un ou plusieurs éléments chimiques ou lacunaires (TM(5)) (voir section 1.1.2.2).

### 1.4.1 Croissance du plomb sur la surface (100) du cristal $\text{Al}_{13}\text{Co}_4$

#### 1.4.1.1 Dépôt à 300 K

Plusieurs dosages, allant de 0.1 à 12 monocouches équivalentes (MLE), ont été effectués sur la surface (100) de  $\text{Al}_{13}\text{Co}_4$ . Les clichés de LEED correspondants montrent une structure orthorhombique avec des paramètres de maille similaires à ceux déterminés sur la surface non revêtue. Au fur et à mesure des expositions, la structure de la surface reste inchangée mais la qualité du cliché de diffraction se dégrade légèrement. Ces observations suggèrent une croissance pseudomorphique des atomes de Pb sur cette surface. La dégradation

du cliché pourrait s'expliquer par un regroupement des adsorbats sous forme d'agrégats sur plusieurs défauts de surface (voir Fig.1.18(b)).

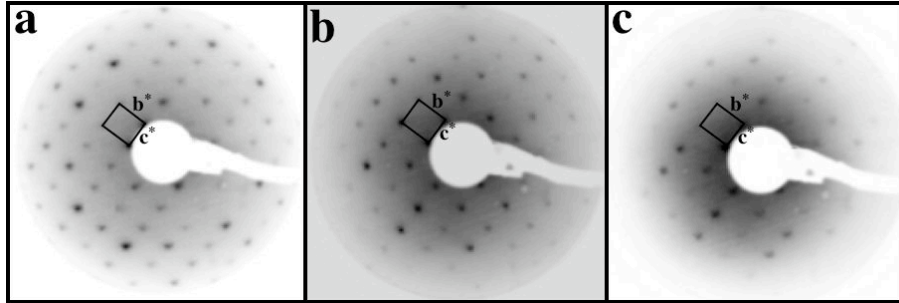


Figure 1.15: *Clichés de LEED enregistrés à 40 eV à la température ambiante en fonction du recouvrement du Pb. (a) surface nue, (b) 1 MLE et (c) 7 MLE.*

A présent, nous nous concentrons sur les résultats obtenus à l'aide de la microscopie à effet tunnel pour les différentes expositions. Lors de l'adsorption à bas recouvrement ( $\leq 0.3$  MLE), les atomes de Pb individuels sont facilement identifiables sur les terminaisons de type T1. A ce stade, nous n'observons pas la formation d'îlots nanométriques. Une partie de ces adsorbats décore clairement les bords de la terminaison T2. Il est relativement difficile d'estimer le nombre d'atomes de Pb piégé au sein même de ce plan T2. Les distances mesurées entre les atomes individuels de Pb correspondent à des multiples des paramètres de maille  $b$  ou  $c$  (Fig.1.16). Ceci indique une adsorption bien ordonnée des adsorbats par rapport au réseau du substrat. Les stries (soulignées par un flèche grise sur la Fig.1.16(a)) sont associées à une forte mobilité des atomes du Pb sur cette surface à 300 K. La Fig.1.16 (flèche blanche) met en

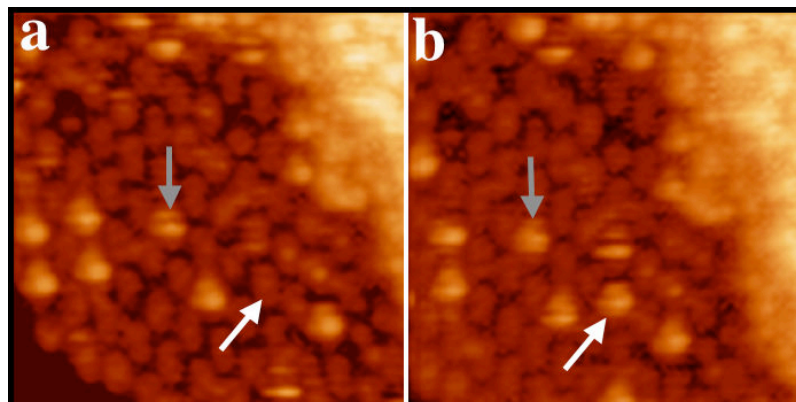


Figure 1.16: (a) et (b) *Comparaison entre deux images STM ( $15 \times 15 \text{ nm}^2$ ) mesurées successivement sur la même région et pour le même dépôt. Les flèches indiquent une mobilité évidente de plusieurs adsorbats entre les deux balayages. Le temps entre les deux mesures est de quelques minutes.*

évidence l'occupation d'un site, jusqu'à présent vacant, par un adsorbat. Pour ce régime de dépôt, les motifs bi-pentagonaux caractérisant le plan  $T1$  sont toujours visibles et particulièrement bien résolus. Une inspection de plusieurs images STM enregistrées consécutivement au même endroit sur la surface, permet d'identifier un site d'adsorption préférentiel des atomes de Pb. Ces derniers se situent au-dessus des motifs bi-pentagonaux et plus précisément entre les deux pentagones qui forment ce dernier (Fig.1.2(c-d)). Ce site paraît relativement réactif car il est parfois décoré par des défauts ponctuels (contamination ou atomes intrinsèques au cristal) sur la surface nue.

Pour un recouvrement de 0.38 MLE, les atomes de Pb se regroupent pour former des rangées atomiques alignées suivant la direction [010] (voir Fig.1.17(a)). Ces rangées atomiques de hauteur  $2.1 \pm 0.1 \text{ \AA}$  croissent à partir des bords du plan  $T2$  et à partir du milieu de la terminaison  $T1$ . Après le dépôt de 0.75 MLE de Pb, la première monocouche ( $\text{Pb}+T2$ ) est pratiquement complète (Fig.1.17(b)). La FFT calculée en sélectionnant uniquement la monocouche de Pb dévoile une structure orthorhombique de paramètres de maille similaires à ceux du substrat.

Une couche complète de Pb, où des régions de  $T2$  restent discernables de part leur contraste spécifique, est obtenue après exposition de la surface à 1.5 MLE (Fig.1.17(c)). Le film est caractérisée par des trous qui repré-

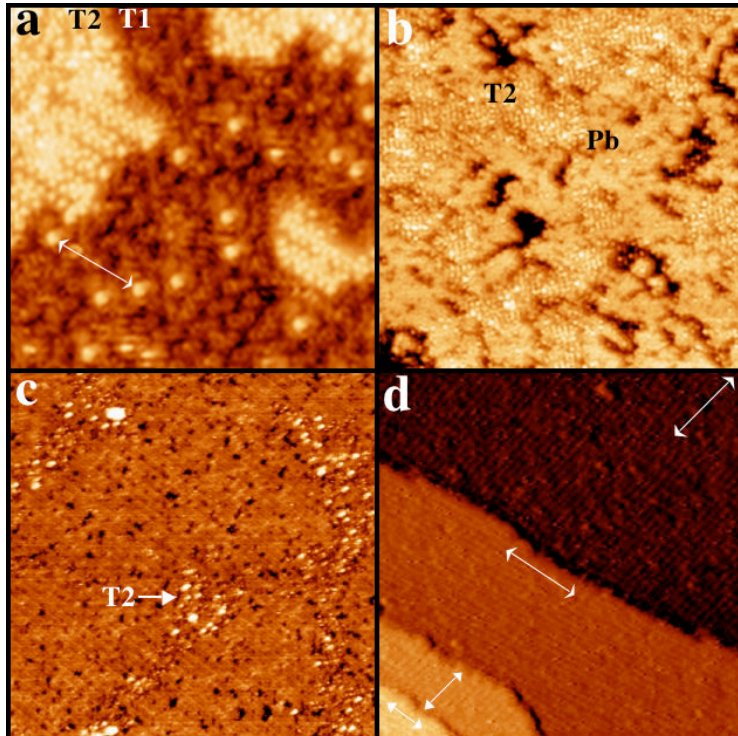


Figure 1.17: *Images STM enregistrées pour 4 dépôts différents de Pb à 300 K. (a) 0.38 MLE ( $20 \times 20 \text{ nm}^2$ ). (b) 0.75 MLE ( $80 \times 80 \text{ nm}^2$ ). (c) 1.5 MLE ( $35 \times 35 \text{ nm}^2$ ). (d) 3.0 MLE ( $50 \times 50 \text{ nm}^2$ ).*

tent près de 4 % de l'aire totale imagée. Les rangées atomiques observées sont espacées de  $\sim 15$  Å le long de la direction [001], i.e. valeur comparable au paramètre de maille  $c$ . La FFT calculée à ce stade est de meilleure qualité et reflète le caractère orthorhombique du film déposé. Les images STM combinées aux clichés de LEED nous permettent de conclure à une croissance pseudomorphique du Pb. Pour des expositions plus importantes (3 MLE), la morphologie du film n'est pas modifiée. Pour certaines conditions de balayage en STM, nous pouvons distinguer des lignes atomiques orientées à  $80^\circ$  entre deux terrasses successives et séparées par  $\sim 10$  Å. Ce phénomène rappelle la rotation déjà observée des motifs bi-pentagonaux d'une terrasse à la suivante (Fig.1.17(d)).

Au-dessus de 1.5 MLE, la morphologie du film de Pb ne change pas et les îlots associés à la formation de la seconde monocouche demeurent inexistant. A priori, il n'est pas possible de former une deuxième couche de Pb sur la surface (100) de  $\text{Al}_{13}\text{Co}_4$ . Un coefficient de collage qui s'annule après le dépôt de la première couche a été rapporté pour les études d'adsorption de Pb sur les surfaces quasicristallines [88, 89]. Les résultats de photoémission XPS obtenus sur la surface de  $\text{Al}_{13}\text{Co}_4$  révèlent une faible interaction entre les atomes d'Al et le Pb. Ajoutée à l'immiscibilité du Pb et de l'Al [90, 91], la formation d'un alliage Al-Pb paraît peu probable. L'analyse des niveaux de coeur Al 2p et Pb 4f lors de l'adsorption du Pb sur les surfaces des quasicristaux et sur l'Al(111) [88, 89, 92] mène à une conclusion identique.

Comme le montre la Fig.1.18, l'évolution du rapport des aires Pb 4f/Al 2p en fonction de l'exposition s'avère rapide jusqu'à la fin de la formation de la première monocouche. Au-delà de ce dosage et en introduisant nos observations STM, l'augmentation de ce rapport peut s'expliquer par un coefficient de collage nul sur les terrasses atomiques et une diffusion des adsorbats jusqu'à des défauts de surface (marches, dislocations) où des amas nanométriques de Pb (largeur  $50 - 60$  nm, hauteur  $2 - 8$  nm) apparaissent Fig.1.18(b)).

#### 1.4.1.2 Dépôt à 573 K

L'adsorption à haute température est réalisée par le dépôt d'une monocouche du Pb sur un substrat maintenu à 573 K. Cette approche améliore considérablement l'ordre structural du film de Pb et de ce fait la qualité des clichés de diffraction (Fig.1.19(a)) et la résolution des images STM (rugosité plus basse mesurée à  $0.16 \pm 0.04$  Å). La maille orthorhombique mesurée est similaire à celle donnée dans le modèle de Grin [66]. Ce résultat est confirmé par le calcul de la FFT (insert Fig.1.19(b)). L'adsorption à haute température (Fig.1.19(b-c)) ne modifie pas le mode de croissance qui reste pseudomorphique. A présent, la structure atomique du film de Pb peut être décrite par un réseau orthorhombique décoré par des motifs pentagonaux irréguliers (Fig.1.19(c)). La longueur moyenne de l'arête d'un pentagone est estimée à  $\sim 4.9$  Å. Cette valeur est approximativement 5/3 fois plus importante que l'arête des pentagones de la sur-

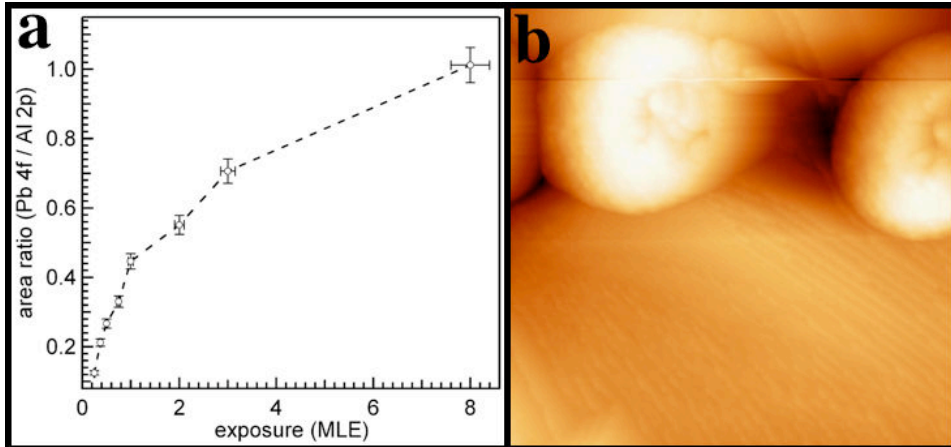


Figure 1.18: (a) Rapport des aires  $\text{Pb } 4f/\text{Al } 2p$  en fonction de l'exposition. (b) Image STM ( $167 \times 167 \text{ nm}^2$ ) dévoilant des amas de Pb obtenus après 3.0 MLE.

face nue de  $\text{Al}_{13}\text{Co}_4$ . Une même longueur a été mesurée lors de la formation d'îlots pentagonaux de Pb sur la surface quasicristalline d' $i$ -Al-Pd-Mn [93]. Une connexion entre points de fortes intensités mène à une structure décrite par des motifs bi-pentagonaux, i.e. similaire à celle du substrat (Fig.1.19(d)). Bien qu'il y ait plusieurs positionnements possibles, un des modèles consiste à superposer le plan corrugé  $P$  du volume de telle sorte que les motifs bi-pentagonaux se situent à l'intérieur des bi-pentagones constitués par les atomes de Pb. Dans cette situation, les atomes dits “ciment” du plan  $P$  coïncident avec les atomes partagés entre les bi-pentagones de Pb. Comme pour les dépôts à la température ambiante, les motifs bi-pentagonaux de la surface non revêtue semblent jouer un rôle déterminant dans la formation de la première monocouche du Pb. Des études expérimentales supplémentaires (LEED dynamique I-V) couplées à des images STM simulées (générées à partir des calculs *d'ab initio*) sont nécessaires pour valider notre modèle structural.

### 1.4.2 Croissance du plomb sur la surface (010) du cristal T-Al<sub>3</sub>(Mn, Pd)

#### 1.4.2.1 Dépôt à 300 K

Comme dans l'étude précédente, l'adsorption du Pb à 300 K sur la surface (010) de la phase T-Al<sub>3</sub>(Mn, Pd) conduit à une structure orthorhombique du film. Les paramètres de maille issus du cliché de LEED et de la FFT pour les différents dépôts (allant de 0.1 à 8 MLE) sont similaires à ceux de la surface nue. La symétrie d'ordre *pseudo*-10 reste présente après une exposition de la surface à 8 MLE de Pb. Les analyses XPS montrent que ce recouvrement correspond en fait à un dépôt entre 1.5 et 2 ML (coefficent de collage du Pb inférieur à l'unité). Ces mesures indiquent une croissance pseudomorphique du Pb sur cette surface d'approximant.

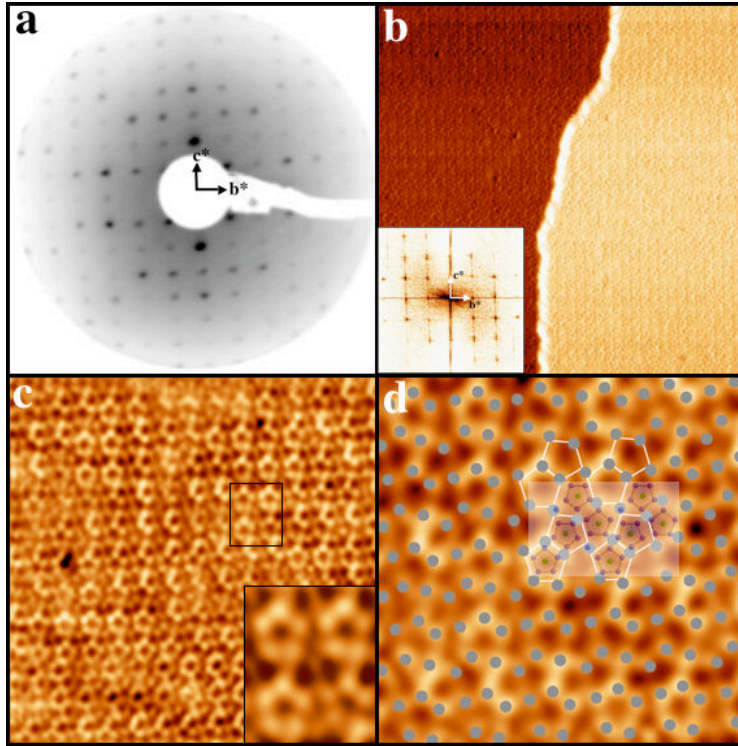


Figure 1.19: Monocouche de Pb déposée à 573 K sur le substrat  $Al_{13}Co_4$ . (a) Cliché de LEED enregistré à 65 eV. (b) Image STM ( $50 \times 50 \text{ nm}^2$ ) présentant deux terrasses atomiques recouvertes d'une monocouche de Pb. Insert: FFT de l'image STM en (b). (c) Image STM ( $18 \times 18 \text{ nm}^2$ ) de résolution atomique. Insert: grossissement du rectangle souligné en (c) permettant de distinguer 4 pentagones irréguliers. (d) Pavage d'une région ( $7.25 \times 7.25 \text{ nm}^2$ ) de (c) en utilisant des motifs bi-pentagonaux (pentagones blancs). Le plan  $P$  du modèle structural de  $Al_{13}Co_4$  a été superposé sur la structure du Pb.

Dans le chapitre 3, nous avons observé la présence de lacunes et de nombreuses imperfections structurales à la surface de cet échantillon (Fig.1.20(a)). Ceci rend particulièrement difficile toute identification de sites préférentiels d'adsorption sur ce substrat. A 0.1 MLE, les atomes du Pb sont mesurés à une hauteur de  $1.76 \pm 0.10 \text{ \AA}$  par rapport au substrat. Une fois les adsorbs regroupés en îlots, la hauteur de marche de ces derniers est mesurée à  $2.15 \pm 0.10 \text{ \AA}$ , indépendamment du nombre de monocouches déposées (Fig.1.20(b-f)). Les îlots ainsi obtenus sont de forme irrégulière. Du fait d'une rugosité importante, la résolution des images STM reste limitée. Au fur et à mesure des dosages, la variation des aires recouvertes par le Pb atteste de l'adsorption de plusieurs monocouches de Pb. Le mode de croissance est de type Frank-van der Merwe (FM) [87]. Bien que nous puissions déposer plus d'une seule couche de Pb, le coefficient de collage est réduit considérablement après la formation de la première monocouche. Cette diminution est confirmée par les analyses de photoémission XPS. De nouveau, nos résultats en photoémission

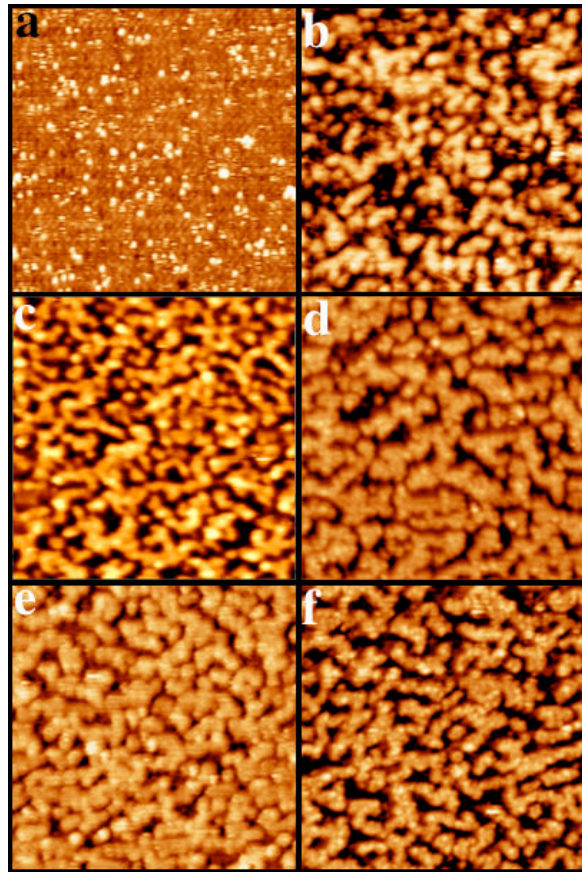


Figure 1.20: *Images STM ( $50 \times 50\text{nm}^2$ ) enregistrées sur la surface (010) de  $T\text{-Al}_3(\text{Mn, Pd})$ , après une exposition au Pb à (a) 0.1 MLE, (b) 0.5 MLE, (c) 1 MLE, (d) 4 MLE, (e) 5.5 MLE et (f) 7 MLE. Le dépôt est effectué à température ambiante.*

montrent que la formation d'un alliage Al-Pb de surface est peu probable.

#### 1.4.2.2 Dépôt à 573 K

L'adsorption de Pb a également été effectuée avec le cristal  $T\text{-Al}_3(\text{Mn, Pd})$  maintenu à 573 K lors du dépôt. Pour 1 MLE, les taches de diffraction de LEED indiquent une structure orthorhombique du film, avec des paramètres de maille en accord avec ceux de la surface nue. La symétrie d'ordre *pseudo*-10 est préservée après le dosage. Par conséquent, les adsorbats adoptent une structure orthorhombique et la FFT calculée à partir d'images STM atteste d'une croissance pseudomorphique du Pb à cette température (Fig.1.21(d)). De par la qualité du LEED et de la FFT, il est évident que la température améliore l'ordre structural du film de Pb déposé sur le cristal  $T\text{-Al}_3(\text{Mn, Pd})$  (Fig.1.21(a-b)). A 0.6 ML, les images STM de haute résolution présentent une structure composée de motifs et de lacunes pentagonaux (voir cercles sur la Fig.1.21(b-c)). Les analyses des dimensions et de la distribution de ces arrangements

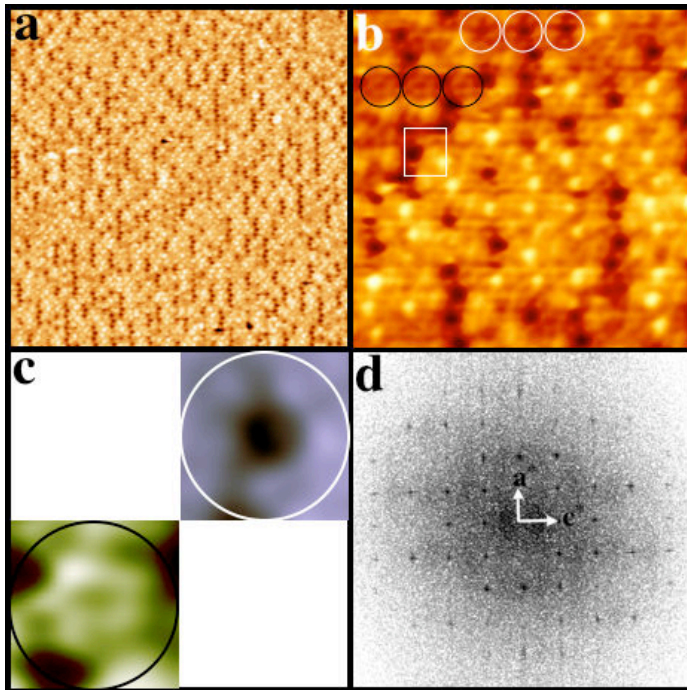


Figure 1.21: (a) Image STM ( $48 \times 48 \text{ nm}^2$ ) enregistrée après le dépôt d'1 MLE de Pb sur le substrat de T-Al<sub>3</sub>(Mn, Pd) maintenu à 573 K. (b) Image STM ( $10 \times 10 \text{ nm}^2$ ) de résolution atomique, où une maille est soulignée. Les lacunes pentagonales (cercles blancs) et certains motifs appartenant aux chaînes pentagonales de la surface nue sont encerclés (cercles noirs). (c) Cercle blanc: grossissement d'une lacune pentagonale, cercle noir: grossissement d'un arrangement pentagonal. (d) FFT calculée à partir d'une image STM ( $23 \times 23 \text{ nm}^2$ ) en sélectionnant uniquement le film de Pb.

pentagonaux démontrent que ces derniers correspondent respectivement aux lacunes et aux pentagones des chaînes pentagonales de la surface propre. La rugosité de la surface dosée est deux fois (0.4 Å) plus grande celle de la surface propre (0.1-0.2 Å). En regroupant toutes ces mesures et en tenant compte de nos mesures de composition par XPS, il apparaît que la monocouche de Pb reste incomplète pour ce taux d'exposition. Une partie du substrat encore visible explique notamment la qualité des clichés de diffraction enregistrés. Les atomes de Pb parfaitement ordonnés sur la surface T-Al<sub>3</sub>(Mn, Pd) correspondent aux motifs les plus intenses sur la Fig.1.21.

### 1.4.3 Conclusions

L'adsorption de Pb sur les surfaces (100) de Al<sub>13</sub>Co<sub>4</sub> et (010) du cristal T-Al<sub>3</sub>(Mn, Pd) a été caractérisée à 300 K et à 573 K. Dans les deux cas, la croissance du Pb est pseudomorphique jusqu'à la formation d'une monocouche. Aucun signe de diffusion de l'adsorbat dans le volume ou de formation

d'un alliage de surface n'a pu être détecté par nos mesures en XPS. Au cours de la phase initiale d'adsorption, un site de nucléation préférentiel a été identifié uniquement sur la surface (100) de  $\text{Al}_{13}\text{Co}_4$ . Il correspond au centre du motif bi-pentagonal. Pour une exposition supérieure à la monocouche, le coefficient de collage du Pb sur la surface de  $\text{Al}_{13}\text{Co}_4$  s'annule. Le dépôt des adsorbats à 573 K améliore considérablement l'ordre structural du film. La structure de cette monocouche peut être défini par un pavage basé sur des motifs bi-pentagonaux. La croissance du Pb sur la surface (010) de l'alliage T-Al<sub>3</sub>(Mn, Pd) mène à la formation d'îlots de formes irrégulières. Bien que le coefficient de collage du Pb diminue au cours des dépôts, il ne s'annule pas et la croissance de couches additionnelles est alors rendue possible. A 573 K, les atomes de Pb adoptent une structure pseudomorphique. Cependant, la surface n'est pas entièrement recouverte de Pb et plusieurs motifs appartenant à la surface propre sont discernables. Ces études d'adsorption de Pb mettent en évidence un comportement différent des adsorbats sur les deux surfaces d'ordre *pseudo*-10 de ces approximants. Notamment, une différence majeure est notée au niveau du coefficient de collage du Pb sur ces deux substrats. Des mesures de la structure électronique (UPS et/ou STS) des premières monocouches du Pb sur ces deux surfaces pourraient éventuellement expliquer ce comportement.

## 1.5 Caractérisation de l'adsorption de Cu sur la surface (100) du cristal $\text{Al}_{13}\text{Co}_4$

Dans le but de former un film quasicristallin ternaire d'Al-Cu-Co, nous avons déposé du Cu sur la surface (100) de l'approximant d' $\text{Al}_{13}\text{Co}_4$ . Les résultats obtenus dans cette étude sont comparés avec ceux obtenus sur des surfaces quasicristallines icosaédriques d'Al-Pd-Mn et d'Al-Cu-Fe. Un des objectifs de cette étude est également de faire croître une monocouche pseudomorphique de Cu sur cette surface de CMA. La croissance de Cu sur la surface d'ordre *pseudo*-10 de l' $\text{Al}_{13}\text{Co}_4$  a été caractérisée en fonction de la température (entre 300 K et 573 K) et des caractéristiques des dépôts, à l'aide des techniques STM, LEED, XPS et XPD. Avant chaque dépôt, la topographie et la composition du substrat sont contrôlées. La température de recuit utilisée pour préparer la surface est choisie afin de préserver uniquement la terminaison *T1*. Cependant, la gamme de températures nécessaire pour sélectionner une seule terminaison à la surface sans la formation des lacunes reste assez étroite. Comme démontré par les clichés de LEED et les images XPD, la symétrie d'ordre *pseudo*-10 est maintenue en surface.

### 1.5.1 Adsorption du Cu à 300 K

L'adsorption de Cu à la température ambiante mène à la formation de deux structures différentes. Pour un recouvrement inférieur ou égale à 1 ML, les

atomes de Cu adoptent la structure orthorhombique du substrat. Les clichés de LEED enregistrés à 0.5 ou à 1 ML sont similaires à ceux de la surface non revêtue (avec des paramètres de maille comparables), et la symétrie d'ordre *pseudo*-10 demeure bien visible (Fig.1.22(a)). Les images XPD constitués d'anneaux formés par 10 taches intenses confirment la symétrie décagonale de la surface. La FFT calculée à partir d'une image STM enregistrée pour une monocouche de Cu montre une structure orthorhombique avec des paramètres de maille semblables à ceux de la surface nue. L'analyse des spectres XPS mesurés pour les niveaux de coeur Al 2s, Co 2p et Cu 2p révèle un film composé des trois éléments chimiques. Ce comportement d'inter-diffusion a été rapporté lors du dépôt de Cu sur la surface Al(111) [94].

La formation de la seconde couche est observée avec une décoration préférentielle des bords de marche avant même que la première monocouche soit complète (Fig.1.22(a)). La hauteur des îlots de la seconde couche est mesurée à  $2.20 \pm 0.20$  Å. A partir de 2 ML, les taches de diffraction indiquent la formation d'une nouvelle structure. Les analyses des clichés de LEED indiquent la formation de deux domaines désorientés l'un par rapport à l'autre de  $\sim 72^\circ$  (Fig.1.22(c)). Les distances calculées à partir du LEED montre une structure de type CsCl orientée suivant la direction (110). Le paramètre de maille de cette nouvelle structure issue du cliché de diffraction est  $a = (2.85 \pm 0.10)$  Å.

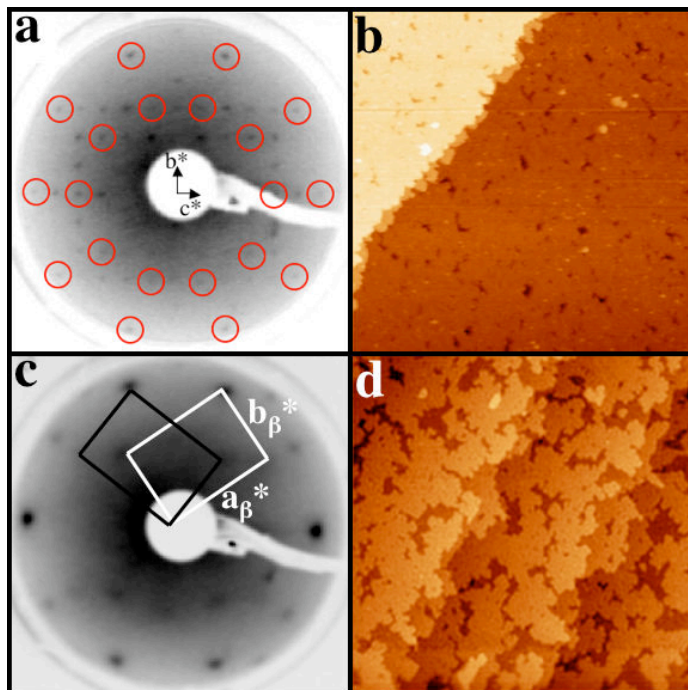


Figure 1.22: 1 ML de Cu déposée à 300 K sur le substrat d' $Al_{13}Co_4$ : (a) Cliché de LEED enregistré à 60 eV et (b) Image STM de  $100 \times 100$  nm $^2$ . (c) Cliché de LEED enregistré à 60 eV, pour un film de 3 ML de Cu. (d) Image STM ( $150 \times 150$  nm $^2$ ) enregistrée pour un recouvrement de 4 ML.

La structure de la phase- $\beta$  de l'alliage ternaire Al(Cu,Co) a été rapportée avec un paramètre de maille égal à  $a = 2.875 \text{ \AA}$  [95]. Pour un recouvrement de 8ML de Cu, le cliché de LEED n'est pas modifié, i.e. la structure de la phase  $\beta$ -Al(Cu,Co) est préservée en surface. L'image STM enregistrée à 4 ML (Fig.1.22(d)) montre une croissance de type couche par couche. Les clichés XPD mesurés pour les niveaux de coeur Cu  $2p_{3/2}$  et Al  $2s$  sont cohérents avec une structure de type CsCl. Des simulations SSC ont été menées en utilisant la structure cubique CsCl pour confirmer la formation de la phase- $\beta$ . Les caractéristiques principales des clichés XPD sont reproduites par les simulations SSC. A 8 ML, l'absence d'une image XPD pour le Co  $2p_{3/2}$  permet de conclure à une phase- $\beta$  formée uniquement d'Al et de Cu. Ce résultat est confirmé par les expériences XPS, qui montrent une augmentation du rapport Al/Co au cours du dépôt. Dans le diagramme de phases Al-Cu, une autre structure possède un paramètre de maille très proche de celui déterminé par le cliché de LEED. Cette phase est l'alliage binaire d'AlCu<sub>3</sub> qui possède un paramètre de maille  $a = 2.956 \text{ \AA}$ . Cette phase est écartée car elle s'avère n'être stable qu'à haute température ( $1052 \text{ K}$ ) [95]. La phase- $\beta$  a déjà été observée lors de l'adsorption de Cu sur la surface d'ordre-5 du quasicristal d'Al-Cu-Fe à  $300 \text{ K}$  [96]. Dans ces travaux, la phase  $\beta$ -Al(Cu, Fe) formée après 2 ML de Cu croît suivant cinq domaines différents orientés avec un angle de  $72^\circ$  les uns par rapport aux autres. Sur la surface orthorhombique de Al<sub>13</sub>Co<sub>4</sub>, nous avons identifié deux domaines orientés à  $72^\circ$  l'un par rapport à l'autre. Dans ces deux systèmes, la croissance de la phase- $\beta$  se développe suivant la direction des lignes atomiques les plus denses. Sur notre substrat, ces lignes correspondent à la direction des deux types de motifs bi-pentagonaux présents dans le plan corrugué  $P$  du modèle structural de Grin et al. [66]. Ces derniers sont orientés dans le plan P avec un angle de  $72.7^\circ$ .

### 1.5.2 Adsorption du Cu pour une température inférieure ou égale à 573 K

Des expériences identiques ont été effectuées entre 473 et 573 K. Comme à température ambiante, les atomes de Cu adoptent une structure pseudomorphique jusqu'à 1 MLE. Les clichés de LEED, XPD et la FFT calculés indiquent que la symétrie d'ordre *pseudo*-10 est conservée dans ces conditions de dépôt (Fig.1.23(b)). Pour un recouvrement inférieur à la monocouche, la densité plus faible des agrégats atomiques en surface s'explique par une coalescence plus prononcée de ces derniers à cette température d'adsorption. La décoration des bords de marches par les atomes de Cu atteste d'une mobilité plus élevée dans ce régime de température. Sur les images STM de haute résolution, des structures fines sont visibles au sein même de ces îlots nanométriques. A ce stade, la rugosité de la surface est faible ( $0.14 \text{ \AA}$ ) en comparaison de celle mesurée à  $300 \text{ K}$  ( $0.23 \text{ \AA}$ ). Plusieurs motifs pentagonaux identifiés dans ce film sont distribués suivant un réseau orthorhombique de dimensions similaires à celui de la surface nue (Fig.1.23(a)). Ces motifs pentagonaux irréguliers possé-

dent une arête de longueur moyenne estimée à  $6.1 \pm 0.5$  Å. La topographie de cette surface dosée reste inchangée en fonction de la polarisation de la pointe STM. Les deux dépôts de Pb et de Cu réalisés sur l'échantillon d' $\text{Al}_{13}\text{Co}_4$  montrent que la croissance de la première monocouche est liée fortement aux motifs bi-pentagonaux de la surface nue. Les structures atomiques exactes de ces couches restent à être déterminer.

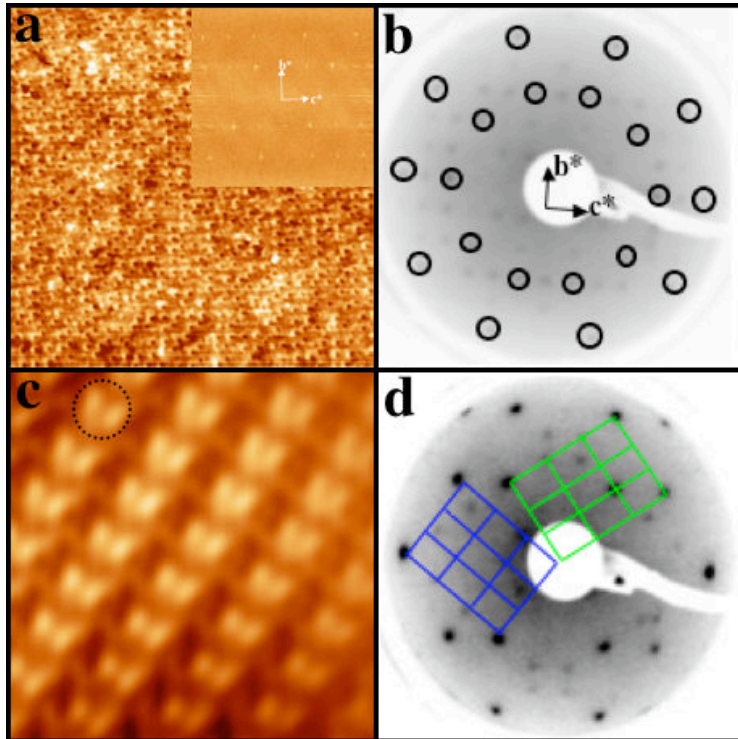


Figure 1.23: (a) *Image STM (filtrée par transformée de Fourier rapide) de résolution atomique enregistrée pour 1 ML de Cu déposée à 573 K sur le substrat de  $\text{Al}_{13}\text{Co}_4$  ( $40 \times 40$  nm $^2$ ) . Insert: FFT de l'image STM en (a).* (b) *Cliché de LEED enregistré à 60 eV sur lequel deux anneaux décagonaux marquent la symétrie d'ordre pseudo-10 de la surface.* (c) *L'image STM ( $6 \times 6$  nm $^2$ ) présente un seul domaine de la structure de  $\gamma\text{-Al}_4\text{Cu}_9$  obtenue pour un recouvrement de 10 ML.* (d) *Cliché de LEED enregistré à 60 eV sur ce film de 10 ML de Cu.*

Après la formation d'une monocouche pseudomorphique, nous assistons à l'apparition de la phase  $\beta\text{-Al}(\text{Cu}, \text{Co})$  à partir d'un recouvrement de 2 ML. Comme à température ambiante, deux domaines [110] sont orientés à 72° l'un de l'autre. Le cliché de LEED correspondant à la phase  $\beta$  est toujours visible jusqu'à une exposition de 4 ML (Fig.1.22(c)). La qualité de ce dernier est supérieure à celle obtenue à 300 K. Au-delà de ce recouvrement (7 ML), des taches additionnelles dans le cliché de diffraction révèlent la formation d'une nouvelle phase. Les paramètres de maille de cette nouvelle structure calculés à partir du LEED et de la FFT sont  $a = 8.68 \pm 0.30$  Å et  $b = 12.54 \pm 0.20$  Å.

Cette maille peut être corrélée aux dimensions d'une surface (110) de la phase  $\gamma\text{-Al}_4\text{Cu}_9$  [95]. Comme pour la phase  $\beta$ , la phase  $\gamma$  croît suivant deux domaines distincts orientés à  $72^\circ$  l'un de l'autre. Pour une exposition à 10 ML, le cliché LEED (Fig.1.24(d)) reste inchangé. L'image STM (Fig.1.24(c)) montre des détails structuraux fins similaires à ceux observés sur la surface (110) du monocristal  $\gamma\text{-Al}_4\text{Cu}_9$  étudié actuellement au sein de notre groupe [65]. La formation de la phase  $\gamma\text{-Al}_4\text{Cu}_9$  comme alliage de surface a été rapportée dans deux études d'adsorption du Cu sur les quasicristaux Al-Cu-Fe [96] et Al-Pd-Mn [97]. Dans toutes ces études, le plan (110) apparaît comme terminaison de surface, il correspond au plan le plus dense de la phase  $\gamma$ .

Les mesures XPD confirment l'apparition d'une nouvelle structure à partir de 8 ML. Pour cette épaisseur, le film est composé essentiellement d'Al et de Cu (absence de structure dans l'image XPD du Co 2p). Les images XPD sont parfaitement reproduites par les simulations SSC établies pour deux domaines (110) (séparés angulairement de  $72^\circ$ ) de la phase  $\gamma\text{-Al}_4\text{Cu}_9$ .

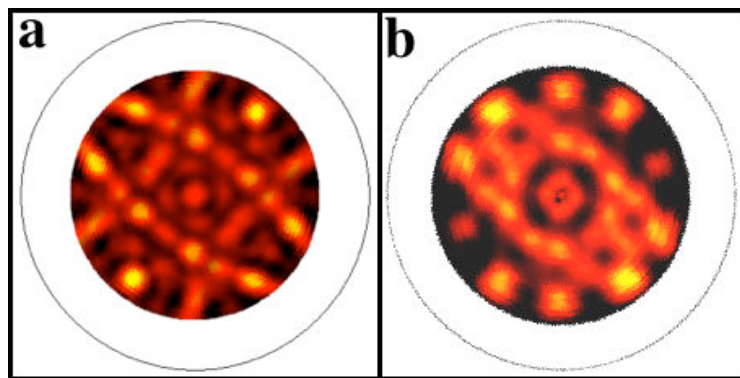


Figure 1.24: (a) Simulation SSC pour le niveau de coeur Cu 2p ( $E_{Kin} = 1166$  eV) résultant de la superposition (avec une rotation de  $72^\circ$ ) de deux simulations SSC, chacune établie pour un domaine (110) de la phase  $\gamma\text{-Al}_4\text{Cu}_9$ . (b) Image XPD mesurée pour le niveau de coeur Cu 2p.

### 1.5.3 Conclusions

La surface (100) du cristal d' $\text{Al}_{13}\text{Co}_4$  a été aussi utilisée comme substrat pour la caractérisation de l'adsorption de Cu. De 300 à 573 K, les atomes de Cu suivent une croissance pseudomorphique jusqu'à la monocouche. A 300 K, la phase  $\beta\text{-Al(Cu, Co)}$  apparaît pour des recouvrements supérieurs à la monocouche. Pour des températures de dépôt supérieures à 300 K, la phase  $\beta\text{-Al(Cu, Co)}$  est suivie par la formation de la phase  $\gamma\text{-Al}_4\text{Cu}_9$ . Les deux phases mènent à la formation de deux domaines (110) désorientés de  $72^\circ$  l'un par rapport à l'autre. La complexité structurale du substrat n'a aucune influence sur la for-

mation de la phase  $\gamma$ -Al<sub>4</sub>Cu<sub>9</sub>. La quantité d'Al et de Cu reste évidemment un point critique pour obtenir cette phase complexe. Le but initial de cette étude était de former la phase décagonale du quasicristal Al-Cu-Co. Des expériences supplémentaires seront nécessaires pour vérifier la possibilité de croître cette phase quasicristalline à la surface.

## 1.6 Conclusions et perspectives

Nous avons réussi à caractériser la surface d'ordre *pseudo*-10 des deux cristaux d'Al<sub>13</sub>Co<sub>4</sub> et de T-Al<sub>3</sub>(Mn, Pd), considérés comme approximants des quasicristaux décagonaux. Ces deux surfaces ont été préparées par des bombardements et des recuits sous ultravide. Chacune de ces surfaces est caractérisée par des terrasses plates séparées par une hauteur de marche équivalente à la moitié du paramètre de maille. La structure des terminaisons a été identifiée dans certains plans des modèles structuraux. Comme pour les quasicristaux, les critères de sélection des terminaisons de surface sont respectés pour nos deux échantillons. En effet, les plans exposés à la surface correspondent aux plans les plus denses et les plus riches en Al. La hauteur de coupe du modèle se réalise à l'endroit où les distances inter-planaire sont les plus importantes. Pour le cristal d'Al<sub>13</sub>Co<sub>4</sub>, la terminaison a été rapportée au plan corrugé incomplet *P*. Nous avons proposé un modèle de surface qui contient 12 atomes (10 Al + 2 Co) avec une désorption de 14 atomes sur les 26 atomes qui forment le plan *P*. Dans le cas de la phase T-Al<sub>3</sub>(Mn, Pd), le plan de la surface consiste en une combinaison des deux plans corrugés du modèle désignés par *P1* et *P2*. En effet, *P1* et *P2* ne sont séparés que par une distance de 0.625 Å. Le clivage se produit ainsi entre les plans *P2* et *P2\** (où *P2\** désigne le miroir de *P2*), où apparaît la séparation la plus large entre deux plans dans le modèle. Comme dans le cas des quasicristaux, aucune ségrégation chimique et/ou reconstruction de surface n'a été observée sur ces surfaces de CMA. Les images STM expérimentales ont été reproduites par les images simulées issues des calculs *ab initio*.

Suite à ces travaux, nous avons utilisé ces surfaces comme substrats pour déposer des films minces du Cu et du Pb. Le dépôt à la température ambiante ou à température plus élevée indique que les adsorbats adoptent une structure pseudomorphique jusqu'à la première monocouche. Ces films représentent des systèmes intermédiaires entre les surfaces propres des cristaux du Pb et du Cu, et les films apériodiques formés sur les surfaces quasicristallines. Ces études offrent la possibilité d'étudier la structure électronique et les propriétés physico-chimiques des films du Pb et du Cu de complexité structurale croissante. Des mesures de photoémission et/ou de spectroscopie à effet tunnel pourraient être effectuées pour caractériser les structures électroniques de ces couches pseudomorphiques. Ces travaux pourraient nous renseigner sur les variations de coefficient de collage du Pb dans ces divers systèmes.

Pour les stades initiaux de dépôt, nous avons identifié avec succès un site

préférentiel de germination des atomes de Pb sur la surface (100) de  $\text{Al}_{13}\text{Co}_4$ . Prochainement, ce travail sera complété par des calculs théoriques pour déterminer les différents sites actifs sur cette surface et générer les images STM associées. Cet échantillon est connu pour son potentiel d'utilisation dans le domaine de la catalyse. Il est par conséquent primordial d'identifier si d'autres sites de capture existent et d'analyser la réactivité de cette surface. Nos études vont être poursuivies par l'adsorption de petites molécules ( $\text{O}_2$ , CO et NO) sur cette surface. A cause du désordre chimique et des imperfections structurales, une étude similaire sur la surface (010) de l'échantillon T-Al<sub>3</sub>(Mn, Pd) semble plus délicate. Enfin, un travail supplémentaire s'impose dans une gamme de températures différente couplée à des flux de dépôt plus importants pour confirmer ou non la possibilité de former la phase quasicristalline *d*-Al-Cu-Co comme alliage de surface. Parallèlement, il est envisagé d'analyser l'évolution de la structure électronique (utilisation de ARPES<sup>13</sup>) pour les phases suivantes:

surface propre → couche pseudomorphique → phase  $\beta$ -Al(Cu,Co) → phase  $\gamma$ -Al<sub>4</sub>Cu<sub>9</sub>.

En raison de la contrainte de temps, il n'a pas été possible d'étudier la croissance du Cu sur la surface (010) de l'échantillon T-Al<sub>3</sub>(Mn, Pd). Il serait intéressant d'étudier les différentes phases qui apparaissent sur cette phase orthorhombique T-Al<sub>3</sub>(Mn, Pd) et de les comparer aux résultats obtenus sur les systèmes Cu/Al(111), Cu/Al<sub>13</sub>Co<sub>4</sub> et Cu/*i*-Al-Pd-Mn.

---

<sup>13</sup>Angle resolved photoelectron spectroscopy

# Chapter 2

## Introduction

### 2.1 General presentation

In conventional crystallography, a crystal can be described by one of the 230 crystallographic space group types (32 geometric crystal classes, 14 bravais lattice types and 7 crystal systems). The rotational symmetry defines an angle with which the object remains structurally invariant after rotation of  $2\pi/n$ . In classical crystallography,  $n$ -fold symmetry is consistent with periodicity for  $n = 2, 3, 4$ , and  $6$  [1]. All these rules and concepts were broken with the discovery of quasicrystals by Dany Shechtman on April 1982 [2], where the icosahedral symmetry was first observed, hence revealing a “forbidden” symmetry (5-fold). Following this breakthrough, other classically forbidden symmetries (8- $f$ , 10- $f$  and 12- $f$ ) were soon discovered in different alloys [98]. Quasicrystals are defined as a new form of solid that differs from crystals and amorphous states. They are intermetallic compounds possessing long-range order, despite their lack of periodicity, and exhibiting rotational symmetries forbidden in classical crystallography. These discoveries changed the definition of a crystal to “**any solid having an essentially discrete diffraction pattern**”<sup>1</sup> [3].

Almost 30 years later, several key questions like “*do we know where the atoms are?*” remain open issues and still generate intensive research effort. In this respect, topics of investigation are dedicated to crystallography, formation, stability, surface physics and properties of this new state of matter [5]. Several issues remain unanswered due to the difficulty encountered by the lack of periodicity in these materials. Recent studies were motivated by fundamental questions related to the surface structural phenomena already observed in periodic crystals. Would step terrace formation, bulk truncation, surface relaxation and reconstruction, chemical segregation and formation of facets be relevant and similar in this new class of materials? Another challenging question is whether or not the physical properties characteristics to the bulk would be maintained at the quasicrystal surfaces? Hence, surface studies of model systems are important in the understanding of the unusual surface properties

---

<sup>1</sup>This definition of crystal was given by the International Union of Crystallography (IUCr) in 1992.

of quasicrystals, such as reduced friction and non-sticking behavior. These properties have led to technological applications of quasicrystals, in the field of coatings for instance [5]. Another promising application of quasicrystals is in catalysis [99], which is related to the chemical and atomic structure of the topmost surface layer. Therefore, fundamental studies on quasicrystal surfaces are of significant importance also from a technological perspective.

To model quasicrystal phases and to perform calculations requiring a finite unit cell, crystalline phases named approximant phases have been introduced [100]. An approximant is a periodic alloy with a large unit cell which is closely related to its quasicrystal parent, both in chemical composition and in atomic structure. It corresponds to a rational cut through the hyperdimensional lattice of the QC. Approximant structures have been successfully used to understand the electronic charge-density distribution at the surface of the icosahedral Al-Pd-Mn quasicrystal [31, 101]. Two approximants grown by the Czochralski technique, namely the  $\text{Al}_{13}\text{Co}_4$  and the T-Al<sub>3</sub>(Mn, Pd) samples have been investigated and are presented in this thesis. These complex metallic alloys are considered as approximants of the decagonal Al-Ni-Co [67, 72, 73] and Al-Pd-Mn [69, 102] quasicrystalline phases, respectively.

Several experimental and theoretical techniques have been used in this work to investigate the crystallographic and electronic surface structures. Scanning tunneling microscopy (STM)<sup>2</sup> is a powerful tool to probe the local surface structure in real space, down to the atomic level [103]. Low energy electron diffraction (LEED) [104] is used to determine in reciprocal space the surface symmetry, the reciprocal lattice vectors and the overall quality/ordering of the sample. LEED is extremely powerful when used as dynamical LEED for quantitative surface structure determination. X-ray photoelectron diffraction (XPD) probes the very local geometrical structure around the selected photoemitter atoms. This method reveals an average short-range ordering at the near surface. Photoelectron spectroscopy (PES) is a widely used method to determine the chemical composition of a surface and to study the electronic structure. It can also be used to study many interesting phenomena such as surface alloying, core-level binding energy (BE) shifts and density of states (DOS) near  $E_F$ . In our experiments, X-ray photoelectron spectroscopy (XPS)<sup>3</sup> and ultraviolet spectroscopy photoelectron (UPS) are used to investigate the chemical composition and the electronic structure of our samples prior and after thin film adsorption. Theoretical methods are used to understand and to interpret our experimental results. Density Functional Theory (DFT) is one of the most widely used methods for *ab initio* calculations of the structure of crystals, molecules, surfaces, and their interactions. DFT can be used to find minimum energy surface structures for clean surfaces and simple adsorbate systems. From *ab initio* calculations, simulated STM images can be generated for comparison to experimental ones. The single-scattering cluster (SSC) approx-

---

<sup>2</sup>Binnig and Rohrer at (1983), were awarded the Nobel Prize in Physics in 1986 for the design of this tool.

<sup>3</sup>It is also known as Electron Spectroscopy for Chemical Analysis (ESCA).

imation has been used to interpret the experimental XPD patterns [105, 106]. SSC simulations are based on the structural bulk model available. This theoretical method allows us to evaluate the agreement between our experimental data and the derived surface structure models.

The work in this thesis has been carried out at Institut Jean Lamour<sup>4</sup> (Ecole Nationale des Mines de Nancy), Nancy, France and at the Empa, nanotech@surfaces<sup>5</sup>, Thun, Switzerland during the period 2006-2009. This work is performed within the European Network of Excellence Complex Metallic Alloys<sup>6</sup>. The NoE *CMA* research structure is based on six Virtual Integrated Laboratories (VILs) in which more than 300 permanent scientists and 60 PhD students are taking part. This network unites 20 partners across Europe. Through this *CMA* network large single crystals, recently grown have been made available and have been investigated as part of the work presented in this thesis.

The thesis is organized in six chapters and an appendix. In the first chapter, we give an overall introduction to the field of quasicrystals and complex metallic alloys and then we present the work performed on CMA surfaces ranging from the surface atomic structure to the growth of thin overlayers of single elements. **Chapter 2** presents a detailed study of the (100) surface of the orthorhombic  $\text{Al}_{13}\text{Co}_4$  crystal. **Chapter 3** discusses the structural investigation of the (010) surface of the orthorhombic T-Al<sub>3</sub>(Mn, Pd) complex metallic alloy. **Chapter 4** shows the results of the growth of lead on the two approximant surfaces. **Chapter 5** presents the study of copper adsorption on the (100) surface of the  $\text{Al}_{13}\text{Co}_4$  crystal. The conclusions and perspective chapter is followed by an appendix which describes in more details the XPD technique and the SSC calculations.

---

<sup>4</sup>Department CP2S, Institut Jean Lamour (UMR7198 CNRS-Nancy-Université-UPV-Metz), Ecole des Mines, Parc de Saurupt, 54042 Nancy Cedex, France.

<sup>5</sup>Empa, Swiss Federal Laboratories for Materials Testing and Research, nanotech @ surfaces Laboratory, Feuerwerkerstraße 39, CH-3602 Thun, Switzerland.

<sup>6</sup>“The *CMA* NoE is dedicated on the one hand to discovering new complex metallic alloys, preferably with attractive properties in view of technological applications, and on the other hand to disseminating the knowledge gained on those compounds toward academia, industry and the Grand Public”. It is coordinated by Jean-Marie Dubois initiator of this network.  
<http://www.cma-ecnoe.org>

## 2.2 Complex metallic alloys systems

### 2.2.1 Definition

Complex metallic alloys (CMA) is a family of intermetallic compounds composed of at least two elements, characterized by a large unit cell containing up to thousands of atoms with highly symmetric clusters being an essential part for the description of the atomic structure. CMAs are characterized also by some disorder due to the clusters which do not fill Euclidian 3D space. The CMA family contains periodic and aperiodic systems (crystals, approximant and QCs). Quasicrystals are aperiodic intermetallic alloys exhibiting a long range atomic order and ‘forbidden’ symmetries in classical crystallographically. They are usually found in a narrow chemical composition range of the phase diagram of the constituting elements. Near to this class, approximants are periodic intermetallic alloys with large unit cells and a local atomic order similar to the local order found in the QCs. The complexity is related to the difficulty to describe the atomic positions due to the large size of the unit cell. To illustrate a complex alloy in the Al-Cu system, we take the case of the cubic phase  $\beta$ -*CsCl*-type [107], where the basic unit cell is the simplest one containing two atoms with the positions of  $(0, 0, 0)$  and  $(\frac{1}{2}, \frac{1}{2}, \frac{1}{2})$  and a lattice parameter of  $2.9 \text{ \AA}$ . Depending on the Al/Cu composition ratio, the presence of vacancies ordered in the lattice increases the size of the unit cell up to 47.7 times that of the basic  $\beta$ -phase and changes the local structural motifs [107]. The  $\gamma$ -Al<sub>4</sub>Cu<sub>9</sub> phase which is an approximant to quasicrystals according to Dong [108] is another typical example. The insertion of two vacancies at precise sites in the *CsCl*-structure favours the formation of defect structures containing the basic pentagonal configuration. Hence, the  $\gamma$ -phase can be regarded as  $3 \times 3 \times 3$  CsCl superstructure while leaving the vertex and center of the large bcc cell vacant. Since there are totally 54 atomic positions in one cell, the cell formula should be expressed as Al<sub>16</sub>Cu<sub>36</sub>V<sub>2</sub> (V= vacancy)<sup>7</sup>.

### 2.2.2 Quasiperiodicity and approximant phases

Classically, a crystal is defined as a 3-dimensional periodic arrangement of identical unit cells. To understand the surface structure of crystals, 2D tilings can be introduced. For simplification, the principle will be explained in a plane. It remains true in 3D space. The aim is to fill the plane by one type of tile without overlap or voids. For the 2-, 3-, 4- and 6-fold rotational symmetry, only one type of tile (rectangles, triangles, squares and hexagons) is necessary to cover completely the plane. In the case of (2- or 4-) fold symmetry, four rectangles (or squares) are required to complete the plane ( $4 \times \frac{2\pi}{4}$ ). Regarding three-fold symmetry, 6 triangles are required ( $6 \times \frac{2\pi}{6}$ ) and 3 hexagons for the six-fold symmetry ( $3 \times \frac{2\pi}{3}$ ). This method can of course be extended to

---

<sup>7</sup>the largest superstructure present in Al-Cu alloys is observed so far at composition Al<sub>36</sub>Cu<sub>48</sub>V<sub>12</sub>.

3D space, but requires for example replacement of rectangles (squares) by parallelepipeds (cubes). The five-fold symmetry is forbidden in the case of conventional crystallography, because the vertex angle of a regular pentagon is  $108^\circ$ . It is not possible to cover the plane with only regular pentagons because the tiling leads to angles of  $360^\circ - (2 \times 108^\circ) = 144^\circ$  and  $360^\circ - (3 \times 108^\circ) = 36^\circ$  which cannot be satisfied by a further pentagonal tile. Therefore, it is necessary to introduce rhombuses or irregular pentagons with vertex angles equal to  $36^\circ$  and  $144^\circ$  ( $324^\circ + 36^\circ = 360^\circ$ ) to fill completely the plane. The equivalent tiling in 3D space consists of replacing pentagons and rhombus by dodecahedrons and rhombohedras. All these symmetries are presented on figure 2.1.

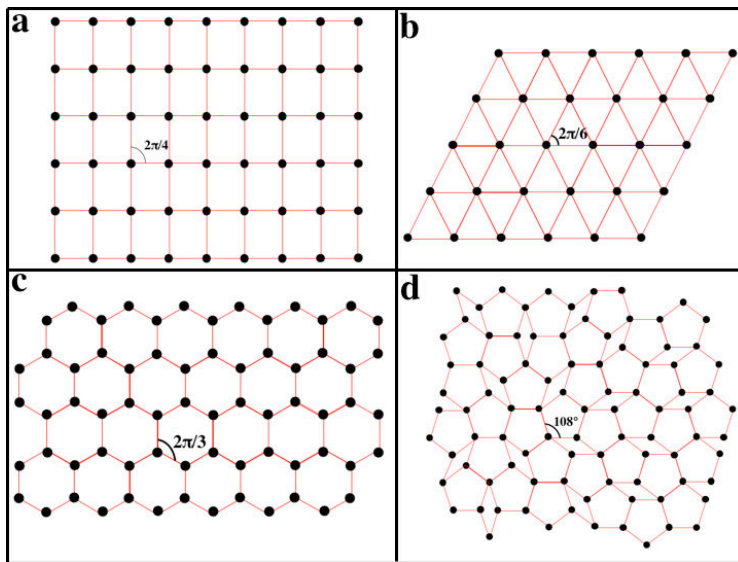


Figure 2.1: Representation of tilings of the plane with: (a) squares (or rectangles), (b) triangles, (c) hexagons and (d) pentagons.

In 1984, Dany Shechtman *et al.* [2]<sup>8</sup> presented, while quenching<sup>9</sup> from the melt, an Al<sub>86</sub>Mn<sub>14</sub> alloy which exhibited a diffraction pattern (indicative of a long-range order) with a 5-fold symmetry. This rotational symmetry is forbidden by classical crystallography. The term “quasicrystal” QC (short for quasi-periodic crystal) was envisaged soon afterwards to describe a new solid state showing a long-range atomic order that shows non-crystallographic (aperiodic) symmetries such as 5-, 8-, 10- and 12-fold rotations. This has led to a new definition of a crystal by the IUCr. Since, several binary, ternary and quaternary QCs have been discovered. The vast majority of quasicrystals are found in the Al-rich systems. Recently, a natural QC of Al-Cu-Fe has been discovered in the Koryak Mountains in Russia, in crystalline mineral of khatyrkite and cupalite samples [109].

<sup>8</sup>published in a paper entitled, “Metallic phase with long-range orientational order and no translational symmetry”.

<sup>9</sup>rapid cooling.

The concept of quasiperiodicity was introduced before the discovery of QC<sub>s</sub>. For example, the function  $f(x, y) = \cos(2\pi \times x) + \cos(2\sqrt{2}\pi \times y)$  is periodic along  $x$  with a period of 1 and along  $y$  with a period of  $1/\sqrt{2}$  and quasiperiodic along  $x = y$ , a quasiperiodic function  $F(x) = f(x, x) = \cos(2\pi \times x) + \cos(2\sqrt{2}\pi \times x)$ . The quasiperiodicity can also be generated by projection or cut from a higher dimensional space along a subspace that is oriented by angles corresponding to the arctangent of an irrational number. To understand the long-range order found in QC<sub>s</sub>, we briefly explain two concepts that can be regarded as 1D and 2D quasiperiodic structures: (i) the Fibonacci<sup>10</sup> sequence and (ii) a two-dimensional Penrose tiling. In 3D space, icosahedral tiling model will be introduced.

### 2.2.2.1 The Fibonacci sequence and the golden ratio:

Step	Sequence	L/S	Ratio $\tau$
0	S	-	-
1	L	1/0	-
2	LS	1/1	1
3	LSL	2/1	2
4	LSLLS	3/2	1.5
5	LSLLSLSL	5/3	1.667
6	LSLLSLSLSSL	8/5	1.6
7	LSLLSLSLSSLSSL	13/8	1.625
8	LSLLSLSLSSLSSLSSLSSLSSLSSLSSL	21/13	1.615
n	$f(n) = f(n-2) + f(n-1)$	$N_L/N_S$	$\tau = 1.61803$

Table 2.1: Generation of the Fibonacci sequence and its relationship to the golden number  $\tau$ .  $N_L$  ( $N_S$ ) represents the number of segments  $L$  ( $S$ ).

The 1D Fibonacci sequence is built with two kinds of 1D “tiles”, a short S and a long L segment. The sequence is generated by using the following substitution rules  $S \rightarrow L$  and  $L \rightarrow LS$  in each step as presented in the table 1.1. One of the interesting characteristics of the Fibonacci sequence is the appearance of the so-called **golden mean**  $\tau$ . For the chain of objects, it is found in the limit value of the relative abundances of the two types of objects (L and S):

$$\lim_{n \rightarrow \infty} \frac{N_L}{N_S} = \tau = 1.618\dots \quad (2.1)$$

Another way to represent the Fibonacci sequence is:

$$0, 1, 1, 2, 3, 5, 8, 13, 21, 34, 55, \dots \quad (2.2)$$

These numbers can be defined by:

$$f(n) = f(n - 2) + f(n - 1) \quad (2.3)$$

<sup>10</sup>Leonardo Pisano Bogollo (1170 - 1250), called Fibonacci, Italian mathematicien

with  $n > 1$ ,  $f(0)=0$  and  $f(1)=1$ , whereas for the sequence of Fibonacci numbers, the golden number is the limiting value of the ratio of two successive terms:

$$\lim_{n \rightarrow \infty} \frac{f(n+1)}{f(n)} = \tau \quad (2.4)$$

The golden number is the only positive solution of the equation:

$$x^2 - x - 1 = 0 \quad (2.5)$$

and it is equal to:

$$\tau = \frac{1 + \sqrt{5}}{2} = 2 \times \cos(2\pi/5) = 1.618033989... \quad (2.6)$$

The terms of the Fibonacci sequence can be also deduced from the Binet formula:

$$F(n) = \frac{1}{\sqrt{5}} \left( \left( \frac{1 + \sqrt{5}}{2} \right)^n - \left( \frac{1 - \sqrt{5}}{2} \right)^n \right) \quad (2.7)$$

The Fibonacci sequence which is comparable to a 1D quasicrystal can be constructed by defining a 2D square lattice  $(R_x, R_y)$  of spacing  $a$ . A second 2D hyperlattice  $(R_{\parallel}, R_{\perp})$  representing respectively the physical and orthogonal spaces, is drawn through the origin of  $(R_x, R_y)$  and rotated by  $\alpha$ . The irrational value of  $\tan(\alpha)$  is chosen as to obtain  $\tan(\alpha) = \tau$ . The lattice points are decorated by objects (or atomic surfaces) which are extended but finite along the orthogonal axis  $R_{\perp}$ . The length  $\Delta$  of the atomic surface is taken such that  $\Delta/a^2 = \rho$ , where  $\rho$  is the atom density. The real atomic positions are located where these objects cut  $R_{\parallel}$ . As a consequence of this projection, a 1D aperiodic structure contains two segments  $L$  and  $S$  which follows the Fibonacci sequence as shown on Fig.2.2.

### 2.2.2.2 The Penrose tiling:

Two-dimensional quasicrystal structures can be illustrated by the Penrose tiling. Ten years before the publication of the discovery of QC by Shechtman *et al.*, Roger Penrose<sup>11</sup> had used two types of tiles to fill space in a well-ordered manner and non-periodically. This tiling shows local five-fold motifs with long-range order [19]. The Penrose tiling shows five-fold symmetry, and its Fourier transform is similar to the diffraction pattern observed by Shechtman *et al.* from the icosahedral quasicrystalline phases (as shown in inset on Fig.2.3(c)). The Penrose tiling (Fig.2.3(c)) is constructed from two types of rhombii with equal edge length and with angles 36° and 144° (skinny rhombus) and 72° and 108° (fat rhombus) assembled according to specific matching rules. The rule is simple, two rhombus are allowed to join if the arrows match on their common edge.

---

<sup>11</sup>British mathematician and physicist, born 8 August 1931.

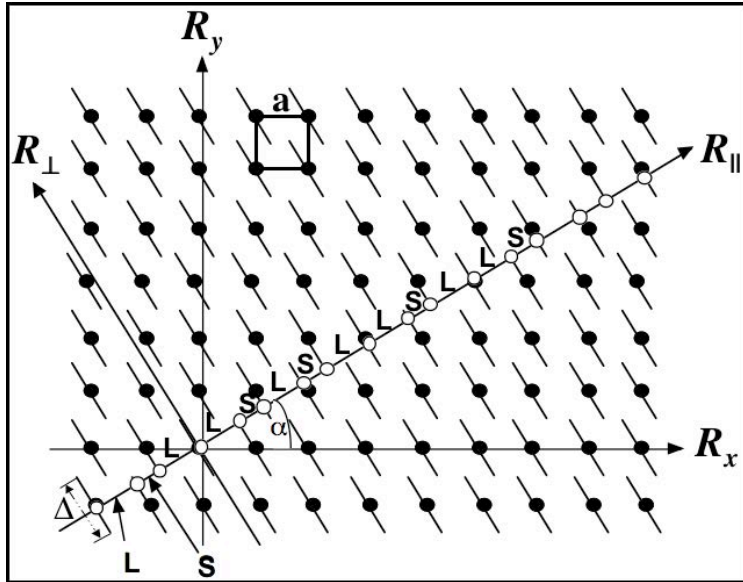


Figure 2.2: *Illustration of the cut method: construction of a 1D approximant from a 2D periodic lattice. Generation of the Fibonacci sequence LSLLSLSLLSLLS (8L/5S).*

### 2.2.2.3 Three dimensional icosahedral tiling models

Linus Pauling<sup>12</sup> solved for the first time in 1955, the structure of a periodic complex metallic alloy NaCd<sub>2</sub>. This CMA contains 768 sodium (Na) and 384 cadmium (Cd) making a total of 1152 atoms in the unit cell with an edge of about 3 nm [110]. In the 1960s, Samson solved the atomic structures of the most complicated intermetallic phases known; the NaCd<sub>2</sub> [111]<sup>13</sup>, Mg<sub>2</sub>Al<sub>3</sub> [112]<sup>14</sup> and Cu<sub>3</sub>Cd<sub>4</sub> [113]<sup>15</sup> (each with over 1000 atoms per unit cell). The atomic structure in these systems can be described using a 3D building-block (cluster models), producing for example icosahedral and tetrahedral polyhedra [110–114]. Models defining the local environments have been proposed based on Mackay or Bergman type clusters as basic motifs for the quasicrystalline structure. The Bergman cluster (Fig.2.4(a)) identified in the crystalline phase Mg<sub>32</sub>(Al, Zn)<sub>49</sub> [23], is composed of 33 atoms distributed as a central atom, an icosahedron (12 atoms) and an external dodecahedron (20 atoms). The Mackay cluster (Fig.2.4(b)) was identified in the study of  $\alpha$ -AlMnSi [115]. This 50 atom cluster consists of one atom in its center, 7 on an inner dodecahedron, 12 atoms on an icosahedron and 30 atoms on an icosidodecahedron. Similarly, the structure of the icosahedral Al-Pd-Mn QC presented on Fig.2.4(c) can be

---

<sup>12</sup>American chemist, physicist and peace activist (1901-1994), double Nobel prizes in chemistry and peace.

<sup>13</sup> $a = 30.56 \text{ \AA}$ , space group:  $Fd\bar{3}m$

<sup>14</sup> $a = 28.32 \text{ \AA}$ , space group:  $Fd\bar{3}m$

<sup>15</sup> $a = 25.87 \text{ \AA}$ , space group:  $F\bar{4}3m$

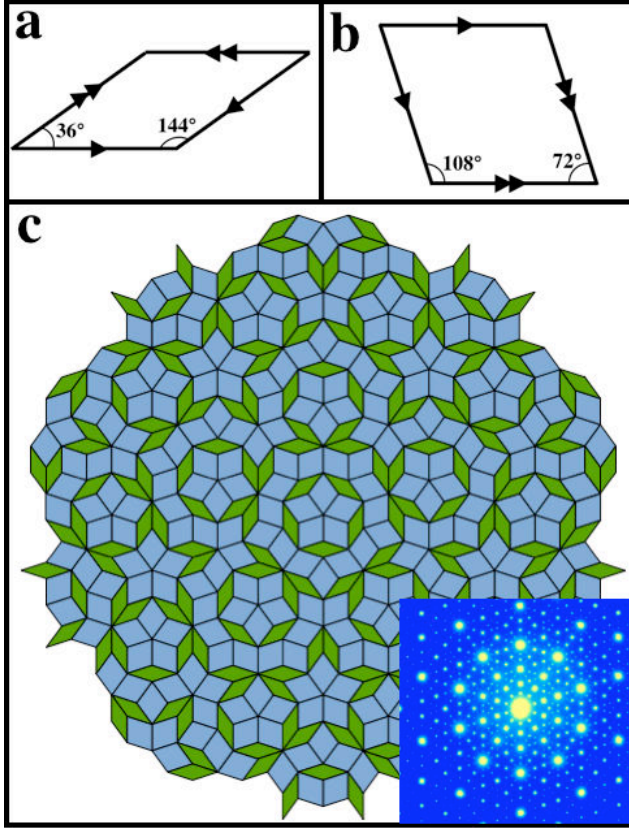


Figure 2.3: *Penrose tiling constructed from two types of rhombii with angles (a) 36° and (b) 72°. (c) The Penrose tiling is 5f symmetric leading to a reciprocal lattice comparable to the one found in QCs (see inset) [19]. Inset: Sharp diffraction pattern along the five-fold axis of the i-QC measured by Shechtman et al. [2].*

described using the so-called *pseudo*-Mackay icosahedron (PMI) model. The innermost shell is occupied by 9 atoms, it is surrounded by a large icosahedron (12 atoms) and the outer shell is a icosidodecahedron (30 atoms) [116]. This cluster corresponds to a three shell cluster of diameter 9.6 Å, and two such PMI-clusters are separated by 20 Å. In the Al-Pd-Mn QC, the majority of the atomic positions can be described by these clusters distributed according to specific rules on a 3D Penrose tiling, involving interpenetrating clusters. The two groups of quasicrystals, which have been the most studied, are the icosahedral and decagonal phases. Decagonal quasicrystals are quasiperiodic in only two dimensions, i.e. quasiperiodic planes are stacked, periodically along the ten-fold axis (e.g. *d*-Al-Ni-Co and *d*-Al-Cu-Co). Icosahedral quasicrystals are quasiperiodic in three dimensions.

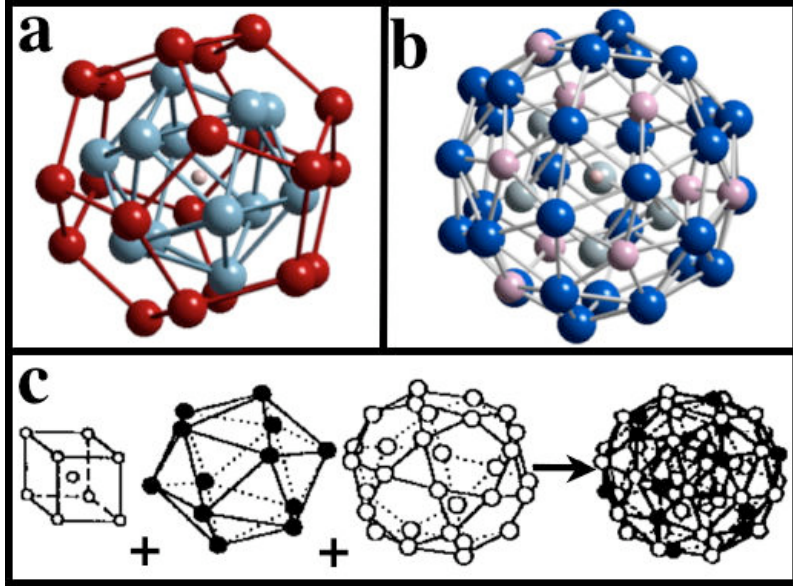


Figure 2.4: (a) Bergman (33 atoms) and (b) Mackay (50 atoms) type cluster found in i-QCs. (c) pseudo-Mackay icosahedron (PMI) built up by three concentric atomic shells and forming the basic cluster of i-Al-Pd-Mn. Reprinted from [5, 22]

### 2.2.3 Physical properties of CMAs

CMAs materials possess attractive properties that differ significantly from the ones of their main constituents. The unusual properties of CMAs make them potentially very useful for industrial applications. These unexpected behaviour of CMAs have generated an intense research to understand their peculiar structure and properties [5]. One of the interesting properties is the depletion of the density of states (DOS) at the Fermi energy ( $E_F$ ), known as the Hume-Rothery *pseudo-gap* [117]. It was shown that the quasicrystals are stabilized electronically through the Hume-Rothery (HR) mechanism [118], where interaction of the *pseudo-Brillouin* or Jones zone with the Fermi surface creates the *pseudo-gap* [12, 119]. The formation of the *pseudo-gap* can also be regarded as a combination of Hume-Rothery scattering of electron waves and *sp-d* hybridization [6–11, 120, 121]. Many of the peculiar properties of quasicrystals have been related to the *pseudo-gap* at  $E_F$ . The transport properties exhibit a more semiconductor-like than metallic-like character. For metals, experimental measurements show that the conductivity decreases as the temperature is increased (Matthiessen rule). Figure 2.5 shows a resistivity measurement below room temperature for several CMAs with structural complexity increasing from bottom (simple compounds) to top (QCs) [14]. The electrical resistivity of CMAs (top of the graph) exhibits large values and uniformly decreases as the temperature increases, i.e. exhibits an inverse Matthiessen behaviour.

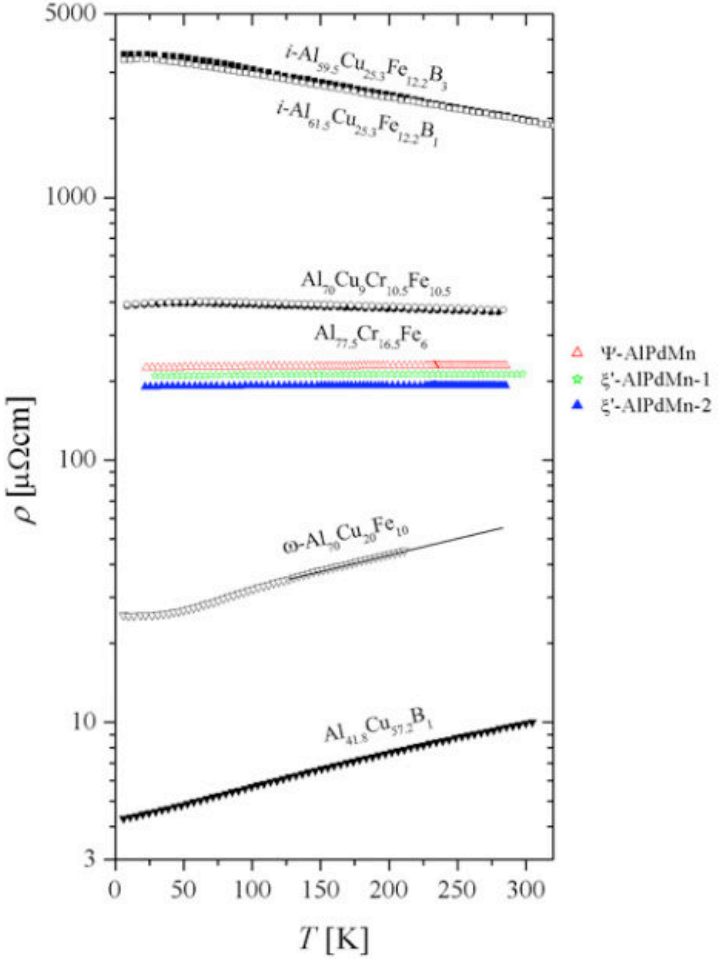


Figure 2.5: *Electrical resistivity data measured on a variety of CMAs with different unit cell sizes. The structural complexity increases from bottom to top of the graph [14].*

The temperature coefficient of resistivity (TCR)<sup>16</sup> changes from positive (characteristic for pure metals) to negative when the unit cell becomes large. For specific approximants, a TCR close to zero is measured in a large temperature range, which indicates that the resistance hardly changes with variations in temperature. It has been shown that upon annealing the resistivity of the *i*-QCs is decreasing. This is explained for instance by an annihilation of defects and phason strain. In the case of a sample containing transition metals with 5d elements like rhenium (e.g. *i*-Al-Pd-Re), the sample can be considered almost as an insulator at the low temperature of 4 K [15, 16].

Another important property of CMA is their surface energy. CMAs and specially QCs are characterized by a very low surface energy ( $\gamma_s$ ) in comparison to their intrinsic constituents (see Table 1.2). The most com-

---

<sup>16</sup>indicates the change of the resistance factor per degree of temperature.

plex CMAs show the lowest values of  $\gamma_s$ . By comparing the  $\gamma_s$  of the tetragonal  $\omega\text{-}Al_7Cu_2Fe$  ( $\gamma_s = 2.2 \text{ J.m}^{-2}$ ) and the icosahedral  $Al_{62}Cu_{25.5}Fe_{12.5}$  ( $\gamma_s = 0.55 \text{ J.m}^{-2}$ ), the origin of this difference can be related to the reduced density of d-states at the Fermi edge (HR-gap) observed in the case of QC system. Hence, several applications make use of these unique surface properties. Unusual tribological properties of QCs includes low coefficients of friction that rival Teflon and good wear-resistance [122]. CMAs are characterized also by a good corrosion resistance [123] and a non-stick behaviour related to their low surface energy [124]. These attractive properties make this new class of materials a powerful candidate for coatings for machine parts and other coatings applications. The explanation of the origin of these properties in relation to the quasicrystalline structure is still an open question. An intriguing suggestion is that the lack of commensurability between a quasicrystalline surface and a surface of a periodic material influences the friction properties [125].

Material	Fe	Cu	Al	$\gamma\text{-}Al_9Cu_4$	$\beta\text{-}Al_{55}Cu_{30}Fe_{15}$	$i\text{-}Al_{62}Cu_{25.5}Fe_{12.5}$
$\gamma_s (\text{J.m}^{-2})$	2.2	1.78	1.15	1.0	0.84	0.55

Table 2.2: *Surface energy comparison between three complex compounds and their constituents [5]*.

## 2.2.4 Growth techniques

Several methods can be used to grow single crystals, such as solution growth, sublimation technique, Czochralski technique, Bridgman technique and flux technique. The crystals used in this study have been grown using the Czochralski and the self flux method.

### 2.2.4.1 Bridgman method

Compared to other growth technique, the Bridgman growth is considered to be the simplest one, but several limitations remain present. The Bridgman method cannot be applied to a material system which decomposes before it melts. This includes systems having components with high vapor pressure, and materials exhibiting destructive solid - solid phase transformations which will compromise the crystalline quality on cooling the crystal at the end of the growth run. The material to be grown is enclosed in a glass or quartz tube and suspended in the furnace having a suitable temperature gradient for the growth. After melting the substance, the ampoule is moved from hot melt zone to the cold freezing zone gradually. The lower part of the ampoule, which contains the melt, has a capillary tip. During the lowering in the temperature gradient, a seed initiates and gradually grows up in the capillary tube until they fill the entire melt region of the ampoule. Illustration of the Bridgman technique is presented on Fig.2.6(a).

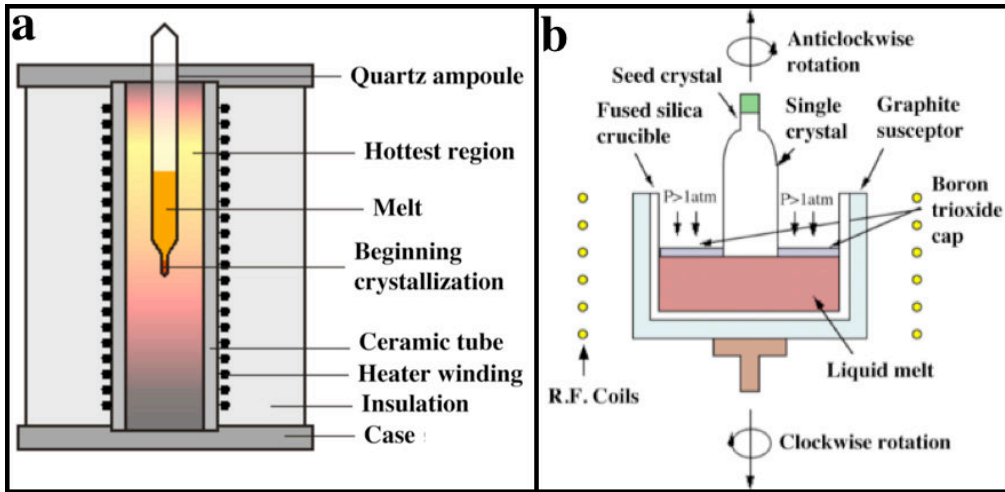


Figure 2.6: *Single crystal growth using (a) the Bridgman and (b) the Czochralski methods.*

#### 2.2.4.2 Czochralski method

The Czochralski method (Fig.2.6(b)) is based on the crystallization of metals (also semiconductors and salts...) by pulling a metallic wire from its native melt. This process has been particularly optimized and is widely employed for the large scale production of silicon for the electronic industry. The procedure consists of wetting a single-crystalline seed by bringing the latter in contact with the surface melt. After having reached equilibrium conditions, the seed is slowly pulled upwards which transfers the original interface to a lower-temperature position. Hence, the driving force for solidification is simultaneously created by the interface shift and the crystal grows downwards with the appropriate pulling rate. To increase the diameter of the crystal, it is necessary at the end of the seeding procedure to decrease the pulling velocity or to apply a slight reduction of the heating power.

#### 2.2.4.3 Flux growth method

Flux crystal growth method (growth from high temperature solutions) is the method that is used to grow single crystals of incongruently melting compounds. The principle of flux growth does not differ significantly from that of the growth in solution: the temperature is higher and related to the melting temperature of the flux (solvent). Simple metals (Ni, Fe...), oxides ( $B_2O_3$ ,  $Bi_2O_3$ ), hydroxides (KOH, NaOH), salts (BaO, PbO,  $PbF_2$  and other halides) can be used as solvents.

## 2.3 Complex metallic alloys surfaces

### 2.3.1 Generality on alloy surfaces and surface phenomena

The surface is of crucial importance as it is the boundary that separates the solid from its environment. The atomic structure of the surface termination can be different to the structure of the bulk. This difference is due to the reduced coordination on one side of the surface (vacuum), in other words to the reduced number of nearest neighbours of atoms at the surface. Hence, the chemical environment for an atom at the crystal surface is different from the chemical environment for the same atom in the bulk. This difference in the structure between the bulk and the surface can produce phenomena like **surface reconstruction**. This process consists of a crystallographic arrangement of surface atoms that differs to the one present in the bulk. The single crystal surfaces will not exhibit the exact atomic arrangement expected from a pure truncation of the bulk structure of a solid, parallel to a particular plane. One of the most well-known example is the  $(7 \times 7)$  surface reconstruction observed at the  $(111)$  surface of the silicon crystal. Another phenomenon which is usually observed is **relaxation**. Relaxation consists of rather small changes of the interatomic distances at the surface due to the reduced coordination. It involves expansion or contraction of the layers spacing perpendicular to the surface. There is no change either in the periodicity parallel to the surface or in the symmetry of the surface. These two phenomena discussed here minimize the surface free energy. They are also observed in alloys. As explained above, the surface of a crystal can have a crystallographic and electronic structure drastically different to that of the bulk. For alloys, the analysis of the surface structure can be even more complex due to potential chemical segregation. Compared to bulk planes, diffusion of atoms to the surface can lead to enrichment or depletion of specific elements within the near surface region and at the topmost surface layers.

### 2.3.2 Surface structures of quasicrystals

In this section, we will present surface studies performed on complex metallic alloys. We will compare the results with the surface phenomena discussed above. Comparison between the surface structure and the bulk model will be mentioned.

#### 2.3.2.1 Surface structure of the *d*-Al-Cu-Co quasicrystal

The first study of a clean surface of a quasicrystal in ultrahigh vacuum (UHV) was achieved on the decagonal Al-Cu-Co quasicrystal. The STM images (Fig.2.7(a)) recorded on the ten-fold surface of the  $d\text{-Al}_{65}\text{Cu}_{20}\text{Co}_{15}$  quasicrystal revealed a step and terrace structure. The terraces showed a corrugation

less than  $0.1 \text{ \AA}$  and a width on the order of  $8 \text{ nm}$ . To identify the fine structure observed on these terraces, the authors calculated the Fast Fourier Transform (Fig.2.7(b)), which confirmed the ten-fold symmetry of the sample. The back filtered Fourier Transform was used to obtain a real space structure presenting a pentagonal quasilattice (Fig.2.7(c)) [24].

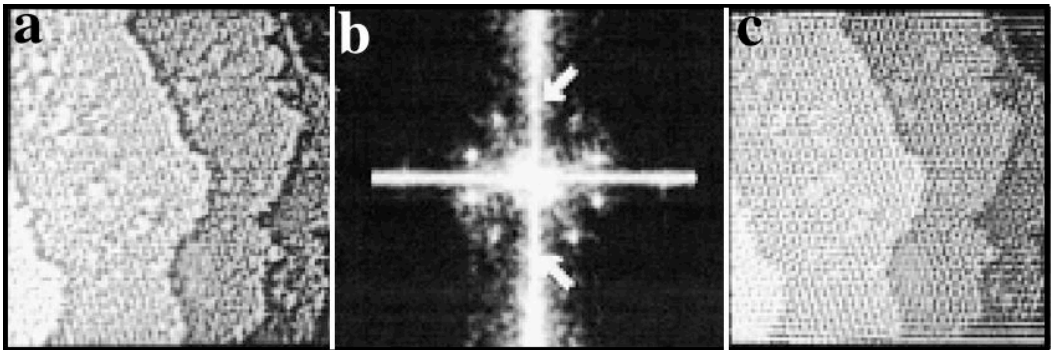


Figure 2.7: *STM image of the quasiperiodic surface of the  $d\text{-Al}_{65}\text{Cu}_{20}\text{Co}_{15}$  QC [24]. (a) High resolution STM image ( $15 \times 15 \text{ nm}^2$ ). (b) The Fast Fourier Transform calculated from (a) displays ten spots forming a decagonal ring. (c) Filtered STM image showing a quasiperiodic structure formed by pentagons. Reprinted from [24].*

### 2.3.2.2 Surface structure of the $d\text{-Al-Ni-Co}$ quasicrystal

The ten-fold surface of the  $d\text{-Al-Ni-Co}$  is one of the most studied aperiodic surface and the bulk structure is relatively well understood [126–128]. The structure is periodic in the direction normal to the 10-fold surface with an interplanar distance of approximatively  $2 \text{ \AA}$  (corresponding to  $c/2$ ), but quasiperiodic in all directions orthogonal to this direction [129]. Several phases of the  $d\text{-Al-Ni-Co}$  QC have been investigated by different techniques, namely LEED, SPA-LEED<sup>17</sup>, HAS<sup>18</sup>, XPD and STM [35, 50, 52, 53, 55–57, 59, 60, 130, 131]. All the different phases found depend on the overall composition and the growth temperature. The composition of Al is about 72 % and the transition metals TM (Ni and Co) composition can vary from Co-rich or Ni-rich phases.

Before being inserted into UHV, the surface of the sample must be polished to obtain a mirror-like surface. The in-vacuum preparation consists of cycles of  $\text{Ar}^+$  ion sputtering followed by annealing between  $973 \text{ K}$  and  $1173 \text{ K}$ . The temperature of annealing changes for each sample, and the surface was prepared at  $973 \text{ K}$  for  $d\text{-Al}_{71.8}\text{Ni}_{14.8}\text{Co}_{13.4}$  [55], at  $1123 \text{ K}$  for  $d\text{-Al}_{72}\text{Ni}_{11}\text{Co}_{17}$  [53], and at  $1173 \text{ K}$  for  $d\text{-Al}_{72}\text{Ni}_{12}\text{Co}_{16}$  [50, 56] samples. The LEED patterns and STM images measured on the ten-fold surface of the  $d\text{-Al-Ni-Co}$  indicate that

<sup>17</sup>Spot profile analyzing - low energy electron diffraction

<sup>18</sup>Helium atom scattering

the surface quality, the long-range order and the width of the terraces increase as a function of annealing time and temperature. The roughness decreases with increasing the temperature of annealing. It is measured at  $0.5 \text{ \AA}$  on atomically flat terraces with the exception of local protrusions. After annealing up to  $875 \text{ K}$  for 90 minutes, the protrusions take a three fold symmetric shape and are preferentially oriented. These protrusions are located on top of pentagonal sites [50]. The LEED patterns and the FFT show a ten-fold symmetry of the surface. The diameter of the decagonal spot rings in the LEED pattern are related by the golden mean  $\tau$ .

Atomically resolved STM images display a fine structure with five-fold symmetric motives which have opposite orientations in two adjacent terraces. The fine structure can be characterized by a rhombic tiling for the  $d\text{-Al}_{71.8}\text{Ni}_{14.8}\text{Co}_{13.4}$  sample [55] or by a random pentagonal tiling for Co-rich phases [50,54,56]. In both cases, the tiling vertices are located at the centers of the  $2 \text{ nm}$  decagonal clusters. The latter are considered as elementary building blocks of the structural model and are arranged as columns along the ten-fold axis. This suggests that the surface has a bulk-like termination with no evident surface reconstruction. This result is in agreement with the x-ray photoelectron diffraction (XPD) patterns recorded on the  $d\text{-Al-Ni-Co}$  sample [60]. *Ab initio* calculations of STM images has been performed by Krajci *et al.* [132] on the ten-fold surface derived from the W-Al-Ni-Co approximant to understand the surface structure and the STM contrast. This approximant is used instead of the QC because a periodic boundary condition and therefore a unit cell is required for the calculations. It has a composition close to that of the Co-rich QCs. Most of the pentagonal features predicted from *ab initio* calculations are observed in the experimental STM images. This study reveals that the electronic density of states (DOS) of Ni and Co atoms around the Fermi level is not symmetric and thus the contrast arising from these elements is dependent on the polarity of the applied bias voltage.

### 2.3.2.3 Surface structure of the $i\text{-Al-Pd-Mn}$ quasicrystal

Prior to insertion into UHV conditions, the five-fold surface of icosahedral  $\text{Al}_{70}\text{Pd}_{21}\text{Mn}_9$  is polished using diamond paste. Once in UHV, the sample is prepared by sputter and anneal cycles [27,133,134]. The sharp LEED patterns recorded after surface preparation displays the expected five-fold symmetry of the QC [35]. The five-fold surface of the  $i\text{-Al-Pd-Mn}$  QC displays a step-terrace morphology with large terraces typically  $100\text{-}300 \text{ nm}$  wide [82]. Two main step heights can be measured, a small one  $S = 4.1 \pm 0.2 \text{ \AA}$  and a large one  $L = 6.5 \pm 0.2 \text{ \AA}$ . The appearance of steps across consecutive terraces follows the Fibonacci sequence. The structure of this surface has been analysed using high-resolution STM images recorded on flat terraces. It reveals pentagonal motifs, dark stars and white flowers (Fig.2.8(a-c)). The structure of the surface can be described using a Penrose ( $P1$ ) tiling of edge length equal to  $8.0 \pm 0.3 \text{ \AA}$  [27,135]. Papadopolos *et al.* have compared the observed structure with the available

bulk model of the icosahedral *i*-Al-Pd-Mn. They concluded that this tiling is consistent with a Penrose tiling obtained from the geometric model based on the 3D tiling [135]. The surface termination consists of two atomic planes separated by a distance of 0.48 Å. This is consistent with previous work carried out by Gierer *et al.* using dynamical LEED calculations [57]. Krajci *et al.* show a resemblance between the *ab initio* calculated and experimental STM images, up to very fine details as presented on Fig.2.8(b-e) [31]. They identify the origin of the white flower and dark star seen in the experimental STM images. These features can be formed by truncated *pseudo*-Mackay clusters and also by surface vacancies. Hence, the five-fold surface of the *i*-Al-Pd-Mn QC, is bulk terminated, with no evident plane reconstruction but with some vertical relaxations of the topmost surface layers [136].

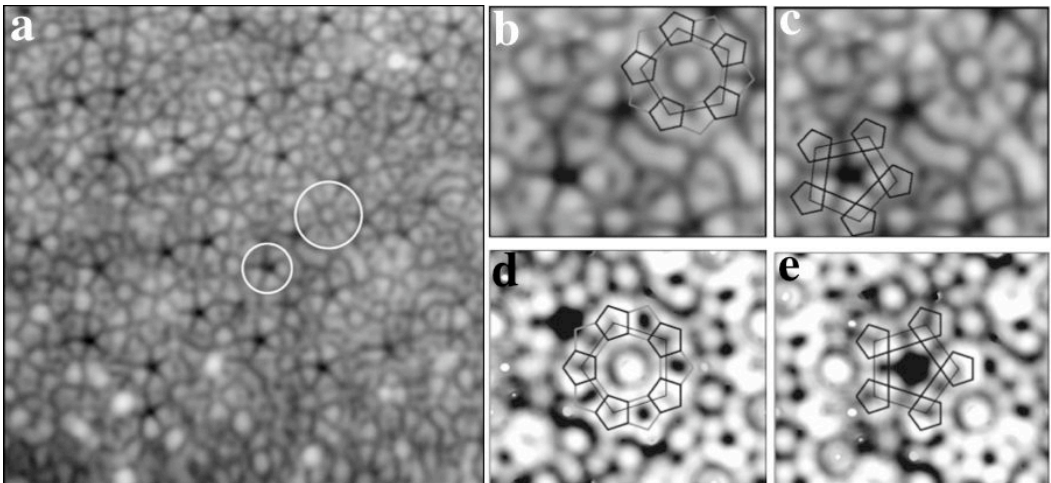


Figure 2.8: (a) high resolution STM image ( $15 \times 15 \text{ nm}^2$ ) of the five-fold surface of *i*-Al-Pd-Mn. In this image, characteristic structural features can be distinguished, namely the “white flower” (WF) and the “dark star” (DS), marked by larger and smaller circles, respectively. (b) and (d) present a comparison of the experimental (b) and calculated (d) STM images ( $3.95 \times 3.29 \text{ nm}^2$ ) of the “white flower”. The “petals” of the WF is formed by pentagons of size  $2.96 \text{ \AA}$ . (c) and (e) present a comparison of the experimental (c) and calculated (e) STM images ( $3.95 \times 3.29 \text{ nm}^2$ ) of the “dark star”. The DS is formed by surface vacancies surrounded by a pentagon of Al atoms separated by  $4.79 \text{ \AA}$  and a pentagon of Pd atoms of the same size forming in the STM image dark “arms” of the DS. Reprinted from [31].

### 2.3.2.4 Surface structure of the *i*-Al-Cu-Fe quasicrystal

Similar experiments have been carried out on the icosahedral Al-Cu-Fe crystal which is considered as isostructural to the *i*-Al-Pd-Mn QC [34], i.e. a similar structure model is used to describe its bulk structure. Then, it is reasonable to expect that the surfaces of both materials will exhibit similar structures. Cai

*et al.* [44] have been investigating the atomic structure of the five-fold surface of *i*-Al-Cu-Fe in UHV using STM. High resolution STM images reveal that the surface structure consists of many flower-like features. The complete “flower” measures approximately 18 Å in diameter and consists of 10 “petals”, giving a local ten-fold symmetry. Many flower-like patterns of similar size have been easily identified within the bulk structural model. They correspond to Al-rich planes, hence leading to the conclusion that the surface is bulk-terminated.

### 2.3.2.5 Surface structure of the *i*-Al-Cu-Ru quasicrystal

The characterization of the five-fold surface of the *i*-Al-Cu-Ru QC [47] reveals an identical step height structure and common features on terraces than on the *i*-Al-Pd-Mn and *i*-Al-Cu-Fe samples. The three systems are considered as isostructural. The first report on the structural analysis of the five-fold surface of *i*-Al<sub>65.5</sub>Cu<sub>19.5</sub>Ru<sub>15</sub> was given by Shimoda *et al.* [47]. A clean surface with terraces and steps can be prepared by ion sputtering and annealing, for instance by several cycles of sputtering (30 min bombardment of 1-3 keV Ar<sup>+</sup> ions) and annealing (up to 1150 K) in a UHV chamber. On the basis of STM measurements, it was found that the atomic arrangement on the surface and the stacking sequence of steps with different heights are fundamentally identical to those of the *i*-Al-Cu-Fe quasicrystal.

### 2.3.2.6 Surface structure of the *i*-Ag-In-Yb quasicrystal

The recent success in growing large single-grain samples of non Al-based QCs, has led to the first study of the Ag-In-Yb surface. The five-fold surface of icosahedral Ag<sub>42</sub>In<sub>42</sub>Yb<sub>16</sub> [137], which is isostructural to the binary icosahedral Cd-Yb quasicrystal, have been investigated using various experimental technique: STM, LEED, RHEED<sup>19</sup> and XPS [138]. The surface reveals large and atomically flat terraces, with roughness comparable to that of Al-based QCs. The quasicrystallinity of this surface is confirmed by the Fourier Transform and the RHEED patterns. The step height distribution and fine structure observed on these terraces are consistent with bulk truncations at Yb-rich dense atomic planes.

## 2.3.3 Surface structure of approximants

As explained above, several surfaces of quasicrystalline phases with different symmetries (2-*f*, 5-*f* and 10-*f*) have been studied. Before the investigations performed in the framework of this thesis, only one approximant phase of the five-fold *i*-Al-Pd-Mn QC, namely the  $\xi'$ -Al<sub>77.5</sub>Pd<sub>19</sub>Mn<sub>3.5</sub> sample had been investigated by Fournée *et al.* [61] and Sharma *et al.* [62]. Recently, the *Y*-Al-Ni-Co and the  $\mu$ -Al<sub>4</sub>Mn approximant phases of the *d*-Al-Ni-Co QC have been investigated at the Empa-Thun [63, 64]. The  $\gamma$ -Al<sub>4</sub>Cu<sub>9</sub> crystal which is

---

<sup>19</sup>Reflection High Energy Electron Diffraction

an approximant to the *i*-Al-Cu-Fe is currently investigated by our group in Nancy.

### 2.3.3.1 Surface structure of the $\xi'$ -Al-Pd-Mn approximant

Fournée *et al.* [61] have characterised two samples of the  $\xi'$ -Al<sub>77.5</sub>Pd<sub>19</sub>Mn<sub>3.5</sub> phase grown by two different techniques, the Bridgman and the self-flux method. The surface preparation consists of annealing the sputtered surface at 823 K for 2-4 h. Following this preparation, the STM studies of the  $\xi'$ -Al-Pd-Mn surface [61] revealed a step-terrace morphology. The terraces are fairly large and the step edges are smooth in contrast to the meandering step edges observed on quasicrystal surfaces (Fig.2.10(a)). It has been further revealed that surfaces prepared under different conditions yield different terrace morphologies and step height formations. Under ideal preparation conditions the surface structure shows steps of a single height of about 8.0 Å and structurally perfect terraces. The surface exhibits long-range order with the symmetry expected from the bulk model. This is demonstrated by the LEED pattern which shows spots with a *pseudo*-10-fold symmetry as shown on Fig.2.9(a). The pattern consists of strong and weak diffraction spots aligned in lines and spaced periodically. In addition to the long-range order observed by LEED, the surface exhibits short-range order with local ten-fold symmetry, as evidenced by XPD (Fig.2.9(b)) [139].

The high resolution images recorded on terraces show bright dot-like features (see Fig.2.10(b)) of approximately 2.0 Å high and 10.0 Å wide. Their nearest distance is about 12.0 Å. The positions of these features are correlated, and not random. This was realized from the Fourier transform of these features, which showed strong maxima with near ten-fold symmetry. Both the fine structure on the terraces and the formation of the different steps can

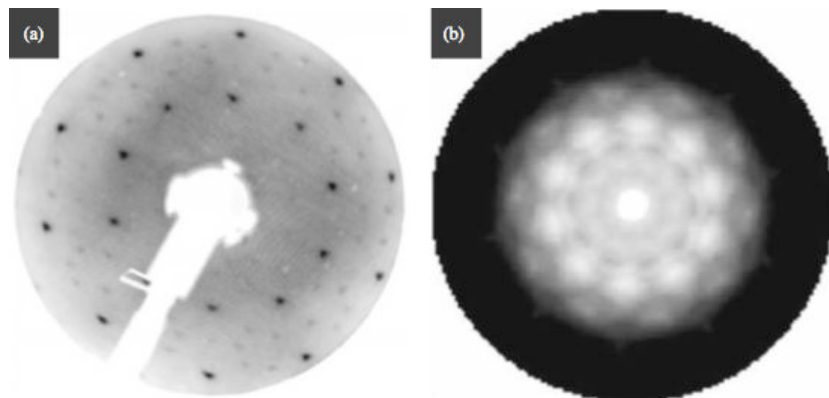


Figure 2.9: (a) LEED pattern recorded at 85 eV from the *pseudo*-10-fold surface of the  $\xi'$ -Al-Pd-Mn approximant (Reprinted from [61]) [58].(b) Stereographic projection of the XPD image of the Pd 3d core level intensity obtained from the same surface [139].

be understood in terms of the bulk model of the  $\xi'$ -Al-Pd-Mn phase [140]. The dots represent the incomplete layer in the bulk model and correspond to groups of Al atoms forming a decagonal ring, which indicates regrowth of these Al atoms during the annealing process. The ring corresponds to part of the 3D Mackay-type clusters, the building blocks of this phase. The regrowth of atoms at the cluster sites during the annealing process suggests that the cluster sites are more energetically favorable than the glue atom sites [61].

Different surface preparations have been used to study the same surface [62]. The first preparation method is performed for a maximum annealing temperature of 853 K, with a total annealing time of about 18 hours. The surface structure reveals a predominant step height of about 8.0 Å. In addition, steps of 16.0 Å height are observed occasionally. The terraces contain a high density of pits, mostly pentagonal in shape, with depths equivalent to the step height of 8.0 Å. The formation of these pits was interpreted in terms of bulk vacancy diffusion at the surfaces upon annealing during the surface preparation. The second preparation method was achieved by three sputter-annealing cycles after the repolishing of the sample. The sample was annealed at 783 K, followed by a flash at 853 K. The total annealing time was about 3 hours. STM images measured on the surface show almost no pits on the terraces. However, occasional screw dislocations were found on the surface. This preparation yields additional steps of 4.0 Å height.

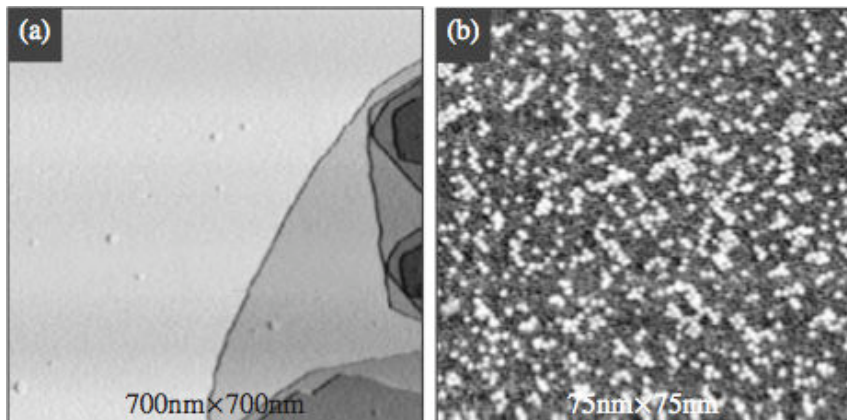


Figure 2.10: *STM images of the pseudo-10-fold  $\xi'$ -Al<sub>77.5</sub>Pd<sub>19</sub>Mn<sub>3.5</sub> surface prepared by annealing up to 853 K. (a) STM image ( $700 \times 700$  nm $^2$ ) showing a step-terrace morphology. (b) High resolution STM image ( $75 \times 75$  nm $^2$ ) showing the atomic surface structure. Reprinted from [62].*

### 2.3.3.2 Surface structure of the 6-fold (001) $\mu$ -Al<sub>4</sub>Mn approximant

The 6-fold (001)  $\mu$ -Al<sub>4</sub>Mn crystal (563 atoms/unit cell) which is structurally and chemically related to the decagonal QC's has been investigated using LEED, XPD/SSC and high-resolution low temperature (5.3 and 77 K) STM

[64]. The atomic surface structure reveals a termination very close to the planes present within the bulk model. The STM images recorded on this surface (only one of the two terminations) of high Mn content are bias depend. Two stable terrace types, separated by the step height of  $c/2$ , have been identified as surface terminations. The most stable termination appears to be related to the mirror planes present within the unit cell. Additional investigations are ongoing to complete the data set.

### 2.3.3.3 Surface structure of the (100) Y-Al-Ni-Co approximant

The  $Y\text{-Al}_{75.8}\text{Ni}_{2.1}\text{Co}_{22.1}$  crystal (32 atoms/unit cell) is considered as an approximant of the two-fold decagonal Al-Ni-Co quasicrystal [63]. The atomic structure of the (100) Y-Al-Ni-Co surface was probed by LEED and STM (XPD/SSC and ARPES was also performed). The results indicate three different surface terminations and three different types of surface reconstructions. A common feature to the three surface reconstruction types is the doubling of the bulk periodicity along the [010] direction (from 4.0 Å to 8.0 Å). All three terminations have been successfully related to the densest bulk layers. In addition, the bias dependency is found also on one of these terminations. The surface structure is highly anisotropic and it is described by atomic columns aligned along the b-axis.

## 2.4 Quasicrystalline surfaces as templates

### 2.4.1 Adsorption sites and role of surface clusters

STM images of the clean five-fold surfaces of the icosahedral quasicrystals exhibits pentagonal dark stars. These stars correspond to surface vacancies and act as preferential nucleation sites for most adsorbates tested so far. This has been demonstrated, for example, by the adsorption of  $C_{60}$  molecules on five-fold *i*-Al-Pd-Mn surfaces [134] and of Al atoms on the five-fold *i*-Al-Cu-Fe surfaces [141]. They have been also identified as preferential adsorbate sites for Cu [142, 143] and Sn [144]. However, for Si atoms, the centers of the truncated Mackay clusters, which appear as white flowers in STM images, are preferential adsorbate sites [145]. The different studies are briefly reviewed below.

#### 2.4.1.1 Al/*i*-Al-Cu-Fe

At submonolayer coverage, Al adatoms deposited at room temperature on the five-fold surface of an Al-Cu-Fe QC form two-dimensional features looking like a “starfish” (see Fig.2.11(a)) [141]. These starfishes of dimensions comparable to the dark stars point in the same direction across the surface. It has been established that the islands are preferentially formed on the pentagonal dark stars. The Al adatoms adopt a structure enforced by the local arrangements of

the quasicrystalline substrate. With increasing coverage, the Al film follows a different growth mode, which excludes the formation of a dense quasiperiodic overlayer.

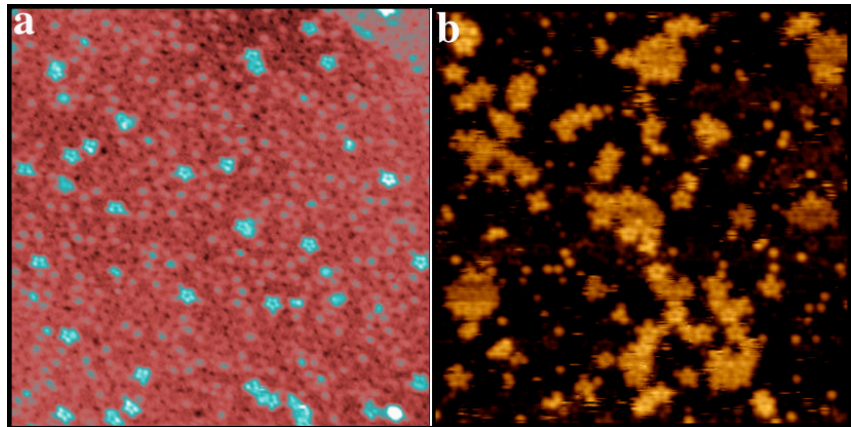


Figure 2.11: (a) STM image ( $45 \times 45 \text{ nm}^2$ ) of the five-fold *i*-Al-Cu-Fe surface after deposition of 0.04 ML of Al. The growth of 2D islands resembling a “starfish” is easily distinguishable. Reprinted from [141]. (b) STM image ( $30 \times 30 \text{ nm}^2$ ) measured for 0.2 ML Pb coverage on the *i*-Al-Pd-Mn surface. The formation of a starfish network is observed. Reprinted from [93].

#### 2.4.1.2 Pb/*i*-Al-Pd-Mn

The initial adsorption of Pb on the five-fold *i*-Al-Pd-Mn surface has been investigated using STM and compared with *ab initio* density-functional calculations. The results show that Pb adatoms are relatively mobile at room temperature and diffuse on terraces to nucleate preferentially above white flower sites as shown on Fig.2.11(b). They form pentagonal islands which are described as a two-shell structure consisting of 10 Pb adsorbates. In addition, the theoretical calculations reveal that this 10-atom starfish is the most stable structure [93].

#### 2.4.1.3 Bi/*i*-Al-Pd-Mn

For Bi adsorption, STM measurements at submonolayer coverage reveal the formation of pentagonal islands on the five-fold *i*-Al-Pd-Mn surface. At the complete monolayer, the Bi thin film is quasiperiodically ordered. The initial nucleation sites have been recently identified as the centers of the white flower motifs [146].

#### 2.4.1.4 Si/*i*-Al-Pd-Mn and Si/*d*-Al-Ni-Co

The objective of these investigations is to stimulate the interaction between the *pseudo*-gap of the quasicrystalline surface and the band-gap of the semi-conducting element. Ledieu *et al.* have reported that the deposition of Si adatoms on the five-fold *i*-Al-Pd-Mn surface produces the formation of an ordered overlayer [145]. The analysis of STM images indicates that the single Si adatoms form a quasiperiodic array (see Fig.2.12(a)). The initial nucleation site is identified as the center of truncated Mackay cluster, i.e. the center of the “white flower” (see Fig.2.12(b)). The ordered overlayer is obtained up to about 0.25 ML.

Leung *et al.* have reported that at a coverage of 0.30 ML, Si adatoms deposited on the ten-fold *d*-Al-Ni-Co surface form pentagonal nanoclusters arranged according to the Fibonacci sequence [147]. In the first stages of adsorption, it is proposed that the adatoms sit in the depressions related to the pentagonal features observed on the clean *d*-Al-Ni-Co substrate. For both quasicrystal surfaces and at higher coverages, the Si overlayer become progressively disordered and form a rough pattern of 3D islands. It has been reported that Si atoms are mobile at room temperature for the decagonal substrate, but not on the *i*-Al-Pd-Mn substrate.

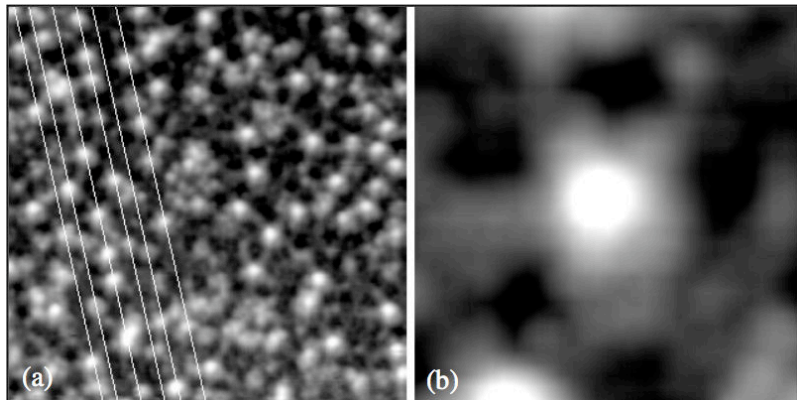


Figure 2.12: (a) STM image ( $20 \times 20 \text{ nm}^2$ ) for a coverage of 0.25 ML of Si on the five-fold surface of *i*-Al-Pd-Mn. A 1D Fibonacci sequence has been extracted from the visible Al-Pd-Mn substrate. The Si adatoms predominantly lie along these lines. (b) STM image ( $3.3 \times 3.3 \text{ nm}^2$ ) showing a Si atom adsorbed on top of the “white flower”. Reprinted from [88].

#### 2.4.2 Periodic overlayers

##### 2.4.2.1 The 10-*f* surface of the *d*-Al-Ni-Co quasicrystal as template

**Au, Pt, Ag/*d*-AlNiCo:** Several metals have been chosen as adsorbates and dosed on the ten-fold *d*-Al-Ni-Co surface. The Au or Pt adatoms form ten rota-

tional domains of  $\text{AuAl}_2$  or  $\text{PtAl}_2$  alloy with the (110) surface plane [148–151]. Each domain is aligned along the high symmetry directions of the substrate, resulting in a 10-fold twinned structure. A similar scenario applies when depositing Ag adatoms on the decagonal surface. Indeed, the growth of Ag leads to a twinned structure composed of ten different domains. Above 10 MLE and at room temperature deposition, the deposited Ag adopts the form of fcc nanocrystals with the (111) plane aligned parallel to the substrate plane [152].

**Xe/*d*-AlNiCo:** Using LEED, the growth of Xe atoms on the decagonal surface of the Al-Ni-Co QC has been reported by Ferralis *et al.* [54]. For coverages up to 2 ML, the Xe atoms grow in layer-by-layer mode at substrate temperatures ranging from 60 to 80 K. In this coverage regime, the LEED does not change the pattern structure but only the spot intensity, which indicates that the growth is pseudomorphic. For coverage higher than 2 ML, new spots appear in the LEED pattern. The pattern is consistent with the formation of five domains of fcc Xe(111), with the (111) axis perpendicular to the substrate plane [54]. The simulations performed using the grand canonical Monte carlo method [153] confirm that the growth of the bulk film starts in the second layer. At coverage lower than 2 ML, the quasicrystalline order is transmitted to the Xe film [153].

#### 2.4.2.2 The 5-*f* surface of the *i*-Al-Pd-Mn quasicrystal as template

**Au, Pt, Ag/*i*-AlPdMn:** The  $\text{AuAl}_2$  or  $\text{PtAl}_2$  structures are also formed when dosing Au and Pt on the five-fold *i*-Al-Pd-Mn surface. The orientation of these domains reflects the high symmetry of the substrate [59, 150, 151]. As on the ten-fold surface, the Ag adsorbed at room temperature develops a twinned structure with five different rotation domains<sup>20</sup>. The formation of Ag nanocrystals with fcc structure is observed for coverages above ten monolayers [38].

**Al/*i*-AlPdMn:** The growth mode of Al on the five-fold surface of the *i*-AlPdMn QC is influenced by the substrate temperature while dosing. For temperatures below 250 K, the structure observed is similar to that observed by dosing Ag, i.e. formation of five domains of bcc Al(111) structure parallel to the surface plane. For temperatures ranging from 250 to 300 K, the growth also developed with 5-*f* twinning, but the (111) plane is not aligned along the surface plane. It is parallel to one of the five three-fold axis of the surface. At high temperature deposition, the inter-diffusion of Al into the bulk is favored which can explain the different film orientations. When the process of inter-diffusion is minimized as a result of the low temperature deposition, the

---

<sup>20</sup>The nanocrystals still retains the symmetry of the substrate on which the growth started at a mesoscopic scale, as evidenced by the n-fold twinning of nanocrystallites, where the index n depends on the substrate symmetry.

Al atoms grow in five domains with the [111] direction perpendicular to the surface plane [154–156].

**Fe/*i*-AlPdMn:** Weisskopf *et al.* have reported the investigation of the deposition of magnetic elements on a clean five-fold surface of an icosahedral Al-Pd-Mn [157]. Fe films were deposited at an elevated substrate temperature of 340 K and the investigation was achieved in reciprocal space by using LEED and in the real space by means of secondary-electron imaging (SEI). In this system, intermixing and interdiffusion dominate the interface between the film and the substrate. The behaviour of the adatoms of Fe depends on the amount of Fe adsorbed. At low coverage, the Fe adatoms diffuses into the bulk leading to a disordering of the quasiperiodic substrate. The LEED pattern revealing the structure of the substrate disappears after dosing of 2 ML. At coverage higher than 8.0 Å (equivalent to 4 ML), the Al atoms diffuse from the substrate to the Fe layer producing a new LEED pattern. The atomic structure of this new surface consists of five-fold twinning of cubic domains rotated with respect to each other by 72° and parallel to the [110] directions. The same structure is observed after deposition of 8 ML, but the domains are tilted by 0.5°. The diffusion of Al into the Fe film leads to the formation of surface alloying. The results obtained indicate magnetic ordering, related to AlFe<sub>3</sub> or Fe diluted with Al [157]. The same magnetic material deposited on the isostructural QC of *i*-Al-Cu-Fe will be discussed below.

#### 2.4.2.3 The *p*-10-*f* surface of the $\xi'$ -Al-Pd-Mn cristal as template

Only two adsorption experiments have been performed on the approximant phase, namely Ag/ $\xi'$ -Al-Pd-Mn and Pd/ $\xi'$ -Al-Pd-Mn. As for quasicrystalline surfaces, twinned structures with two different domains have been observed when dosing Ag on the *pseudo*-10-fold surface of this approximant [158]. Fournée *et al.* have reported that Pd atoms form rough tiny particles and no ordering or flat islands could be observed. The size of these particles increases with increasing film thickness, up to 3 nm at 7 ML coverage. The Pd particles do not coalesce with time and are relatively stable upon annealing up to 920 K [139].

### 2.4.3 Pseudomorphic overlayers

The main objective of these growth studies is to obtain pseudomorphic quasicrystalline thin films composed of a single element. Among the several elements deposited on different CMA substrates, only a limited number of systems are found to yield quasiperiodically ordered films. These systems of reduced chemical complexity can now be used to study the exclusive relationship that exists between quasicrystalline order and its associated physical properties.

#### **2.4.3.1 Bi, Sb/*d*-Al-Ni-Co**

The first quasicrystalline monolayers were observed by Franke *et al.* by depositing Bi or Sb on the five-fold surface of *i*-Al-Pd-Mn and the ten-fold surface of *d*-Al-Ni-Co QC [159, 160]. The films were deposited at an elevated substrate temperature of about 573 K, which is above the multilayer desorption temperature. Hence, only a single atomic layer of the adatoms could be adsorbed. The films were characterized by LEED and He scattering. Because low energy He atoms are scattered above the topmost surface atoms, the information gained by He scattering comes exclusively from the monolayers. Both the diffraction pattern from He scattering and LEED measurements from the monolayers show the same symmetry and peak positions as those from the respective clean surfaces. This demonstrates the quasicrystalline structure of the adsorbed monolayers. The large number of diffraction spots observed in the LEED patterns after the deposition of the adatoms can be understood by a higher electron-scattering cross-section expected for the “heavier” Sb and Bi adatoms. The Sb (and Bi) films were found to be stable up to 1023 K (673–873 K), revealing a strong interaction between the substrate and adatoms.

#### **2.4.3.2 Pb/*i*-Al-Pd-Mn**

Ledieu *et al.* [88] used the five-fold surface of the *i*-Al<sub>70</sub>Pd<sub>21</sub>Mn<sub>9</sub> as a template to grow a Pb quasiperiodic monolayer. They observed the formation of pentagonal Pb islands that interconnect to form a quasiperiodic monolayer as shown on figure 2.13(a). This structure can be defined, as for the clean surface, by the Penrose *P1* tiling. However, the tiles used (the regular pentagon, the rhombus, the boat and the pentagonal star) are inflated by  $\tau$  compared to similar structural elements present in the underneath quasiperiodic substrate. This quasiperiodic structure formed just by one element display a *pseudo-gap* in the density of states at Fermi level as evidenced by using UPS and STS. The reduction of states at  $E_F$  is directly related to the quasiperiodic structure of the Pb film.

#### **2.4.3.3 Pb/*d*-Al-Ni-Co**

Pb adatoms have been deposited on the ten-fold surface of the *d*-Al<sub>72</sub>Ni<sub>11</sub>Co<sub>17</sub> QC at room temperature. The overlayer grows through nucleation of nanometer-sized irregular shaped islands up to 1 MLE at which point the coverage saturates. Five-fold hollows present within the Pb film are circled on figure 2.13(b) (small circle). Also circled, is another larger five-fold feature (large circle) which is reminiscent of the motifs found on the five-fold surfaces of icosahedral quasicrystals [27] and on the clean surface of *d*-Al-Ni-Co QC [130]. The observation of these features indicates that the structure of the quasicrystalline overlayer has similarities to that of the underneath clean surfaces. The overlayer is quasiperiodically ordered as evidenced by LEED measurements and the FFT of STM images. LEED measurements also in-

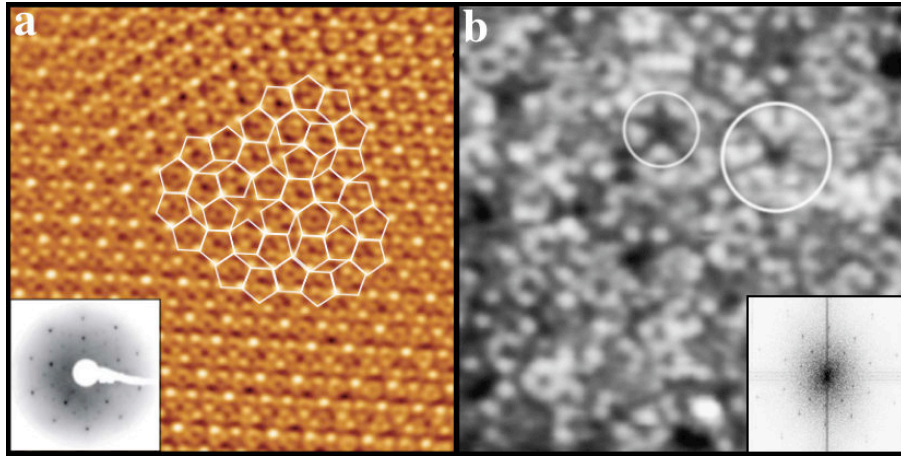


Figure 2.13: (a) Fourier filtered STM image ( $25 \times 25 \text{ nm}^2$ ) of 1.0 ML of Pb adsorbed on the 5-fold surface of the *i*-Al-Pd-Mn QC. A Penrose tiling ( $P1$ ) is superimposed on the Pb monolayer which emphasises the quasiperiodic nature of the deposited monolayer. The tiles used are  $\tau$ -inflated compared to those found for the clean surface. Inset: The LEED pattern recorded at 80 eV for the same coverage reveals a well-ordered quasiperiodic structure. Reprinted from [88]. (b) STM image ( $15 \times 15 \text{ nm}^2$ ) shows a quasicrystalline Pb film deposited on the *d*-Al-Ni-Co QC at room temperature. The circles indicate pentagonal motifs defining 5-fold hollows. Inset: FFT of a  $50 \times 50 \text{ nm}^2$  image from this coverage. The spot distribution (decagonal rings) is consistent with a quasiperiodic ordering. Reprinted from [92].

dicate that annealing the film to  $600 \text{ K}$  improves the structural quality, but causes the film to develop pores as observed by STM. Using XPS, the chemical interaction of the Pb atoms is shown to be weak with the substrate, i.e. no charge transfer or sign of alloying.

#### 2.4.3.4 Bi/*i*-Al-Cu-Fe

Bi has been deposited at room temperature on the five-fold *i*-Al-Cu-Fe surface. The Bi adatoms grow quasiperiodically at monolayer coverage and below with a pseudocubic (100) orientation (as indicated by the RHEED pattern on the inset of Fig.2.15(a)) [161]. Krajci *et al.* have studied using *ab initio* calculations the adsorption of Bi on the same decagonal surface. The theoretical results confirm the formation of a quasiperiodic monolayer [31]. At high coverage, Bi thin film forms rectangular and flat islands (see Fig.2.15(a)) aligned in five preferred directions rotated from each other by  $72^\circ$ . These directions correspond to the high symmetry directions of the substrate. This 3D Bi islands are formed on top of a quasicrystalline Bi wetting layer, not on the clean substrate [161].

#### 2.4.3.5 Sn/*i*-Al-Cu-Fe

This pseudomorphic growth mode has also been observed by dosing Sn on the same substrate [144]. Sharma *et al.* have reported the formation of a quasiperiodic monolayer by dosing Sn adatoms on the five-fold surface of *i*-Al-Cu-Fe. Up to one monolayer and on a substrate kept at 573 K, the deposited Sn grows smoothly and forms a monolayer film of Sn. This is confirmed by the STM images showing a step height of about 1.5 Å corresponding to half of the lattice constant of tetragonal Sn along the *c*-axis (*c*/2). In the structural bulk model of *i*-Al-Cu-Fe, the layers are not separated by a distance of 1.5 Å which confirms that the step height formed on the substrate monolayer is associated with the film of Sn. Atomic resolved STM images show pentagonal motifs related to the intrinsic stars of the clean surface. This confirms that the substrate enforces the formation of the first quasiperiodic monolayers. The quasiperiodicity/long-range order of this structure is confirmed using FFT. It shows decagonal rings related by factor  $\tau$ .

#### 2.4.3.6 Cu/*i*-Al-Pd-Mn

Using STM and LEED, Ledieu *et al.* investigated the growth of Cu on the 5-*f* Al-Pd-Mn surface at room temperature [142, 143]. Up to 8 ML, Cu grows smoothly in a layer-by-layer mode. The stacking of the monoatomic layers along the surface normal is periodic with a period of 1.9 Å. At coverage higher than 8 ML, Cu adsorption transits to a 3D growth mode. The LEED pattern indicative of the clean substrate is gradually reduced in intensity between 1 ML and 2 ML, and new diffraction spots appear between 3 ML and 25 ML. The new LEED pattern is clearly 10-*f* symmetric, and reveals a quasiperiodic ordering on the Cu film (Fig.2.14(d)).

The STM image reveals also a quasiperiodic ordering of the film. The structure of the film is described by a sequence of Cu rows, with two types of spacings  $S = 4.5$  Å and  $L = 7.3$  Å (see Fig.2.14(a-b)). The ratio of these distances L/S is close to the golden mean,  $\tau$ . The rows are arranged aperiodically according to a Fibonacci sequence LSLLSLSLL (as shown in the profile on Fig.2.14(c)). The pentagonal dark stars of the substrate are separated by the same intervals ( $S$  et  $L$ ), indicating that the quasiperiodic rows of the Cu film adopt the substrate structure. The row structure is propagated from one layer to the next with increasing coverage. The Cu rows are oriented in five different directions, rotated from each other by 72°. The periodicity along the row is measured at 2.5 Å, which is consistent with the nearest neighbor distance of the bulk Cu. This periodic order is confirmed by the LEED patterns recorded at low temperature of 85 K.

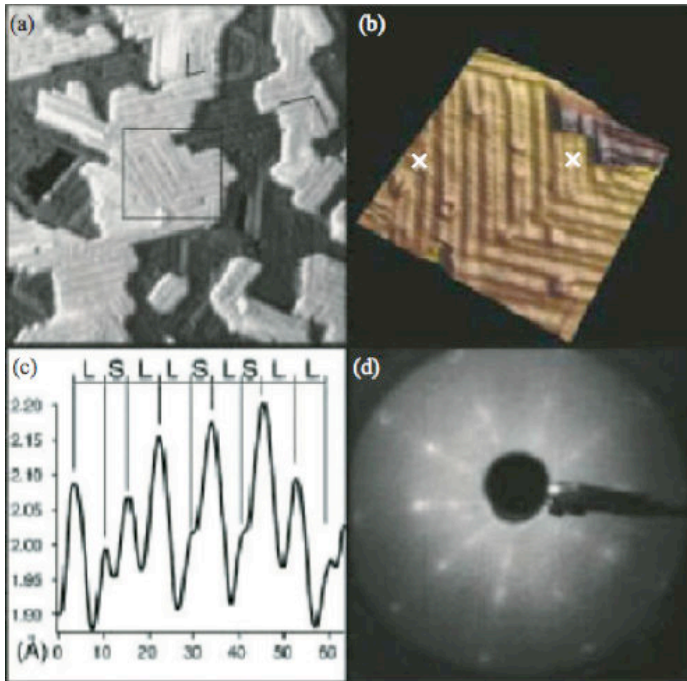


Figure 2.14: (a) STM image ( $40 \times 40 \text{ nm}^2$ ) recorded after deposition of 5.5 ML of Cu on the 5-f *i*-Al-Pd-Mn surface. (b) STM image ( $10 \times 10 \text{ nm}^2$ ) enlarged from the square indicated on (a). (c) The height profile is measured between the two points marked with a cross in (b). (d) LEED pattern (beam energy 50 eV) measured from this phase. Reprinted from [142].

## 2.4.4 Nanoislands with “magic heights”

### 2.4.4.1 Quantum size effects

Another interesting phenomenon associated with the overlayer growth is the formation of islands of specific heights, called “magic heights”. Fournée *et al.* [161] observed this process during the growth at room temperature of Bi and Ag thin films on the five-fold surface of the Al<sub>63</sub>Cu<sub>24</sub>Fe<sub>13</sub> and the Al<sub>72</sub>Cu<sub>19.5</sub>Fe<sub>8.5</sub> quasicrystal, respectively. This phenomenon has been observed previously only at low temperature while growing metal films on a semiconductor [162–165] or on metal surfaces [166, 167]. The formation of islands with magic heights correspond to the stacking of a specific number of atomic layers. This unusual growth morphology is interpreted in terms of quantum size effects (QSE), resulting from the confinement of electrons within the thin film in the direction perpendicular to the substrate. The interface of film/substrate (Bi/*i*-Al-Cu-Fe or Ag/*i*-Al-Pd-Mn) has the property to confine electrons in the film, if the energy of the adsorbates (Bi or Ag) *s p* electrons lies within a gap of the surface projected bulk electronic states of the substrate [161]. It was thought that the magic island heights are thus a direct manifestation of the electronic structure associated with the quasiperiodicity of the substrate. However, as shown by

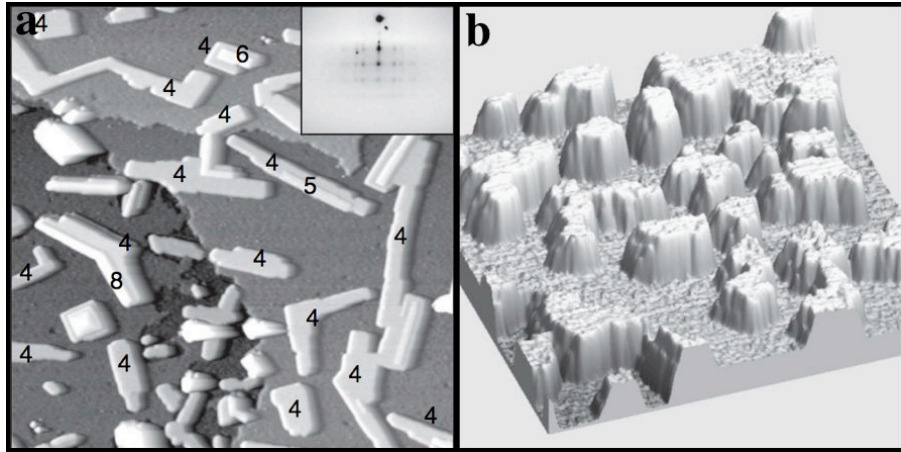


Figure 2.15: (a) STM image ( $400 \times 400 \text{ nm}^2$ ) showing the topography of the five-fold *i*-Al-Cu-Fe surface dosed with 4.5 ML of Bi. Island heights are indicated in units of monolayers. Inset: a typical RHEED pattern observed for the Bi thin film. (b) STM image ( $243 \times 243 \text{ nm}^2$ ) showing the five-fold surface of the *i*-Al-Pd-Mn after deposition of 1 ML of Ag. Flat-top islands grow directly onto the clean quasiperiodic substrate, without formation of a first wetting layer. Reprinted from [161].

Moras *et al.* the incompatible symmetry group could be an alternative explanation [168].

#### 2.4.4.2 Bi/*i*-Al-Cu-Fe

As presented before (see Sect.2.4.3), the Bi film adopts a structure with a pseudocubic [100] orientation (the interlayer distance along this direction is  $d_{[100]} = 3.28 \text{ \AA}$ ). After deposition of 4.5 ML at room temperature on the *i*-Al-Cu-Fe sample, STM images show the formation of 3D islands (see Fig.2.15(a)). The height of the islands measured from the wetting layer was found to be  $13 \text{ \AA}$  ( $= 4 \times d_{[100]}$ ), or a multiple of this height. The observed heights correspond to the stacking of four atomic layers, or multiples of this height. In a few STM images, bi-layer islands (of height  $6.5 \text{ \AA}$ ), which had irregular shape, were observed immediately after deposition, but these islands tended to disappear with time. Interestingly, single-layer or triple-layer Bi islands were never observed. The islands with specific height manifest as stable structure on this system [161].

#### 2.4.4.3 Bi/*i*-Al-Pd-Mn and Bi/*d*-Al-Ni-Co

Similar observations could be observed by dosing Bi on these two quasicrystals [48]. Recently, Sharma *et al.* reported that at room temperature the deposited Bi yields a quasicrystalline film up to one monolayer. Then, up to 5 ML, Bi

forms nanoislands with a (100) surface orientation. The islands have magic heights, which correspond predominantly to the stacking of four atomic layers, which is the most stable configuration. 2-layer high islands reshape themselves into 4-layer height island or coalesce with the neighboring 4-layer high islands. For higher coverage ( $> 5$  ML), Bi grows with monoatomic step height (not with magic height) and reflects the three-fold symmetry expected from the bulk Bi. If the deposition of the Bi is carried out at a substrate temperature of 523 K, only the first quasiperiodic monolayer (not the multilayers) can be adsorbed for the three quasicrystals. This temperature is high enough to activate terrace diffusion resulting in the assembling of Bi adatoms and forming a smooth quasiperiodically ordered structure at one monolayer coverage. At this temperature, multilayers do not adsorb.

#### 2.4.4.4 Ag/*i*-Al-Pd-Mn

Fournée *et al.* [161] reported another example of “magic height”, by depositing Ag on the five-fold *i*-Al-Pd-Mn surface. The STM image recorded after the deposition of one monolayer at 365 K shows islands formed directly on the clean quasicrystalline surface, without formation of a first wetting layer (see Fig.2.15(b)). Opposed to the highly faceted Bi islands, the Ag islands in this case exhibit a rather irregular shape. Up to 0.3 ML, most of the islands display a height of 1 or 2 atomic layers. Above 0.3 ML, more than 80 % of the Ag islands are 4- or 5-layer high, whereas the remaining 20 % of the total population of the islands show heights of 1 to 3 layers. At 300 K and for coverage of 1 ML, islands initiate nucleation at specific trap sites of the quasiperiodic substrate lattice. The growth proceeds vertically with the appearance of needle-like features corresponding to selective heights of 4 and 5 layer high islands [38].

## 2.5 Conclusions

The motivation of this first chapter was to present the background and the state-of-the-art in the field of surface science of complex metallic alloys. The phenomena discussed in this review will be crucial for a better understanding of the following chapters. A lot of effort has been put into the characterisation of clean CMA surfaces, as this constitutes an indispensable step before any reasonable study of thin film growth can be initiated. The structures of the sputter-annealed surfaces have been characterized using a large range of experimental and theoretical techniques. Most of these studies have revealed that the surfaces after appropriate cycles of preparation are considered as bulk-truncated. Other surface phenomena such as surface relaxation and facetting have been also observed, but surface reconstruction has not yet been found. These studies suggest that dense Al-rich planes are preferentially selected as topmost surface layers. The pseudomorphic growth of several materials on different types of CMAs surfaces has been achieved successfully. One of the

main objective was to obtain a pseudomorphic and therefore quasiperiodically ordered thin film of a single element, to reduce the chemical complexity inherent to the CMA surfaces. Such films are of particular interest as they provide an opportunity to study the aperiodic order independently of the chemical complexity. The next four chapters present the characterization of the clean surfaces of  $\text{Al}_{13}\text{Co}_4$  and T- $\text{Al}_3(\text{Mn, Pd})$  approximants and adsorption studies of single elements carried out on these two *pseudo*-10-fold surfaces. Using similar adsorbates as those deposited on QC surfaces, this work should allow us to assess, for instance, the influence of a large periodicity and of a cluster substructure within the unit cell on the growth mode of the thin film.

# Chapter 3

## Investigation of the (100) surface of the Al<sub>13</sub>Co<sub>4</sub> crystal

### 3.1 Introduction

Over the last fifteen years, the surface structures of icosahedral and decagonal quasicrystals have been intensively studied both from an experimental and a theoretical viewpoint [146]. One major task has been to understand the interplay which exists between their fascinating crystallographic structure and the unusual physical properties measured for surfaces of Al-based CMAs (high hardness, low coefficient of friction...) [5]. With the growth of single element quasiperiodic monolayers on quasicrystalline templates, it has been recently possible to show how the electronic structure of a thin film was influenced by its aperiodic structure [88]. Due to the structural complexity inherent to the aperiodic order, approximant phases have often been introduced to model their parent quasicrystal and to perform calculations requiring periodic boundary conditions and therefore a finite unit cell. For instance, approximant structures have been employed successfully to understand the electronic charge density distribution at the surface of the icosahedral Al-Pd-Mn quasicrystal [101]. From *ab initio* calculations, simulated STM images have been generated and they nicely reproduce the local motifs observed on the experimental STM images recorded on quasicrystalline surfaces [31]. This agreement validates further the use of such periodic crystals to model aperiodic structures.

Up to now, the surface study of only one approximant crystal has been reported using scanning tunneling microscopy (STM) and low energy electron diffraction (LEED) [61, 62]. The analysis carried out on the  $\xi'$ -Al-Pd-Mn surface revealed that large flat terraces are separated by a minimal step height which corresponds to half the period along the *pseudo-10-fold* (*p-10f*) axis. This indicates preferential surface termination at specific atomic layers, which are related by a mirror plane. The incomplete topmost surface layers and the atomic fine structures imaged by STM can be interpreted using planes perpendicular to the *p-10f* axis of the bulk structure model. The fine structure imaged by STM on a single terrace can be interpreted using the bulk structure model and reveals the existence of an incomplete top layer which consists of

decagonal rings of atoms decorating the orthorhombic unit cell. These decagonal rings of atoms are part of the 3D cluster units used to describe the  $\xi'$  phase [61].

Recent achievements in the growth of centimeter-sized single crystals [169] have allowed the investigation of other CMA surfaces. Here we report the study of the (100) surface of the orthorhombic  $\text{Al}_{13}\text{Co}_4$  approximant using scanning tunneling microscopy (STM), low-energy electron diffraction (LEED), ultra-violet and x-ray photoelectron spectroscopy (UPS, XPS), x-ray photoelectron diffraction (XPD) and *ab initio* density functional calculations. The model of the bulk structure has been proposed by Grin *et al.* [66] and is presented in Sect.3.2. Following the description of the experimental details in Sect.3.3, the surface preparation along with the identification of the different surface terminations will be explained in Sect.3.4. The calculated electronic density of states at the Fermi level and the measured valence band will be compared in Sect.3.5. From *ab initio* calculations, simulated STM images will allow us to interpret our STM measurements. We demonstrate that the most preferred surface termination is related to an incomplete puckered layer of the bulk structure in the topmost surface plane.

## 3.2 Model of the bulk structure

The  $\text{Al}_{13}\text{Co}_4$  sample is an approximant of the decagonal Al-Ni-Co quasicrystal (DQC) [67, 72, 73], whereas the  $\xi'$ -Al-Pd-Mn sample has a structure related to the icosahedral Al-Pd-Mn quasicrystals [140, 170]. This orthorhombic crystal belongs to the space group  $Pmn2_1$  and has a unit cell containing 102 atoms (78 Al and 24 Co atoms) with the following lattice parameters (Pearson's symbol  $oP102$ ):  $a = 8.158 \text{ \AA}$ ,  $b = 12.342 \text{ \AA}$  and  $c = 14.452 \text{ \AA}$  [66, 74, 171, 172]. Its bulk structure has been investigated using x-ray single crystal and powder diffraction techniques [66]. The  $\text{Al}_{13}\text{Co}_4$  structure is related to several other complex metallic alloys like the monoclinic  $\text{Al}_{13}\text{Fe}_4$  [75, 76] and other  $\text{Al}_{13}\text{Co}_4$  [77] phases, the  $\text{Al}_{13}(\text{Pd, Fe})_4$  [78] and the  $\epsilon$ - $\text{Al}_3\text{Co}$  [72] phases. The bulk structure of this approximant is described by the stacking along the [100] direction of two types of layers, a flat ( $F$ ) and a puckered ( $P$ ) plane, separated by a mean distance of 2.0  $\text{\AA}$ . These layers have a  $p-10f$  symmetry and appear in the following sequence:  $F_{0.0}P_{0.25}F_{0.5}P_{0.75}$ , where  $P_{0.75}$  and  $P_{0.25}$  are mirrored against  $F_{0.5}$ . The  $F$  layer contains 17 Al and 8 Co atoms. The  $P$  layer contains 22 Al and 4 Co atoms and it is therefore slightly Al-rich compared to the  $F$  layer and denser by one atom. All atomic sites are fully occupied in this model.

The structure of a single  $F$  layer can be described by a tiling composed of pentagons and rhombi obtained by connecting Co atoms in the plane. The pentagonal tiles are decorated in two different manners: either by 5 Al atoms forming a highly distorted pentagon or by an Al-centred pentagon forming a decagonal ring with the Co pentagon (Fig.3.1(a)). The connection between the Co pentagons is completed by one type of rhombus decorated by atoms belonging to both pentagonal tiles. As proposed by Henley *et al.* [79], the

structure along the [100] direction of the  $\text{Al}_{13}\text{Co}_4$  crystal can be described using the so-called “pentagonal bipyramid” (PB) cluster as basic building block (left of Fig.3.1(c)). The PB is a 23 atoms cluster containing 16 Al and 7 Co atoms. This 3-dimensional atomic arrangement can be dissected into three

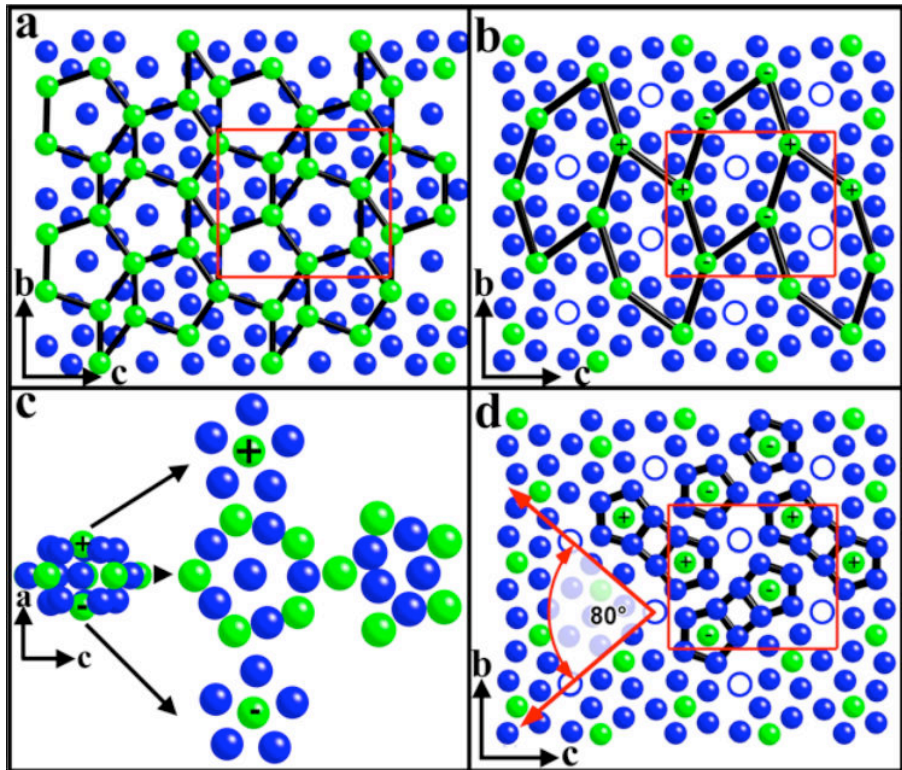


Figure 3.1: *The structure of the orthorhombic  $\text{Al}_{13}\text{Co}_4$  crystal [66] is presented along the [100] direction. Solid black (blue) spheres correspond to Al atoms, open circles to Al atoms referenced as “glue” atoms and grey (green) spheres to Co atoms. The orthorhombic unit cell is outlined by a rectangle. By connecting Co atoms, a tiling composed of pentagons and rhombi is drawn on the flat layer (a) and a tiling made of elongated hexagons (edge length around  $6.5 \text{ \AA}$ ) is superimposed on the puckered layer (b). The basic building block of the bulk structure is the so-called “pentagonal bipyramid” (PB) clusters [67, 73, 79]. Stacked along this  $p-10f$  axis, the PB clusters form pentagonal channels. (c) Description of the 23 atoms PB cluster: (left) a three-dimensional view of the complete PB cluster. The labels (+) and (-) outlined the Co atoms belonging to the top and bottom caps, (middle) dissected cluster showing the Al-centered flat layer with a top and bottom 6-atoms cap, (right) the PB junction layer. (d) Within the puckered layer, each cobalt is surrounded by five Al atoms. Depending on the height of the Co atoms ((+) or (-)) within the puckered planes, two sets of bi-pentagonal motifs are present. A bi-pentagonal motif is formed by two adjacent alike caps. The edge lengths of the individual pentagons shown on (d) range from  $2.66$  to  $3.05 \text{ \AA}$ .*

layers (centre of Fig.3.1(c)); an Al-centered equatorial layer consisting of a decagonal ring of alternating Al and Co atoms is capped (top and bottom) by two 6-atoms puckered layers consisting of small Al pentagons centred by Co atom [67]. Along the [100] direction, the PB clusters alternate with “junction” layers (Fig.3.1(c), right). Hence, the two pentagons drawn on Fig.3.1(a) correspond either to the equatorial or to the junction layers discussed above.

Regarding the P layer (Fig.3.1(b)), the connection of Co atoms leads to a tiling composed of a unique elongated hexagon. The hexagonal tiles pointing in two different directions are rotated from each other by  $36^\circ$ . Each Co atom is surrounded by a pentagon composed of five Al atoms. These small pentagons highlighted on Fig.3.1(d) correspond either to the bottom or top caps of the PB cluster. Hence the Co atoms sit either on top or below (labelled respectively “+” and “−”) the smallest Al pentagons. Consequently, the structure of the P layer can be understood as being composed mainly of bottom and top caps of the PB cluster linked by extra Al atoms labelled “glue” atoms (Fig.3.1(d)). At this stage it is worth mentioning that a bi-pentagonal motif (for instance made by 2 bottom caps) would be rotated by  $80^\circ$  from one puckered layer to the next one.

### 3.3 Experimental details

The  $\text{Al}_{13}\text{Co}_4$  samples ( $\text{Al}_{76.5}\text{Co}_{23.5}$  at.%) used in this experiment have been grown by the Jülich and the Munich group using the Czochralski method from Al-rich solutions. Crystal growth was done by pulling along the [100] direction using native seeds [169]. The crystals are oriented using back reflection Laue x-ray diffraction and are cut perpendicular to their [100] direction. The surfaces have been mechanically polished using diamond paste with decreasing grain size down to  $1/4 \mu\text{m}$  and using Syton<sup>®</sup> for the final polishing cycles. At this stage, the appearance of the samples is mirror-like. After insertion in ultrahigh vacuum (UHV), the preparation of the samples consists of cycles of  $\text{Ar}^+$  sputtering and annealing between  $1073 \text{ K}$  and  $1173 \text{ K}$ . The Ar ion beam energy is progressively reduced from  $1.5 \text{ kV}$  to  $1.0 \text{ kV}$  and the sputtering cycle lasts 20 min. The base pressure of the system is  $5 \times 10^{-11} \text{ mbar}$ . As explained later on (see Sec.3.4.1), the annealing time is varied between 40 min and 2 hours per cycle. The temperature of the sample is monitored using an infrared optical pyrometer with the emissivity set to 0.35. The electronic structure of the sample is investigated using x-ray and ultra-violet photoelectron spectroscopy (XPS, UPS) while the overall surface structure is assessed by low energy electron diffraction. The sample is considered clean when the XPS spectra show no traces of contaminants. The local atomic arrangement is probed using a Omicron variable temperature AFM/STM (VT-AFM) operated in the STM mode at room temperature. In a separate UHV chamber (Empa Thun), x-ray photoelectron diffraction (XPD) measurements have been carried out using non-monochromatised  $\text{Al K}_\alpha$  radiation and a modified Omicron photoelectron

spectrometer equipped with an EA 125 HR electron analyser operated in Constant Analyser Energy (CAE) mode. The spectrometer has been calibrated to the Au 4f<sub>7/2</sub> binding energy of 83.8 eV. Prior to XPD measurements, the structural quality of the surface is verified using LEED.

## 3.4 Experimental results

### 3.4.1 Surface preparation

After annealing the sample to 1103 K for 1 hour, the LEED pattern is sharp with a low background (Fig.3.2(a)). The surface structure is orthorhombic with the ratio of the unit cell dimensions ( $\frac{c}{b} = 1.186$ ) similar, within the accuracy of our measurements, to those reported by Grin *et al.* [66] ( $\frac{c}{b} = 1.171$ ). Compared to other *p*-10*f* surfaces of approximants [61, 71], the *p*-10*f* symmetry within the LEED patterns recorded is less noticeable. As we will see later on, the *p*-10*f* symmetry is very pronounced in the local structure probed by XPD.

After annealing to 1115 K, STM images (Fig.3.2(b)) reveal atomically flat terraces of various widths separated by a single step height. The latter is equal to  $4.2 \pm 0.2 \text{ \AA}$  which corresponds to half of the lattice parameter ( $a/2$ ) along the [100] direction. High resolution STM images (not shown here) reveal that the surface structure is similar on all terraces investigated and this termination is labelled *T*1 on Fig.3.2(b). On terraces of width greater than 20 nm, patches of an incomplete surface termination (labelled *T*2) decorate the upper step edges of the terraces. As shown on Fig.3.2(c), increasing the annealing time to 2 hours leads to the formation of larger terraces. Now, two distinct terminations are easily distinguishable at the surface. The one closer to the step edge (height =  $a/2$ ) is attributed to *T*1 and the remaining part of the surface is assigned to *T*2 (see Fig.3.2(c)). The mean height difference between *T*1 and *T*2 is measured at  $2.2 \pm 0.2 \text{ \AA}$  which corresponds to the distance between the flat and the puckered layer in the bulk model. The roughness calculated on both terminations using the root-mean square height ( $Z_{rms}$ ) are 0.30  $\text{\AA}$  and 0.57  $\text{\AA}$  for *T*1 and *T*2 respectively. Following this surface preparation, the step edges are always *T*2 deficient. Hence, *T*1 is only observed on the lower and upper sides of the step edges over a 30 nm wide region. As shown on Fig.3.2(d), a drastic change in the surface morphology is observed when annealing the sample to 1165 K for 1 hour. At this temperature, *T*2 is preferentially desorbed leaving *T*1 as the dominant surface plane. The complete evaporation of *T*2 has been achieved by annealing the Al<sub>13</sub>Co<sub>4</sub> to 1173 K for 2 hours. However, this marks the start of the evaporation of *T*1 as indicated by the presence of depressions across the top most surface layer. The LEED patterns recorded during these different surface preparations are qualitatively identical but drastic changes have been observed within the intensity distribution of the diffraction peaks.

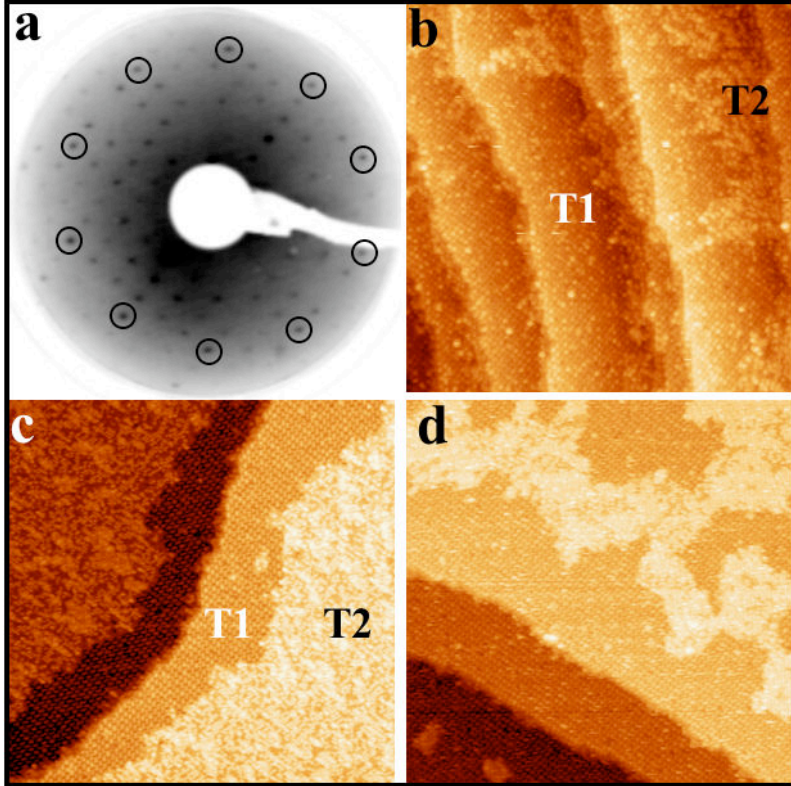


Figure 3.2: (a) LEED pattern (inverted contrast for clarity) recorded at 80 eV on the surface annealed to 1103 K for 1 hour. (b-d)  $100 \times 100 \text{ nm}^2$  STM images showing the terrace and step morphology for different annealing time and temperatures: (b)  $T = 1115 \text{ K}$  for  $t = 1 \text{ hour}$ , (c)  $T = 1115 \text{ K}$  for  $t = 2 \text{ hours}$  and (d)  $T = 1165 \text{ K}$  for  $t = 1 \text{ hour}$ . The two types of terminations are labelled T1 and T2 on (b) and (c).

### 3.4.2 Investigation of the surface structure

We now turn into the identification of the atomic structures for both surface terminations using higher magnification STM images. At first (see Fig.3.3(a)), the structure observed on T1 can be described using a centered elongated hexagon. The orientation of this hexagon is different on successive terraces and an angle of  $80^\circ$  is measured between the two possible alignments. From atomically resolved STM images, it appears that the centre and the vertices of this hexagon are decorated by bi-pentagonal motifs resembling those presented on Fig.3.1(d). The dimensions of individual pentagon and of the unit mesh are consistent with those from the puckered layer ( $x=0.25$  or  $x=0.75$ ). This is further confirmed by the fast Fourier transform (FFT) (inset of Fig.3.3(b)) calculated from the T1 region which exhibits an orthorhombic structure with the lattice parameter dimensions ( $b = 12.6 \pm 0.3 \text{ \AA}$  and  $c = 14.5 \pm 0.1 \text{ \AA}$ ) expected from the bulk structural model [66]. However, only one set of bi-pentagonal features pointing in one direction within each plane is preserved at the surface.

These pentagons correspond either to bottom or top caps of the PB cluster. As it will be demonstrated further using simulated STM images, the presence of both sets of bipentagonal motifs would have led to a full puckered layer with a completely different topography (see Fig.3.7(a) for instance). Consequently, the puckered layer is not as dense as in the bulk model and atomic desorption (both Al and Co atoms) is encountered during the surface preparation. The rising question is which out of the two possible pentagons remain at the surface. Additional analytical tools (for instance *ab initio* calculations) will be required to discriminate between the two possibilities. An atomically resolved STM image from a region of  $T_2$  is shown on Fig.3.3(c). This termination is not complete as revealed by the presence of several holes and of irregularly decorated unit cells. From the densest area, atomic lines and local hexagonal-like features are readily distinguishable (outlined on Fig.3.3(c)). Although not complete,  $T_2$  is well ordered as indicated by the FFT presented on Fig.3.3(d). Similarly, the dimensions of the orthorhombic unit cell are comparable to those measured on  $T_1$ . Within the diffraction spots observed on the FFT pattern, six intense spots are arranged in a hexagonal manner (see Fig.3.3(d)). In the following section, we propose a structural model to explain our STM observations on the  $T_2$  termination and the intensity distribution obtained within the FFT.

### 3.4.3 Structural model of both surface terminations

The thorough inspection of several STM images allows us to identify a recurrent atomic arrangement within the  $T_2$  region (Inset of Fig.3.4(a)). The analysis of denser area observed on  $T_2$  is hindered by a limited STM resolution. To understand its orientation and position with respect to the crystal structure, a mesh representing the surface orthorhombic unit cell has been drawn on the  $T_1$  region and has been extended over the  $T_2$  layer (Fig.3.4(a)). To a first approximation, this motif or superstructure is described as an oblique surface net with 4 atoms or clusters of atoms at the positions  $(0, 0)$ ,  $(\frac{1}{2}, 0)$ ,  $(\frac{1}{4}, \frac{1}{2})$  and  $(\frac{3}{4}, \frac{1}{2})$  with respect to the sample orthorhombic unit cell (inset of Fig.3.4(b)). Squashed hexagons as the one presented on Fig.3.3(c) can be generated from this basic unit. The corresponding diffraction pattern of this superstructure has been calculated and is presented on Fig.3.4(b). The intensity distribution of the Bragg spots have been simulated and vary according to the following structure factor:

$$S(h, k) = 1 + \exp(i\pi h) + \exp[i(\frac{\pi}{2}h + \pi k)] + \exp[i(\frac{3}{2}\pi h + \pi k)] \quad (3.1)$$

Around the central spot, the next 6 most intense peaks form a hexagonal motif (Fig.3.4(b)). The overall pattern obtained from our proposed superstructure is in good agreement both qualitatively and quantitatively with the calculated FFT from the  $T_2$  region (see Fig.3.3(d)).

Using the grid shown on Fig.3.4(a) as a reference, it has been possible to

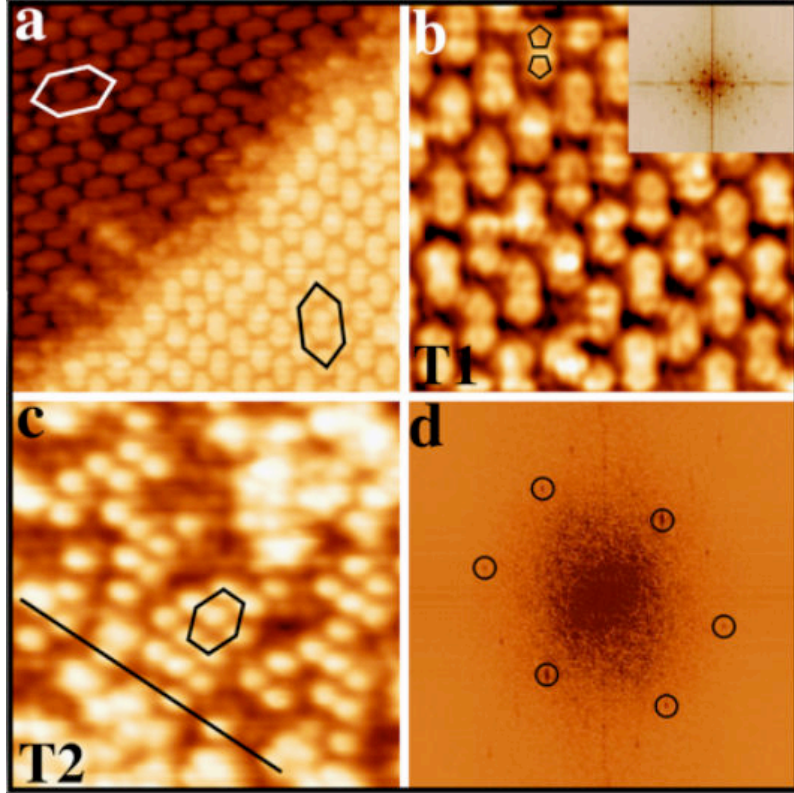


Figure 3.3: (a)  $20 \times 20 \text{ nm}^2$  High resolution STM image presenting two successive terraces separated by a single step height equal to  $a/2$ . The elongated hexagons (longest edge equal to  $19 \text{ \AA}$ ) are rotated from one puckered layer to the next one by  $80^\circ$ . (b) Atomically resolved STM image ( $10 \times 10 \text{ nm}^2$ ) recorded from T1. Bi-pentagonal motifs are highlighted on the image (Inset: FFT calculated from T1 termination shown on (b)). (c) Atomically resolved STM image ( $10 \times 10 \text{ nm}^2$ ) measured on T2. The arrangements of bright features are highlighted by an atomic line and a hexagonal motif. (d) Corresponding FFT calculated from a ( $30 \times 50 \text{ nm}^2$ ) region of T2. Within the orthorhombic mesh, six intense spots forming an elongated hexagon are circled.

superimpose part of the STM image representing the T2 layer over the T1 region (not shown here). The projection of the two terminations is presented on Fig.3.4(c) where crosses indicate the estimated position of the oblique net over a complete puckered layer from the bulk model. The superposition of the two structures shows that the crosses are positioned between Al pentagons defined as the bottom and top caps of the PB cluster (see Fig.3.1(c-d)). Hence, the crosses are located on top of interstitial sites of the puckered layer. Next, the structure of the flat layer situated above the puckered layer in the bulk model is investigated. In particular, we seek for any correspondence between the oblique cell and atomic positions within the F layer. As shown on Fig.3.4(d), a reasonable fit is identified between the position of crosses and several sites

decorated by Al atoms. These atoms are labelled Al5, Al6, Al7 and Al8 by Grin *et al.* [66] and are represented by the largest spheres on Fig.3.4(d). The crosses at mid-edge position along the  $<010>$  direction of the orthorhombic unit cell do not coincide perfectly with the Al atoms marked by arrows. This small shift could be related to a possible surface relaxation, a consequence of the reduced atomic density of the F layer at the surface. Alternatively, an electronic contribution from the atoms beneath the topmost layer could provide a higher local density of states at the mid-edge position along the  $<010>$  direction. Hence we tentatively assign the decoration of the oblique net by Al atoms belonging to the F layer. If we consider the above measurements (step height, calculated FFT, local atomic arrangement), we believe that  $T_2$  corresponds to the incomplete F layer in the bulk model, where the density of the flat layer or  $T_2$  at the surface depends on the sample preparation.

We now focus on the potential atomic structure of the  $T_1$  termination. To this end, our STM measurements suggest that only one type of bi-pentagonal motifs is preserved with the topmost layer. Investigation of numerous STM images point also to a desorption of glue atoms (see Fig.3.1(b,c)). In an attempt to test this hypothesis, the surface has been analysed using X-ray photoelectron diffraction. The measurements have been carried out after annealing the  $\text{Al}_{13}\text{Co}_4$  crystal to 1073 K for 2 hours. As explained in § 3.4.1, the majority of the surface consists of relatively narrow terraces with  $T_1$  as the topmost termination. Fig.3.5(a-b) exhibits the Al 2s and Co 2p<sub>3/2</sub> photoemission line intensity for different angular and polar emission angles, represented in stereographic projection. Normal emission corresponds to the center of the XPD pattern while the outer ring represents an emission angle of 85°, i.e almost parallel to the crystal surface. The bright and dark contrasts on these stereographic projection indicate high and low intensity respectively. The XPD patterns measured for both selected emitter (Al 2s and Co 2p<sub>3/2</sub>) reveal typical features of decagonal symmetry elements. Indeed, several rings of ten equivalent intense spots and a central 10-*f* symmetry axis dominate both patterns. These decagonal patterns resemble the XPD images of Al 2s and Co 2p<sub>3/2</sub> emission obtained from the *d*-Al-Ni-Co quasicrystal surface [60]. The diffraction images presented on Fig.3.5(a-b) are also similar to those observed on the decagonal quasicrystal overlayer grown on the five-fold surface of the *i*-Al-Pd-Mn sample [173]. As XPD probes the local real-space environment around the selected emitting atoms, these measurements reveal an average short-range decagonal ordering around the Al and Co atoms at the near-surface. From the cluster arrangements described in paragraph 3.2, it is not too surprising to observe these patterns along the *p*-10*f* axis of the  $\text{Al}_{13}\text{Co}_4$  surface. To interpret the experimental patterns, Single Scattering Cluster (SSC) simulations for the Al 2s and Co 2p<sub>3/2</sub> emission have been performed based on the  $\text{Al}_{13}\text{Co}_4$  structural bulk model available [66]. Following the previous analysis, three separate clusters have been generated to encounter for the different atomic configurations observed at the surface. Hence, the surface of the 3 models is either terminated by a complete F plane, by a complete P plane or by an incomplete

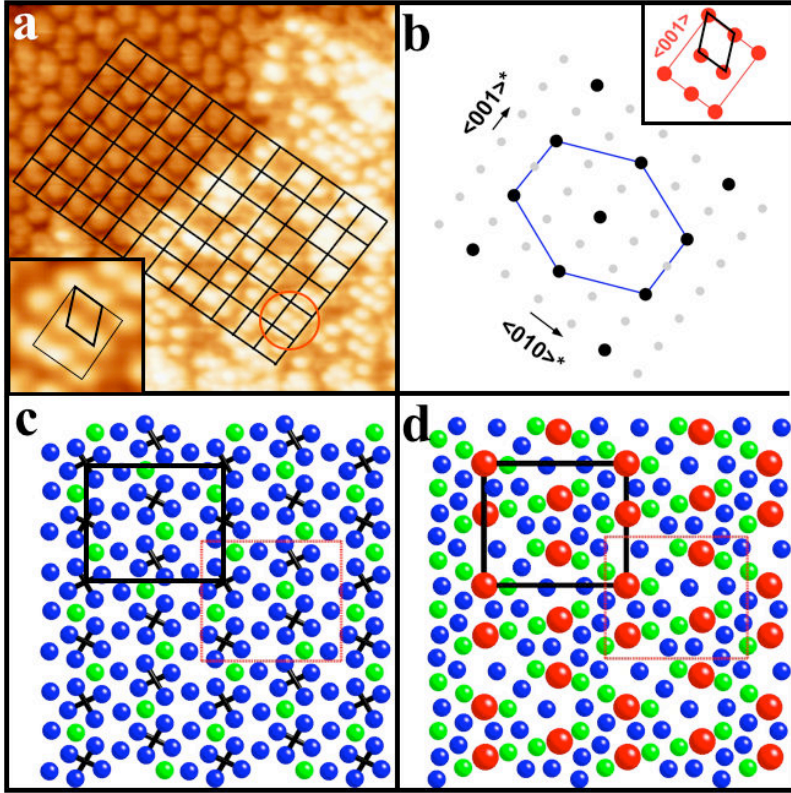


Figure 3.4: (a)  $20 \times 20 \text{ nm}^2$  STM image showing both T1 and T2 terminations. The orthorhombic lattice determined on the T1 region has been extended over the T2 layer. Inset ( $3 \times 3 \text{ nm}^2$ ): magnification of the atomic arrangement circled on the STM image. The oblique net is outlined on this motif which is often observed within the T2 structure. (b) Inset: schematic representation of the correspondence between the oblique net and the orthorhombic unit cell. Calculated diffraction pattern from the superstructure described in the inset. The most (black) and less (grey) intense Fourier spots are indicated in the pattern. (c) Superposition of the oblique net (crosses) and the complete puckered layer (Black (blue): Al atoms, grey (green) Co atoms). (d) Correspondence between the crosses and atomic positions within the flat layer of the bulk model. The largest spheres represent Al5, Al6, Al7 and Al8 in the bulk model [66] (atoms labelled as in (c)).

P layer where only bi-pentagon motifs have been preserved as suggested by our experimental and simulated STM images. The cluster used to carry out the calculations consists of 3016 atoms with 358 Al and 136 Co as emitters. The photoelectron intensity maps obtained for each emitter appear similar regardless of the models chosen. As shown on Fig.3.5(c-d), the experimental XPD patterns can be nicely reproduced by the Single Scattering Cluster (SSC) simulations. The latter has been obtained for the incomplete P layer. There is a good agreement between the position and the intensity maxima between

the XPD and SSC images. In addition, they both display decagonal rings with 10 distinct and equivalent spots. Consequently, the similarity between XPD and SSC patterns suggests that the bulk structure is maintained at the near-surface region. However, it is not possible to discriminate between the preferred topmost surface termination. To gain more insight into the possible surface structures and into the electronic charge density distribution, the use of *ab initio* electronic structure calculations is introduced in the following section.

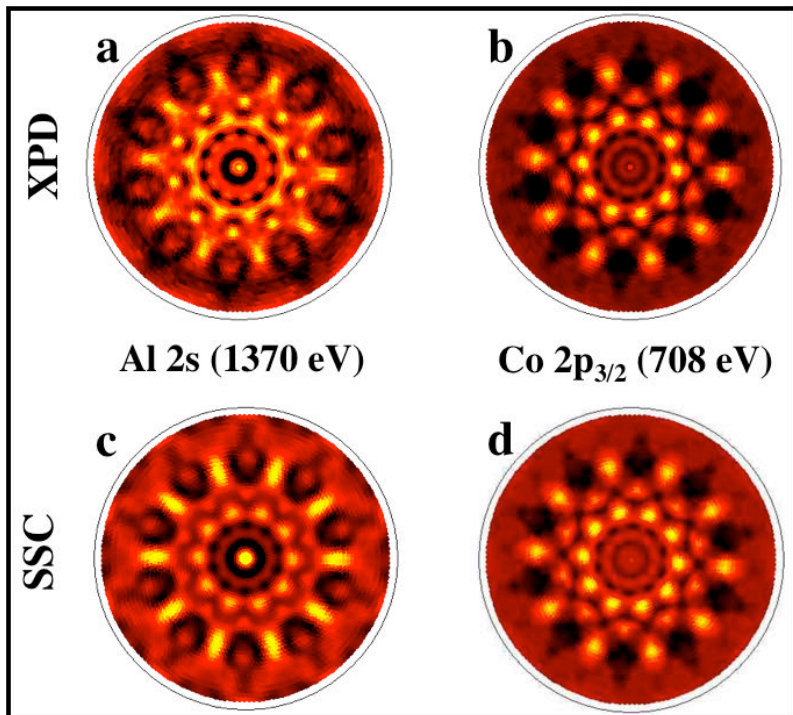


Figure 3.5: *Experimental XPD patterns of (a) Al 2s and (b) Co 2p<sub>3/2</sub> core levels measured on the Al<sub>13</sub>Co<sub>4</sub> (100) surface with an Al K<sub>α</sub> (1486.7 eV) X-ray source. (c-d) Single Scattering Cluster simulations for Al 2s ( $E_{Kin} = 1370$  eV) and (d) Co 2p<sub>3/2</sub> ( $E_{Kin} = 708$  eV) emission based on a cluster of 3016 atoms derived from the bulk model [66] described on Fig.3.1.*

### 3.5 Electronic structure calculations

In this section, we study the electronic structure of the Al<sub>13</sub>Co<sub>4</sub> crystal. We present electronic density of states (DOS) calculations and simulations of STM images that we have used to interpret experimental results.

### 3.5.1 Computational details

The present calculations have been performed within the Density Functional Theory (DFT) framework. Specifically, we have used (i) the Vienna *ab initio* simulation package (VASP) [174,175] to determine the geometry of the Al<sub>13</sub>Co<sub>4</sub> (100) system, by a conjugate gradient minimisation of the forces acting on the atoms, (ii) the PWscf code of the Quantum Espresso distribution [176] to calculate the density of states and simulate the STM images. Both codes solve the Kohn-Sham equations in a plane wave basis. Our calculations are made within the Perdew-Burke-Ernzerhof (PBE) approximation for the exchange-correlation functional [177]. Ultrasoft potential has been used for cobalt [178] while norm-conserving potentials have been employed for aluminium [179]. The DOS calculations are carried out at a fixed cutoff energy of 400 eV, and the irreducible Brillouin zone was sampled by 4  $k$ -points.

The density of states of the bulk Al<sub>13</sub>Co<sub>4</sub> alloy is calculated from the relaxed structural model. The starting structure is the experimental derived model detailed in Ref. [66]. The cell geometry, its volume and the atomic positions were allowed to relax in the process. The resulting structure is still described by an orthorhombic cell built on the [100] ( $a = 8.207 \text{ \AA}$ ), [010] ( $b = 12.403 \text{ \AA}$ ) and [001] ( $c = 14.420 \text{ \AA}$ ) vectors. Using the supercell technique, (100) surfaces of Al<sub>13</sub>Co<sub>4</sub> were simulated by repeated slabs separated by a vacuum region in the  $z$  direction. Several surface terminations are considered in this study. The simplest model consists of a bulk truncation along the (100) plane. Two cases are examined: in the  $F_m$  model the flat layer is selected as the topmost surface layer while in the  $P_m$  model the puckered layer is chosen as the surface termination. In the second structural model (labelled  $P_m^+$  model), the puckered layer is selected as the surface layer and only bi-pentagonal patterns formed by the top caps are preserved at the surface (Co “+” atoms in Fig3.1(c-d)). For the third structural model (labelled  $P_m^-$  model), bi-pentagonal patterns formed this time by the bottom caps of the PB cluster are maintained at the surface (Co “-” atoms in Fig3.1(c-d)). A complete relaxation of all these systems remains a challenging computational task for at least the following reasons: the slab has to be thick enough so that (i) the model represents a termination of the bulk structure in a realistic way and (ii) the bottom surface has no influence on the studied surface. This demands to consider generally at least 6 atomic planes in the slab, that means 153 atoms if the model is built by a bulk truncation along the (100) plane. We have estimated the surface relaxation only in the case of the  $P_m^+$  and  $P_m^-$  models. The STM images calculated from these relaxed surfaces are not drastically different than those simulated from the unrelaxed models.

STM images have been simulated using the Tersoff-Hamann approximation [180] where the tunneling current is derived from the local density of states at the Fermi energy and a point-like tip is considered. Within this model, the constant current STM images are simulated from electronic structure calculations by considering surfaces of constant local density of states integrated over

an energy window from  $E_F$  to  $E_F + V_{bias}$ , where  $V_{bias}$  is the voltage applied between the sample and the tip. The bias  $V_{bias}$  and the tip-sample distance have been chosen to match the experimental settings ( $V_{bias}=-1.3$  V,  $I=0.08$  nA).

### 3.5.2 Calculated DOS and experimental valence band

Calculated partial and total DOS of bulk  $\text{Al}_{13}\text{Co}_4$  are reported on Fig.3.6. The density of states contains a *pseudo-gap* lying to the left-hand side of the Fermi energy. Here the Fermi energy is taken as the origin for the binding energies. The total DOS shows an intense feature lying at about 2.0 eV from the Fermi energy. This feature is made mainly from the partial Co *d*-states, forming a set of peaks lying between -3.3 and -0.5 eV. The intensity of the Co *s*-states is about 85 times lower than the Co *d*-states in the occupied region and consequently they do not contribute significantly to the occupied band. Aluminium *s*-states are present mainly in the range from -1.0 eV to -11.2 eV. These latter overlap with the Al *p*-states leading to a slight *s-p* hybridization. At the energy of the intense feature of the partial Co *d*-states, a set of peaks is also present in the Al *p*-states.

Our results for the DOS are in good agreement with the DOS calculations performed on the *m*- $\text{Al}_{13}\text{Co}_4$  [67] system. Since the orthorhombic *oP*102 and the monoclinic *mP*102 structures of the  $\text{Al}_{13}\text{Co}_4$  crystals share identical local building blocks and differ only in their global arrangement [67], a similar shape for both DOS was expected.

UPS experiments have been performed to probe the valence band of the  $\text{Al}_{13}\text{Co}_4$  surfaces using He I radiation (21.2 eV). The experimental spectrum is shown in the upper pannel of Fig.3.6. The spectrum is dominated by the Co *d* levels in the energy range of -0.5 to -2.5 eV below the Fermi energy. Some small discrepancies exist between the experimental and the calculated positions of the features. The experimental bands are shifted by about 0.5 eV to lower binding energies compared to the calculated ones. These differences could be due to final state effects in the photoemission process and/or to a surface effect not taken into account in the calculation of the bulk DOS.

### 3.5.3 Simulated STM images

STM images have been simulated for various structural models of the  $\text{Al}_{13}\text{Co}_4$  (100) surface. These models, that are built using the supercell approach, are made by non relaxed slabs composed of 4 atomic planes and a 9.7 Å thick vacuum region. We have checked that the same results are obtained with supercells containing 6 non relaxed atomic planes and a 9.4 Å thick vacuum region. Four structural models have been examined: two models ( $P_m$  and  $F_m$ ) containing 102 atoms and two models ( $P_m^+$  and  $P_m^-$ ) containing 88 atoms as 14 atoms (2 Co and 12 Al atoms) of the unit cell are removed. Fig.3.7 (parts *a* to *e*) shows the corresponding STM images calculated from the surface charge

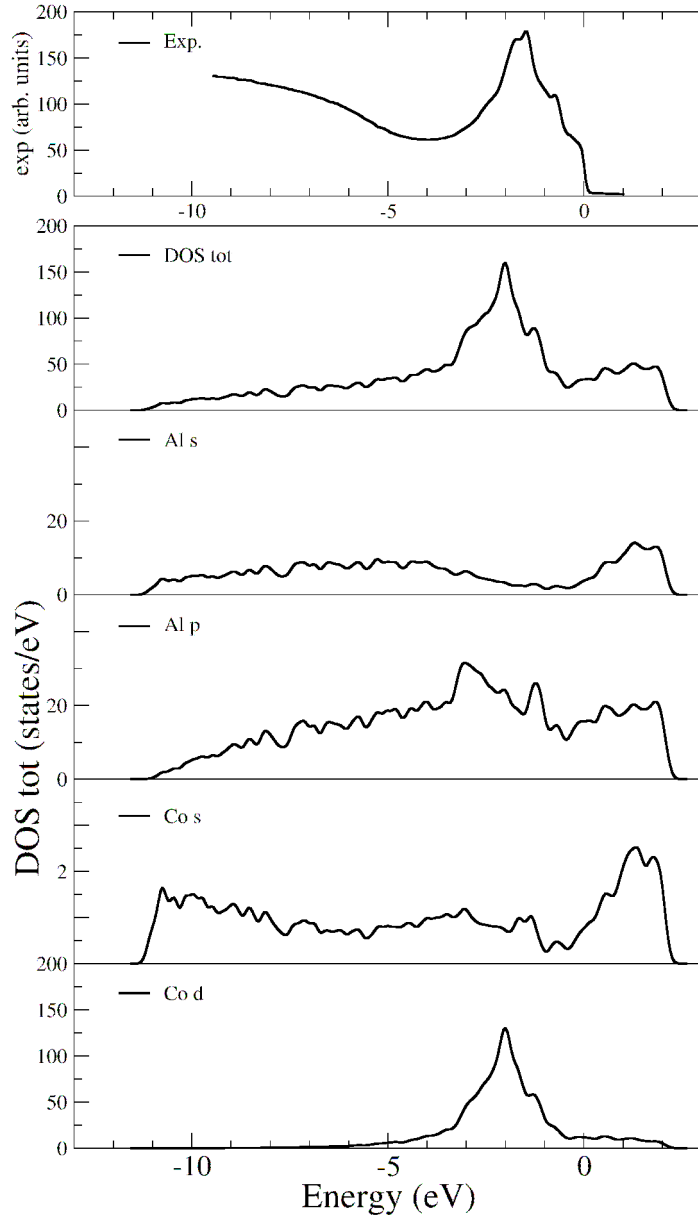


Figure 3.6: *Calculated partial and local DOS for  $\text{Al}_{13}\text{Co}_4$  crystal. The calculated DOS are compared with the ultra-violet photoelectron spectroscopy measurements (top).*

density distribution.

The influence of the surface relaxation on the simulated STM images has been checked only for the  $P_m^+$  and  $P_m^-$  models (see Fig.3.7(d) and (f)). As the thickness of the slab containing 4 atomic planes may be too small to support the surface during a relaxation by interatomic forces, a slab containing 139 atoms distributed on 6 atomic planes ( $F_{0.0}P_{0.25}F_{0.5}P_{0.75}F_{1.0}P_{1.25}^{modif}$  where  $P_{1.25}^{modif}$  is the incomplete P termination) separated by a 9.4 Å thick vacuum region has been

used instead. During the relaxation process, the cell geometry, its volume and the positions of atoms lying at the first four layers (atoms lying in the surface plane (S), in the subsurface (S-1) and in planes S-2 and S-3) were allowed to relax while the positions of atoms lying in the two bottom planes were fixed to model the bulk behavior. The relaxation process was considered to be achieved when the atomic forces for atoms lying in planes S, S-1, S-2 and S-3 were less than 0.02 eV/Å. The relaxation did not affect significantly the geometry of the orthorhombic supercell (the norms of the crystal cell vectors are modified by less than 1.7%). The relaxation  $\Delta_{ij}^{\%} = \frac{d_{ij}^R - d_{ij}^{NR}}{d_{ij}^{NR}}$  where  $d_{ij}^R$  (resp.  $d_{ij}^{NR}$ ) is the interlayer spacings for the relaxed models (resp. non relaxed model) has been evaluated. For the  $P_m^+$  model, the outermost layer spacing is contracted by 9.5% ( $d_{12}^R = 1.72$  Å,  $d_{12}^{NR} = 1.90$  Å) relative to the bulk interlayer spacing, while the spacing of the second and the third plane is expanded by less than 1% ( $d_{23}^R = 2.05$  Å,  $d_{23}^{NR} = 2.04$  Å). For the  $P_m^-$  model, the outermost layer spacing is equal to  $d_{12}^R = 1.88$  Å while the spacing of the second and the third plane is  $d_{23}^R = 2.15$  Å. The interlayer spacing relaxations calculated here are much larger than those obtained experimentally from LEED analysis [181–184] (0.9-2.2%) and from GGA calculations [185, 186] (1.06-1.35%) on pure Al(111). However, our results are comparable with the relaxations measured by dynamical LEED analysis (10%) on the ten-fold surface of the decagonal Al-Ni-Co quasicrystal [54]. It has to be mentioned that this strong contraction of the uppermost layer does not modify drastically the simulated STM images (see Fig.3.7(c-d)). In the following, the STM simulations are made with unrelaxed and relaxed structural models.

Fig.3.7 shows STM images calculated from the surface charge density distribution obtained for the structural models described in Sect.3.5.1 and the experimental STM image recorded with  $V_{bias} = -1.3$  V ( $I = 0.08$  nA). The crystallographic structure of the surface planes is superimposed on the calculated images. Fig.3.7(a, b) correspond to two simulated STM images calculated from the complete puckered and flat layers. These terminations have been generated by a cut perpendicular to the [100] direction of the bulk model. The resulting fine details of these simulated images bear no resemblance with the structure of the experimental STM image presented on Fig.3.7(g). This drastic difference precludes both complete puckered and flat layers to be surface termination. Fig.3.7(c-f) have been respectively simulated from the structural models containing 88 atoms described in Sect.3.5.1 as  $P_m^+$  and  $P_m^-$  models. As for the experimental STM image, these simulated images display bi-pentagonal motifs, all of comparable size and pointing in the same direction. The bright contrasts visible on Fig.3.7(c-d) originate from the position of Co atoms sitting slightly above the Al atoms. Such high intensity in the middle of each pentagonal motif is not observed on Fig.3.7(g). However, the best agreement is obtained with Fig.3.7(e-f). For the unrelaxed  $P_m^-$  model, the bi-pentagonal patterns reveal a bright outline and a dark centre consistent with our experimental observations. Upon relaxation, the two outermost Al atoms situated at both ends of the pentagonal motifs move slightly inward, hence producing

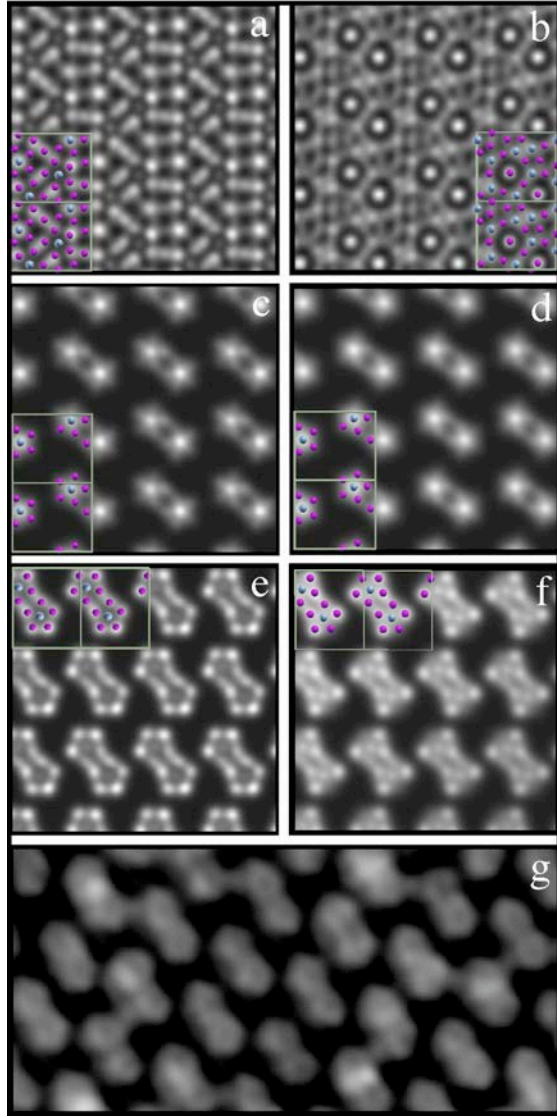


Figure 3.7:  $5 \times 5 \text{ nm}^2$  simulated STM images ( $V_{bias} = -1.3 \text{ V}$ ) compared to the experimental ( $5 \times 10 \text{ nm}^2$ ) STM image recorded with  $V_{bias} = -1.3 \text{ V}$  and  $I = 0.08 \text{ nA}$  (g). The upper simulated images correspond to the (a) puckered and (b) flat planes perpendicular to the [100] direction of the bulk structural model. (c-d) show simulated images of the unrelaxed and relaxed  $P_m^+$  (see text) structural model. (e-f) Simulated images corresponding to the unrelaxed and relaxed  $P_m^-$  structural model respectively described in the text.

a dimmer contrast. In comparison, the two Co atoms located in the centre of the pentagons present a minor outward relaxation. However, they still remain below the mean surface plane and should overall appear as depressions in the bi-pentagonal motifs. From these observations, we propose that the topmost surface layer consists of bottom caps of the PB cluster (model in Fig.3.7(e-f)) while the top caps are preferentially desorbed upon annealing.

### 3.6 Discussion

At the surface of the  $\text{Al}_{13}\text{Co}_4$  (100) crystal, two different surface terminations have been identified. The area covered by termination  $T_2$  depends largely on the surface preparation whereas  $T_1$  planes are always present. The complete desorption of the  $T_2$  layer can eventually be achieved as explained previously. A strain-related mechanism [187] introduced by surface defects (i.e step edges) has been observed at the surface of the  $\text{Al}_{13}\text{Co}_4$  crystal. This strain effect is manifested by a systematic depletion of  $T_2$  termination (“denuded zone”) on the ascending and descending edges of the steps over a relatively wide region. These step edges are similar in shape to those reported on the  $\xi'$ -Al-Pd-Mn surface [61]. Hence, the step roughness or diffusivity appears qualitatively lower than on quasicrystal surfaces [82].

The structural analysis of both surface terminations using LEED, STM and XPD indicates that there is no evident lateral surface reconstruction. The results obtained using XPS confirm that there is no chemical segregation at the surface of the  $\text{Al}_{13}\text{Co}_4$  crystal. These observations (no segregation) is in favor of a stronger Al-Co interaction strength compared to bonding of similar atoms [188]. Both surface layers can be related to bulk planes although their density is drastically altered (incomplete layers). The surface unit cell of  $T_1$  plane is composed of 10 Al and 2 Co atoms compared to 22 Al and 4 Co atoms for a complete puckered layer. It is also frequent to observe an additional Al atom or “glue atom” (i.e not belonging to the PB cluster) in between bi-pentagonal motifs. In addition, the atomic decoration of the remaining  $T_2$  patches has been attributed to remaining Al atoms from the flat layers. These results reveal that ultimately the Al-richest plane (puckered layer) is favored at the surface. Even after partial desorption, the  $T_1$  plane is still largely Al-rich. If no reconstruction and no chemical segregation are encountered at the surface, one way to minimise the surface free energy can be achieved by exposing planes with the lowest surface energy. On all CMA surfaces studied so far, atomic planes have been reported to be laterally bulk-terminated. For Al-based CMA, the topmost surface planes always correspond to layers having the highest concentration of Al atoms, i.e the element possessing the lowest surface energy within the alloy. This selection mechanism of surface plane is also verified for the  $\text{Al}_{13}\text{Co}_4$  crystal.

The  $\text{Al}_{13}\text{Co}_4$  (100) surface presents several similarities with the  $p\text{-}10f$  surface of the  $\xi'$ -Al-Pd-Mn crystal [61]. In both cases, a single step height equal to half of the lattice parameter along the  $p\text{-}10f$  axis is measured. The LEED pattern is described as sharp and  $p\text{-}10f$  symmetric. Each terrace is composed of several atomic terminations. The fine atomic structures observed within terraces are interpreted as originating from incomplete bulk planes. As we know, the atomic structures of both systems are based on elementary atomic clusters as building blocks. Within the incomplete surface layers, part of these clusters are preferentially maintained. Hence, they can be considered as energetically more stable than the surrounding glue atoms. In the case of the

$\text{Al}_{13}\text{Co}_4$  crystal, an additional question arises on why only one type of bi-pentagonal motif is kept at the surface. Along the  $p\text{-}10f$  axis, the structure can be visualised as an arrangement of columns of PB clusters. The puckered layer corresponds to a perpendicular cut across these columns. This implies that PB clusters are dissected at different heights and this is manifested by two different bi-pentagonal patterns within the plane. The selective desorption of one type of bi-pentagonal feature suggests that PB clusters are relatively independent entities at the surface. Indeed, the shape of the remaining cut clusters are not altered. This apparent stability indicates that the strongest chemical bonds may be localised within the cluster along the columns and not between clusters of separate columns. Although, it has been shown that favorable interactions exist between clusters [189], this difference may be a direct consequence of the reduced symmetry at the surface. Recent studies based on quantum mechanical calculations [190] supported by nuclear magnetic resonance experiments [191] suggest that the Co-Al-Co molecular groups present within the 23 atoms PB cluster should be considered as guests trapped in Al and Co cages of the  $\text{Al}_{13}\text{Co}_4$  complex metallic alloy. The corresponding two Co atoms belonging to such a molecular group are labelled “+” and “−” on Fig.3.1c and the Al atom decorates the center of the flat layer of the PB cluster. Our study suggests that bi-pentagonal motifs topped with Co“+” atoms vanish from the topmost surface layer. At the surface, the Co-Al-Co molecular groups are not confined anymore along the [100] direction between cages. It is reasonable to postulate that this break in the symmetry could increase the mobility of the guest within the cage. This could lead to the instability of the bi-pentagonal motif and explain eventually the observed selective desorption upon annealing the sample to 1073 K. If the molecular groups or part of it desorb upon annealing, the remaining five Al atoms of the top cap (see Fig.3.1c) may also evaporate due to a structural instability.

Consequently, the symmetry of the topmost layer is modified due to the reduction of the atomic density. With only one type of bi-pentagonal motifs preserved, this selection leads eventually to a different intensity distribution within the LEED pattern (reduced  $p\text{-}10f$  symmetry). However, the local atomic arrangement within the near surface region exhibits a decagonal symmetry as shown by XPD measurements and SSC calculations.

Finally, the electronic density of states have been calculated for the orthorhombic  $\text{Al}_{13}\text{Co}_4$  crystal. The results are consistent with the DOS calculated for the monoclinic system in previous studies [67] and with the measured valence band. Simulated STM images have been generated and have allowed us to discriminate between different possible surface terminations. The relatively large unit cell and the unusual surface structure reported here should stimulate the use of the  $\text{Al}_{13}\text{Co}_4$  (100) surface in adsorption studies as an highly corrugated potential energy surface is expected [153].

### 3.7 Conclusions

We have investigated the (100) surface of the recently grown orthorhombic  $\text{Al}_{13}\text{Co}_4$  crystal. Atomically flat terraces separated by a step height equal to half of the unit cell parameter ( $a/2$ ) exhibit two possible surface terminations depending on the annealing time and temperature selected. Both surface layers have been related to incomplete planes present within the bulk structural model. Upon annealing to 1173 K, only one termination which has been attributed to an incomplete puckered layer consisting of 12 atoms per surface unit cell is maintained at the surface. This preferential plane selection leads to a reduced *pseudo*-10-fold symmetry of the sharp LEED pattern. Finally, the close match between simulated and calculated STM images validates our proposed surface model.

# Chapter 4

## Structural Investigation of the (010) surface of the orthorhombic T-Al<sub>3</sub>(Mn, Pd) crystal

### 4.1 Introduction

Within the large family of CMA [4], the Al-Pd-Mn system has attracted much interest [61, 135, 146, 152, 192]. This is partly motivated by the presence in the phase diagram of stable and metastable quasicrystalline phases and orthorhombic phases which possess “giant” unit cells. The latter are periodic phases and were identified as approximants of either icosahedral or decagonal quasicrystals [100]. Among the various approximants, the  $\xi$  and  $\xi'$  phases are situated on the Pd-rich side of the ternary phase diagram while the Taylor’s (T) or Robinson’s (R) orthorhombic phases, which are related to the decagonal state, are found in the Mn-rich region [81, 193]. For instance, the orthorhombic T-Al<sub>3</sub>Mn crystal [81] with a  $b$  unit cell parameter equal to 12.43 Å parallel to the *pseudo*-10-fold axis ( $p\text{-}10f$ ) is closely related to the decagonal Al-Pd-Mn quasicrystal of similar periodicity along the 10-fold axis [69, 102]. The structure within the planes perpendicular to the  $p\text{-}10f$  axis of both T- and R-phases can be understood as a periodic stacking of two different tilings based on a single tile  $H$  with the shape of a squashed hexagon. While the R-phase can be seen as a parallel packing of the tiles, in the T-phase the tiles form a “zig-zag” pattern. In the structurally more complex decagonal phase, additional tiles are required [69, 121].

Approximant phases have often been introduced to model the physical and chemical properties of their parent quasicrystal and to perform electronic structure calculations requiring a periodic cell [101, 121, 194]. While the surface of the *i*-Al-Pd-Mn quasicrystal has been intensively investigated [146], only a limited number of experimental surface studies have been reported on approximant phases in the Al-Pd-Mn system. The T-Al<sub>3</sub>Mn phase has been fortuitously observed using scanning tunneling microscopy (STM) on the five-fold surface of the Al-Pd-Mn quasicrystal as a consequence of the decomposition of

the sample at elevated temperature [195]. To our knowledge, the work reported by Fournée *et al.* on the  $\xi'$ -Al-Pd-Mn phase marks the first surface study carried out on single crystals of approximants [61]. Two sets of  $\xi'$  samples were produced either by Bridgman or self-flux technique. Following a similar preparation, both surfaces exhibit a  $p\text{-}10f$  low energy electron diffraction (LEED) pattern. Using STM, differences in the local atomic arrangements have been identified on terraces between both samples. However, the STM images can be interpreted for both cases as a representation of planes perpendicular to the  $p\text{-}10f$  axis of the bulk model derived by Boudard *et al.* [140]. In the same study and in parallel, several crystalline phases were induced on the five-fold surface of the *i*-Al-Pd-Mn quasicrystal by sputter annealing at “low” and “high” temperatures compared to the optimised temperature range known to produce bulk like terminated quasicrystal surfaces [25, 27]. While the low-temperature phase could not be identified with a known bulk phase, the unit cell parameters of the high-temperature phase matched the lattice parameters of the T-Al<sub>72.3</sub>Pd<sub>3.2</sub>Mn<sub>24.5</sub> approximant (labeled T-Al<sub>3</sub>(Mn,Pd) hereafter). As a consequence of the “high” annealing treatment, the chemical composition in the near surface region could have been shifted out of the stability range of the icosahedral phase, leading to the formation of this T phase [61]. The limited resolution of the STM images precluded the identification of the surface structure. It was speculated that it should correspond to a particular pair of layers related by a mirror plane. The atomic structure of this approximant is isopseudomorphic to the T-Al<sub>3</sub>Mn phase and has been described by Klein *et al.* [68].

In this chapter, we report a study of the (010) surface of the orthorhombic T-Al<sub>3</sub>(Mn,Pd) single crystal using STM, LEED, x-ray photoelectron diffraction (XPD), ultraviolet and x-ray photoelectron spectroscopy (UPS, XPS). The model of the bulk structure of the T-Al<sub>3</sub>(Mn,Pd) approximant is presented in Sect. 4.2. The experimental details and the surface preparation are described in Sect. 4.3. Following the description of the computational details in Sect. 4.4, we present atomically resolved STM images and identify the surface structure in Sect. 4.5.

*Ab initio* density-functional methods (see Sect. 4.4) have been used to calculate the simulated STM images, the electronic structure, and the simulated photoemission spectra.

The bias dependency observed in STM images is also confirmed by simulated STM images. The electronic structure of several complex metallic alloys and in particular of the Al-Pd-Mn quasicrystal is characterized by a reduced density of states at the Fermi level ( $E_F$ ), termed a *pseudo-gap* [6]. It has been found to play a critical part in the alloy stability and in transport properties [5, 10, 194]. On valence band spectra, it manifests itself by a decrease of the spectral intensity in the vicinity of  $E_F$  compared to the sharp Fermi edge observed for metals. The asymmetry of core level line shapes can also be indicative of the density of states near  $E_F$  [83, 196]. This is the case for the Mn 2p core level in the *i*-Al-Pd-Mn which displays a particularly low asym-

metry effect related to the presence of a *pseudo*-gap at  $E_F$  [197, 198]. Hence, a comparison of the Mn 2p core level and of the valence band region close to the Fermi edge between the *i*-Al-Pd-Mn quasicrystal and the T-Al<sub>3</sub>(Mn,Pd) crystal will be presented in part 4.5. Finally, the results will be discussed in Sect.4.6.

## 4.2 Model of the bulk structure

As for the T-Al<sub>3</sub>Mn phase [81], the orthorhombic T-Al<sub>3</sub>(Mn,Pd) crystal is an approximant of the stable decagonal Al-Pd-Mn quasicrystal. Its atomic structure was determined by single-crystal x-ray diffraction with an atomic composition of Al<sub>72.3</sub>Pd<sub>3.2</sub>Mn<sub>24.5</sub> [68, 80]. The space group is *Pnma*, the unit cell contains 156 atoms and the lattice parameters are  $a = 14.717 \text{ \AA}$ ,  $b = 12.510 \text{ \AA}$  and  $c = 12.594 \text{ \AA}$ .

According to Klein *et al.* [68], the bulk structure of this approximant (see Fig.4.1) is described along the **b**-axis by two types of layers, a flat (F) layer and a puckered (P) layer which can be divided into two sublayers *P*<sub>1</sub> and *P*<sub>2</sub>. The F layer located at  $y = 1/4$  contains a maximum of 22 atoms per unit cell with 14 Al and 8 Mn atoms. As shown on Fig.4.1(a), the interconnection of Mn atoms leads to the formation of a tiling composed of pentagons and rhombi. The puckered layer *P*<sub>1</sub> located at  $y \approx 0.38$  contains 12 Al atoms arranged in pentagonal chains (Fig.4.1(b)). The atomic positions of both *F* and *P*<sub>1</sub> layers are all fully occupied while this is not the case for the *P*<sub>2</sub> plane. The puckered layer *P*<sub>2</sub> located at  $y \approx 0.43$  contains 16 atoms and all three elements. Four positions are fully occupied by 2 Al and 2 Mn atoms (blue (black)/pink (grey) spheres on Fig.4.1(c)). In addition, there are 10 mixed Al-Mn sites and 2 mixed Pd-Al sites. When linked, the Al and mixed sites form pentagonal chains while fully occupied Mn sites form zigzag chains (Fig.4.1(c)) [68]. Along the [010] direction, the atomic structure can be viewed as columns of interpenetrating icosahedral clusters (see Fig.4.1(d)) resulting from the alternate stacking of pentagonal prisms (*p*) and antiprisms (*a*), each separated by one atom in the sequence *apaapa* [69]. The columns intersect *F*, *P*<sub>1</sub> and *P*<sub>2</sub> planes at a position labelled *x* on Fig.4.1(a-c). As shown on Fig.4.1(e), the stacking layers along the [010] direction has the following sequence:

$$P2P1FP1P2P2^*P1^*F^*P1^*P2^* \quad (4.1)$$

where *F* ( $y = 0.25$ ) and *F*<sup>\*</sup> ( $y = 0.75$ ) are mirror planes. *P*<sub>1</sub><sup>\*</sup>, *P*<sub>2</sub><sup>\*</sup> and *F*<sup>\*</sup> have a two fold rotational symmetry against *P*<sub>1</sub>, *P*<sub>2</sub> and *F*. The distance between the different layers are  $d_{P1P2}=0.625 \text{ \AA}$ ,  $d_{FP1}=1.626 \text{ \AA}$  and  $d_{FP2}=2.251 \text{ \AA}$  [68].

The unit cell thus consists of two blocks of planes (*P*<sub>2</sub>*P*<sub>1</sub>*F*<sup>\*</sup>*P*<sub>1</sub><sup>\*</sup>*P*<sub>2</sub><sup>\*</sup>) and (*P*<sub>2</sub><sup>\*</sup>*P*<sub>1</sub><sup>\*</sup>*F*<sup>\*</sup>*P*<sub>1</sub><sup>\*</sup>*P*<sub>2</sub><sup>\*</sup>) related by a two fold symmetry. The thickness of each block is  $b/2$ .

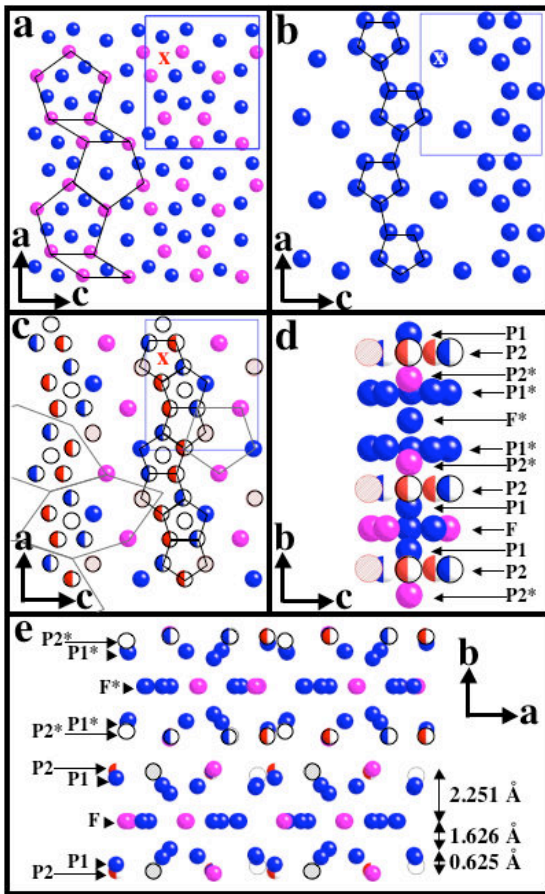


Figure 4.1: (a-c) The structure of the orthorhombic  $T\text{-Al}_3(\text{Mn, Pd})$  [68, 80] is presented along the  $[010]$  direction. Blue (dark gray) spheres correspond to Al atoms, pink (light gray) spheres to Mn atoms and others to mixed atomic sites. The orthorhombic unit cell is outlined by a rectangle. (a) Representation of the flat layer ( $F$ ). Connecting the Mn atoms leads to a tiling composed of pentagons and rhombi. (b) The puckered layer ( $P1$ ) is composed only of Al atoms arranged in almost perfect pentagonal chains. (c) The second puckered layer ( $P2$ ) is composed of Al, Pd and Mn atoms and several positions have a mixed occupancy. The blue (black) and white spheres correspond to mixed Mn-Al (0.5/0.5) sites (referred as TM(1) and TM(2) sites by Klein et al. [68]), the red (grey) and white spheres correspond to mixed Mn-Al (0.3/0.7) sites (TM(3) and TM(4)), the shaded spheres correspond to mixed Mn-Al (0.15/0.85) sites (TM(5)) and the empty circles correspond to mixed Pd-Al (0.625/0.375) sites (TM(6)). Mn atoms are organized as a zigzag line while other sites form pentagonal chains. Several H tiles are also drawn. (d) Schematic view along the  $[010]$  direction of one column of interpenetrating icosahedral clusters centered at point x marked on (a-c). (e) Representation of the stacking of layers perpendicular to the  $b$ -axis in the unit cell of the model structure.

### 4.3 Experimental details

The T-Al<sub>3</sub>(Pd, Mn) crystal with the chemical composition Al<sub>78</sub>Pd<sub>4</sub>Mn<sub>18</sub> (at.%) used in this experiment has been grown by the self-flux technique. The high-purity starting materials were sealed in an alumina crucible under protective argon atmosphere. Crystal growth was performed in a chamber furnace at a cooling rate of 1 K/h. After growth, the crystals were annealed for 120h at 1073 K. The high structural quality of the material was characterized by phase-contrast optical microscopy, scanning electron microscopy and transmission electron microscopy. A sample for surface investigation was oriented using back reflection Laue x-ray diffraction and was cut perpendicular to its [010] direction. The surface has been mechanically polished using diamond paste with decreasing grain size down to 0.25  $\mu\text{m}$  and using Syton<sup>®</sup> for the final polishing cycles. At this stage, the sample appearance is mirror-like. The sample is investigated under UHV condition with a base pressure below  $5 \times 10^{-11}$  mbar. The preparation of the crystal consists of cycles of Ar<sup>+</sup> ion sputtering at 2 keV for 30 min and annealing to temperatures ranging from 853 K to 923 K from 40 min to 2 hours. The temperature of the sample is monitored using an infrared optical pyrometer with the emissivity set to 0.35 coupled with a K type thermocouple. This preparation method results in a step-terrace morphology of the surface. In the chosen temperature range, no significant changes in composition, surface structure and morphology are found. The composition and electronic structure of the sample are monitored using x-ray (resolution 0.8 eV) and ultra-violet (resolution 100 meV) photo-electron spectroscopy while the overall surface structure is assessed by LEED. The STM measurements have been performed at room temperature using an Omicron variable temperature AFM/STM (VT-AFM). The XPD measurements have been carried out in a separate UHV chamber (Empa Thun) using a non-monochromatised Al K <sub>$\alpha$</sub>  radiation and a modified Omicron photoelectron spectrometer equipped with an EA 125 HR electron analyser operated in Constant Analyser Energy (CAE) mode. The calibration of the spectrometer has been done with respect to the Au 4f<sub>7/2</sub> binding energy of 83.8 eV. The structural quality of the surface is monitored using LEED technique prior to XPD measurements.

### 4.4 Computational details

The theoretical *ab initio* investigations are based on density-functional theory (DFT). In our previous study [121] of the approximant phases in decagonal Al-Pd-Mn we used the LMTO method to calculate the electronic structure. In the present work we have used the Vienna Ab-initio simulation Package VASP [174, 199] to perform electronic structure calculations and structural optimizations. VASP performs an iterative solution of the Kohn-Sham equations within a plane-wave basis. A semilocal gradient-corrected functional [200] (PW91) is

used to describe electronic exchange and correlation. The projector-augmented wave (PAW) method [199,201] is used to describe the electron–ion interactions. The essential input information for the calculation of simulated STM images is the energy-resolved charge density distributions. STM images of surfaces have been calculated according to the Tersoff-Hamann approximation [180].

As the bulk structure model of Klein *et al.* [68] contains fractional and mixed occupancies of the sites, it cannot be directly used for the *ab initio* calculations. Instead we have used a model derived by Mihalkovič and published in the alloy database (Ref. [202]). The model exhibits optimized geometry and chemical decorations of the sites. The sites with fractional and mixed Pd-Al and Mn-Al occupancies were resolved with respect to the *Pnma* space group symmetry of the unit cell. The cell parameters of  $a = 14.784\text{\AA}$ ,  $b = 12.496\text{\AA}$ , and  $c = 12.606\text{\AA}$  are in good agreement with the experimental data. The composition of the model is  $\text{Al}_{79.5}\text{Mn}_{15.4}\text{Pd}_{5.1}$ , i.e. closer to the bulk composition of the sample used in this study. A calculation of the heat of formation has confirmed that the optimized model represents a stable phase in the Al-Mn-Pd phase diagram.

A model for the surface is constructed by cutting a thick slab from the bulk structure. The thickness of the slab must be large enough to stabilize the surface. Our model of the surface consists of a slab with the thickness of a single unit cell and a vacuum layer of  $10\text{\AA}$ . The position of atoms in the model were relaxed by the Hellmann-Feynman interatomic forces. The positions of atoms in the top 5 atomic planes were free to relax, the atoms in the bottom 5 planes were kept at their bulk positions.

## 4.5 Results

### 4.5.1 Identification of the surface structure

After annealing the T-Al<sub>3</sub>(Mn, Pd) sample to  $863\text{ K}$  for 2 hours, the surface is well ordered as indicated by the sharp LEED patterns shown on Fig.4.2. The latter are dominated by almost perfect decagonal rings made of 10 bright diffraction spots of equal intensity. For the LEED pattern recorded at  $55.9\text{ eV}$  (see Fig.4.2(b)), one can distinguish an inner and an outer decagonal ring. Because all spots are periodically spaced, the symmetry of the LEED pattern is referred as *p-10f*. The surface structure is orthorhombic with the axial ratio ( $a = 14.58 \pm 0.43\text{\AA}$  and  $c = 12.40 \pm 0.4\text{\AA}$ , giving  $\frac{a}{c} \approx 1.18$ ) in agreement, within the accuracy of our measurements, to that reported by Klein *et al.* [68] ( $\frac{a}{c} = 1.17$ ). The reciprocal lattice vectors of the orthorhombic lattice are outlined on the LEED pattern shown on Fig.4.2(a).

At this stage, the STM investigation of the T-Al<sub>3</sub>(Mn, Pd) sample surface reveals a step-terrace morphology. The width of the atomically flat terraces ranges from  $0.1$  to  $0.3\text{ }\mu\text{m}$  (Fig.4.3(a-b)). Based on a qualitative comparison to other approximant samples (Al<sub>13</sub>Co<sub>4</sub> [70],  $\xi'$  and T- phase approximants [61,82] for instance), the roughness of the step edges observed on the T-Al<sub>3</sub>(Mn, Pd)

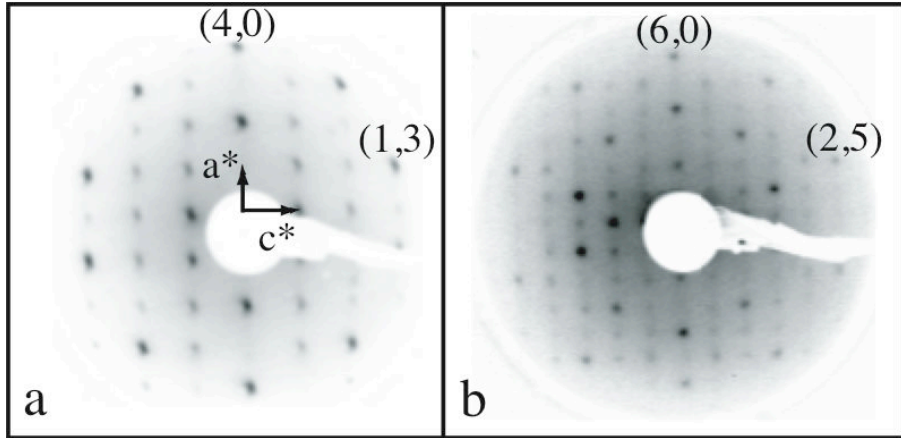


Figure 4.2: (a-b) LEED patterns (inverted for clarity) recorded on the clean surface at 25 eV and 55.9 eV respectively. The pseudo-10-fold symmetry is made evident on both patterns by the presence of decagonal rings consisting of 10 darker diffraction spots.

surface appears to be more pronounced. Height profiles measurements across several terraces exhibit a main step height of  $6.3 \pm 0.3 \text{ \AA}$  which corresponds to half of the lattice parameter along the [010] direction ( $\simeq \mathbf{b}/2$ ). As shown on Fig.4.3(b), an extra step height equal to  $2.25 \pm 0.10 \text{ \AA}$  is often observed on very narrow terraces. This specific height can be related to the  $d_{FP2}$  (2.251 Å) or to  $d_{P1^*P2}$  (2.378 Å) interlayer distances present in the bulk model. The roughness calculated on large terraces using the root-mean square height ( $Z_{rms}$ ) ranges from 0.1 to 0.2 Å depending on the scan size and bias applied. These values are almost two times smaller than the  $Z_{rms}$  values measured on quasicrystal surfaces [203]. The fast Fourier transform (FFT) calculated from the clean surface displays an orthorhombic structure (Fig.4.3(d)) with the lattice parameter dimensions expected from that of the bulk structural model.

While the LEED patterns and the calculated FFT suggest a well-ordered surface, high resolution STM images recorded on single terraces exhibit a high degree of structural imperfections. This is demonstrated on Fig.4.4(a) which displays an STM image recorded on a single terrace. Here, the surface consists of areas of homogeneous contrast and structure. These well-ordered patches are distributed non-uniformly across the terrace but are in registry with the orthorhombic periodic lattice beneath. This topography is representative of what has been observed across the surface sample independently of the annealing time and temperatures used in our study. In addition to the difficulty introduced by the surface imperfections to interpret the surface structure, STM images are strongly bias dependent. The influence of the scanning parameters is demonstrated on Fig.4.4(b-e) where an identical surface region has been imaged for different bias values at a constant current of 40 pA. As it will be shown later, a much higher tunneling current is required to discern finer structures

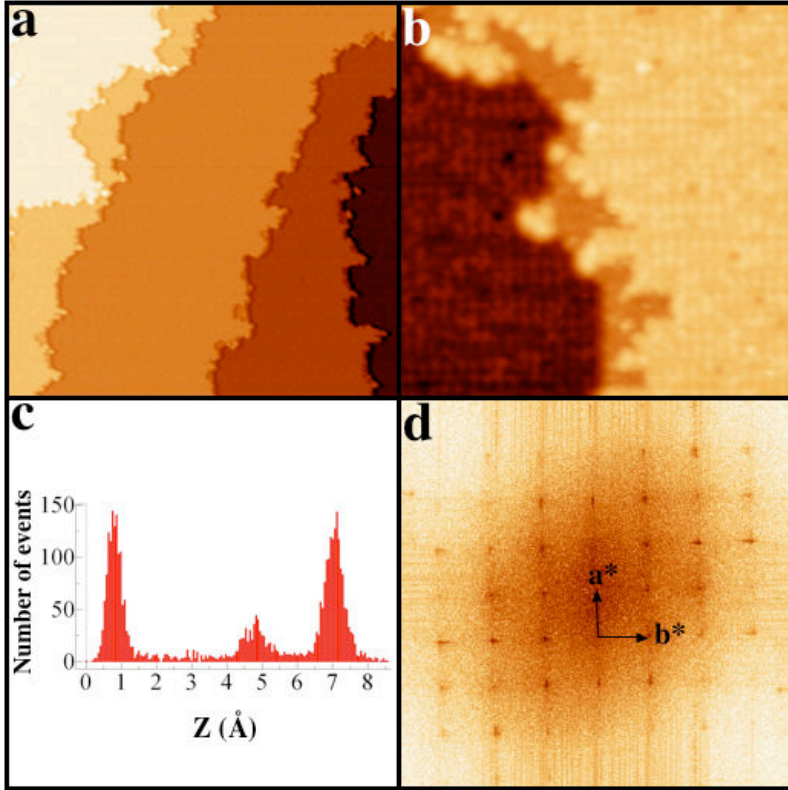


Figure 4.3: (a) STM image ( $250 \text{ nm} \times 250 \text{ nm}$ ) showing the step and terrace morphology. (b) STM image ( $40 \text{ nm} \times 40 \text{ nm}$ ) showing a narrow terrace on the step edge. (c) The height histogram calculated from a  $20 \text{ nm} \times 20 \text{ nm}$  STM image exhibits the three possible step heights observed across terraces. (d) Fast Fourier Transform calculated from a  $50 \text{ nm} \times 50 \text{ nm}$  high resolution STM image.

and to obtain atomic resolution. As a reference point, a common defect has been outlined by an arrow at the same position on all images. When scanning the unoccupied states near the Fermi level, the topography is dominated by broad and bright features which highlight the orthorhombic nature of the surface structure (see Fig.4.4(b)). In comparison, the STM images acquired at negative bias appear less corrugated and are dominated mainly by zig-zag chains propagating in the [100] direction (Fig.4.4(c)). Darker contrasts usually associated with depressions are also distinguishable when probing both the occupied and unoccupied states. As demonstrated by the circles drawn at the same position on Fig.4.4(b-e), the depressions present on Fig.4.4(b) almost disappear on Fig.4.4(e) where new ones emerge at negative bias.

Using a higher tunneling current, the fine structural details of the experimental STM images are now comparable to those observed on simulated images (see Fig.4.8). Fig.4.5(a-b) presents two atomically resolved STM images recorded on two different regions on the T-Al<sub>3</sub>(Mn, Pd) surface. Fig.4.5(b) has

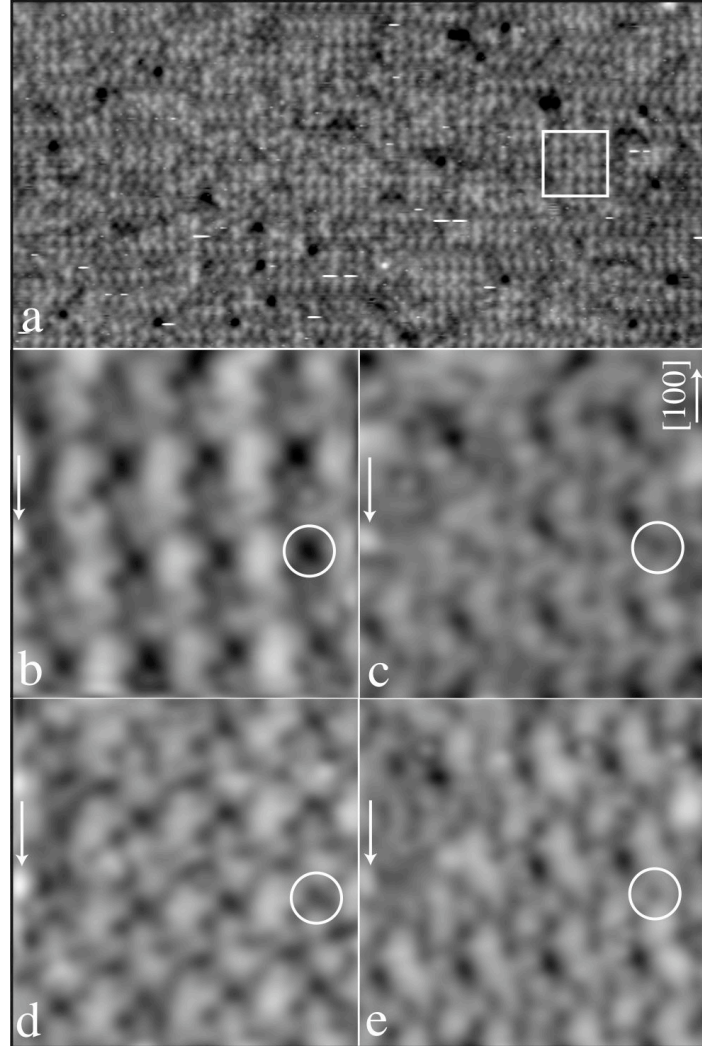


Figure 4.4: (a)  $70 \text{ nm} \times 35 \text{ nm}$  STM image recorded on a terrace for  $V_b = 2 \text{ V}$  and  $I_t = 0.06 \text{ nA}$ . The white frame outlines a patch of homogeneous contrast. (b-e) STM images ( $5.1 \text{ nm} \times 5.1 \text{ nm}$ ) acquired on the same region using a constant-current of  $40 \text{ pA}$  and a bias of  $0.8 \text{ V}$  (b),  $-0.8 \text{ V}$  (c),  $0.4 \text{ V}$  (d), and  $-0.4 \text{ V}$  (e). The arrows point to a common defect visible on all images. As shown by the circles located at the same position on all images, the contrast varies drastically with the applied bias.

been acquired in a region referred as homogeneous in contrast to Fig.4.5(a). Both images display pentagonal depressions resembling dark stars but Fig.4.5 (b) has been rotated by  $\pi$  to display the pentagonal depressions in the same orientation as on Fig.4.5 (a). This effect is to be expected from the two-fold rotational symmetry between  $P1^*$ ,  $P2^*$  and  $F^*$  against  $P1$ ,  $P2$  and  $F$ , i.e. on adjacent terraces separated by a step height equal to  $b/2$ . Fig.4.5(a) exhibits local pentagonal motifs and individual atoms arranged in a zig-zag manner propa-

gating along the [100] direction. These atomic features are less discernible on Fig.4.5(b). Indeed, this latter STM image is dominated by brighter and more diffuse features (outlined by a white pentagon on Fig.4.5(d)) which hinder the resolution of several pentagonal motifs, and consequently of isolated atoms. To interpret these observations, the structures present on both STM images have been compared to individual planes present within the bulk model proposed by Klein *et al.* [68] and described on Fig.4.1. Because of the sizes and the arrangements of the pentagons in chains, the surface structures are compatible with both *P*1 and *P*2 puckered layers (Fig.4.1(b-c)) but no agreement has been found with the *F* layer. To discriminate between the two possible puckered layers, one has to consider the alignment of isolated atoms (zig-zag) with respect to the chain of pentagonal motifs. Hence, a tiling corresponding to the skeleton of the *P*2 structure has been superimposed on both images (Fig.4.5(c-d)). As shown on Fig.4.5(c), the isolated atoms are aligned with shared edges of pointing “up” and “down” pentagons which belong to the chains propagating in the [100] direction. This local arrangement is consistent with the atomic positions present within the *P*2 layer but does not match those of the *P*1 layer. Based on these measurements, the surface structure shown on Fig.4.5 (a-b) is assigned to a *P*2 type termination.

We now analyze the origin of the contrast differences observed between both STM images. To this end, larger pentagons (outlined in white) have been placed on high intensity patches observed on Fig.4.5(d). The pentagon edge length is chosen such as to decorate two of its opposite vertices with the isolated atoms arranged in a zig-zag manner, i.e. atomic positions fully occupied by Mn atoms in the *P*2 layer. A similar pentagon is drawn on the *P*2 structure presented on Fig.4.1(c). The three remaining vertices correspond to vertices of smaller pentagons which form the chains propagating along the [100] direction. Two out of these three atomic positions correspond to mixed Mn/Al sites referred as TM(3) and TM(1) by Klein *et al.* [68] with occupation factors of 0.3Mn-0.7Al and 0.5Mn-0.5Al, respectively. The third one, which belongs to the adjacent pentagonal chain, is fully populated by an Al atom. The remaining vertex of the pentagon is populated by an Al atom. Similar “white” pentagons are positioned identically on Fig.4.5(c) but, this time, dimer and darker contrasts associated with depressions appear within the motifs. Consequently, Fig.4.5(c) exhibits additional hollow sites which are not periodically distributed in the image. This approach allows us to pinpoint and to attribute the drastic variation in the intensity distribution between both STM images (Fig.4.5(a-b)) to the decoration within these large pentagons. Along the pentagonal chains (see Fig.4.5(d)), one of the vertices of the small pentagons (pointing “down”) lies alternatively inside the large “white” pentagons or inside the dark stars. In the structural model, these two sites labeled TM(5) are occupied by a Mn-Al (0.15/0.85) mixture. Upon annealing, preferential desorptions of Al/Mn atoms decorating the TM(5) sites could explain the formation of dark stars observed on both images of Fig.4.5. Similarly, the chemical disorder associated with the TM(5) site could partially explain the bright

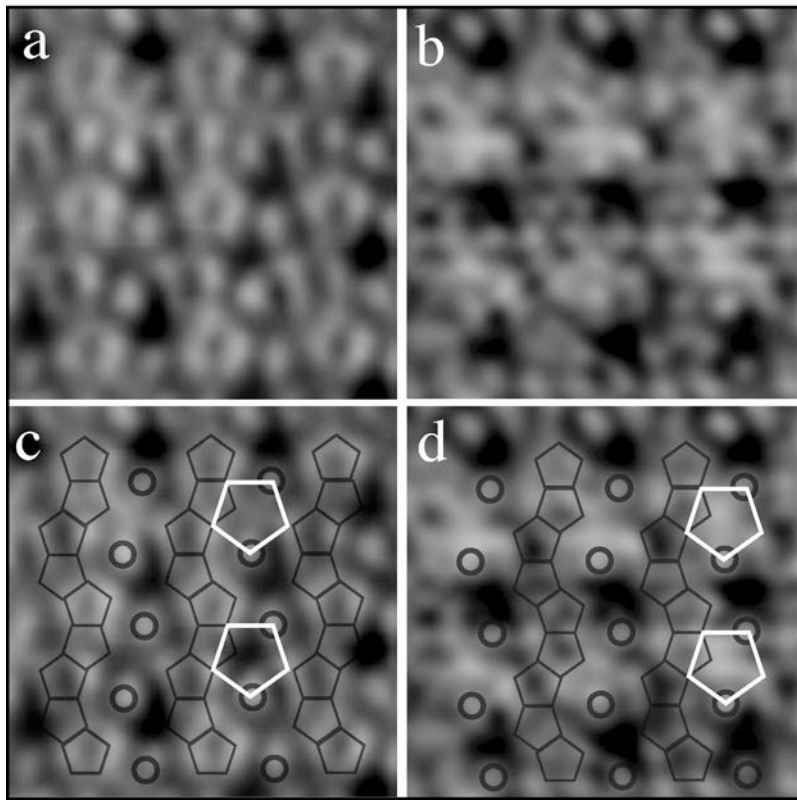


Figure 4.5: (a) and (c) Atomically resolved STM image ( $4 \text{ nm} \times 4 \text{ nm}$ ) recorded from the clean surface at  $V_{bias} = -0.4 \text{ V}$  and  $I_t = 0.36 \text{ nA}$ . This image has been filtered to emphasize the structure. (b) and (d) Atomically resolved STM image ( $4 \text{ nm} \times 4 \text{ nm}$ ) recorded on a different region of the same sample at  $V_{bias} = 0.6 \text{ V}$  and  $I_t = 0.50 \text{ nA}$ . This image has been rotated by  $\pi$  for comparison purposes. (c-d) A tiling corresponding to the P2 layer has been superimposed on both images. The pentagonal chains arranged in a zig-zag manner and individual Mn atoms are clearly discernable. While positioned identically with respect to the tiling, the contrast inside the largest pentagons varies drastically within the same image (c) as a consequence of compositional disorder, and between images (c) and (d) with the reversed sign of the bias voltage.

and diffuse features obtained inside the “white” pentagons, hence limiting the resolution of the pentagonal chains. Evidently, a contribution in the contrast variation from the surrounding sites, which possess also some substitutional disorder, cannot be excluded.

#### 4.5.2 *Ab initio* determination of cleavage plane

Regarding crystals with complex atomic structures, there is always a question where is the position of the cleavage plane, which atomic plane appears at the

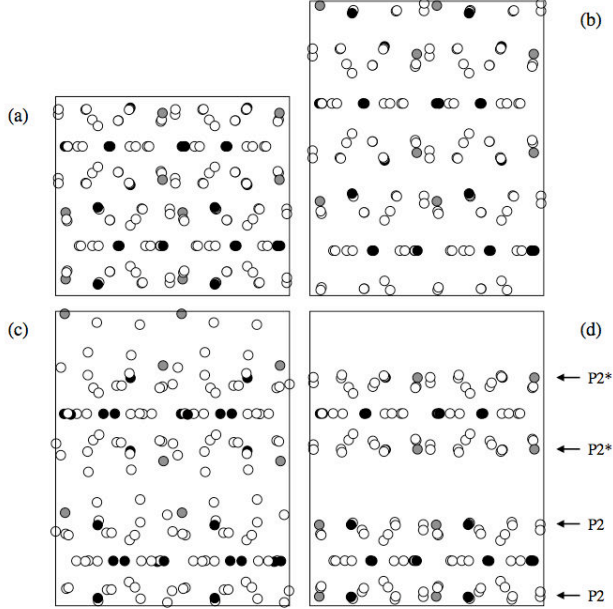


Figure 4.6: *Determination of the position of the cleavage plane from an ab initio simulation.* Here, the mixed Pd-Al sites are replaced by Pd atoms (grey) while the mixed Mn-Al sites are all replaced by Al atoms (white circles). Mn atoms appear as black spheres. The unit cell of the bulk structure (a) is expanded in the [010] direction (vertical direction) by 50 % (b). After the structural relaxation, the bulk structure has cleaved between the  $P_2$  and  $P_2^*$  planes (d). As the unit cell consists of two symmetry-equivalent blocks of atomic planes, two vacuum layers between the blocks are formed. Panel (c) shows an intermediate state when the structure begins to cleave.

surface. In this work based on a comparison of the experimentally observed STM patterns with the structure of individual atomic planes, see Sec. 4.5.1, it was concluded that the surface planes of the T-Al<sub>3</sub>(Pd, Mn) samples are the  $P_2$  planes. Recently, Steurer [204] proposed a method for the determination of the position of the cleavage plane from an *ab initio* simulation. The method is demonstrated on Fig.4.6. In a model of the bulk structure in the direction [010], the lattice parameter  $b$  is expanded by 50 %. This leads to a tensile stress in the unit cell larger than the ideal strength of the structure. Fig.4.6 shows that after a structural relaxation, the bulk structure has cleaved between the  $P_2$  and  $P_2^*$  planes. As the unit cell consists of two symmetry-equivalent blocks of atomic planes two vacuum layers between the blocks are formed. This simulation thus confirms the conclusion deduced from the experiment that the T-Al<sub>3</sub>(Pd, Mn) crystal cleaves between the  $P_2$  and  $P_2^*$  planes. At this stage, it has to be mentioned that the width of the gap between  $P_2$  and  $P_2^*$  planes is the largest interlayer spacing present in the bulk structure.

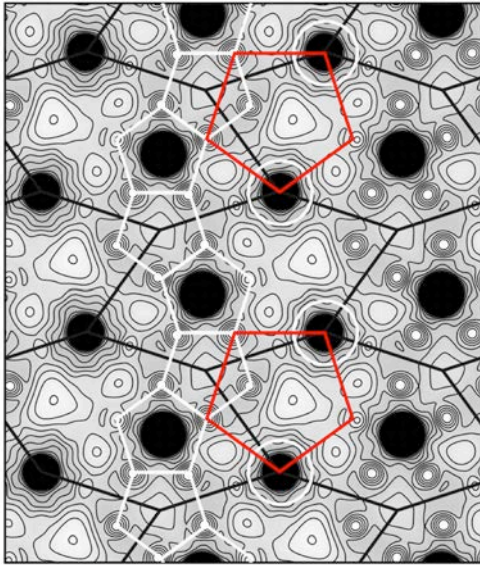


Figure 4.7: *The valence charge density distribution at the surface  $P2$  plane in the area  $25.19 \text{ \AA} \times 29.43 \text{ \AA}$  corresponding to  $2 \times 2$  unit cells. The global structure is represented by a tiling of squashed hexagons  $H$  (black lines). The pentagons of Al atoms are arranged in chains (white pentagons). Between two neighboring Mn atoms (marked by white circles) decorating the vertices of the  $H$  tiles there is a large charge density depression. Its position is approximately marked by a big (red, gray) pentagon.*

#### 4.5.3 STM images from *ab initio* calculations

For understanding the structure of the surface and the simulated STM images, it is very helpful to look first at the valence charge density distribution at the surface. Fig.4.7 shows the charge density distribution at the surface  $P2$  plane in the area of  $2 \times 2$  unit cells. The global structure is represented by a tiling of squashed hexagons  $H$ . Three vertices of the same, say even, parity are occupied by Mn atoms. At the other three vertices of odd parity, there are hollow sites surrounded by a pentagon of Al atoms. Inside the  $H$  tile one can see a Pd atom surrounded by the same pentagon of Al atoms but with opposite orientation. The Al pentagons are arranged in chains. The picture of the charge density distribution reveals one remarkable structural feature that is not immediately obvious from structural model of the surface. Between two neighboring Mn atoms decorating the vertices of the  $H$  tiles there is a large charge density depression. Its position is approximately marked by a big pentagon. While the chains of small pentagons and the chains of Mn atoms are arranged in the characteristic zig-zag pattern, these charge density minima are aligned with much smaller deviations from a straight line. In the simulated STM images these large charge density depressions are seen as dark spots.

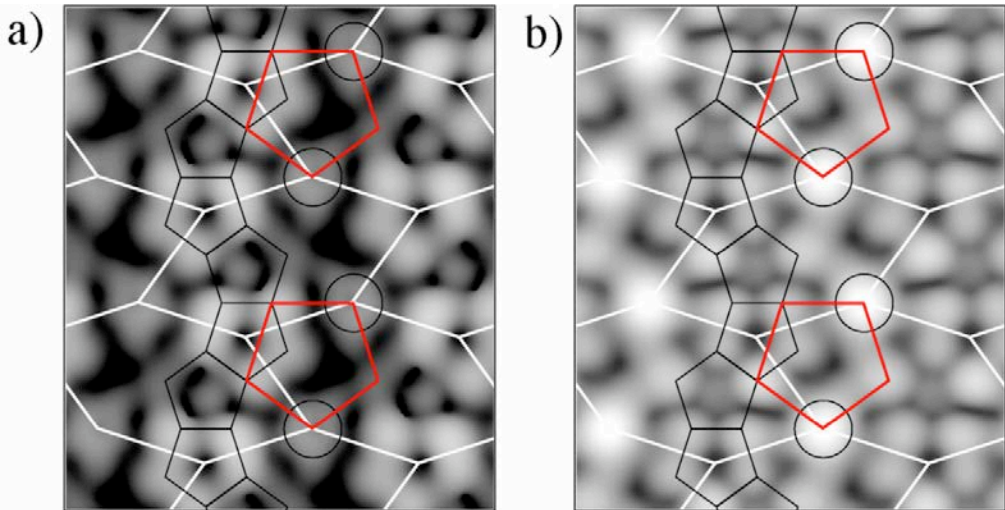


Figure 4.8: *Simulated STM images of the surface P2 plane. Images of the surface (a) and (b) are simulated for the bias voltages  $-0.4$  V and  $+0.4$  V, respectively. The area corresponds to  $2 \times 2$  unit cells. The chains of the small pentagons (black), big pentagons (red, gray), circles (white) and the tiling of squashed hexagons represent the structural features of the surface described on Fig.4.7. The bias dependency of the images observed experimentally is also seen on the simulated images.*

Fig.4.8 presents simulated STM images of the same model of the P2 surface. The images are calculated for a constant tunneling current and the bias voltages of  $V_{bias} = -0.4$  V and  $+0.4$  V corresponding to the occupied and unoccupied states around the Fermi level, respectively. The bias dependency of the images observed experimentally is clearly seen also on the simulated images. The contrast inside the big pentagon is substantially changed. The position and the darkness of the spot inside the pentagon varies with the bias voltage. Large variations of the contrast with the bias are observed also at the Mn sites and near the center of the H tiles. The bright spots corresponding to the Al pentagons around the odd vertices of the H tiles can be well recognized at both bias voltages. The simulated images qualitatively reproduce characteristic features observed in the experimental images. However, because of the chemical disorder inherent to the real structure and because only one chemical variant has been considered in our calculations, a one to one comparison between the simulated and experimental STM images would be meaningless.

#### 4.5.4 Surface investigated by XPD measurements

The same surface has been further analyzed using X-ray photoelectron diffraction. The measurements have been carried out after annealing the T-Al<sub>3</sub>(Pd,Mn) crystal to 873 K for 1 hour. Figures 4.9(a-c) exhibit the Al 2s, Pd 3d<sub>5/2</sub> and Mn 2p<sub>3/2</sub> photoemission line intensity for different angular and

polar emission angles. Normal emission ( $0^\circ$ ) corresponds to the central spot of the XPD pattern while the outer ring represents an emission angle of  $70^\circ$ . The bright and dark contrasts on these stereographic projections indicate high and low intensity, respectively. The XPD patterns measured for selected emitters (Al 2s, Pd 3d<sub>5/2</sub> and Mn 2p<sub>3/2</sub>) using Al K <sub>$\alpha$</sub>  radiation (1486.7 eV) reveal typical features of decagonal symmetry elements. Indeed, several rings of ten equivalent intense spots and a central 10-*f* symmetry axis dominate all XPD

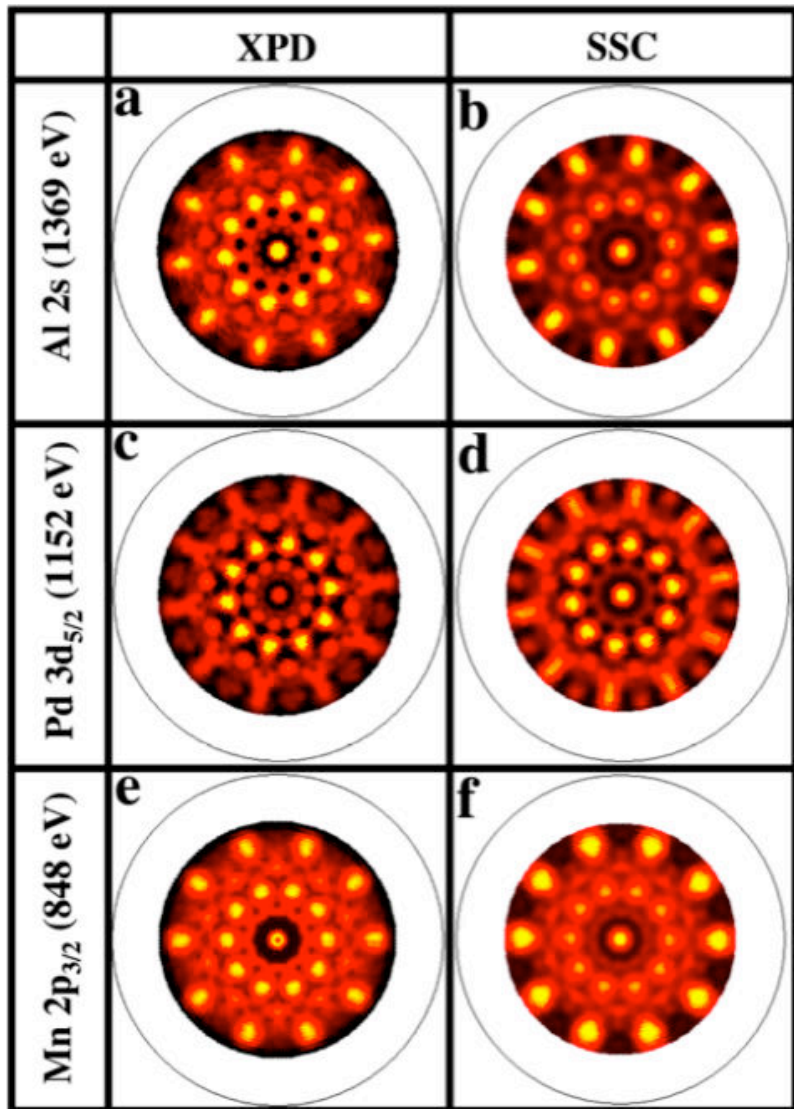


Figure 4.9: Experimental XPD patterns of (a) Al 2s (c) Pd 3d<sub>5/2</sub> and (e) Mn 2p<sub>3/2</sub> core levels measured on the T-Al<sub>3</sub>(Mn, Pd) (010) surface with Al K <sub>$\alpha$</sub>  (1486.7 eV) X-ray source. Single Scattering Cluster simulations for (b) Al 2s ( $E_{Kin} = 1369$  eV), (d) Pd 3d<sub>5/2</sub> ( $E_{Kin} = 1152$  eV) and (f) Mn 2p<sub>3/2</sub> ( $E_{Kin} = 848$  eV) emission based on a cluster derived from the bulk model [68] described on Fig.4.1.

patterns. The patterns presented on Fig.4.9(a-c) are similar to those observed on the *d*-Al-Ni-Co [34], on the decagonal quasicrystal overlayer grown on the five-fold surface of the *i*-Al-Pd-Mn sample [60] and recently on the Al<sub>13</sub>Co<sub>4</sub> crystal [70]. As XPD probes the local real-space environnement around the selected emitting atoms, these measurements reveal an average short-range decagonal ordering around the Al, Pd and Mn atoms at the near-surface. To interpret the experimental patterns, Single Scattering Cluster (SSC) simulations for the Al 2s, Pd 3d<sub>5/2</sub> and Mn 2p<sub>3/2</sub> emission have been performed based on the available T-Al<sub>3</sub>(Mn,Pd) structural bulk model [68]. The model used for the SSC simulations contains 1248 atoms (8 unit cells), 20 atomic plans along the [010] direction and has the following dimensions: 29.434 Å × 25.020 Å × 25.188 Å. Five separate clusters have been generated to represent the different atomic configurations that can be observed at the surface. Hence, the surface of the 5 models is either terminated by the 2 layers F-P1 (*F* layer as topmost termination, *P*1 is the layer below the *F* layer), P1-F, P2-P2, P1-P2 or by P2-P1. The cluster used to carry out the calculations consists of 1248 atoms with 107 Al, 11 Pd and 44 Mn as emitters. The photoelectron intensity maps obtained for each emitter appear similar regardless of the model chosen. The SSC patterns presented on the Fig.4.9 have been obtained for the P2-P1 configuration. The experimental XPD patterns for the Al 2s, Pd 3d and Mn 2p can be nicely reproduced by the SSC simulations (Fig.4.9(b), (d), and (f )) which display the expected decagonal rings made of 10 distinct spots. The patterns are well reproduced in terms of positions but differ slightly in the intensity distribution. However, the intensity distributions are well reproduced, for instance for the Mn emitter with the external decagonal ring situated at  $\theta = 62^\circ$  (Fig.4.9(f)). The position and intensity in the two decagonal rings situated on  $\theta = 36^\circ$  and  $\theta = 48^\circ$  are accurately reproduced for the Pd emitter too. While a relatively good agreement is obtained between XPD maps and SSC images, it is not possible to discriminate between the most preferred topmost surface termination. However, it clearly appears that the *p*-10*f* symmetry of the bulk structure is preserved within the near-surface region.

#### 4.5.5 Electronic character of the surface

We now turn into the characterization of the T-Al<sub>3</sub>(Mn, Pd) electronic structure using XPS and UPS techniques. The photoemission spectra are compared to those obtained on the icosahedral Al-Pd-Mn quasicrystal. The UPS valence band (VB) spectra in the near E<sub>F</sub> region collected on both the *i*-Al-Pd-Mn quasicrystal (dashed line) and on the T-Al<sub>3</sub>(Mn, Pd) sample (solid line) are presented on Fig.4.10. The valence band spectrum of the Taylor phase up to 9 eV is presented in the inset where the main peak around 4.5 eV corresponds to Pd 4d states. It is known that Mn d-states dominate the density of states (DOS) around E<sub>F</sub> in *i*-Al-Pd-Mn and Al-Mn alloys. The rounded shape of the spectral intensity near E<sub>F</sub> has been considered as the signature of the *pseudo-gap*, i.e. a reduction in the DOS at the Fermi level [194, 198, 205–207].

From the comparison of two spectra normalized at 2 eV, the Fermi edge of T-Al<sub>3</sub>(Mn, Pd) appears much sharper than the one observed on the *i*-Al-Pd-Mn quasicrystal. This is partly explained by an enhanced Mn *d*-DOS at E<sub>F</sub> due to a higher concentration of Mn in T-Al<sub>3</sub>(Mn, Pd) crystal than in the *i*-Al-Pd-Mn sample. Nevertheless, the decrease of the spectral intensity between the Fermi edge and 0.5 eV below E<sub>F</sub> could be interpreted as an evidence for a shallow *pseudo-gap* in the DOS of the T-Al<sub>3</sub>(Mn, Pd) phase. However, the procedure introduced by Mori *et al.* [208] to quantify the depth and width of

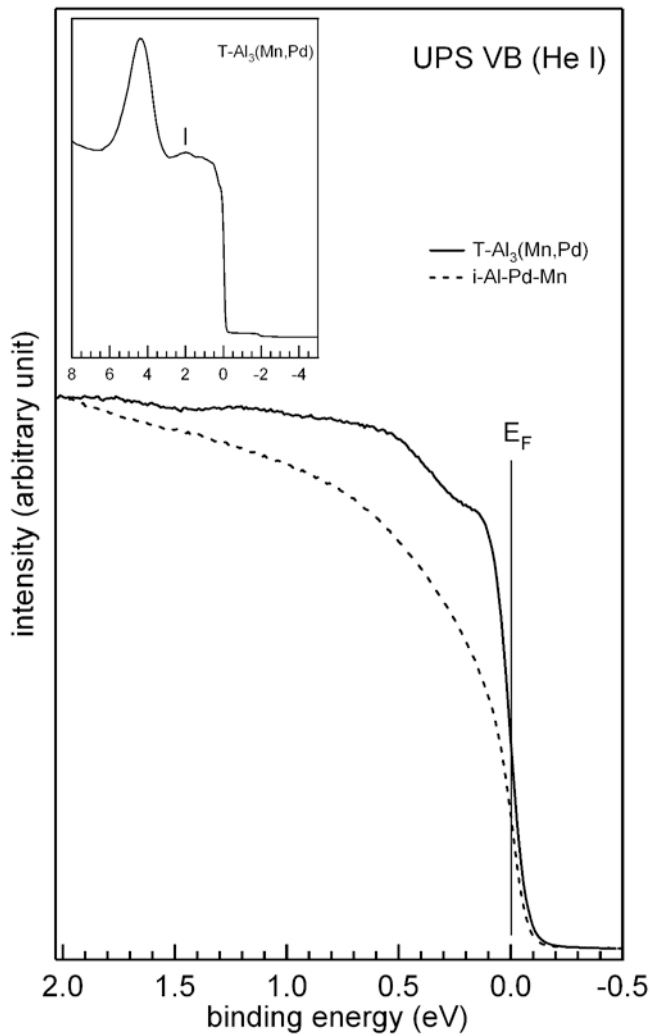


Figure 4.10: Near E<sub>F</sub> UPS valence band spectra of T-Al<sub>3</sub>(Mn, Pd) (solid line) and *i*-Al-Pd-Mn (dashed line). The position of E<sub>F</sub> is indicated by a dashed line. Spectra are normalized to have the same height at 2 eV binding energy. Inset: valence band spectrum of the T-Al<sub>3</sub>(Mn, Pd) up to 9 eV. The main peak at 4.5 eV corresponds to Pd 4d states and the vertical line is located at 2 eV.

the *pseudo*-gap measured on the icosahedral quasicrystal cannot be applied here as the DOS near  $E_F$  cannot be considered as a smooth function of the energy. From a qualitative perspective, the presence of the *pseudo*-gap is not evident in the T-Al<sub>3</sub>(Mn, Pd) VB spectrum and the T-phase sample exhibits a more metallic character than its quasicrystal counterpart.

The UPS valence band spectra of the T-Al<sub>3</sub>(Mn, Pd) and *i*-Al-Pd-Mn samples have been calculated using the bulk DOS. The Katz-Gratias-Boudard (KGB) model is used in our calculations of the *i*-Al-Pd-Mn properties [194, 209]. This is justified as most of the UPS signal comes from the near surface region for He I radiation (21.2 eV). The UPS spectrum is approximated by summing the orbital contributions of the DOS of Al, Mn, and Pd weighted by the corresponding cross-sections for He I energies. The experimental broadening are not taken into account in the calculations. As shown on Fig.4.11, the spectra have been normalized to have the same height at the energy of 2 eV as per Fig.4.10. The calculated UPS VB spectra exhibit a very deep *pseudo*-gap at  $E_F$  for the *i*-Al-Pd-Mn quasicrystal but a much shallower *pseudo*-gap for the T-Al<sub>3</sub>(Mn, Pd) crystal. This is in agreement with both spectra presented on Fig.4.10. The position of the main features (Pd 4d states for instance) are also comparable between the large scale UPS spectra (inset of Fig.4.10) and

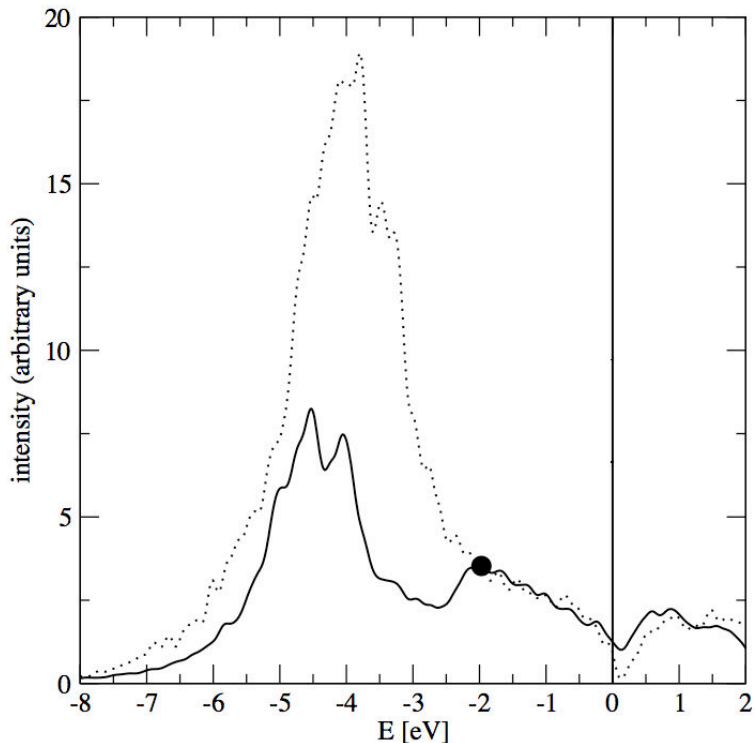


Figure 4.11: Calculated UPS VB (He I) spectrum for the bulk of T-Al<sub>3</sub>(Mn, Pd) (full line) and *i*-Al-Pd-Mn (dashed line) samples. The spectra are normalized to have the same height at the energy of -2 eV indicated by a black dot.

the calculated curve (see Fig.4.11). The less intense Mn 3d peak at 2 eV below  $E_F$  on the experimental UPS spectra compared to the calculated curve could be explained by the atomic decoration used for the DOS calculation and/or by a loss of resolution due to instrumental broadening.

An alternative, although indirect, approach to assess the DOS at  $E_F$  is to study the asymmetry of the Mn 2p core level line shape. Line shape of the Mn 2p core level has been well studied for *i*-Al-Pd-Mn, Al-Mn alloys and Mn metal using Doniach-Šunjić (DS) function [86, 197, 198, 207, 210]. Metallic core-levels are asymmetric because of electron-hole pair excitation across  $E_F$  and the DS asymmetry parameter ( $\alpha$ ) is given by [85]:

$$\sum_{q < 2q_F} \frac{|V_Q|^2}{|\epsilon(q, 0)|^2} \frac{N(0)}{qV_F} \quad (4.2)$$

where  $N(0)$  is the DOS at  $E_F$ ,  $V_Q$  is the core-hole potential,  $q$  is the momentum vector,  $V_F$  is the Fermi velocity and  $\epsilon$  is the dielectric function. Thus, the estimation of the asymmetry parameter  $\alpha$  is an indirect probe of the DOS at  $E_F$   $N(0)$ . It should be noted that the DS asymmetry parameter ( $\alpha$ ) for *i*-Al-Pd-Mn is significantly lower than that of Mn metal. This has been related to the low  $N(0)$  in the *i*-Al-Pd-Mn due to the presence of the *pseudo-gap* [197]. The  $\alpha$  parameter of the Mn 2p core level was found to be 0.46 for Mn metal and it turned out to be as low as 0.14-0.18 for *i*-Al-Pd-Mn. Recently, it has been shown that the value of  $\alpha$  of Mn 2p for Mn metal has been over estimated due to the lack of consideration of the 1 eV satellite while simulating the core level line shape. Indeed, the Mn 2p core level of bulk like Mn film has been studied using high-resolution photoemission spectroscopy and an unusual satellite feature at 1 eV higher binding energy (BE) from the main peak has been observed [86]. It originates from the intra-atomic multiplet effect related to Mn atoms with large local moment [86]. Taking into account this satellite in pure Mn leads to a lower value of the  $\alpha$  parameter which is then equal to 0.34 [86]. This satellite feature was not observed in the Mn 2p core level of *i*-Al-Pd-Mn and Al-Mn alloys and only one DS function was sufficient to simulate the Mn 2p core level for such systems [86, 197, 198, 207]. Strong Al 3s, *p*-Mn 3d hybridization was suggested to be responsible for the suppression of 1 eV satellite feature in *i*-Al-Pd-Mn and Al-Mn alloys [86, 207].

Fig.4.12 shows the Mn 2p<sub>3/2</sub> core level spectrum for the T-Al<sub>3</sub>(Mn, Pd) (a) and for the *i*-Al-Pd-Mn (b) samples. Both the spectra have been recorded with similar analyser settings and thus with similar energy resolution. Visual inspection of the two spectra shows that the core level line shape is more asymmetric towards the higher BE side for T-Al<sub>3</sub>(Mn, Pd) compared to *i*-Al-Pd-Mn. We have performed a least-square fitting to simulate the Mn 2p<sub>3/2</sub> line shape of T-Al<sub>3</sub>(Mn, Pd) and *i*-Al-Pd-Mn using a DS function. The intrinsic lifetime broadening of the core level ( $2\gamma$ ),  $\alpha$ , intensity and position of core level, and the iterative background are varied independently during the fitting. The residuals on Fig.2.2(a,b) show the good quality of the fit. For *i*-Al-Pd-Mn,

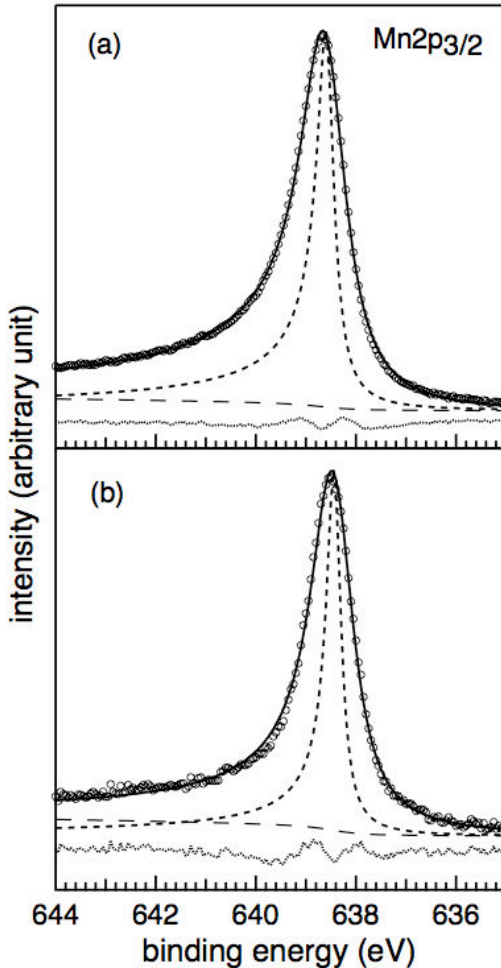


Figure 4.12:  $Mn\ 2p_{3/2}$  core-level spectra (open circles) for  $T\text{-Al}_3(\text{Mn, Pd})$  (a) and (b)  $i\text{-Al-Pd-Mn}$ . The fitted spectra (thin solid line), the spectra deconvoluted from experimental broadening (short dashed line), the iterative background (long dashed line) and the residual (dots) are also shown.

we obtained a value  $\alpha = 0.140 \pm 0.015$  while  $2\gamma$  turned out to be  $0.32 \pm 0.02$ . These values are in good agreement with the values obtained from the DS line shape simulation of high resolution  $Mn\ 2p$  core level of  $i\text{-Al-Pd-Mn}$  reported in the literature [83, 198]. DS line shape simulation of  $Mn\ 2p_{3/2}$  line for  $T\text{-Al}_3(\text{Pd, Mn})$  resulted in  $\alpha (= 0.200 \pm 0.013)$  while  $2\gamma$  was equal to  $0.36 \pm 0.01$ . This is consistent with a shallower *pseudo-gap* in the  $T\text{-Al}_3(\text{Mn, Pd})$  phase compared to the  $i\text{-Al-Pd-Mn}$  sample due to an enhanced  $Mn\ d$  contribution to the DOS near  $E_F$ .

## 4.6 Discussion

The analysis of the (010) surface of T-Al<sub>3</sub>(Mn, Pd) indicates that there is no evident lateral surface reconstruction but a high degree of structural imperfections. While some of the contrast disparities on STM images are expected due to the chemical disorder intrinsic to the bulk model, hollow sites resembling “dark” stars have been observed within the topmost surface layer. These surface vacancies exhibit similar sizes as those encountered on the five-fold Al-Pd-Mn quasicrystal surface, then attributed to the irregular structure of the first shell of the *pseudo*-Mackay cluster [84]. On the T-Al<sub>3</sub>(Mn, Pd) surface, the origin of these depressions, which are not present in the structural model, have been tentatively attributed to missing atoms at sites referred as TM(5) by Klein *et al.* [68]. The latter atomic positions are supposedly occupied by a mixture of Mn/Al atoms. In fact, when populated, this site contributes significantly to the intensity of the STM image (see Fig.4.5(b)). Atomic desorptions have been recently reported by Addou *et al.* [70] when investigating the Al<sub>13</sub>Co<sub>4</sub>(100) approximant surface. In that case, only 10 out of 20 Al atoms per surface unit cell are preserved within the topmost plane. This selective desorption was interpreted by a particular bonding present within the 23-atom bipentagonal pyramid clusters [67, 191]. Here, the TM(5) site belongs to interpenetrating icosahedral clusters that form the column, basic structural constituent, presented on Fig.4.1(d). While information about the inter-cluster bonding along the [010] direction remain scarce [211], the erratic occupation of TM(5) sites could be explained by the decoration of the in-plane nearest neighboring sites, namely TM(1) and TM(3). As mentioned previously, both sites also exhibit a substitutional disorder and can be populated by either Al or Mn atoms. Depending on the elements present at TM(1) and TM(3) sites, the bonding with Mn<sub>0.15</sub>-Al<sub>0.85</sub> atoms at TM(5) site should be considerably different. Hence, it is reasonable to assume that stronger or weaker (attractive/repulsive) interactions between atoms at TM(5) positions with the surrounding will result. In addition, the reduced coordination of Mn/Al atoms at TM(5) site at the surface could favor desorption.

The structural analysis of atomically resolved STM images and a qualitative comparison with simulated images indicate that the surface is terminated by a *P*2 like plane present in the bulk model. The step height measurements equal to  $b/2$  are in agreement with only one type of surface termination, with the exception of the limited regions at the edges of the terraces. Step heights values consistent with half of the lattice parameter have also been measured on other approximant surfaces [61, 62, 70]. With *P*1 lying theoretically at 0.625 Å beneath *P*2, the combined planes lead to a denser surface than if a flat layer would be selected as the surface termination. Statistically, the puckered surface (*P*2+*P*1) should also be Al rich compared to the flat layer. The surface termination is then created by a cut through the bulk model at the widest interlayer gap along the [010] direction. All these results are consistent with previous studies performed on approximant and quasicrystal surfaces where

the exposed surface layers correspond to a cleavage through the bulk model at largest gaps [42]. The (-) five-fold and (-) ten-fold surface planes have been also reported to be laterally bulk-terminated. [25, 27, 32, 54, 84] It has to be mentioned that the  $\xi'$ -Al-Pd-Mn (010) and the  $\text{Al}_{13}\text{Co}_4$  (100) topmost surfaces correspond to incomplete bulk planes. [61, 70] For Al-based quasicrystals like the five-fold *i*-Al-Pd-Mn surface, the average density of the two terminating planes [27] and the Al concentration are high [84]. Out of the two topmost planes (only 0.38 Å apart [32]), the layer having the highest concentration of Al atoms, is exposed at the surface. This plane selection is not verified for the T-Al<sub>3</sub>(Mn, Pd) (010) surface. If *P*2 and *P*1 layers are combined to form a single termination *P*, they form the densest Al-rich surface plane compared to the *F* termination. However, the layer containing TM elements (mainly Mn atoms) is this time favored as the topmost surface layer. As explained above, the cleavage plane necessary to generate the surface layers is always positioned in between consecutive puckered *P* (*P*2+*P*1) layers. Due to their Al-rich/pure content, the bonding between *P*1 and *F* layers can be considered in a first approximation as originating from an Al-Al atomic interaction. The bonding between two TM-rich *P*2 layers should be considerably different and may influence the cut height through the bulk model. As confirmed by DFT calculations (see Fig.4.6), the cleavage plane is indeed in between *P*2 and *P*2\* layers. From the surface structural imperfections and the chemical disorder inherent to the bulk model, it is not possible to estimate the overall TM concentration at the extreme surface. However, the results obtained using XPS ( $\text{Al}_{75.4}\text{Pd}_{3.3}\text{Mn}_{21.3}$  with an error of 10%) show that there is no chemical segregation at the surface of the T-Al<sub>3</sub>(Mn, Pd) crystal.

In addition using LEED and XPD techniques, it has been shown that the *pseudo*-10 fold symmetry is clearly maintained at the sample surface. The LEED patterns exhibit sets of decagonal rings which are more distinguishable here than on the LEED patterns recorded on the *p*-10*f* surface of the orthorhombic  $\text{Al}_{13}\text{Co}_4$  approximant. However, it remains less apparent than on the  $\xi'$ -Al-Pd-Mn sample [61]. In both cases, the surface planes have been related to layers present in the bulk models. The difference in the diffraction patterns can be explained by denser planes at the T-Al<sub>3</sub>(Mn, Pd) surface than on the  $\text{Al}_{13}\text{Co}_4$  approximant, where the surface terminations consist of incomplete puckered layers [70]. For both approximants, SSC calculations reproduce the local decagonal symmetry expected at the near surface region around each emitter but does not allow to discriminate between preferred surface terminations.

It has been demonstrated that a structure-induced *pseudo*-gap in the Al band exists in the decagonal  $\text{Al}_{70}\text{Pd}_{13}\text{Mn}_{17}$  sample and its approximant phases [121, 212]. The *sp-d* hybridization plays a crucial role in the formation of the *pseudo*-gap [120]. In the case of the T-Al<sub>3</sub>Mn phase and compared to decagonal quasicrystal, the high concentration of Mn atoms should broaden the Mn band which would then overlap with the Fermi level, hence leading to a higher DOS at  $E_F$ . The high concentration and the chemical order of Mn atoms should lead

to a bonding-antibonding splitting characteristic of transition metal  $d$  bands, due to the loss of the impurity character of the  $d$  band [121]. As shown on Fig.4.10, a higher spectral intensity is also observed for the T-Al<sub>3</sub>(Mn, Pd) phase compared to the quasicrystal sample. In addition, several components which can be related to the Mn  $d$  band have been observed near  $E_F$ . From an additional Mn 2p core level analysis, it appears that the T-Al<sub>3</sub>(Mn, Pd) surface presents a more metallic character than the 5-fold *i*-Al-Pd-Mn quasicrystal surface, i.e. a *pseudo*-gap of reduced depth.

## 4.7 Conclusions

We have investigated the (010) surface of the recently grown orthorhombic T-Al<sub>3</sub>(Mn, Pd) crystal [71]. The LEED patterns and the XPD patterns show the expected *pseudo*-10 fold symmetry of the surface. Upon annealing the sample to 923 K, we observe atomically flat terraces separated mainly by a single step height equal to one half of the unit cell parameter ( $b/2$ ). Despite the presence of structural imperfections, the surface termination has been related to the puckered layer present in the structural bulk model. From the STM analysis and the *ab initio* simulation of the cleavage process, we conclude that the surface topmost layer consists of the *P*2 plane (containing transition metal elements) with the *P*1 plane (Al rich) 0.65 Å beneath. The drastic bias dependency observed on experimental images is also verified on simulated STM images calculated from the *P*2 layer. From UPS and XPS measurements, we have shown that this Taylor phase exhibits a higher density of states at the Fermi level compared to the *i*-Al-Pd-Mn quasicrystal.

# Chapter 5

## Lead adsorption on orthorhombic $\text{Al}_{13}\text{Co}_4$ and T- $\text{Al}_3(\text{Mn}, \text{Pd})$

### 5.1 Introduction

Understanding the role of the chemical and/or structural complexities of quasicrystals on their physical properties remains today a challenge. There can be different approaches to resolve the chemical complexity from the structural one and thus facilitate the comprehension of their individual role. Therefore, in the last few years, considerable attention has been focused on finding quasicrystals with a less complex chemical composition. A major step towards that direction was made with the recent discovery of the icosahedral binary quasicrystal [213, 214]. Another alternative relies on the use of quasicrystalline surfaces as templates for the growth of single-element pseudomorphic thin films [88, 142, 144, 153, 159, 215–219]. Such films are of particular interest as they provide an opportunity to study the aperiodic order without the associated chemical complexity. Recently, Pb adsorption on various Al-rich quasicrystalline surfaces have resulted in the formation of quasiperiodic Pb monolayer (ML) [88, 89, 92, 209]. The choice of Pb adatoms was driven by several parameters like for instance its low surface energy which should promote the wetting of the substrate and its immiscibility with Al, hence reducing the possibility of intermixing phenomena and surface alloy formation. Quantum size effects in Pb thin films grown on noble metals or semiconductors have been reported in several works [167, 220–224]. Due to the electronic confinement within the film, the growth of Pb adatoms is altered and this is manifested by the formation of islands with magic heights. In general term, the gap needs to be a projected one in the direction perpendicular to the surface, this can be the [111] for a (111) surface (in the cubic system) but can be of course any other direction in general. Thus, the presence and the effect on the growth mode of the *pseudo*-gap at  $E_F$  on several CMA systems was another motivation for the selection of Pb as adsorbates.

The first study of the Pb deposition on a quasicrystalline surface (icosahedral  $\text{Al}_{70}\text{Pd}_{21}\text{Mn}_9$ ) was performed by Ledieu *et al.* [88] using scanning tunneling microscopy (STM), low energy electron diffraction (LEED) and photoemission

spectroscopy (PES). It was shown that the quasiperiodic Pb monolayer can be formed within a broad range of temperatures from 57 to 653 K. Its structural quality is improved upon subsequent annealing below 653 K. The density of the Pb monolayer (0.09 atom/ $\text{\AA}^2$ ) has been found to be very similar to the density of 1 ML Pb adsorbed on an Al(111) surface. This quasiperiodic Pb monolayer exhibits properties which are fundamentally different from those of bulk Pb. The most striking evidence is the presence of a wide *pseudo*-gap in the electronic density of states (DOS) at  $E_F$  observed by scanning tunneling spectroscopy and ultraviolet photoemission spectroscopy. The structure of the monolayer is  $\tau$ -inflated compared to the surface structure of the substrate. Similarly, the growth of Pb on the 10-*f* surface of the *d*-Al<sub>72</sub>Ni<sub>11</sub>Co<sub>17</sub> quasicrystal at room temperature has been studied using STM and LEED [92]. The adsorption leads also to the formation of a well-ordered quasiperiodic overlayer of Pb on this quasicrystal surface. As in the Pb/*i*-Al-Pd-Mn study, pentagonal features of dimensions of 4.9  $\text{\AA}$  on this quasicrystalline surface too are discernible within the first monolayer. However, the growth mechanism of the first monolayer in the Pb/*d*-Al-Ni-Co system is different to that of the Pb/*i*-Al-Pd-Mn case. The first monolayer of Pb on the *i*-Al-Pd-Mn self-assembles via a network of pentagonal islands. These 5-fold clusters are a consequence of an heterogeneous nucleation of Pb adatoms at submonolayer coverage [209]. On the *d*-Al-Ni-Co surface, the growth proceeds with the lateral expansion of Pb islands instead of the formation of a dispersed network of pentagonal clusters as seen on the *i*-Al-Pd-Mn substrate. This indicates a higher mobility for adsorbing Pb atoms on the 10-*f* compared to the 5-*f* quasicrystalline surface. In addition, the growth of Pb thin films has been carried out on the 5-*f* surface of the *i*-Al<sub>63</sub>Cu<sub>24</sub>Fe<sub>13</sub> quasicrystal [89]. Here again, the monolayer exhibits a quasiperiodic ordering and the nucleation is characterized as heterogeneous, i.e. Pb nucleate at specific adsorption site. X-ray photoemission spectroscopy (XPS) shows consistently throughout these studies that there is hardly any shift in the Al and Pb core levels with increasing deposition of Pb, indicative of a weak Pb and Al atoms interaction [88, 89, 92]. For these three quasicrystalline substrates, the sticking coefficient for Pb adsorption drops to zero upon completion of the  $\tau$  inflated pseudomorphic monolayer. Interestingly, the scenario is different for the growth of Pb on ordinary metals. For example, the growth mode of Pb on Al(111) is of Frank-Van der Merwe type (layer-by-layer). The relatively weak interaction between Pb adatoms and the Al(111) substrate generates a moiré structure [89]. Moreover, the growth of Pb on Cu(111) develops into 3D islands due to quantum size effects [167]. Differences in the sticking behavior of Pb on quasicrystalline and metallic substrates may be correlated to the quasicrystal structural complexity compared to “ordinary” periodic metals. An alternative explanation for the apparent “non-stick” behavior of Pb adatoms would be fast diffusion of the adsorbate on the wetting layer leading to the formation of Pb mounds separated by large distances and hardly detectable by STM or XPS measurements. While chemically and structurally closely related, approximant systems are less complex

than quasicrystals as they possess a finite-size unit cell. On the other hand, approximants remain much more complex than usual elemental metals due to their giant unit cell, whose basis structure is best characterized using highly symmetric clusters. Therefore, Pb deposition on approximant surfaces provides an opportunity to study the adsorption on a surface which is structurally intermediate to elemental metals and quasicrystals. This work will also be important to assess the influence of periodicity on the adsorbate growth mode while keeping a relatively high degree of structural complexity.

The experimental details will be presented in Sect. 5.2. Then, the adsorption of Pb adatoms on the *pseudo*-10 fold (*p*-10*f*) surface of the Al<sub>13</sub>Co<sub>4</sub> crystal and T-Al<sub>3</sub>(Mn, Pd) at room temperature and at 573 K will be described in Sect. 5.3 and Sect. 5.4, respectively. Finally, the main results will be discussed Sect 5.5.

## 5.2 Experimental details

Two approximant surfaces, namely the *pseudo*-10*f* surfaces of both the Al<sub>13</sub>Co<sub>4</sub> and T-Al<sub>3</sub>(Mn, Pd) surfaces, have been used as substrates for Pb deposition. The preparation procedure applied to both surfaces includes cycles of Ar<sup>+</sup> ion sputtering followed by annealing cycles (for more details refer to Chapter 2 and 3). The cleanliness, the topography and the overall structure of the surface were checked using XPS, STM and LEED. The surface structural quality was systematically checked prior to depositions. Lead adsorption was carried out at room temperature using Omicron electron beam cell which is flux monitored. The deposition rate was calibrated using STM by measuring the fractional area covered with successive Pb depositions. The flux was set to  $4.2 \times 10^{-3}$  ML/s throughout this study. The pressure during depositions was kept in the low  $10^{-10}$  mbar range. The STM studies were performed at room temperature in constant current mode using an Omicron variable-temperature STM. XPS experiments were carried out using a non-monochromatized MgK<sub>α</sub> source (1253.6 eV).

## 5.3 Structural investigation of Pb adsorption on the Al<sub>13</sub>Co<sub>4</sub> (100) surface

### 5.3.1 Deposition at 300 K

#### 5.3.1.1 Low energy electron diffraction analysis

Figure 5.1 shows the LEED patterns recorded for the clean surface of the Al<sub>13</sub>Co<sub>4</sub> sample and after successive (1-12 MLE nominal exposure) Pb coverages. The orthorhombic structure of the clean Al<sub>13</sub>Co<sub>4</sub> surface is evident from the diffraction pattern shown on Fig.5.1(a). Within the accuracy of our

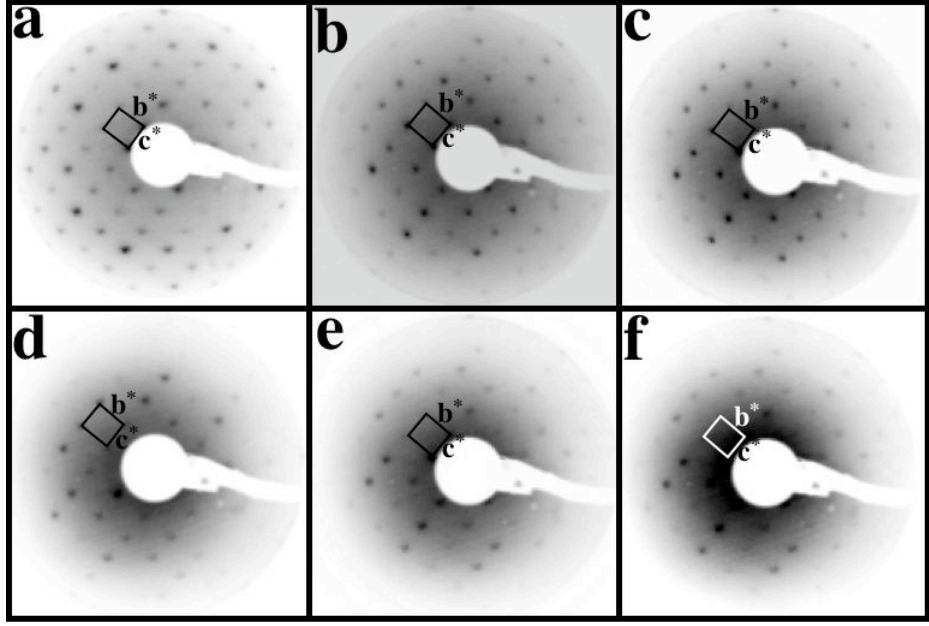


Figure 5.1: LEED patterns (inverted for clarity) recorded as a function of Pb coverage on the  $\text{Al}_{13}\text{Co}_4$  (100) surface at 40 eV beam energy: (a) clean, (b) 1 MLE, (c) 2 MLE, (d) 4 MLE, (e) 7 MLE, and (f) 12 MLE.

measurements, the measured lattice parameter dimensions are consistent with those reported by Grin *et al.* for the bulk model [66]. Up to 2 monolayer equivalent (MLE) dosage, the diffraction patterns stay reasonably sharp with a low to medium background. Upon additional Pb exposure, the patterns start to degrade with a clear background increase. However, the overall orthorhombic structure is still preserved even for the highest exposure. At each stage of the deposition, the magnitude of the reciprocal lattice vectors remain unchanged. These measurements clearly demonstrate that the Pb adatoms adopt a pseudodomorphical structure on the  $\text{Al}_{13}\text{Co}_4$  substrate in the whole exposure range. The reduced quality of the LEED pattern for high dosage may have several explanations. For instance, adsorption of Pb atoms at defect sites could be the reason for the slight degradation in the LEED patterns for the higher Pb exposure. As we will see below, the high adsorbate mobility combined with a reduced sticking coefficient above 1 ML may lead to the formation of large disordered clusters across terraces. Depending on their height and roughness, they could be difficult to detect using STM technique.

### 5.3.1.2 Scanning tunnelling microscopy measurements

After annealing the sample to 1120 K for 1 h, the majority of the clean  $\text{Al}_{13}\text{Co}_4$  surface consists of relatively narrow terraces with  $T1$  termination as the dominant topmost surface layer (see Chapter 2). Figure 5.2(a) presents a STM image of the clean  $\text{Al}_{13}\text{Co}_4$  surface prior to Pb dosing. While the major-

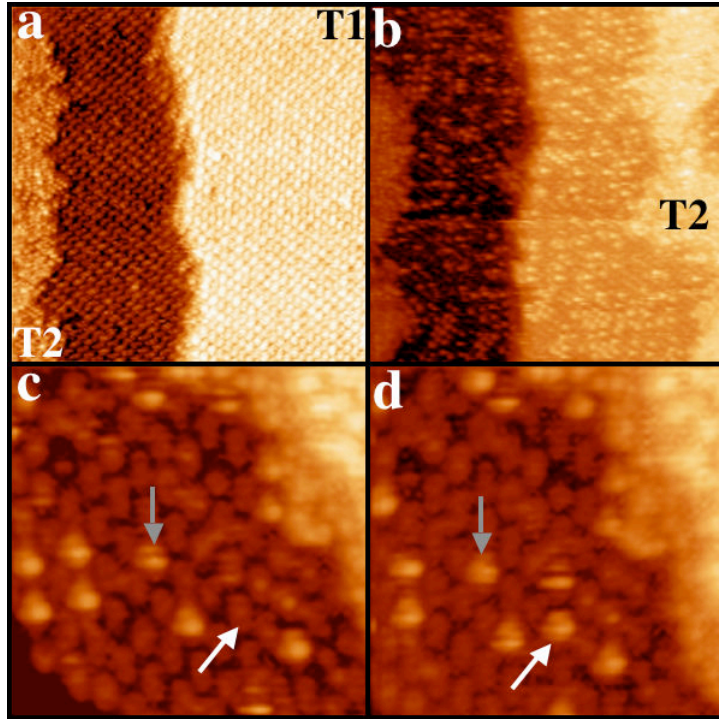


Figure 5.2: (a) STM image of the clean  $Al_{13}Co_4$  substrate ( $50 \times 50 \text{ nm}^2$ ). (b) STM image recorded after deposition of 0.13 MLE of Pb at room temperature ( $100 \times 100 \text{ nm}^2$ ), (c) and (d) comparison between two STM images ( $15 \times 15 \text{ nm}^2$ ) recorded successively on the same region and for the same coverage. The arrows point to Pb atoms which have moved during the scan.

ity of the terraces is indeed composed of  $T1$  termination, a small fraction of the image is covered by the  $T2$  termination. In the following Chapter, it will be shown that annealing to higher temperatures lead to a surface exclusively terminated by  $T1$  layers. Figure 5.2(b) shows a STM image recorded after the deposition of 0.13 MLE of Pb at 300 K. Within this submonolayer regime, the diffusion length of adsorbates is such that adatoms are individually distributed across the terraces, i.e. there is no sign of cluster or island growth. While the adsorbates are easily distinguishable on  $T1$ , it is rather difficult to estimate the amount of Pb atoms located on the  $T2$  region. Because of its low density, Pb adatoms decorating the edges and/or filling several interstices of the  $T2$  layer remain strong possibilities. However, the adsorbates do not nucleate on top of  $T2$  termination (no height difference measured). The scarce intense dots on the  $T2$  termination could be related to either individual adatoms or atoms intrinsic to the  $T2$  plane.

We now focus on Pb adsorption on the  $T1$  region and compare STM images recorded successively on the same region (Fig.5.2(c-d)). The bipentagonal motifs characteristic of the incomplete puckered plane (as discussed in Chapter 2) are still well-resolved in both STM images. Individual Pb adatoms which ap-

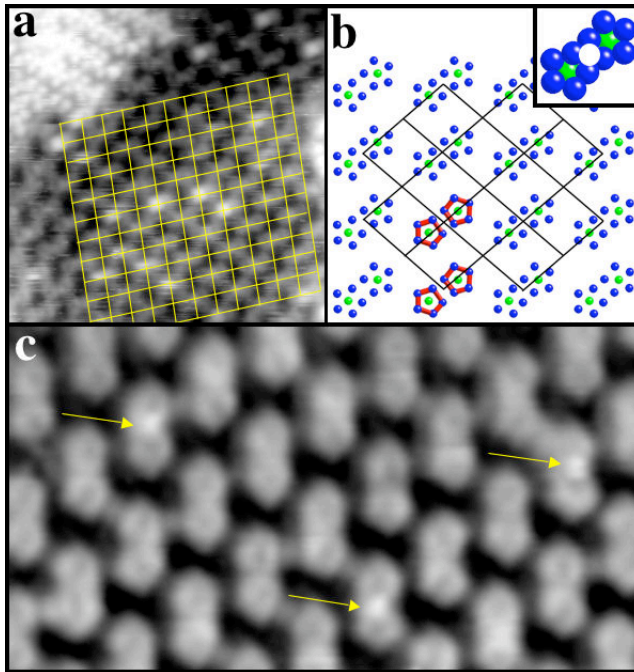


Figure 5.3: (a) *STM image* ( $15 \times 15 \text{ nm}^2$ ) recorded after dosing 0.38 MLE of Pb at 300 K on the  $\text{Al}_{13}\text{Co}_4$  substrate. A grid representing the diagonals of the orthorhombic unit cell has been superimposed on this STM image. (b) *Schematic representation of the superposition of the grid above the incomplete P layer (T1 termination).* Half of the grid nodes are situated in between the small pentagons. Inset: the white circle indicates the preferential adsorption site of Pb atoms as deduced from (a). (c) *STM image* ( $11 \times 6 \text{ nm}^2$ ) of the clean  $\text{Al}_{13}\text{Co}_4$  surface. The arrows indicate that extra atoms (intrinsic or impurities) remaining after the standard surface preparation nucleate preferentially in the middle of bipentagonal motifs, i.e. as for Pb adatoms.

pear as bright protrusions in the images are located on top of the bipentagonal motifs. This is also supported by the distances measured between individual atoms which correspond to multiples of the lattice parameters along  $b$  and  $c$  axis. Hence, Pb atoms deposited on this substrate are not arranged randomly.

The streakiness associated with Fig.5.2(c-d) is related to the motion of adatom on the surface at 300 K. The grey arrows on both STM images point to a stable adsorbate over the scanning period. The white arrows demonstrate that an empty site is populated over few minutes. At this stage, we cannot rule out that this effect is related to a tip induced motion. To identify the precise nucleation site of Pb atoms on the bipentagonal motifs, a two dimensional grid has been superimposed on the T1 termination (Fig.5.3(a)). The lines of the grid follow the diagonal of the  $\text{Al}_{13}\text{Co}_4$  unit cell. Half of the grid vertices are located exactly in between the remaining two small pentagons forming the bipentagonal motifs (see the detailed arrangement on Fig.5.3(b)). The brightest features corresponding to individual Pb atoms sit systematically on

the grid nodes and above these bipentagonal motifs. The other set of vertices located above surface vacancies (dark patches) is not occupied by Pb atoms at this low coverage. A comparison between Fig.5.3(a) and (b) suggests that Pb atoms are trapped in the hollow sites present between the two pentagons of the bipentagonal features (see inset of Fig.5.3(b)). Interestingly, the same site, as indicated by the arrows on Fig.5.3(c), is sometimes decorated after a standard surface preparation by “extra” atoms either intrinsic to the materials or regarded as impurities (although undetectable by XPS). Thus, it is reasonable to consider these hollow sites as particularly reactive on the  $\text{Al}_{13}\text{Co}_4$  (100) surface.

For 0.38 MLE coverage, the area which encompasses both the Pb structure and the remaining T2 layer is estimated at 59.9 % of the total area of the STM image shown on Fig.5.4(a). It has to be mentioned that the amount of T2 considerably differs between terraces (see Chapter 2). The  $Z_{RMS}$  roughness calculated from the mixed layer ( $T2 + \text{Pb}$  structures) is estimated at  $0.46 \pm 0.06 \text{ \AA}$ . At this coverage, the FFT from the mixed layer only is similar

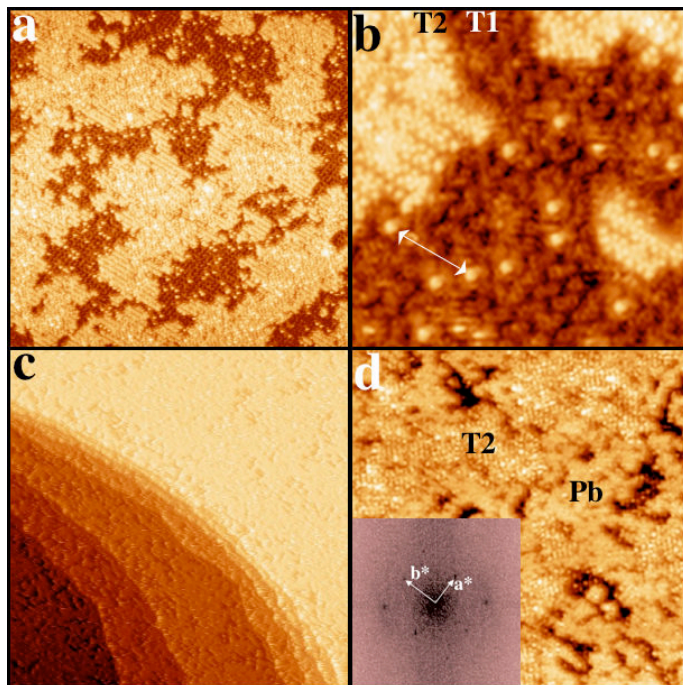


Figure 5.4: (a) Large STM image ( $100 \times 100 \text{ nm}^2$ ) recorded after the deposition of 0.38 MLE of Pb at 300 K on the  $\text{Al}_{13}\text{Co}_4$  substrate. (b) High resolution STM image ( $20 \times 20 \text{ nm}^2$ ) showing the surface structure after deposition of 0.38 MLE. (c) Large STM image ( $200 \times 200 \text{ nm}^2$ ) recorded after 0.75 MLE Pb deposition. (d) STM image ( $80 \times 80 \text{ nm}^2$ ) recorded after 0.75 MLE Pb deposition. The T2 termination and the Pb region forming the first monolayer are indicated by “T2” and “Pb”. Inset: FFT calculated from the STM image in (d).

to that observed from the clean surface. In addition to the presence of both surface terminations and individual Pb adatoms (see Fig.5.4(a)), the terraces are covered with row structure in the [010] direction. In addition to the  $T1$  and  $T2$  type surface terminations and individual Pb atoms there are regions exhibiting a pronounced row structure. These region have an apparent height which is very similar to the  $T2$  termination, but can be well distinguished from the later by their specific adatom arrangement along a specific direction on the substrate. These latter correspond to arrangement of adsorbates along a specific direction of the substrate. As presented on the high resolution STM image on Fig.5.4(b), this alignment corresponds to the [010] direction, i.e the closest in-plane distance between bipentagonal motifs ( $b$  axis). The majority of the Pb rows originate first from the edges of the fractioned  $T2$  area. They can also spontaneously grow from the middle of the  $T1$  layer as displayed on the bottom right hand corner of Fig.5.4(b). The average height difference between the substrate ( $T1$ ) and the Pb structure is measured at  $2.1 \pm 0.1$  Å. Upon further exposure (0.75 MLE), the first Pb monolayer is almost completed (Fig.5.4(c)) with still no sign of the onset of the second layer growth. Regardless of their lateral width, all terraces are equivalently populated. Using higher magnification STM images, a clear difference persists between  $T2$  and the Pb structures. Despite being well-ordered as evident from the previous LEED analysis, the resolution on the Pb region is lower than on the  $T2$  patches at this coverage. The FFT at this coverage (inset Fig.5.4(d)) reveals an orthorhombic unit cells with dimensions in agreement with those measured from the clean (100) surface of  $\text{Al}_{13}\text{Co}_4$  crystal.

Figure 5.5(a) presents two terraces separated by a single step height after 1.5 MLE Pb exposure. The surface is now well-covered by a thin (non-continuous) Pb monolayer. A closer inspection reveals that some structural defects (vacancy like depressions for instance) remain within the deposited film. The pores observed at this coverage represent  $4.0 \pm 0.4$  % of the total scanned area. As shown by the arrow on Fig.5.5(b), patches of  $T2$  can still be easily identified. The quality of the FFT calculated from this image (Fig.5.5(c)) has improved as indicated by an increase in the number of sharp spots. This is explained by a better image contrast upon completion of the monolayer. The lattice parameters calculated from the orthorhombic structure obtained in this FFT is in perfect agreement with the LEED measurements which suggest a pseudomorphic Pb growth mode. Within the Pb region, the STM resolution allows us to distinguish parallel atomic lines spaced by  $\sim 15$  Å along the [001] direction, i.e. comparable to the lattice parameter  $c$ . These latter do not rotate from one terrace to the next as they correspond to the row structures aligned along [010] direction observed at submonolayer coverage. For 3 MLE exposure, the surface topography (Fig.5.5(d)) consists of a terrace-step like morphology with a step height of  $4.12 \pm 0.20$  Å ( $\simeq a/2$ ). Each terrace is characterized by the presence of parallel lines separated by  $9.96 \pm 1.00$  Å which is equivalent to half of the diagonal of the surface unit mesh. If one interconnects the bipentagonal motifs pointing in the same direction using parallel lines, the

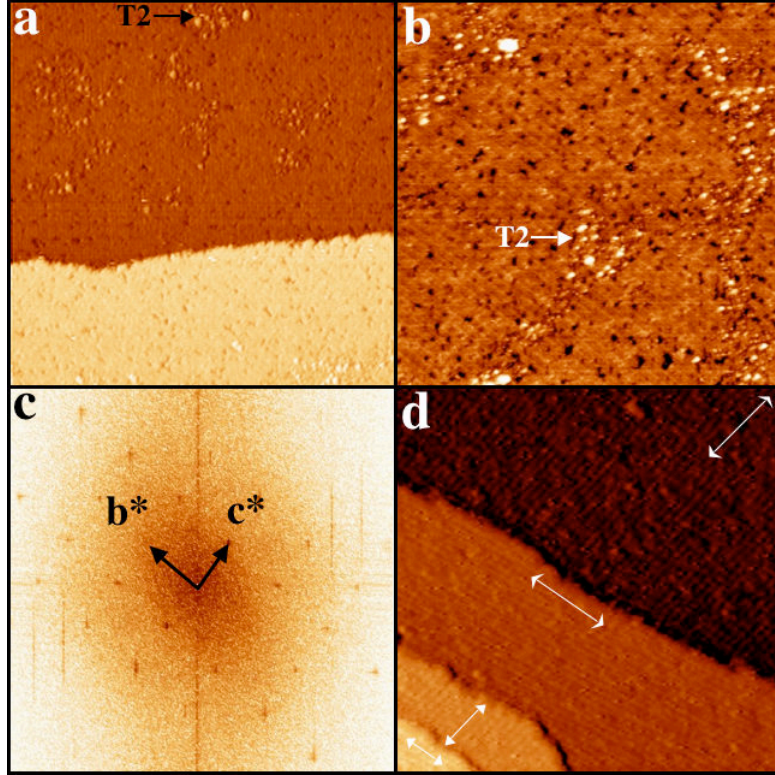


Figure 5.5: (a) STM image ( $167 \times 167 \text{ nm}^2$ ) recorded after 1.5 MLE Pb exposure at  $300 \text{ K}$  on the  $\text{Al}_{13}\text{Co}_4$  substrate. (b) STM image ( $35 \times 35 \text{ nm}^2$ ) showing a complete layer composed of the Pb structure and T2 termination. (c) FFT calculated from the STM image presented in the panel (b). (d) STM image ( $50 \times 50 \text{ nm}^2$ ) recorded after 3 MLE Pb deposition at  $300 \text{ K}$  on the  $\text{Al}_{13}\text{Co}_4$  substrate. As indicated by the arrows, the parallel lines present on each terrace rotated successively by  $80^\circ$ .

spacing between these latter is  $\sim 10 \text{ \AA}$ , hence explaining the above measurements. These atomic lines are rotated by  $80^\circ$  on successive terraces. In the sub 1 MLE case, the alignment of the rows follows the structural sequence of the bi-pentagonal motives and therefore the surface unit cell, which is the same for successive terraces. In the case of the coverage higher than 1.5 MLE, the alignment of the line follows the elongation of the bi-pentagonal motives, which rotates by 80 degrees from terrace to terrace. Different tunneling conditions combined with a denser film (less depressions at 3 MLE exposure) could explain the emphasis of these rotating lines on the STM image at the expense of those visible on Fig.5.5(b). Indeed, the bipentagonal motifs present on the clean surface rotate with an identical amount on adjacent terraces separated by a single step height [70]. Hence, this implies that the surface reconstruction, if any, of the underneath substrate must be minimum. At this stage, the FFT reveals an orthorhombic unit cells with dimensions very close to that observed for clean the  $\text{Al}_{13}\text{Co}_4$  surface. The  $Z_{rms}$  for this coverage is about

$0.22 \pm 0.03$  Å. The investigation of all the STM images recorded for this coverage reveals a total absence of individual adatoms or Pb islands forming the second monolayer.

### 5.3.1.3 X-ray photoelectron spectroscopy analysis

To fully characterise the growth mode of Pb adatoms on the Al<sub>13</sub>Co<sub>4</sub> (100) surface, XPS measurements have been carried out for each exposure. The area ratio of the adlayer (Pb 4f) to the substrate signal (Al 2p) is plotted on Fig.5.6(a) as a function of Pb coverage. While the substrate signal (Al 2p) is steadily decreasing, the adlayer signal (Pb 4f) increases continuously up to 1 MLE. Above this exposure, the rate of increase is reduced but remains almost linear up to the highest Pb depositions. A similar behavior has been observed for the layer-by-layer growth of Pb on the Al(111) surface [89]. However, STM images clearly show here the absence of the growth of a second ordered layer. Only one complete pseudomorphic Pb monolayer has been deposited up to the highest Pb exposure used in our study. Large (2 – 8 nm high and 50 – 60 nm wide) and disordered Pb mounds have been frequently observed in the STM images (see Fig.5.6(b)). These features are thought to correspond to agglomeration, probably at defect sites, of Pb adatoms diffusing across the terraces when the first layer has been completed. The growth of such Pb clusters will be favored upon additional Pb exposure. Consequently, the Pb/Al area ratio signal should continuously increase as observed by XPS measurements (Fig.5.6(a)). It clearly indicates that the sticking of Pb on the pseudomorphic Pb monolayer decreases above 1 MLE exposure. Upon further deposition, the lateral growth of these Pb mounds should eventually cover a larger part of the

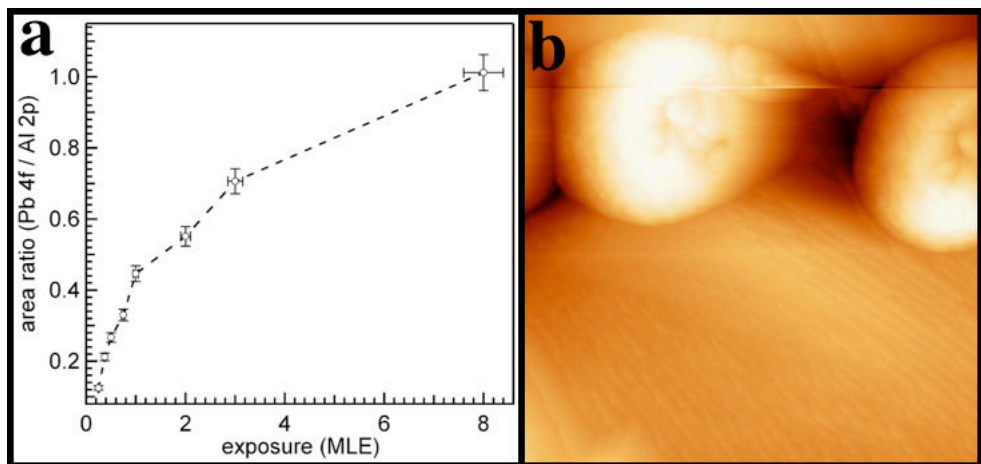


Figure 5.6: (a) The area under the peak ratio for Pb 4f to Al 2p as a function of the adsorbate coverage. The uncertainty in the coverage and area ratio is estimated around  $\pm 5\%$ . (b) STM image ( $167 \times 167$  nm $^2$ ) showing Pb mounds on the substrate after 3 MLE Pb exposure.

films. This would lead to an increase in the LEED background (see Fig.5.1(f)).

Fig.5.7(a) shows the evolution of the Al 2p core level spectra as a function of Pb exposure. All the spectra have been normalized to have the same peak height which enables to track any changes in the core level lineshape with increasing coverage. The binding energy (BE) of Al 2p measured at 72.9 eV is not modified during the deposition. Similarly, the core level lineshape (broadening) of Al 2p is not altered upon Pb dosage. The Pb 4f core level spectra as a function of Pb coverage is presented on Figure 5.7 (b). Up to 1 MLE, the Pb 4f core level shifts towards higher binding energy. Its BE equal to  $136.35 \pm 0.05$  eV for the lowest coverage (0.25 MLE) reaches finally  $136.55 \pm 0.05$  eV with the completion of the monolayer. For coverages  $\geq 1$  MLE, the Pb 4f core level position is not shifted ( $= 136.55$  eV)<sup>1</sup> and the Pb 4f core level lineshape is not modified either.

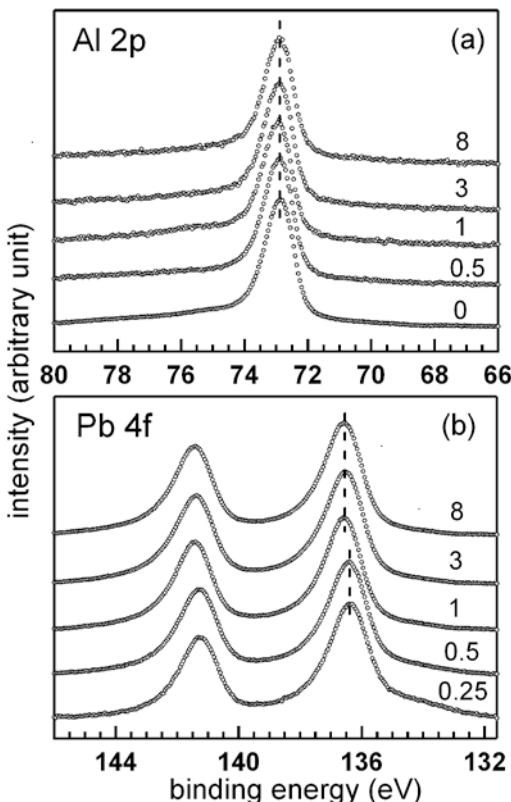


Figure 5.7: (a) The Al 2p core level spectra as a function of Pb exposure on the  $\text{Al}_{13}\text{Co}_4$  (100) surface. (b) The Pb 4f core level spectra as a function of Pb exposure. In each case, the spectra have been normalized to have the same peak height and staggered along the vertical axis. The Pb exposures are indicated in terms of MLE on the right hand side of the spectra.

---

<sup>1</sup>This value corresponds to the bulk Pb 4f.

### 5.3.2 Pb deposition at 573 K

To improve the structural ordering within the Pb thin film, the  $\text{Al}_{13}\text{Co}_4$  sample has been kept at 573 K during the 1 MLE deposition. The corresponding LEED pattern (see Fig.5.8(a)) is consistent with a pseudomorphic growth mode of Pb adatoms. The lattice parameter ratio ( $(\frac{c}{b})_{\text{measured}} = 1.154$ ) extracted from this LEED pattern is close, within the accuracy of our measurements, to those reported by Grin *et al.* ( $(\frac{c}{b})_{\text{bulk}} = 1.171$ ). Compared to room temperature deposition (see Fig.5.1(b)), there is a remarkable enhancement in the quality of the diffraction pattern. This higher temperature deposition does not change the growth mode of the adsorbates. As shown on Fig.5.8(d), terraces are now completely covered by a Pb thin film, with no sign of a second layer growth. Here, the widths of the terraces prohibit the presence of the T2 terminations [70]. The structural quality of the film is indeed improved as revealed by the reduced percentage of pores within the monolayer Fig.5.8(c) and the relatively low roughness, with  $Z_{\text{rms}}$  measured at  $0.16 \pm 0.04 \text{ \AA}$ . This STM image exhibits fine structural details distributed periodically on both terraces. To determine the lattice parameters of this monolayer, a FFT has

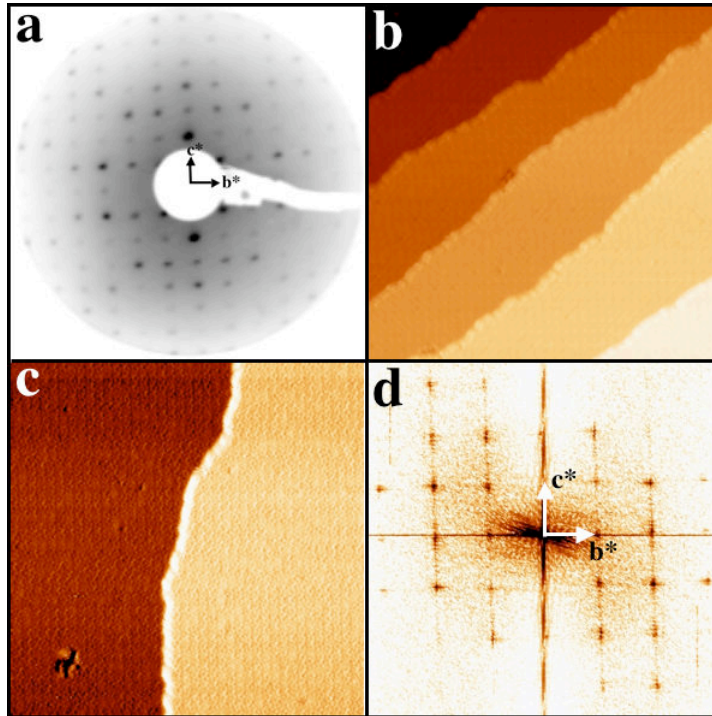


Figure 5.8: 1 MLE Pb has been deposited at 573 K on the  $\text{Al}_{13}\text{Co}_4$  substrate. (a) LEED pattern (inverted for clarity) recorded at 65 eV beam energy. (b) STM image ( $50 \times 50 \text{ nm}^2$ ) showing a step-terrace morphology. (c) STM image ( $50 \times 50 \text{ nm}^2$ ) showing two terraces which exhibit fine structural details. (d) FFT calculated from the STM image presented in the (c) panel.

been calculated from Fig.5.8(c). The size of the orthorhombic unit cell has been measured with  $b = 12.59 \pm 0.50 \text{ \AA}$  and  $c = 14.76 \pm 0.70 \text{ \AA}$ , hence  $(\frac{c}{b}) = 1.172$ . From the LEED and the FFT analysis, it appears that the Pb thin film has adopted the underneath template structure. Higher resolution STM images are now required to investigate the local atomic structure of the adsorbates.

Fig.5.9(a) corresponds to an atomically resolved STM image recorded from one region of Fig.5.8(c). The surface plane is mainly composed of pentagonal atomic arrangements distributed on an periodic network. Two sets of pentagons either pointing up or down with respect to the [001] direction can be defined. The unit cell dimensions of this structure ( $b = 12.72 \pm 0.50 \text{ \AA}$  and  $c = 14.58 \pm 0.70 \text{ \AA}$ ) match those of the clean substrate. As seen from one unit cell outlined in the inset of Fig.5.9(a), the pentagons are not regular in shape regardless of their orientation. In fact, their edge lengths vary between 4.1 and 6.1  $\text{\AA}$ , with a mean value estimated at  $4.83 \pm 1.00 \text{ \AA}$ . Interestingly, the ratio of this average value to the mean edge lengths (2.88  $\text{\AA}$ ) of the pentagons forming the bipentagonal motif on the clean surface is equal to  $\sim 1.67$ , i.e. very close to the golden mean  $\tau (= 1.618\dots)$ . The film structure has been analyzed using a tiling approach. Each bright contrast within one unit cell has been associated with a single Pb adatom. The resulting arrangement has been distributed periodically across the surface plane (Fig.5.9(b)). Connecting

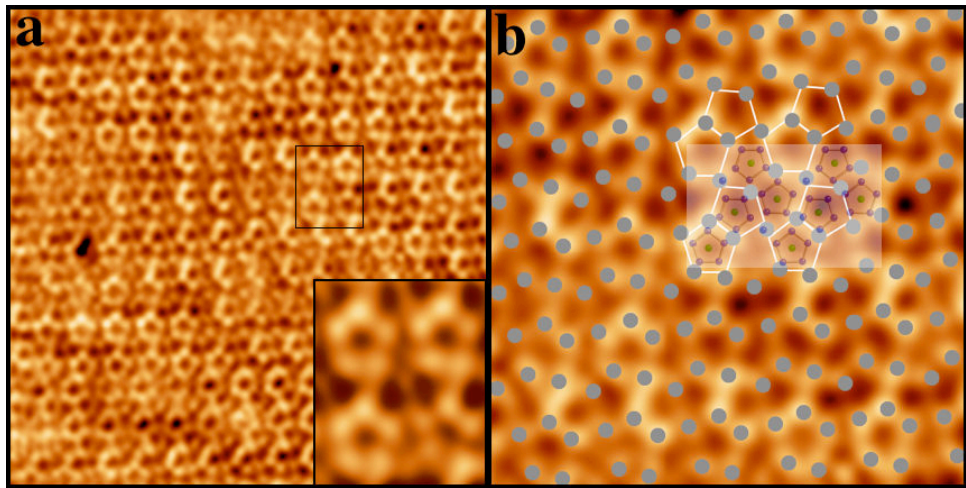


Figure 5.9: A complete Pb monolayer has been deposited at 573 K on the  $\text{Al}_{13}\text{Co}_4$  substrate. (a) The high resolution STM image ( $18 \times 18 \text{ nm}^2$ ) indicate that the structure is composed of pentagonal features. Inset: close-up view ( $2.6 \times 3.2 \text{ nm}^2$ ) of the rectangle displayed on image (a). (b) Tiling using irregular pentagons of a region ( $7.25 \times 7.25 \text{ nm}^2$ ) extracted from the STM image presented in (a). The surface structure can be described as interconnected bipentagonal motifs (see white pentagons). To analyse the monolayer formed, the structure of the P plan (bi-pentagonal motifs pointing in two directions and glue atoms) has been superimposed on the Pb structure.

several points of the tiling leads to an interpretation of the thin film structure as composed of connected bipentagonal motifs. This arrangement is obviously closely related to the clean surface which consists of smaller bi-pentagonal motifs (see Fig.3.3, Chapter 2). The structure of the puckered P layer has been superimposed on the Pb layer. The bi-pentagonal motifs are located inside the large bi-pentagonal formed by the Pb atoms. The glue atoms of the puckered P plan coincide with the Pb atoms shared between the large bi-pentagonal (white pentagons in Fig.5.9(b)). Further experimental studies (dynamical LEED I-V for instance) coupled with simulated STM images (generated from *ab initio* calculations) are necessary to validate the proposed model. Thus, the bipentagonal motifs present on the bare surface must also play a crucial part in the formation of the Pb monolayer at 573 K. The LEED and the STM analysis demonstrate that the growth of Pb adatoms on the Al<sub>13</sub>Co<sub>4</sub> substrate is pseudomorphic from 300 K to 573 K.

## 5.4 Structural investigation of Pb adsorption on the T-Al<sub>3</sub>(Mn, Pd) (010) surface

### 5.4.1 Deposition at 300 K

#### 5.4.1.1 Low energy electron diffraction analysis

As for the Pb/Al<sub>13</sub>Co<sub>4</sub> system, the LEED patterns recorded for different Pb exposures at 300 K on the T-Al<sub>3</sub>(Mn, Pd) (010) surface exhibit an orthorhombic unit cell. Figure 5.10 presents a comparison between the diffraction patterns measured from the clean surface and after deposition of 4 and 8 MLE respectively. The size of the unit cell measured from the LEED patterns for different coverage and for several beam energy is equal to  $a = 14.85 \pm 0.70$  Å and  $c = 12.70 \pm 0.30$  Å, with the experimental ratio  $(\frac{a}{c})_{LEED} = 1.1693$  similar to the one calculated from the bulk model ( $(\frac{a}{c})_{bulk} = 1.1685$ ) [68]. The *p-10f* symmetry observed on the clean surface is preserved even at the highest Pb exposures (Fig.5.10). These measurements suggest that Pb atoms grow pseudomorphically on the T-Al<sub>3</sub>(Mn, Pd) (010) surface.

#### 5.4.1.2 Scanning tunnelling microscopy analysis

The growth mode of Pb atoms at room temperatures on the T-Al<sub>3</sub>(Mn, Pd) surface is now investigated using STM technique. Figure 5.11 presents several STM images for depositions ranging from 0.1 to 7 MLE of Pb. For the initial exposure (0.1 MLE), the substrate structure is still resolved (Fig.5.11(a)). Due to the bias dependency and the structural imperfections inherent to the T-Al<sub>3</sub>(Mn, Pd) surface (see Chapter 3), it has not been possible to identify if a preferential nucleation site exists at the initial stage of Pb adsorption. At submonolayer regime, the average height of Pb islands is measured at  $1.76 \pm 0.10$  Å. The step height measurements ( $6.5 \pm 0.2$  Å) are in agreement with

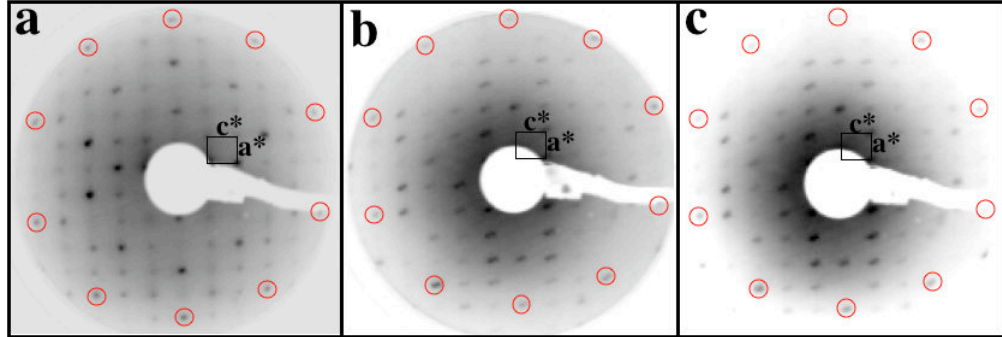


Figure 5.10: *LEED patterns recorded at 55 eV beam energy from the T-Al<sub>3</sub>(Mn, Pd) (010) surface (inverted for clarity). (a) clean surface , (b) after deposition of 4 MLE and (c) 8 MLE of Pb adatoms at 300 K.*

those reported for the clean T-Al<sub>3</sub>(Mn, Pd) (010) surface. With increasing coverage, the individual Pb islands remain irregular in shape. With the island distribution observed at low coverage, the mobility of Pb adatoms appears much more reduced here than on the Al<sub>13</sub>Co<sub>4</sub> approximant surface where lines of adsorbates start to propagate rapidly along the [010] direction. After 1 MLE Pb exposure (Fig.5.11(c)), the first monolayer stays incomplete with almost 25 % of the surface uncovered.

Upon further adsorption, the growth mode is not altered and proceeds in an apparent layer-by-layer manner. Due to a higher corrugation of the film (interconnected islands), the resulting STM images have a rather limited resolution. For 4 MLE exposure, the height measured of the Pb islands at this coverage has increased to  $2.15 \pm 0.10$  Å. Nevertheless, the adatom islands have kept their random shape (Fig.5.11(d-f)). For the highest deposition carried out in this study (7 MLE), the FFT (not shown here) still exhibits an orthorhombic unit mesh. It is not trivial to assess the island density versus the deposition for the following reasons. From the successive depositions performed on the T-Al<sub>3</sub>(Mn, Pd) surface at room temperature, we clearly do not adsorb the expected Pb amount as seen by STM. This discrepancy could be partly explained by a reduction of the adsorbate sticking coefficient upon the completion of the first monolayer. Such effects have already been reported when dosing Pb atoms on other complex metallic alloy systems [88,92]. To the contrary of the previous studies and of the Pb/Al<sub>13</sub>Co<sub>4</sub> system, the sticking coefficient does not vanish completely here. Using STM measurements, the fractional area covered with successive Pb depositions has been estimated as a function of the exposure (Fig.5.12). Due to the variation obtained in the measurements, additional layers can clearly be adsorbed on the first Pb monolayer. However, an uncertainty persists on the precise number of deposited Pb layers. Once the monolayer has been almost completed, exposing the surface to an additional 3.0 MLE leads to an area covered by islands around 67 % (Fig.5.12). This is highly similar, within the accuracy of the measurements

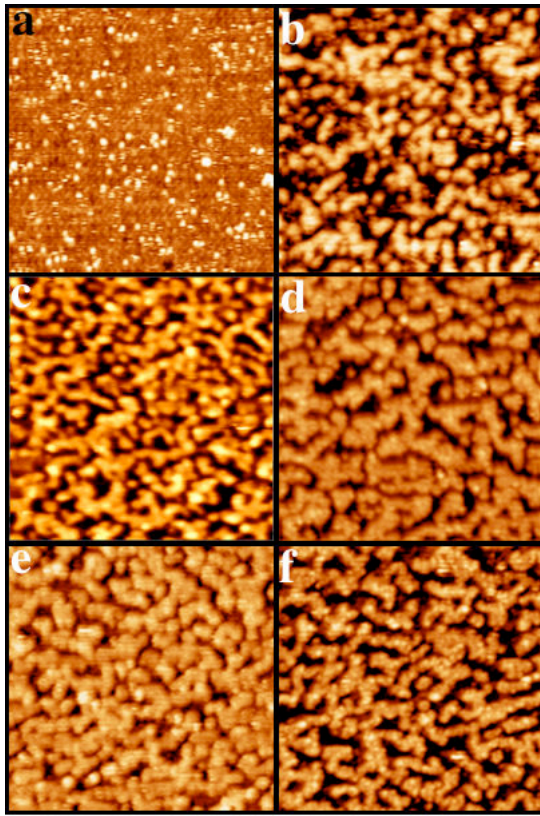


Figure 5.11:  $50 \times 50 \text{ nm}^2$  STM images recorded on the (010) surface of the  $T\text{-Al}_3(\text{Mn, Pd})$  crystal (a) for 0.1 MLE, (b) for 0.5 MLE, (c) for 1 MLE, (d) for 4 MLE, (e) for 5.5 MLE and (f) for 7 MLE of Pb adsorbed at room temperature.

( $\pm 10\%$ ), to the fractional area determined for 1 MLE coverage. Adding another 1.5 MLE brings the measured area to about 74 %, i.e almost unchanged. Interestingly, another exposure to 1.5 MLE (7 MLE in total) brings the Pb covered area to 55 %. It is also interesting to notice that the island size remains the same, which means that no coarsening takes place. Consequently, additional compositional measurements are necessary to determine the precise surface composition, i.e. the number of Pb layers and the rate of deposition.

#### 5.4.1.3 X-ray photoelectron spectroscopy (XPS) study

To further characterize the adsorbate growth mode, XPS measurements have been carried out for each deposition stage. Fig.5.13 presents the area ratio of the adlayer (Pb 4f) to the substrate signal (Al 2p) as a function of Pb coverage. While the substrate signal (Al 2p) decreases, the adlayer signal (Pb 4f) increase rapidly up to 1 MLE. For higher Pb depositions, the rate of increase of the area ratio is considerably reduced but retains its linear character.

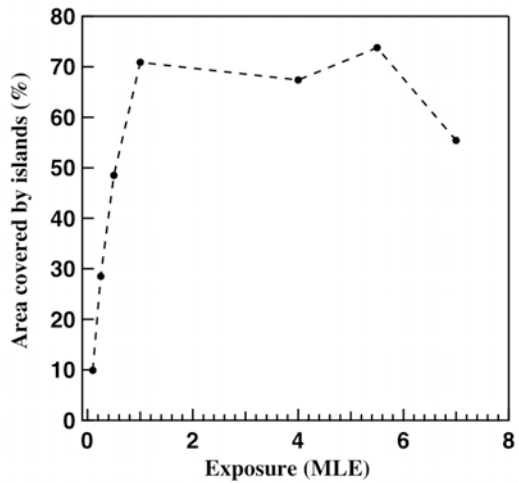


Figure 5.12: *STM measurements of the fractional area covered by successive Pb depositions at 300 K on the T-Al<sub>3</sub>(Mn, Pd) (010) surface.*

Fig.5.14 shows the Al 2p and the Pb 4f core level spectra recorded as a function of Pb coverage on the T-Al<sub>3</sub>(Mn, Pd) surface. All the spectra have been normalized to have the same peak height which enables to track any changes in the core level lineshape with increasing coverage. There is no

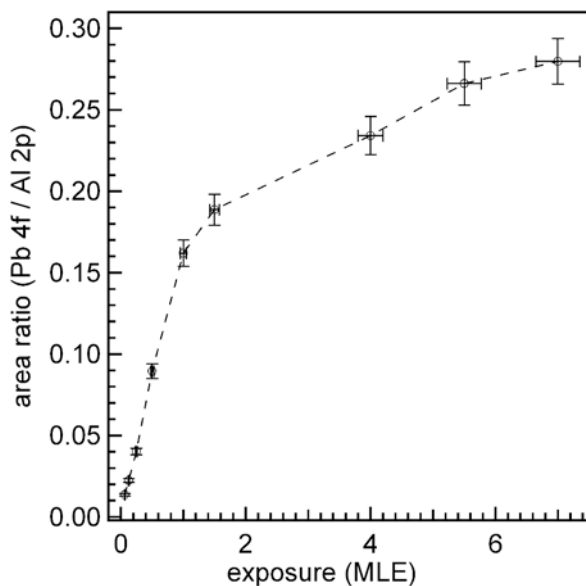


Figure 5.13: *The area under the peak ratio for Pb 4f to Al 2p as a function of Pb coverage. The uncertainty (indicated by the error bars) in the coverage and area ratio is estimated at  $\pm 5\%$ .*

apparent shift in the binding energy (BE) and no lineshape broadening of the Al 2p core level upon Pb exposure. However, the BE of Pb 4f shifts towards the higher BE side as the Pb coverage is increased up to 1 MLE. The overall difference in the Pb 4f binding energy between the sub-monolayer and 1 MLE coverage is  $0.1 \pm 0.05$  eV. For coverages  $\geq 1$  MLE, there is no shift or broadening associated with the Pb 4f core level. These observations are identical to those made on the Pb/Al<sub>13</sub>Co<sub>4</sub> system.

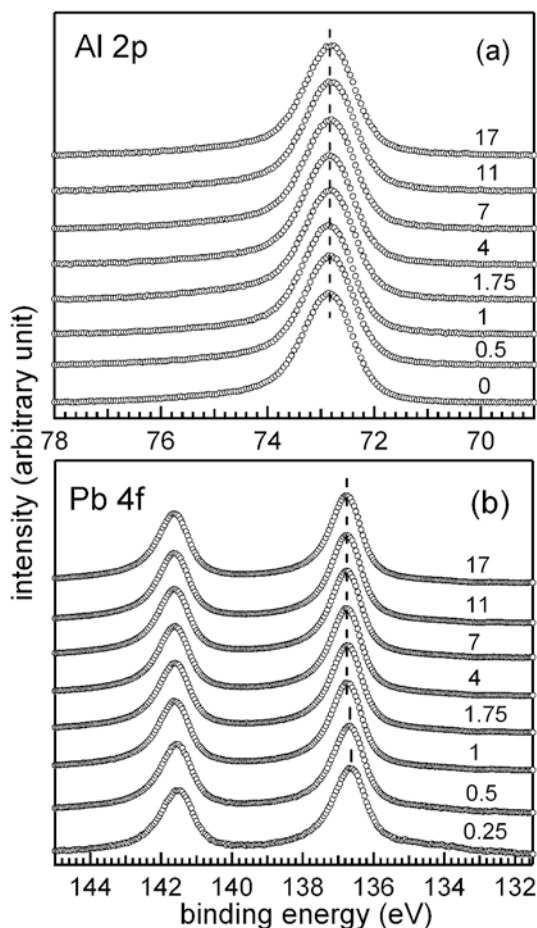


Figure 5.14: (a) (a) Al 2p core level spectra as a function of Pb exposure on the T-Al<sub>3</sub>(Mn, Pd) (010) surface. (b) Pb 4f core level spectra as a function of Pb coverage. In each case, the spectra have been normalized to have the same peak height and staggered along the vertical axis. The Pb coverages are indicated in terms of MLE on the right hand side of the spectra.

The thickness of Pb adlayers for different deposition times have been determined from the variation of the Pb 4f and substrate related Al 2p core level intensities. These spectra are recorded under similar conditions, i.e. comparable analyzer settings, X-ray source intensity and sample position. The photoelec-

trons suffer inelastic loss of kinetic energy by plasmon excitations, and electron-electron scattering for instance. Hence, for a layer-by-layer growth, the intensity of the substrate signal ( $I_S$ ) after  $n$  ML deposition is given by [225, 226]

$$I_S = I_\infty^S [\exp(-nd/\lambda \cos\theta)] \quad (5.1)$$

where  $I_\infty^S$  is the substrate signal without adsorption layer,  $d$  is the thickness of each monolayer and  $\lambda$  is the inelastic mean free path of the electrons. The adlayer signal ( $I_A$ ) is given by

$$I_A = I_\infty^A [1 - \exp(-nd/\lambda \cos\theta)] \quad (5.2)$$

where  $I_\infty^A$  is the intensity for the bulk adlayer material.  $I_S$  and  $I_A$  are extracted by calculating the area under the Al 2p and Pb 4f peaks, which have been MgK $\alpha_{3,4}$  X-ray satellite subtracted and inelastic background subtracted using the Tougaard method [227]. The above equations have been modified and generalized for a substrate covered by  $n$  integral ( $\geq 1$  ML) and  $z$  fractional ( $< 1$  ML) to be [225, 226, 228]:

$$I_S = I_\infty^S [(1 - z)\exp(-n/\lambda_S \cos\theta) + z\exp(-(n + 1)/\lambda_S \cos\theta)] \quad (5.3)$$

$$I_A = I_\infty^A [z(1 - \exp(-(n + 1)/\lambda_A \cos\theta)) + (1 - z)(1 - \exp(-n/\lambda_A \cos\theta))] \quad (5.4)$$

where  $I_\infty^S$  and  $I_\infty^A$  are taken to be the photoionization cross-sections of Al 2p and Pb 4f core levels respectively [229].  $\lambda_S$  and  $\lambda_A$  are the inelastic mean free paths of the Al 2p and Pb 4f photoelectrons respectively [225].  $\theta$  is the emission angle of the photoelectrons with respect to the surface normal, which is 45° in our case. Equations 5.3 and 5.4 have been used to calculate the coverages. Here, a monolayer is defined as a closed packed layer covering the substrate completely. We have used the similar procedure to calculate the adlayer coverages for the growth of metal adlayers on quasicrystalline and metal surfaces [228, 230–232]. The results demonstrate that the sticking coefficient is considerably reduced above 1 ML. After 7 MLE Pb exposure, the calculations indicate one complete first ML plus 0.4 ML coverage in the second layer. The presence of a sharp LEED pattern for 8 MLE exposure is then expected as it corresponds to a coverage below 2 ML, with the first monolayer being pseudomorphic.

### 5.4.2 Deposition at 573 K

The adsorption of Pb adatoms has been performed on the T-Al<sub>3</sub>(Mn, Pd) surface while keeping the substrate at 573 K. The corresponding LEED patterns recorded for 1 MLE Pb exposure reveal a sharp orthorhombic unit cell with a *p*-10-*f* symmetry (outlined by circles on Fig.5.15). The unit cell dimensions measured from the LEED patterns ( $a = 14.86 \pm 0.30$  Å and  $c = 12.43 \pm 0.30$  Å)

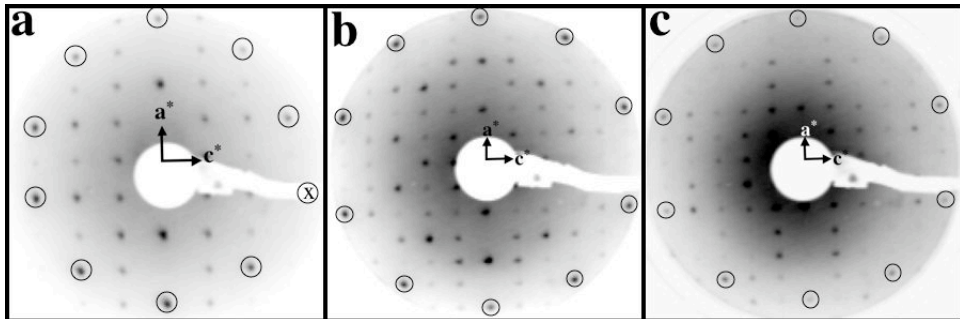


Figure 5.15: (a,b) 25 eV and 50 eV LEED patterns recorded after the deposition of 1 MLE and (c) 2 MLE (50 eV) at 573 K. The 10 intense spots forming a decagonal ring are outlined. The orthorhombic unit cell is also indicated by the reciprocal lattice vectors.

match the lattice parameters of the surface prior to dosing. This indicates that the Pb adlayer adopts the structure of the underlying substrate under these dosing conditions. Pseudo-10-*f* symmetric diffraction patterns of lower quality have also been observed for 2 MLE exposure (Fig.5.15(c)).

Under the same adsorption conditions, STM images (Fig.5.16(a-b)) reveal the formation of a thin Pb film on the T-Al<sub>3</sub>(Mn, Pd) terraces. The pattern obtained from the FFT (Fig.5.16(d)) is consistent with the LEED results, i.e. with an orthorhombic structure of lattice parameters equal to  $a = 15.00 \pm 0.60$  Å and  $c = 12.95 \pm 0.51$  Å. An atomically resolved STM image of the film is presented on Fig.5.16(b). The roughness measured as  $Z_{rms}$  (0.4 Å) across the terrace is relatively high compared to the clean surface (0.1 – 0.2 Å). The surface is characterized by the presence of points like depressions arranged as discontinuous vertical lines. The latter, of depth equal to  $1.2 \pm 0.3$  Å, correspond to the pentagonal hollow sites or “dark stars” present on the clean T-Al<sub>3</sub>(Mn, Pd) (010) surface (see Chapter 3). The remaining part of the STM image is composed of regularly ordered protrusions (brightest contrasts) and of two types of pentagons. Several of these pentagonal motifs are outlined on Fig.5.16(b-c). The edge lengths of the smallest and largest pentagons are measured at  $3.17 \pm 0.68$  Å and  $4.77 \pm 0.55$  Å, respectively. From their dimensions and their distributions in the vicinity of holes, we believe that they correspond to the pentagons arranged in a zig-zag manner along [100] direction on the clean T-Al<sub>3</sub>(Mn, Pd) surface. Using a thresholding image analysis tool, we estimate the Pb coverage to  $0.6 \pm 0.1$  ML (coverage estimated from XPS measurements equal to 0.58 ML) for 1 MLE exposure. An FFT calculated from an STM image with only the Pb adatoms selected is shown on Fig.5.16(d). The pattern is consistent with a pseudomorph growth mode of Pb adatoms. While pseudomorph, the growth mode of Pb atoms on the T-Al<sub>3</sub>(Mn, Pd) (010) surface is different at 300 and 573 K. At room temperature, the same exposure gives a higher coverage. The adsorbates form irregularly shaped islands which interconnected to complete the monolayer. In the high temperature ad-

sorption regime, the quality of the LEED pattern is greatly enhanced and so is the resolution on STM images. The higher Pb mobility on the surface leads to a better ordered structure.

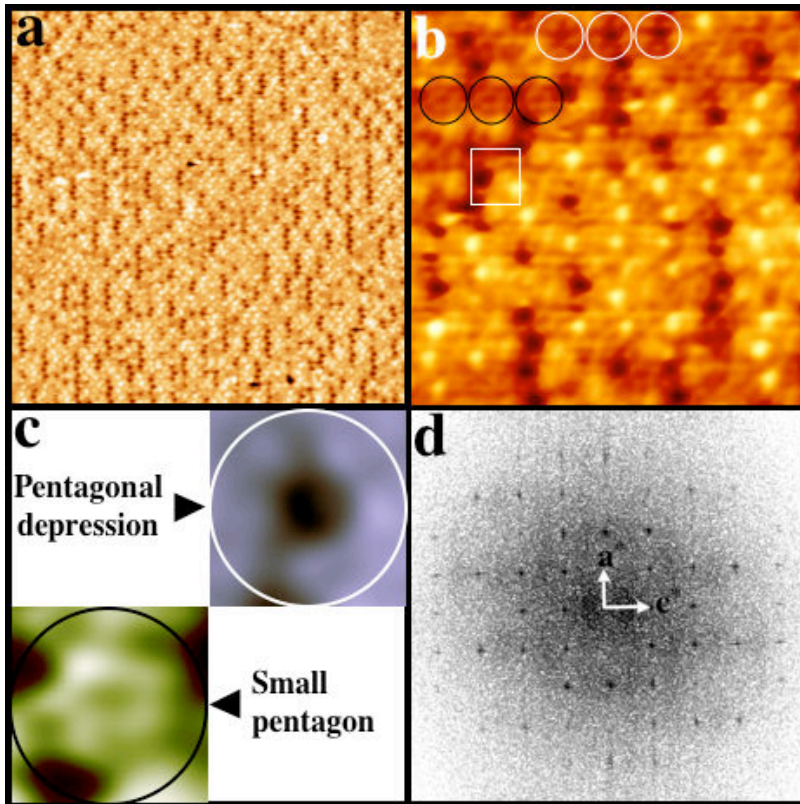


Figure 5.16: (a)  $48 \times 48 \text{ nm}^2$  STM image recorded on one terrace after 1 MLE Pb exposure on the T-Al<sub>3</sub>(Mn, Pd) (010) surface maintained at 573 K. (b) Higher magnification STM image ( $10 \times 10 \text{ nm}^2$ ) where one unit cell has been outlined along with pentagonal depressions (white circles) and small pentagons (black circles). (c) Magnification of a pentagonal depression and a small pentagon. (d) FFT calculated from a STM image ( $23 \times 23 \text{ nm}^2$ ) where only Pb adatoms have been selected using a thresholding image analysis tool.

## 5.5 Discussion

We have characterized the adsorption of Pb atoms on two approximant surfaces. On the Al<sub>13</sub>Co<sub>4</sub> (100) surface, Pb adatoms adsorb initially in hollow sites located in the centre of bipentagonal motifs, i.e. in between neighboring caps of the pentagonal bipyramidal clusters. In time series STM images, jumps of the Pb atoms can be observed indicating their mobility on the surface at sub-monolayer coverage. Interestingly, the adsorbates do not nucleate in surface vacancies present in between bipentagonal motifs within this low coverage

regime. Upon further deposition, we observe the formation of small Pb islands that grow with a row structure preferentially along the [010] direction. The step edges of the remaining *T*2 termination acts also as defect sites for Pb nucleation. Upon the completion of the first monolayer, it is not possible within the deposition flux used in our study to grow a second layer. Both LEED and STM analysis indicate a pseudomorphic growth mode. This adsorption behavior is to compare with previous adsorption works performed on aperiodic surfaces [88,89,92]. A preferential nucleation site has also been identified for Pb adsorption on the *i*-Al-Pd-Mn five-fold surface. It corresponds to equatorially dissected clusters known as *pseudo*-Mackay clusters. The decoration of these unique adsorption sites leads to the formation of pentagonal islands ( $Pb_{10}$ ) dubbed “starfish” and eventually to a quasiperiodic Pb monolayer. Similarly, the surface vacancies (“dark stars”) present across the *i*-Al-Pd-Mn surface terraces do not act as trapped sites for low Pb coverage. On periodic or aperiodic CMA surfaces, the clusters appear to play a crucial part at the initial stages of the nucleation. Their density and inter-distances on terraces may be the decisive parameters to obtain a pseudomorphic monolayer. The Pb mobility seems comparable on approximant and aperiodic surfaces. In addition, the surface relaxation of the quasicrystalline substrate is thought to be minimum upon Pb adsorption [209]. On the Pb monolayer adsorbed on the  $Al_{13}Co_4$  surface, the fine structures which rotate by  $80^\circ$  from successive terraces are directly related to the orientation of the underneath bipentagonal motifs. Hence, it is likely that the same conclusion can be drawn regarding the surface relaxation of the approximant but additional calculation (*ab initio* for instance) would be required to ascertain this point. For the  $Al_{13}Co_4$  surface, it was not possible to grow a second ordered layer once the completion of the first pseudomorphic monolayer has been achieved (vanishing sticking coefficient of Pb above 1 MLE). As mentioned above, this trend is consistent with the sticking behavior of Pb atoms reported on quasicrystalline surfaces [88,89]. The energy position and lineshape (absence of extra component) of the Al 2*p* core level remain unchanged with increasing coverage which suggests a weak interaction between the Pb and Al atoms. This phenomenon is expected considering the bulk immiscibility of Pb and Al [90,91]. A similar behavior of the Al 2*p* peak has been observed in the works of Pb adsorption on quasicrystalline and on the Al(111) surfaces [88,89,92]. The small shift ( $0.2 \pm 0.05$  eV), measured on the Pb 4*f* core level below 1 MLE, may be due to the substrate related initial or final state effects. At sub-monolayer coverages, the Pb 4*f* core-hole may be strongly screened by the Al conduction electrons which could eventually reduce the BE of the Pb 4*f* core level.

For higher temperature deposition, the quality of the LEED patterns is clearly improved which suggests a greater structural ordering within the Pb thin film. This is indeed the case as demonstrated by the atomically resolved STM images. The structure of the film is described by a periodic arrangement of irregular pentagons of average edge lengths equal to  $4.9\text{ \AA}$ . This dimension

is similar to several pentagonal features present within the pseudomorphic Pb films formed on the *i*-Al-Pd-Mn and *d*-Al-Ni-Co [92,209]. The Pb structure can tentatively be understood as connected bipentagonal motifs which are larger than those observed on the clean Al<sub>13</sub>Co<sub>4</sub> surface. Compared the “isolated” Al bipentagonal motifs present on the clean surface, the Pb bipentagons share several common vertices. This is a direct consequence of the larger adsorbate atomic size compared to Al atoms.

The investigation of the Pb adsorption on the T-Al<sub>3</sub>(Mn, Pd) (010) surface reveals several differences with other Pb dosed CMA surfaces. The initial monolayer adopts the substrate structure as confirmed by the orthorhombic LEED pattern and by the FFT calculated from STM images. As explained in Chapter 3, the structural imperfections along with the chemical disorder add to the complexity of analysing the clean T-Al<sub>3</sub>(Mn, Pd) surface. Hence, it has not been possible to identify if a preferential nucleation site exists on this approximant surface. The diffraction pattern is observed even for 8 MLE Pb coverage. Regardless of the adsorbate exposure used in our study, the STM images exhibit the same morphology (similar step height) and a similar distribution of islands across terraces. The sticking coefficient of Pb adatoms on the Al<sub>13</sub>Co<sub>4</sub> and the quasicrystalline surfaces vanishes upon completion of the first monolayer. Once the first monolayer equivalent has been deposited (0.7 ML) on the T-Al<sub>3</sub>(Mn, Pd) surface, we observed the growth of additional layers. However, severe uncertainty persists on the exact numbers of deposited layers as measured using STM images. From the XPS measurements, it appears that the sticking coefficient is considerably reduced above 1 MLE but does not vanish completely. Consequently, the LEED pattern observed for 8 MLE may correspond to a coverage between 1.5 and 2 ML as estimated from the XPS analysis, hence explaining the persistence of a sharp diffraction pattern. The behavior of the Al 2p and Pb 4f core level spectra with increasing coverage stays similar to that observed for the Pb/Al<sub>13</sub>Co<sub>4</sub> system. It indicates that the Pb interacts weakly with the Al-rich T-Al<sub>3</sub>(Mn, Pd) (010) surface. For 573 K deposition, the growth mode is also pseudomorphic as confirmed by the diffraction patterns and the FFT calculated from the Pb adatoms only. A comparison between the LEED patterns and STM images obtained at 300 K and at 573 K indicates a greater ordering of the deposited film for higher temperature deposition. Unlike room temperature experiment, Pb adatoms do not diffuse across terraces to form islands. Among the fine structural details distinguishable on the T-Al<sub>3</sub>(Mn, Pd) (010) surface, pentagonal hollow sites and small pentagons are related to structural motifs present on the clean surface structure. This conclusion is drawn mainly on the pentagon edge length dimensions. For both approximants, the improvement in the structural quality of the films for the high temperature deposition/annealing is related to an increase in the Pb mobility with elevated temperatures.

## 5.6 Conclusions

We have investigated the deposition of the Pb adatoms on the -decagonal  $\text{Al}_{13}\text{Co}_4$  (100) and T- $\text{Al}_3(\text{Mn, Pd})$  (010) surfaces. In both cases, Pb adsorption follows a pseudomorphic growth mode up to one monolayer. There is no sign of intermixing or alloy formation upon Pb dosing. A preferential nucleation site has been identified only on the  $\text{Al}_{13}\text{Co}_4$  (100) surface for the initial stage of adsorption. It corresponds to the centre of bipentagonal motifs. With further dosage, Pb islands show a row structure and preferentially extend preferentially along the [010] direction. This is not the case on the T- $\text{Al}_3(\text{Mn, Pd})$  (010) surface where the growth proceeds with the formation of irregular shaped islands. Above one monolayer, the sticking coefficient of Pb deposited on the  $\text{Al}_{13}\text{Co}_4$  surface vanishes. To the contrary, while drastically reduced on the  $\text{Al}_{13}\text{Co}_4$  (100) surface, it remains sufficient for the growth of additional layers on the T- $\text{Al}_3(\text{Mn, Pd})$  (010) surface. Deposition of the adsorbates at 573 K leads to an enhanced structural ordering within the Pb adlayers. On the  $\text{Al}_{13}\text{Co}_4$  (100) surface, the monolayer can then be described using a tiling based on bipentagonal motifs. The improved ordering is reflected in the quality of the diffraction patterns and of the STM images. Equivalent exposure on the T- $\text{Al}_3(\text{Mn, Pd})$  (010) surface results in a coverage below 1ML. However, the adsorbates adopt the structure of the underneath template as indicated by the calculated FFT and the LEED patterns. Under these conditions, the pentagonal chains and the depressions propagating along the [100] direction of the T- $\text{Al}_3(\text{Mn, Pd})$  (010) surface are still distinguishable.

# Chapter 6

## Copper adsorption on the (100) surface of the Al<sub>13</sub>Co<sub>4</sub> crystal

### 6.1 Introduction

Some properties of CMAs are indeed different compared to usual metallic alloys and to aluminium. As an example, the resistivity values of many CMAs are several orders of magnitude larger than for pure Al, and the temperature coefficient of the resistivity is negative [233]. A characteristic feature of their electronic structure is the existence of a reduced density of states (DOS) in the vicinity of the Fermi level. The origin of this so-called *pseudo*-gap has been interpreted as a Hume-Rothery effect combined with *sp-d* hybridization [120, 234]. These materials are also renowned for their low coefficient of friction, low adhesion and high oxidation resistance compared to their main constituents [52, 123, 235–237]. Hence, most of the CMA based applications rely on the surface properties of these materials and their use as coatings. To understand the origin of these surface phenomena, a lot of effort has been put first into the determination of the surface structures of CMA samples. Recently [238], the icosahedral and decagonal quasicrystal surfaces have been intensively investigated by most of the available surface science techniques applicable on compounds lacking translational symmetry. With the recent growth of centimeter size crystals, the studies have been extended to the surface structures of several approximants [61, 70, 89, 144]. These approximant phases have often been introduced to model the physical and chemical properties of their parent quasicrystal and to perform electronic structure calculations requiring a unit cell [101, 194]. With the relatively well understood atomic structure of the CMA surfaces studied so far, these latter have been used as templates for several adsorption studies. One of the main objectives has been the growth of pseudomorphic single element monolayers (ML) on these complex substrates. This approach should allow us to probe the influence of aperiodicity and “giant” unit cells on the physical and chemical properties independently of the chemical complexity inherent to these alloys. Towards this end, several adsorption experiments have been performed with a large selection of adsorbates. Among the different attempts, the adsorption of Bi, Sb, noble gas, methane

and Pb adatoms on quasicrystal surfaces have successfully led to a pseudo-morphic growth mode [88, 153, 159, 219, 239, 240]. Apart from the quasiperiodic Pb monolayer where a structure related *pseudo*-gap has been measured, information on the physical properties associated with these thin films remain scarce. In the process of forcing quasiperiodicity into the adsorbed overlayers, an one-dimensional aperiodic arrangement of Cu adatoms has been observed on the icosahedral Al-Pd-Mn surface [142]. The growth mode proceeds in a layer-by-layer fashion up to 8 ML at which point 3D islands are obtained [143]. The LEED patterns exhibit ten-fold symmetry with sharp diffraction spots, revealing long-range quasicrystalline order on the Cu layers. The STM images shows for coverage higher than 5 ML atomic rows spaced according to a Fibonacci sequence. Comparable LEED patterns and similar STM images suggest also a one-dimensional aperiodic arrangement of Co adatoms on the 5-fold quasicrystal surface [241]. Additionally, the adsorption of Cu adatoms on the 2-fold *i*-Al-Pd-Mn surface yields to a quasiperiodic structure as confirmed both by STM and LEED techniques [242]. The adsorption of Cu atoms has also been performed on the 5-fold surface of the icosahedral Al-Cu-Fe (alloy isostructural to the *i*-Al-Pd-Mn sample) [243, 244]. For coverages up to 8 ML of Cu, five rotational domains of (110) orientated  $\beta$ -Al(Cu, Fe) phase are observed by LEED and STM. Above this dosage, the LEED patterns are consistent with bulk-like Cu growing with five rotational domains with the [111] axis normal to the surface. As for the *i*-Al-Pd-Mn sample, annealing the 20 ML Cu dosed *i*-Al-Cu-Fe quasicrystal to 573 K leads to the formation of five domains of  $\gamma$ -Al<sub>4</sub>Cu<sub>9</sub> (110) [97, 244]. Interestingly, the formation of the  $\gamma$ -phase approximant as a surface alloy has been also obtained by annealing Al thin films deposited on a Cu(111) surface [245]. For a thick enough coverage (higher than 12 ML) and depending on the annealing temperature chosen, additional phase transformations occur within the near-surface region (see Table 6.1).

Phases	Al( $1 \times 1$ )	$\alpha_{Al}$ -( $2 \times 2$ )	Al <sub>4</sub> Cu <sub>9</sub> (110)	c( $4 \times 2$ )	$\alpha_{Cu}$ -( $1 \times 1$ )
T°(K)	[300-388]	[300-444]	$\geq 444$	[444-615]	$\geq 615$

Table 6.1: *The p*( $2 \times 2$ ) and the *c*( $4 \times 2$ ) superstructures formed on an Al-rich (111) and on a Cu-rich (111) substrate respectively.  $\alpha$ -(Al) and  $\alpha$ -(Cu) are both solid solutions. The  $\gamma$ -phase is the only complex metallic alloy that could be formed using this method [245].

Due to the highly symmetric clusters present within the “giant” unit cells, extra physical length scales in addition to the lattice dimensions are introduced in CMA samples. To investigate the effect of such a complex periodic structure on the growth mode of metals, the adsorption of Cu adatoms will be investigated for the first time on an approximant surface. Depending on the initial coverage and on the annealing treatment, the different surface alloys and the possible surface reconstructions will be characterised using LEED, STM, XPD

and photoemission spectroscopy. One of the main objectives is to investigate if a pseudomorphic growth mode can be achieved on such a complex surface. As reported by Grenet *et al.* [246], a stable icosahedral *i*-Al-Cu-Fe phase has been successfully prepared during the heat treatment of multilayers films of Al/Cu/Fe/Cu/Al deposited at room temperature (RT) on saphire substrates. In a similar manner, the second objective of our study will be to test the possibility of forming a quasiperiodic surface alloy of decagonal type, i.e the *d*-Al-Cu-Co quasicrystal. If successful, this approach could lead to new understanding on the mechanism stabilising the long range order and aperiodic structures.

As demonstrated above, it is possible to form the  $\gamma$ -Al<sub>4</sub>Cu<sub>9</sub> approximant phase for thick enough deposition of Cu adatoms on quasicrystal or of Al layers on Cu(111) surfaces followed by short annealing to approximately 573 K. Because of the recurrence of this  $\gamma$  phase in several systems, its atomic structure will be first presented in Sect. 6.2. Following the experimental details, the characterization of the clean *p*-10*f* surface of the Al<sub>13</sub>Co<sub>4</sub> crystal will be shown in Sect. 6.4.1. Then, the adsorption of Cu adatoms on the *pseudo*-10-fold (*p*-10*f*) surface of the Al<sub>13</sub>Co<sub>4</sub> crystal at room temperature and up to 573 K will be described in Sect. 6.4.2 and 6.4.3 respectively. Finally, the main results will be discussed in Sect. 6.5.

## 6.2 Structural Models: from $\beta$ - to $\gamma$ -phase

The B2-type CsCl structure of the binary alloy Al-Cu is named the  $\beta$ -phase and its superstructure can be regarded as an approximant. The cubic  $\beta$ -structure contains two types of atoms positioned on the vertex and at the center of the cubic cell. The lattice parameter is about  $3.0 \pm 0.1$  Å. The structure along the [110] direction exhibits *pseudo*-5 fold or *pseudo*-10 fold symmetric features and can be described using a network based on the Penrose tiling [247, 248]. The complex structures showing the icosahedral or decagonal symmetry can be generated from the basic cell of B2 structure by local twinning at the atomic level, called chemical twinning mode [249]. The  $\beta$ -phase can be formed also in the ternary Al-Cu-Co alloy with Al<sub>50</sub>Cu<sub>x</sub>Co<sub>50-x</sub> composition.

The structure of the cubic  $\gamma$ -Al<sub>4</sub>Cu<sub>9</sub> (Al<sub>31.9</sub>Cu<sub>68.1</sub>) belongs to the P43m space group and has a lattice parameter *a* equal to 8.7068 Å [95, 250]. Along the [110] direction, local atomic structures are closely related to icosahedral and decagonal quasicrystals. This phase has been identified as an approximant of the *i*-Al-Cu-Fe quasicrystal [251]. It is a Hume-Rothery alloy with physical properties intermediate between a simple metal and a quasicrystal. The structure can be described as a  $3 \times 3 \times 3$  superstructure of the CsCl type structure, containing 52 atoms and two vacant sites, with formula unit Al<sub>16</sub>Cu<sub>36</sub>V<sub>2</sub> (V is a vacancy site). This structure of  $\gamma$ -Al<sub>4</sub>Cu<sub>9</sub> is well known as a vacancy-ordered phase, where the vacancies are not considered as a structural defect. As shown on Fig.6.1b, the role of vacancy sites is to generate local five-fold structure like the small pentagons outlined on the flat (F) layers. Therefore, the formation

of structures containing pentagonal configurations is facilitated by increasing the number of vacancy sites. Along the [110] direction where the periodicity is equal to  $12.3133 \text{ \AA}$  ( $\sqrt{2}a$ ), six layers are stacked in the following sequence (see Fig.6.1(a)): FPpf'P'F with the two types of layers labelled as flat (f and F) and puckered (p, p', P and P') layers. The 4 types of planes F, f, P and p are shown on Fig.6.1. Both f and p layers are related to F and P by a mirror operation lying at the middle of P and p with a  $\frac{1}{2}[110]$  translation. Both P' and p' are related to P and p by mirrors lying on F and f respectively. The puckered layers are denser than the flat layer. The F layer contains 15 atoms (with 4 Al and 11 Cu) and one vacancy, the f layer contains 16 atoms (with 4 Al and 12 Cu) and the puckered layers p and P are composed of 18 atoms (with 6 Al and 12 Cu). As defined by Dong *et al.* [251], the structure on each layer can be defined by two types of elongated hexagonal subunits consisting of one convex pentagon and one concave pentagon. The small pentagons in the structure of  $\gamma\text{-Al}_4\text{Cu}_9$  are aligned along the [110] direction and can be represented as parallel packing of pentagonal columns. The layer stacking and the periodicity of about  $2.0 \text{ \AA}$  along the (110) direction are similar to those present in the decagonal Al-Mn quasicrystalline structure [252].

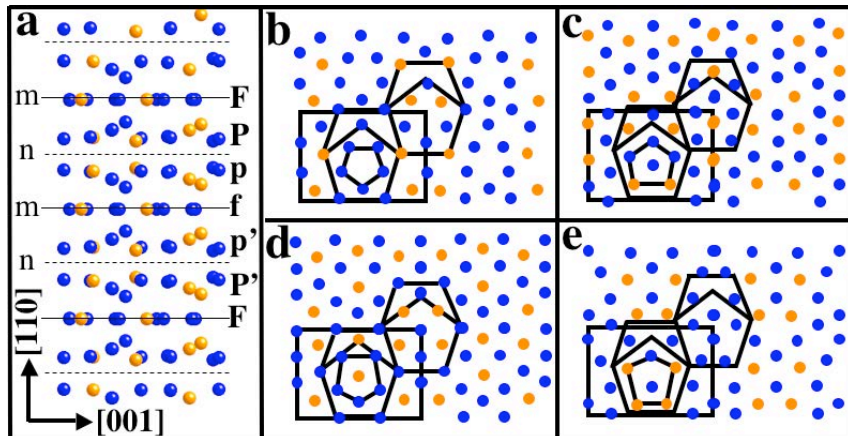


Figure 6.1: Blue circles represent Cu atoms and orange circles Al atoms (a) Stacking sequence of flat (f, F) and puckered (p, P, p', P') planes along the [110] direction of the  $\gamma\text{-Al}_4\text{Cu}_9$  phase. The atomic arrangements of flat and puckered planes are shown in (b) F layer, (c) P layer, (d) p layer and (e) f layer. The unit cell is outlined by a rectangle [95]. The vacancy sites are all on the flat layers and they are closed by the smallest pentagons.

### 6.3 Experimental details

Scanning tunneling microscopy (STM), low energy electron diffraction (LEED) and x-ray photoemission spectroscopy (XPS) measurements have been conducted in a UHV multi-chamber system with a base pressure of the  $5\times 10^{-11}$

mbar. STM experiments were performed using an Omicron variable temperature AFM/STM operating in STM mode at constant current. Non-monochromatised Mg K <sub>$\alpha$</sub>  source (E=1253.6 eV) and EA 125 electron energy analyser were used to perform XPS experiments. The polished orthorhombic Al<sub>13</sub>Co<sub>4</sub> surface was cleaned by repeated cycles of Ar<sup>+</sup> sputtering (1.5 keV, 20 minutes) and annealing (1.5 hours) up to 1173 K. The temperature of the sample is monitored using an infrared optical pyrometer with the emissivity set to 0.35. After each preparation cycle and prior to dosage, the surface structure of the substrate is assessed by low energy electron diffraction (LEED) and scanning tunneling microscopy (STM). Surface cleanliness was checked by recording the O KLL Auger signal. This surface preparation method produces step-terrace surface morphology, with a chemical composition of the near-surface region close to the bulk composition. The deposition of Cu (purity of 99.999%) was performed using an e-beam evaporator (EFM 3, Omicron) and the pressure was  $5 \times 10^{-10}$  mbar during the deposition. The Cu coverage was estimated from STM images recorded for sub-monolayer regime at 300 K. X-ray photoelectron diffraction (XPD) measurements have been carried out in a separate UHV chamber (Empa, Thun) by using a non-monochromatised Mg K <sub>$\alpha$</sub>  radiation and a modified Omicron photoelectron spectrometer equipped with an EA 125 HR electron analyser operated in Constant Analyser Energy (CAE) mode. The spectrometer has been calibrated to the Au 4f<sub>7/2</sub> binding energy of 83.8 eV. Prior to XPD measurements, the structural quality of the surface is verified using the LEED technique. The Cu adsorption was carried out for sample temperatures ranging from 300 K to 573 K. After the adsorption, the sample is maintained at deposition temperature for 15 minutes. The temperature is monitored by the optical pyrometer and/or a K type thermocouple. Coverages for the XPD measurements were calibrated using the quartz crystal microbalance and have been cross-checked with the LEED measurements.

## 6.4 Experimental results

In the following sections, we present the results obtained for the clean Al<sub>13</sub>Co<sub>4</sub> (100) surface prior to dosing and for the adsorption of Cu carried out on this orthorhombic crystal surface, first at 300 K and then to higher temperatures. Depending on the Cu film thickness, several surface structures and phases will be formed. As shown below, these latter will be systematically characterized by means of STM, LEED, XPS and XPD techniques.

### 6.4.1 The clean surface of the *p-10f* Al<sub>13</sub>Co<sub>4</sub> crystal

The investigation of the (100) surface of the Al<sub>13</sub>Co<sub>4</sub> has been reported recently by Addou *et al.* [70]. The LEED pattern recorded from the clean surface (Fig.6.2(a)) shows sharp diffraction spots and the expected orthorhombic unit cell, i.e. comparable with  $b = 12.342$  Å and  $c = 14.452$  Å from Grin *et al.* [66].

The  $p\text{-}10f$  symmetry which characterize this surface is not very apparent at the beam energy of 60 eV. An STM image from the clean surface (Fig.6.2(b)) reveals a step-terrace like morphology with terraces of lateral dimensions in the order of 100 nm. The step height between successive terraces is measured to be  $4.20 \pm 0.20$  Å.

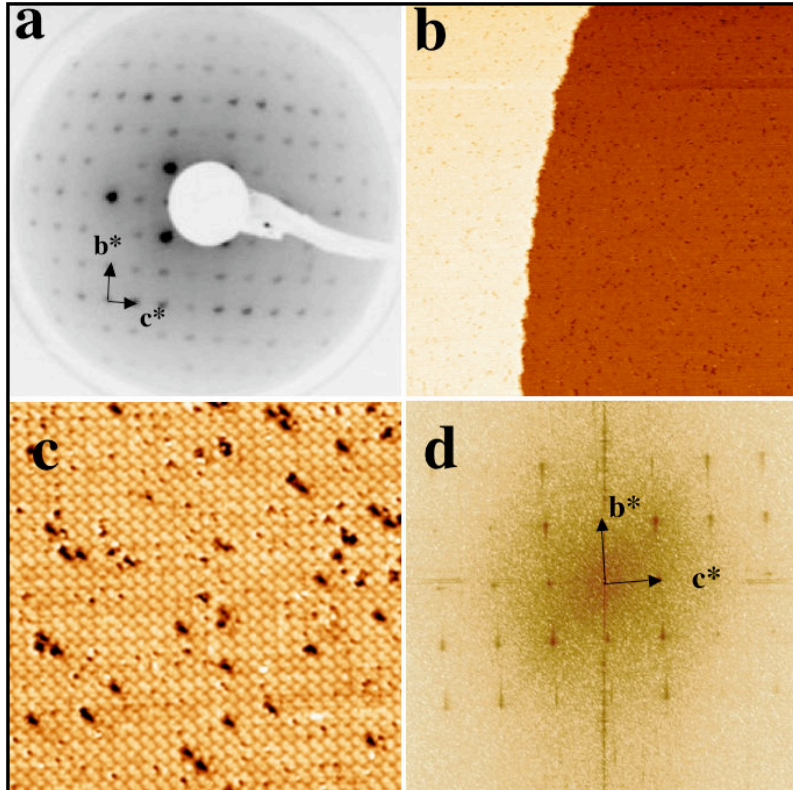


Figure 6.2: (a) LEED pattern (inverted for clarity) obtained at 60 eV beam energy from the  $p\text{-}10f$  surface of the  $\text{Al}_{13}\text{Co}_4$  sample . (b) STM image of the clean surface ( $200$  nm  $\times$   $200$  nm,  $V_b = 1.25$  V,  $I_t = 0.10$  nA). (c) High resolution STM image ( $40$  nm  $\times$   $40$  nm,  $V_b = 1.50$  V,  $I_t = 0.40$  nA) showing the only surface termination observed across terraces. (d) Fast Fourier transform calculated from a  $50$  nm  $\times$   $50$  nm STM image.

A high resolution STM image of this surface is presented on Fig.6.2(c). Only one type of termination is observed at the topmost surface. This surface termination, labelled  $T1$  in Addou *et al.* [70], consists of bipentagonal motifs pointing in the same direction within the terrace (see Fig.3.3 in chapter 3). The complete desorption of the  $T2$  termination is explained by the annealing temperature (up to 1173K) and time (90 min). With only one termination remaining at the surface, we observed the formation of few hollow like defects with an estimated depth of 2 Å on the terraces (Fig.6.2(c)). The fast Fourier transform obtained from the STM image (see Fig.6.2(d)) displays the unit cell parameters expected from the bulk model [66]. The XPD patterns measured

before deposition along with the SSC calculations confirm the  $p-10f$  symmetry of the  $\text{Al}_{13}\text{Co}_4$  (100) surface (see Fig. 3 in chapter 3). Using XPS, the surface composition determined from the Al  $2s$  and Co  $2p$  core levels is estimated at  $\text{Al}_{83}\text{Co}_{17}$ , i.e close to the bulk composition. The structural analysis of the surface termination using LEED, STM and XPD indicates that there is no evident lateral surface reconstruction. Hence, these results are entirely consistent with the previous study reported by Addou *et al.* [70] and demonstrate the possibility to prepare the  $\text{Al}_{13}\text{Co}_4$  (100) surface with only one type of surface termination.

#### 6.4.2 Investigation of Cu adsorption at 300 K

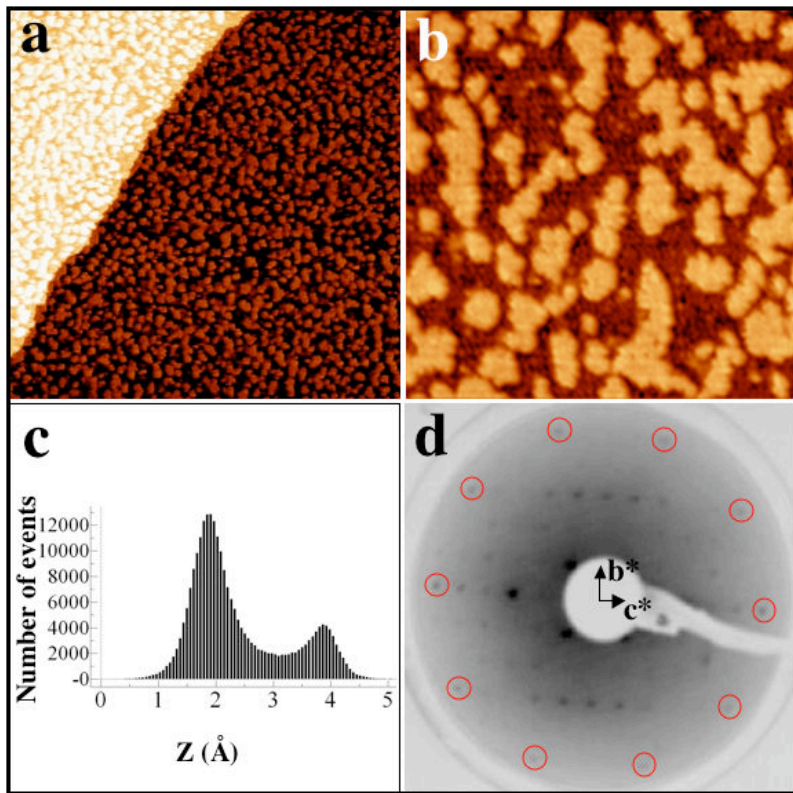


Figure 6.3: *Deposition of 0.5 ML of Cu on the  $\text{Al}_{13}\text{Co}_4$  (100) surface at 300 K:* (a)  $160 \text{ nm} \times 160 \text{ nm}$  STM image showing two terraces separated by a single step height ( $V_b = 1.30 \text{ V}$ ,  $I_t = 0.15 \text{ nA}$ ). (b) High magnification STM image ( $40 \text{ nm} \times 40 \text{ nm}$ ,  $V_b = 1.30 \text{ V}$ ,  $I_t = 0.15 \text{ nA}$ ). (c) Height histogram calculated from the STM image presented in (b). (d) LEED pattern (inverted for clarity) recorded for a beam energy of 60 eV. The ten brightest outer spots are encircled.

As shown on Fig.6.3(a), the adsorption of 0.5 ML Cu at room temperature on the  $\text{Al}_{13}\text{Co}_4$  (100) surface leads to the formation of nano-sized islands irregular in shape. At this stage, the island density is estimated at  $2.85 \times 10^{-4} / \text{\AA}^2$ .

For submonolayer coverage, there is no evidence for preferential decoration of Cu at terrace step edges. The island distribution across the terraces suggests a limited mobility of Cu adatoms at this temperature. Using higher magnification STM images (Fig.6.3(b)), one can still distinguish the atomic structure of the substrate. From the height histogram presented on Fig.6.3(c), the island height is measured at  $1.97 \pm 0.11$  Å on each terrace. This monoatomic height is comparable to the one reported while dosing Cu atoms on the five-fold surface of the *i*-Al-Pd-Mn quasicrystal [142, 143]. At this stage, the LEED pattern (Fig.6.3(d)) still displays an orthorhombic structure with the lattice parameters consistent with those of the clean surface, i.e  $b = 12.19 \pm 0.20$  Å and  $c = 14.34 \pm 0.20$  Å. While the overall quality of the LEED pattern starts to degrade, interestingly the *p-10f* symmetry of the substrate is more pronounced as shown by the remaining ten outer spots forming a decagonal ring (outlined on Fig.6.3(d)).

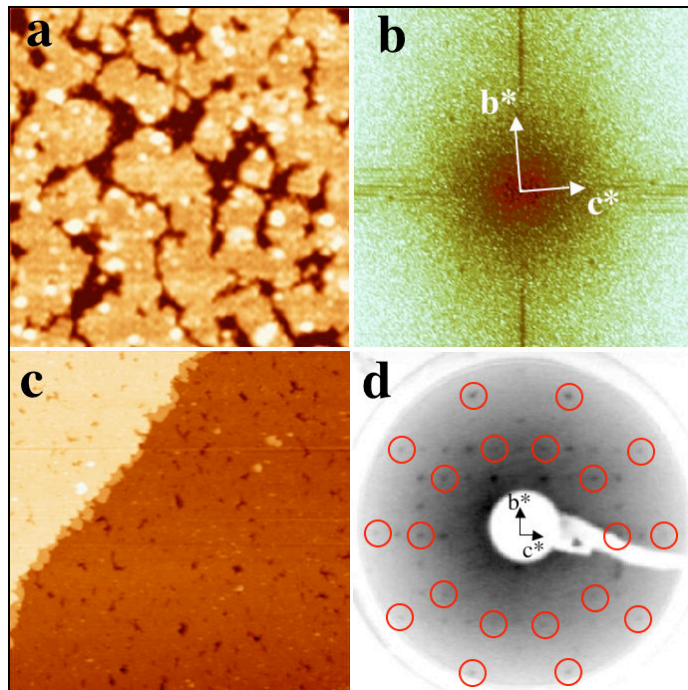


Figure 6.4: (a)  $40\text{ nm} \times 40\text{ nm}$  STM image obtained for 0.85 ML of Cu adsorbed at 300 K on the (100) surface of  $\text{Al}_{13}\text{Co}_4$  crystal. (b) FFT calculated from (a). (c)  $100\text{ nm} \times 100\text{ nm}$  STM image for 1 ML coverage at 300 K. (d) Corresponding LEED pattern (inverted for clarity) recorded at 60 eV beam energy. The two decagonal rings indicative of a *p-10f* symmetry are highlighted.

Upon further Cu deposition, individual islands increase in size and coalesce to form larger domains. As seen on Fig.6.4(a), these latter appear ordered as they exhibit some fine and periodic structural details. This is confirmed by the calculated FFT presented on Fig.6.4(b). Here, the two lattice vectors indicated on the FFT are comparable in magnitude ( $b = 12.22 \pm 0.20$  Å and  $c = 14.34 \pm$

$0.40 \text{ \AA}$ ) and orientation to those of the clean surface. For 1 ML deposition, the growth of the second layer has already started while the first layer is not fully completed. This time, the growth mode of the second layer begins with the decoration of the step edges (see Fig.6.4(c)). The island heights on the second monolayer are measured at  $2.20 \pm 0.20 \text{ \AA}$ . The quality of the LEED pattern recorded for 1 ML coverage (see Fig.6.4(d)) has improved compared to the one recorded at 0.5 ML. All the diffractions spots appear commensurate with those found on the orthorhombic LEED pattern recorded for the clean surface. Two decagonal rings related to the  $p-10f$  symmetry of the dosed surface are also highlighted. While the overall quality of the diffraction pattern remains lower than prior to the deposition, the combined STM and LEED measurements suggest the growth of a pseudomorphic monolayer.

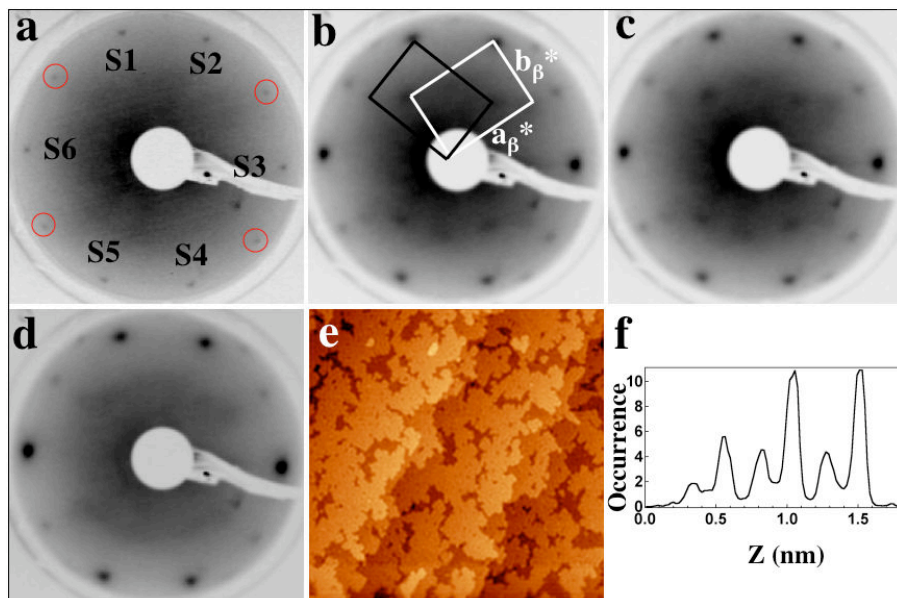


Figure 6.5: (a-d) LEED patterns (inverted for clarity) recorded at 60 eV after deposition of Cu adatoms at 300 K for different coverages: (a) 1.5 ML, the six most intense spots are labelled S1 to S6, (b) 3.0 ML, (c) 5.0 ML and (d) 7.5 ML. (e)  $150 \text{ nm} \times 150 \text{ nm}$  STM image ( $V_b = 1.30 \text{ V}$ ,  $I_t = 0.30 \text{ nA}$ ) measured for 4.0 ML coverage. (f) Height histogram calculated from the STM image shown in (e).

The LEED patterns recorded for coverages ( $\theta$ ) ranging from 1.5 ML to 7.5 ML are presented on Fig.6.5. The intensity distribution and the structure of the diffraction patterns are considerably different to those recorded up to 1 ML. Both the reciprocal lattice vectors and the inner decagonal ring characteristic of the orthorhombic structure of the first monolayer have disappeared. Only the outer decagonal ring is preserved on the LEED pattern recorded for 1.5 ML coverage (see Fig.6.5(a)). Within this ring, six out of the ten spots labelled S1 to S6 on Fig.6.5(a) appear remarkably brighter. Structurally similar

LEED patterns have been observed up to  $\theta \approx 2.5$  ML. While the intensity of the weakest diffraction spots encircled on Fig.6.5(a) remains unchanged, the intensity of the six spots ( $S_1$  to  $S_6$ ) increases with the Cu deposition. This is clearly demonstrated on the LEED pattern recorded for 3.0 ML (Fig.6.5(b)). In addition to the six most intense spots, extra diffraction spots are now easily discernible. The diffraction pattern presented on Fig.6.5(b) is now well understood using two rectangular unit meshes rotated from each other by  $72 \pm 1^\circ$  and mirror symmetric with the  $b$  axis. For each domain, the lattice parameters measured from the LEED pattern are equal to  $a_\beta = 2.85 \pm 0.10$  Å and  $b_\beta = 3.95 \pm 0.10$  Å, hence  $b_\beta \approx \sqrt{2}a_\beta$ . The rectangular unit mesh associated with each domain suggests the formation of either a new orthorhombic structure or a cubic structure with the (110) plane exposed at the surface. Despite a weakening of the intensity of several diffraction spots, the same structure is observed up to 7.5 ML of Cu deposition, i.e. the highest coverage dosed. The STM image recorded for 4.0 ML coverage demonstrates that the Cu grows in the layer-by-layer fashion (Fig.6.5(e)). The corresponding height histogram (Fig.6.5(f)) indicates a mean step height equal to 2.25 Å. Because the surface could not be atomically resolved, the identification of the new phase relies mainly on the diffraction and photoemission measurements. From the different possibilities of phases [95], the structure observed is consistent with two (110) domains of the  $\beta$ -phase of Al(Cu, Co). Indeed, this phase has its lattice parameter close to  $a_\beta$  (*a fortiori*  $b_\beta$ ) measured from the LEED pattern.

#### 6.4.2.1 X-ray photoelectron diffraction measurements

The XPD patterns of the Al 2s and Co 2p<sub>3/2</sub> core levels have been measured on the clean (100) surface of the Al<sub>13</sub>Co<sub>4</sub> sample using a non-monochromatized Mg K $\alpha$  (1253.60 eV) source. These latter exhibit the characteristic features expected for local decagonal ordering around the Al and Co elements (see Fig.2.5, chapter 2). The local real-space environment around Cu emitters has been investigated for several film thickness (2.0 ML, 4.0 ML, 8.0 ML and 15 ML coverage) deposited at room temperature. The corresponding XPD patterns of the Al 2s ( $E_{Kin} = 1135.6$  eV), the Co 2p<sub>3/2</sub> ( $E_{Kin} = 475$  eV) and the Cu 2p<sub>3/2</sub> ( $E_{Kin} = 320$  eV) core levels are displayed on Fig.6.6. In this experiment, we have measured the hemispherical emission intensity maps from 0°-70° polar angle with respect to the surface normal and from 0°-360° azimuthal angle with a total of 3458 points. The data are represented using a stereographic projection of the hemispherical emission intensity pattern with the center showing normal emission and the circle showing emission at 360° polar angle. In all XPD patterns, 2-fold averaging and gaussian polar background correction has been applied. High intensity in these maps directly represents the direction of near neighbor atoms around each emitter in real space and therefore the local geometric arrangement.

At 2.0 ML coverage, the XPD patterns recorded for both Al 2s and Co 2p core levels reveal a decagonal symmetry. The positions of the decagonal rings

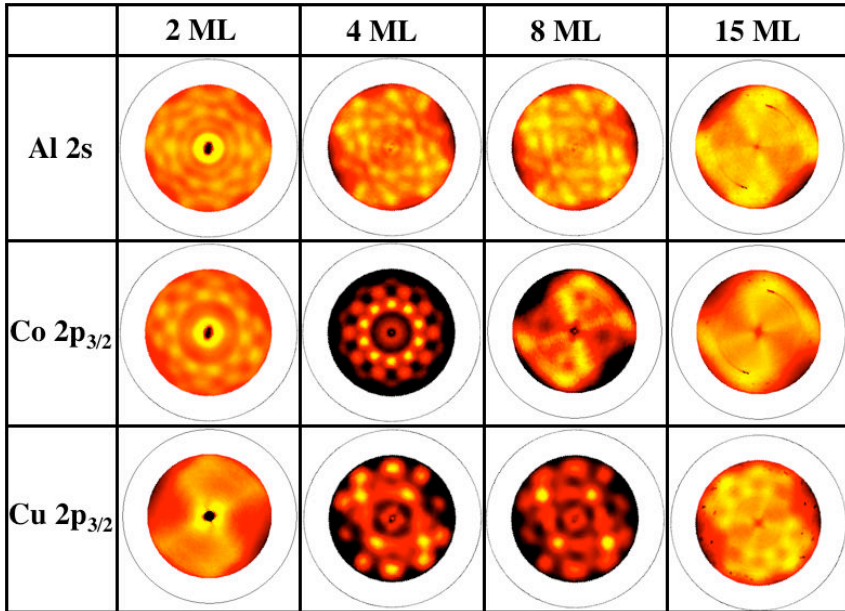


Figure 6.6: Experimental XPD patterns of the Al 2s ( $E_{Kin} = 1135.6$  eV), the Co 2p<sub>3/2</sub> ( $E_{Kin} = 475$  eV) and the Cu 2p<sub>3/2</sub> ( $E_{Kin} = 320$  eV) core levels. These patterns have been measured for the following Cu film thickness deposited at 300 K:  $\theta \approx 2.0$  ML, 4.0 ML, 8.0 ML and 15 ML dosage.

remain identical to those obtained on the clean surface patterns. This confirms that the  $p\text{-}10f$  symmetry of the substrate is preserved at this coverage. However, a broadening of all diffraction spots is clearly observed and the inner decagonal ring of the Co 2p pattern has disappeared.

While no pattern was obtained for the Cu 2p core level, STM and LEED measurements suggest that Cu grows pseudomorphically on this surface up to 1 ML monolayer. For 4.0 ML Cu deposition, three decagonal rings now dominate the XPD pattern of the Co 2p<sub>3/2</sub> emission. The intensity distribution and the position of the maxima are different compared to those measured at lower coverage. In fact, this pattern is qualitatively similar to the one obtained prior to Cu dosing (see Fig.2.5, chapter 2). Regarding the Al 2s emission, an inner decagonal ring is surrounded by ten spots non-equivalent in intensity, hence breaking the overall  $p\text{-}10f$  symmetry. The photoelectron intensity map corresponding to the Cu 2p core level indicates an ordered structure around this element. The pattern is characterized by four intense spots around its center forming a rhombus with internal angles measured at 72° and 108°. The outer diffraction spots (polar angle equal to 60°) are arranged as a decagonal ring but they are non-equivalent in intensity as in the Al 2s case. It has to be mentioned that the brightest spots present on the XPD pattern of Cu 2p are all found at the same position on the Al2s photoelectron intensity map.

Upon further deposition (8 ML), the quality of the XPD pattern for the Co emitters is drastically degrading to become featureless at 15 ML. At 8 ML

Cu coverage, both Al 2s and Cu 2p<sub>3/2</sub> emissions are qualitatively similar and exhibit a 2-fold symmetric pattern. The spots associated with this new short-range structure are commensurate with those recorded at 4 ML coverage. At higher coverage (15 ML), no XPD pattern could be obtained for the Al 2s core level. However, the photoemission intensity map for the Cu 2p emission shows an almost perfect *p*-10f pattern instead of a 2-fold symmetric one. Two clear decagonal rings are indeed observed at this 15 ML coverage. The overall pattern remains unchanged upon annealing to 513 K for 45 min. A new motif is obtained only if the film is annealed to 640 K for 30 min. Then, the XPD patterns resemble those obtained for high temperature deposition. This new structure known as the  $\gamma$ -phase will be described in the Sect.6.4.3.

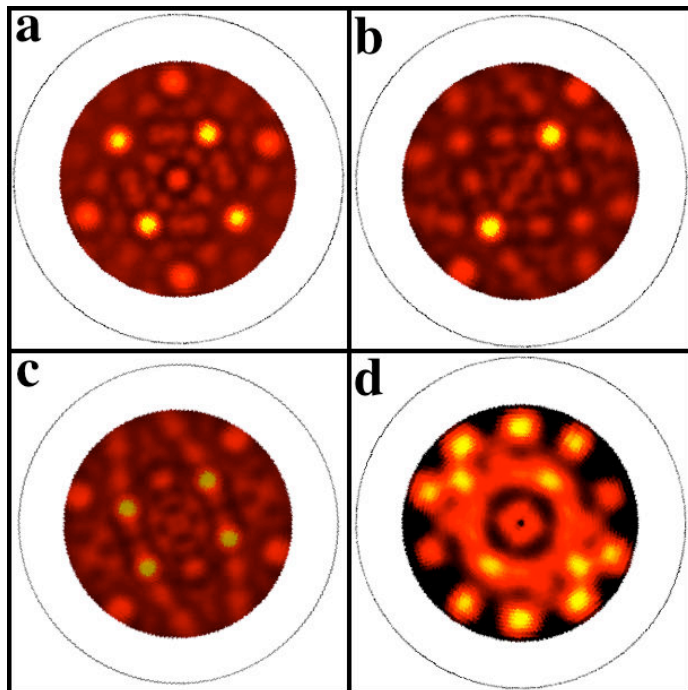


Figure 6.7: *Single Scattering Cluster simulations for (a) Al 2s ( $E_{Kin} = 1370 \text{ eV}$ ) and (b) Cu 2p<sub>3/2</sub> ( $E_{Kin} = 1166 \text{ eV}$ ) emission based on a cluster of 91 atoms derived from the bulk model of the CsCl type structure. (c) SSC pattern generated by averaging the SSC simulation displayed in (b) with itself rotated by 72°. (d) XPD pattern recorded for the Cu 2p<sub>3/2</sub> emitter at 4 ML coverage. The brightest features are well reproduced in the SSC simulation shown in (c), although some discrepancies exist within the intensity distribution.*

For  $\theta \geq 3.0$  ML, STM and LEED measurements reveal the formation of a new surface structure. This latter is described as two (110) domains of a  $\beta$  phase rotated by 72° from each other. To interpret the experimental XPD patterns, Single Scattering Cluster (SSC) simulations for the Al 2s ( $E_{Kin} = 1370 \text{ eV}$ ) and Cu 2p<sub>3/2</sub> ( $E_{Kin} = 1166 \text{ eV}$ ) emission have been performed based on a CsCl type structure. The cluster used to carry out the calculations

consists of 91 atoms with 64 Al and 27 Cu atoms. As a first approximation, the SSC simulations were performed for 20 emitters of Al 2s and 7 emitters of Cu 2p<sub>3/2</sub>, ignoring at this stage Co emitters. The photoelectron intensity maps obtained for each emitter are presented on Fig.6.7(a),(b). The resulting SSC simulations, calculated for both Al 2s and Cu 2p<sub>3/2</sub> emitters, reproduce perfectly the observed XPD pattern. For instance, all the main features in the XPD pattern (Fig.6.7(d)) for the Cu core level are well reproduced by the SSC simulation with itself rotated then by 72° (Fig.6.7(c)). However, there exist discrepancies between the intensity distribution observed experimentally and obtained from our SSC simulations. These are not yet fully understood. To the contrary of the model used in our SSC calculations, unbalanced occurrence of domains at the crystal surface in the two directions may explain the differences observed within our simulations.

#### 6.4.2.2 X-ray photoelectron spectroscopy measurements

The evolution of the intensity ratio among the Al 2s, Co 2p and Cu 2p core levels as a function of Cu coverage are plotted on Fig.6.8. The substrate signal (Al 2s and Co 2p) decreases continuously with increasing Cu coverage as evident from the Al 2s to Cu 2p and Co 2p to Cu 2p area ratios (Fig.6.8(a),(b)).

However, the rate of decrease of the Al 2s signal is much slower than for the Co 2p signal. Figure 6.8(b) shows that Co 2p signal becomes very weak for  $\theta \geq 2$  ML. Figure 6.8(c) demonstrates that the Al to Co ratio is increasing with increasing coverage. This plot suggests a relative Al (Co) enrichment (depletion) at the near surface region. Hence, the topmost surface layer should be mainly composed of Al and Cu atoms. Large intermixing have been previously reported at room temperature for transition metal (TM) thin films grown on an Al substrate and vice-versa. Depending on the system studied (Al dosed on a TM surface or vice-versa), the intermixing width could differ considerably. For instance, the width length of Cu on an Al surface is found to be 6 times larger than for Al atoms on a Cu substrate [253]. Hence, we believe that Cu adatoms are likely to diffuse more into the substrate than Al atoms into the Cu film.

Figure 6.9 shows the Al 2s, Co 2p and Cu 2p core level spectra recorded as a function of Cu coverages. All the spectra have been normalised to the dominant peak. It enables to track any changes in the core level lineshape with increasing Cu dosage. For the Al 2s spectrum, the peak at 124 eV binding energy (BE) corresponds to the Cu 3s core level. The lineshapes (broadening) of the peaks have not been altered upon Cu deposition. The insets of Fig.6.9 show the evolution of the binding energy of the core levels as a function of the Cu coverage. No changes in the BE (no chemical shift) of the Al 2s core level could be detected upon dosing. However, there is a continuous shift in the BE of Co 2p and Cu 2p core levels towards lower BE side with increasing Cu coverage. There is a total shift of 0.5 eV between the BE of Co 2p corresponding to the clean surface (indicated by 0 ML) and after dosing 5 ML of Cu. For

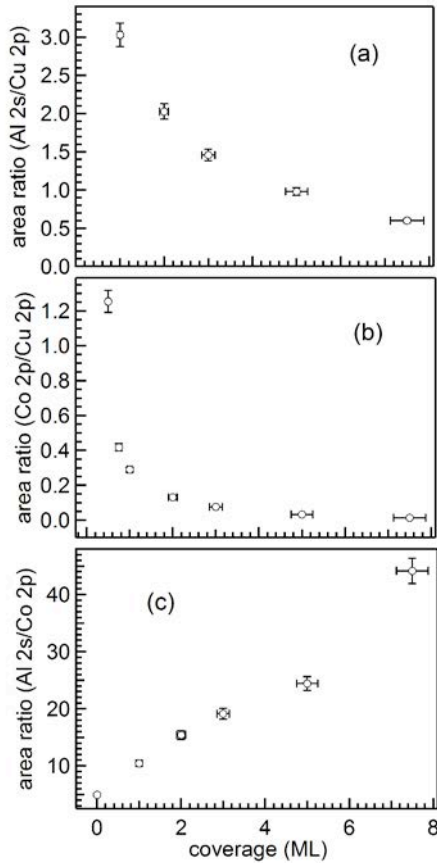


Figure 6.8: The intensity ratio of (a) Al 2s to Cu 2p, (b) Co 2p to Cu 2p, and (c) Al 2s to Co 2p core levels are presented upon Cu depositions at 300 K.

$\theta \geq 5$  ML, the BE position of the Co 2p peak remains unchanged, i.e. equal to 778.0 eV. Similarly, there is total shift of 0.5 eV between the BE of Cu 2p at 0.5 ML and at 7.5 ML Cu coverage. The BE of both elements shift towards the values measured on Co (Co 2p at 778.15 eV) and Cu (Cu 2p at 932.70 eV) single crystals respectively.

We could not determine accurately the film composition from our XPS measurements as the probing depth of this technique is larger than the highest coverage investigated here. The substrate contribution to the XPS signal remains important for such coverages. In addition, a composition gradient normal to the surface should be expected due to the inhomogeneous intermixing of Al and Cu atoms. Hence, the XPS analysis is taken as indicative of alloy formations and of relative enrichment of the surface region in one element.

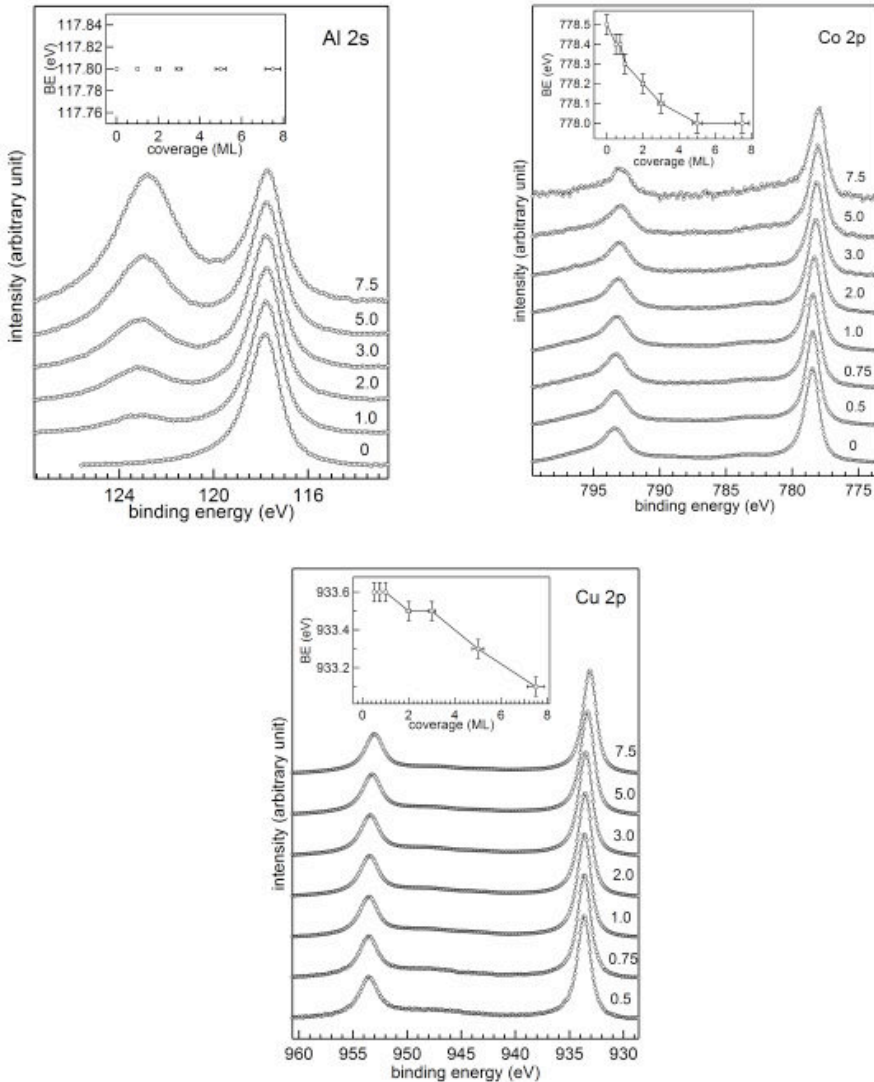


Figure 6.9: *The evolution of the Al 2s, Co 2p and Cu 2p core level spectra as a function of Cu coverage deposited at room temperature. For each elements, the spectra are normalized to the highest peak height. The corresponding Cu dosage are indicated in equivalent ML on each spectrum. The insets show the binding energy variation of each core level as a function of Cu coverage.*

### 6.4.3 Investigation of Cu adsorption up to 573 K

#### 6.4.3.1 LEED and STM measurements

We turn to the characterization of Cu adsorption on the  $\text{Al}_{13}\text{Co}_4$  sample held at 473 K. Compared to room temperature deposition (see Fig.6.3) and for similar coverage (0.5 ML) and flux, the number of individual islands has drastically reduced (Fig.6.10(a)). This is explained partly by the formation of larger islands, a consequence of an increased adatom mobility across the ter-

races at 473 K. Under these conditions, the step edges are well decorated. At this submonolayer coverage, the growth mode proceeds already via the coalescence of irregularly shaped islands (Fig.6.10(a)). Using higher magnification STM images, fine structural details are observed within those islands and the bare substrate is still atomically resolved (Fig.6.10(b)). Indeed, the bipentagonal motifs characteristics of the Al<sub>13</sub>Co<sub>4</sub>(100) surface remains clearly distinguishable. The corresponding height histogram indicates an island step height equal to  $2.25 \pm 0.20 \text{ \AA}$ . At this coverage ( $\sim 0.5 \text{ ML}$ ), the FFT calculated from Fig.6.10(b) and the associated LEED pattern exhibit an orthorhombic surface unit mesh (see Fig.6.10(c-d)) with lattice parameters consistent with those of the underlying substrate. To avoid any contribution of the substrate structure, only the islands present on Fig.6.10(b) have been selected using a thresholding image analysis tool to calculate the FFT pattern. At this stage, the  $p-10f$  symmetry of the substrate is still preserved as evident from the decagonal ring outlined on the LEED pattern (Fig.6.10(d)).

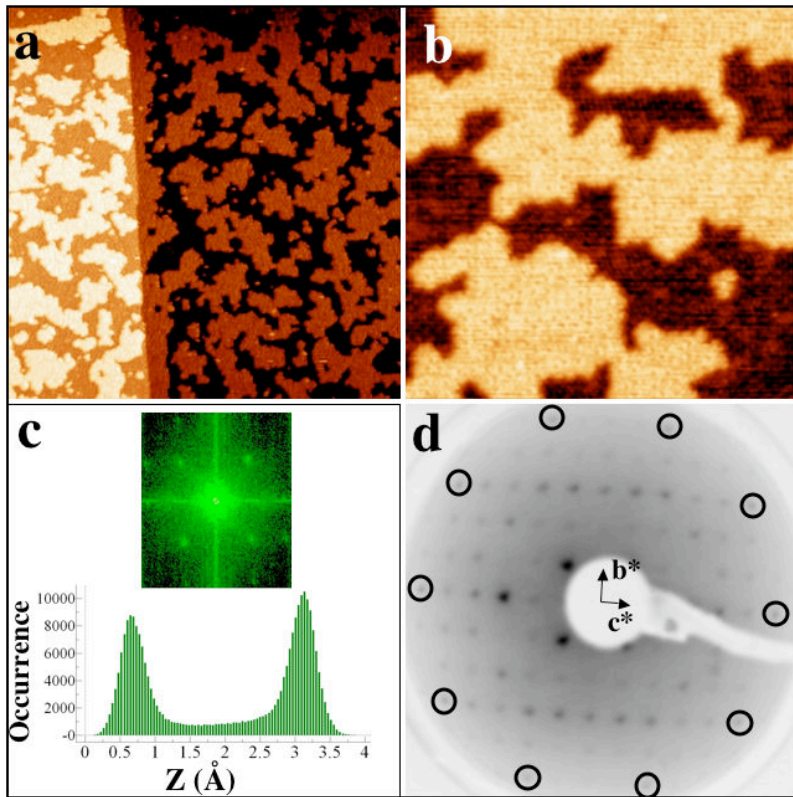


Figure 6.10: *Adsorption of 0.5 ML of Cu adatoms with the sample held at 473 K:* (a)  $200 \text{ nm} \times 200 \text{ nm}$  STM image ( $V_b = 1.85 \text{ V}$ ,  $I_t = 0.30 \text{ nA}$ ). (b)  $40 \text{ nm} \times 40 \text{ nm}$  high resolution STM image ( $V_b = 1.2 \text{ V}$ ,  $I_t = 0.15 \text{ nA}$ ). (c) Histogram calculated from a  $50 \text{ nm} \times 50 \text{ nm}$  STM image, inset: FFT calculated from the STM image presented in (b). (d) LEED pattern recorded at  $60 \text{ eV}$  beam energy (inverted for clarity).

The STM images recorded for  $\sim 1$  ML Cu coverage at 473 K are presented on Fig.6.11(a-b). The completion of a full monolayer has been successfully achieved prior to the growth of the second layer (Fig.6.11(a)). In comparison with room temperature adsorption, the roughness measured on each terrace is slightly reduced ( $Z_{RMS}$  equal to 0.14 Å compared to 0.23 Å for room temperature deposition), indicative of an improved surface ordering. Indeed, this is confirmed by the fine structure observed on Fig.6.11(b), by sharp spots in the FFT (Fig.6.11(c)) and by the improved quality of the corresponding LEED pattern (Fig.6.11(d)). The local atomic arrangements measured on the STM images along with the unit cell parameters obtained from the FFT ( $b = 12.51 \pm 0.10$  Å and  $c = 14.30 \pm 0.05$  Å) and from the LEED patterns ( $b = 12.58 \pm 0.10$  Å and  $c = 14.13 \pm 0.20$  Å) point towards a pseudomorphic growth mode. As it will be demonstrated below using XPS measurements, it is likely that intermixing occurs at the earliest stages of the adsorbate deposi-

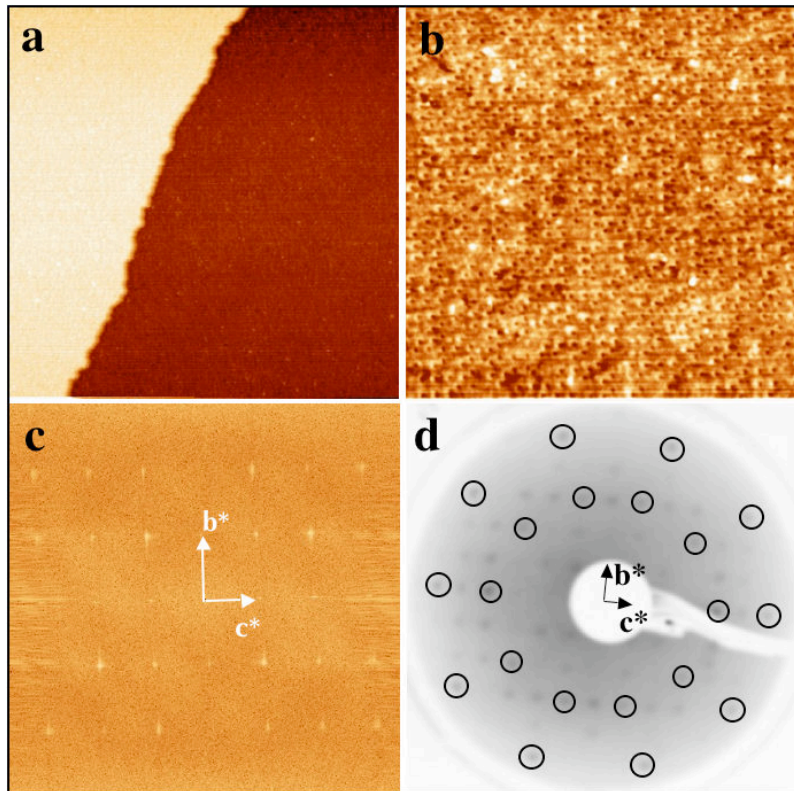


Figure 6.11: *Deposition of 1.0 ML of Cu with the sample held at 473 K: (a) 150 nm  $\times$  150 nm STM image showing atomically flat terraces ( $V_b = 1.50$  V,  $I_t = 0.40$  nA). (b) 40 nm  $\times$  40 nm high resolution STM image ( $V_b = 1.0$  V,  $I_t = 0.05$  nA). (c) Fast Fourier transform calculated from the STM image presented in (b). (d) LEED pattern recorded at 60 eV beam energy (inverted for clarity). Two decagonal rings resulting from the pseudo-10f symmetry of the surface are outlined.*

tion. Hence, the pseudomorphic monolayer formed should contain at least two chemical elements.

As revealed on Fig.6.11(b) and Fig.6.12, the film structure is dominated by donut-like features. At higher magnification and using a Fourier filtering process to enhance the overall structure of the film, these motifs observed within the monolayer (Fig.6.12(b)) can be understood as pentagons of edge lengths equal to  $6.1 \pm 0.5$  Å. In addition, a closer inspection of the complete monolayer indicates that structural disorder remains within the thin film. This is manifested by an uneven distribution, although periodic, of those pentagonal motifs within the layer. It has to be mentioned that the topography of the monolayer is unchanged upon bias inversion.

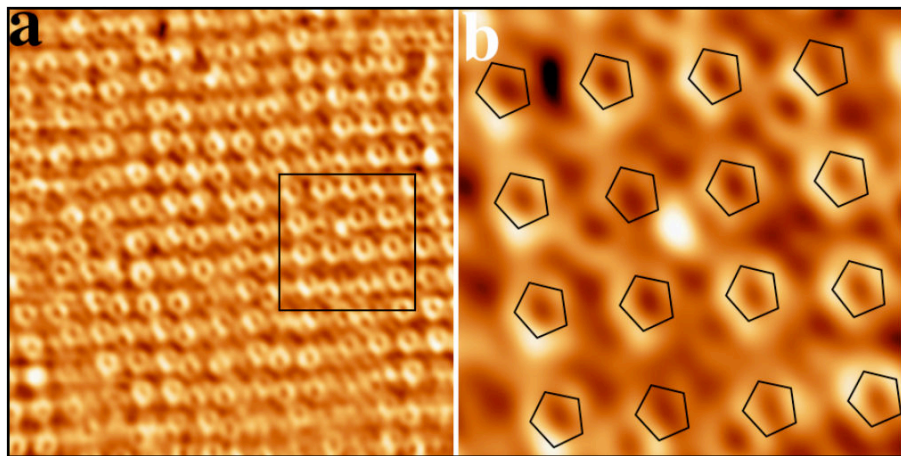


Figure 6.12: (a) The STM image ( $21\text{ nm} \times 21\text{ nm}$ ,  $V_b = 1.5\text{ V}$ ,  $I_t = 0.07\text{ nA}$ ) has been Fourier filtered to enhance the overall structure of the film. (b) STM image ( $6\text{ nm} \times 6\text{ nm}$ ,  $V_b = 1.0\text{ V}$ ,  $I_t = 0.02\text{ nA}$ ) corresponding to the region highlighted in (a). At this magnification, part of the film structure can be described using pentagons.

Adsorption at higher dosage with the sample maintained at 473 K leads to the formation of several surface alloys. The STM images and the LEED patterns of Fig.6.13 present successive phase transitions. At 2 ML Cu coverage, a layer-by-layer growth mode (step height measured at 2.25 Å) is still preserved (Fig.6.13(a)). However, two separate surface morphologies are identified (Fig.6.13(b)) within the terraces<sup>1</sup>. While the phase on the left hand side appears relatively disordered (no clear spots in the FFT), one dimensional streaks dominate the second phase on the right hand side of the image. At this stage, the LEED pattern can be interpreted as two (110) domains of  $\beta\text{-Al(Cu, Co)}$  rotated from each other by  $72^\circ$ , i.e. similar to the diffraction pattern observed while depositing Cu adatoms at 300 K (see Fig.6.5).

Upon further adsorption (4 ML), only one phase could be identified on the large flat terraces presented on Fig.6.13(d). The topography is comparable

---

<sup>1</sup>These two phases are not related to the two domains observed in the LEED patterns

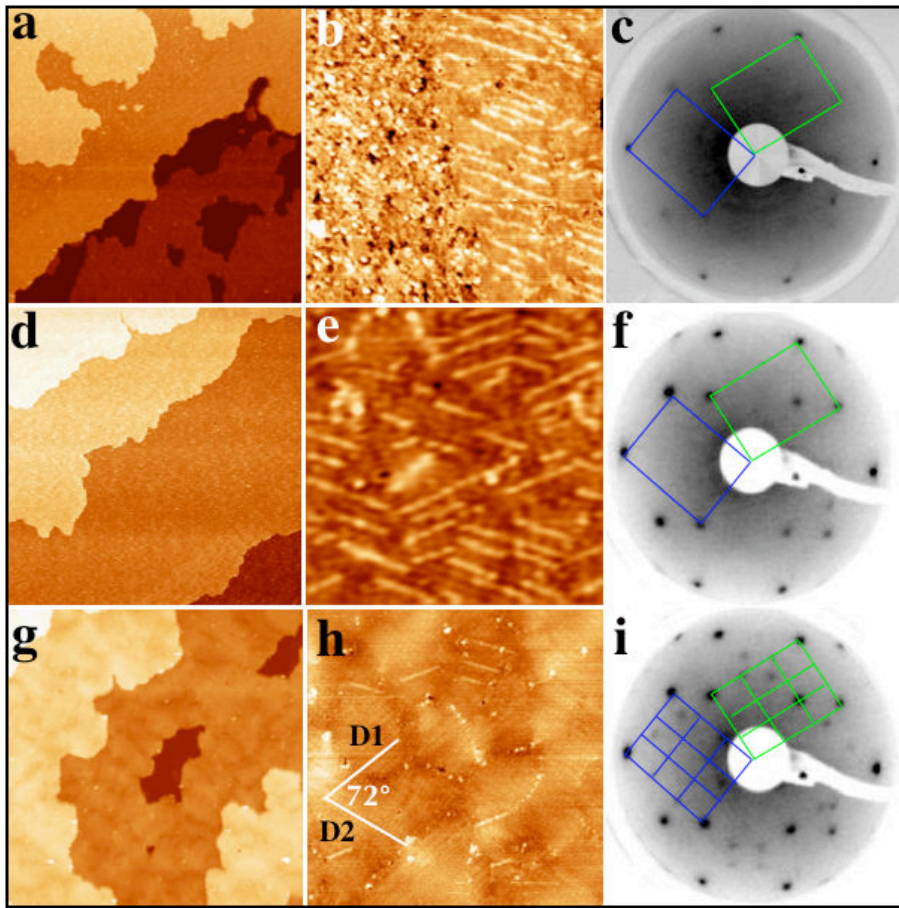


Figure 6.13: All STM images and LEED patterns (inverted for clarity) are measured after deposition of Cu adatoms with the sample held at 473 K. The LEED patterns are recorded at 60 eV beam energy. Top row: (a) 200 nm  $\times$  200 nm STM image recorded at 2.3 ML Cu coverage ( $V_b = -1.50\text{ V}$ ,  $I_t = 0.10\text{ nA}$ ). (b) 55 nm  $\times$  55 nm high resolution STM image ( $V_b = 1.50\text{ V}$ ,  $I_t = 0.30\text{ nA}$ ). (c) corresponding LEED pattern. Middle row: (d) 475 nm  $\times$  475 nm STM image recorded at 4.0 ML deposition ( $V_b = 2.00\text{ V}$ ,  $I_t = 0.10\text{ nA}$ ). (e) 50 nm  $\times$  50 nm high resolution STM image ( $V_b = 1.50\text{ V}$ ,  $I_t = 0.02\text{ nA}$ ). (f) corresponding LEED pattern. Bottom row: (g) 150 nm  $\times$  150 nm STM image recorded at 10 ML dosage ( $V_b = 1.30\text{ V}$ ,  $I_t = 0.15\text{ nA}$ ). (h) 46 nm  $\times$  46 nm high resolution STM image ( $V_b = 1.30\text{ V}$ ,  $I_t = 0.20\text{ nA}$ ). The directions of the two domains are indicated by D1 and D2. The angle between both orientations is estimated at 72°. (i) corresponding LEED pattern with additional diffractions spots compared to (c) and (f).

to the right hand side part of Fig.6.13(b) after 2 ML deposition. However, two sets of streaks are now oriented at  $72 \pm 1^\circ$  from one another. The LEED pattern is sharper at this coverage and it is still described by two domains of the  $\beta$  phase rotated by  $72 \pm 1^\circ$ . The dimensions of the unit cell measured

from the two domains are  $a_\beta = 2.85 \pm 0.10 \text{ \AA}$  and  $b_\beta = 4.14 \pm 0.10 \text{ \AA}$ , with  $b_\beta \approx \sqrt{2}a_\beta$ , hence also consistent with the lattice parameters obtained from the  $\beta$ -phase formed at 300 K for high coverages.

The layer-by-layer growth mode is still preserved above 4 ML Cu deposition (see Fig.6.13(g)). For the highest coverage deposited, the step height associated with those islands remains at 2.25  $\text{\AA}$ . A high resolution STM image (Fig.6.13(h)) indicates that the film is composed of two domains rotated from each other by 72° with their directions labelled as D1 and D2. The apparent overall buckling of the film could be partly explained by dislocations within the near-surface region [245]. Individual domains and domain boundaries are still decorated by defects appearing as bright protrusions and lines on Fig.6.13(h). The structural change observed by STM upon Cu dosage suggests the formation of a new surface phase. This is indeed confirmed by the appearance of additional diffraction spots within the LEED pattern. While similar to the diffraction pattern presented on Fig.6.13(f), those new spots of weaker intensity define smaller reciprocal lattice vectors, i.e. a larger unit cell in real space. Hence, the unit cell described on Fig.6.13(f) can be subdivided into 3 sub-units as shown on the LEED pattern of Fig.6.13(l). The corresponding dimensions of this new unit cell are  $a_\gamma = 8.68 \pm 0.30 \text{ \AA}$  and  $b_\gamma = 12.54 \pm 0.20 \text{ \AA}$ , with  $b_\gamma \approx \sqrt{2} \times a_\gamma$  and  $b_\gamma = 3 \times b_\beta$ . The lattice parameter of this new unit cell can be related to the lattice parameters of the (110) surface of the  $\gamma\text{-Al}_4\text{Cu}_9$  phase [95, 251]. A similar LEED pattern of the  $\gamma$ -phase is already observed at 7.5 ML coverage but the STM images are not as well resolved as for 10 ML Cu dosage. It is important to note that along the (1, 0) axis, only the (3, 0) spot has appreciable intensity in this structure. The formation of  $\text{Al}_4\text{Cu}_9$  has been reported in similar studies during the annealing of Al/Cu/Fe thin films [254], by phase transformation in Cu-Al thin films [255] and by annealing Cu/Al multilayer thin films [256].

As expected from the analysis above, the FFT calculated from the STM image shown on Fig.6.13(h) is composed of two orthorhombic networks rotated by 72° from each other (Fig.6.14(a)). Fourier transforms generated from individual domains (7 nm × 7 nm wide, high resolution STM images) aligned either along D1 or D2 directions exhibit only one set of spots in agreement with an orthorhombic lattice (Fig.6.14(b)). In these cases, the dimensions of the orthorhombic unit cells are consistent with two (110) domains of the  $\gamma$ -phase. Compared to the structures observed below 4 ML coverage (see Fig.6.13(b) and(e)), the surface roughness ( $Z_{rms}$ ) of the  $\gamma$ -phase is lower (less than 0.2  $\text{\AA}$ ). A Fourier filtered STM image of one domain is displayed on Fig.6.14(c). The surface structure observed on this high resolution STM image is characterized by bright “Y”-like motifs. As shown on Fig.6.14(d), similar local atomic arrangement can be recognized on the (110) surface of the  $\gamma\text{-Al}_4\text{Cu}_9$  single crystal. On the latter sample, two terminations related to the puckered planes present within the bulk model coexist as surface layers [257].

While depositing 16 ML of Al on Cu(111) followed by short annealing to 510 K [245], the formation of the the  $\gamma\text{-Al}_4\text{Cu}_9$  phase as a surface alloy has

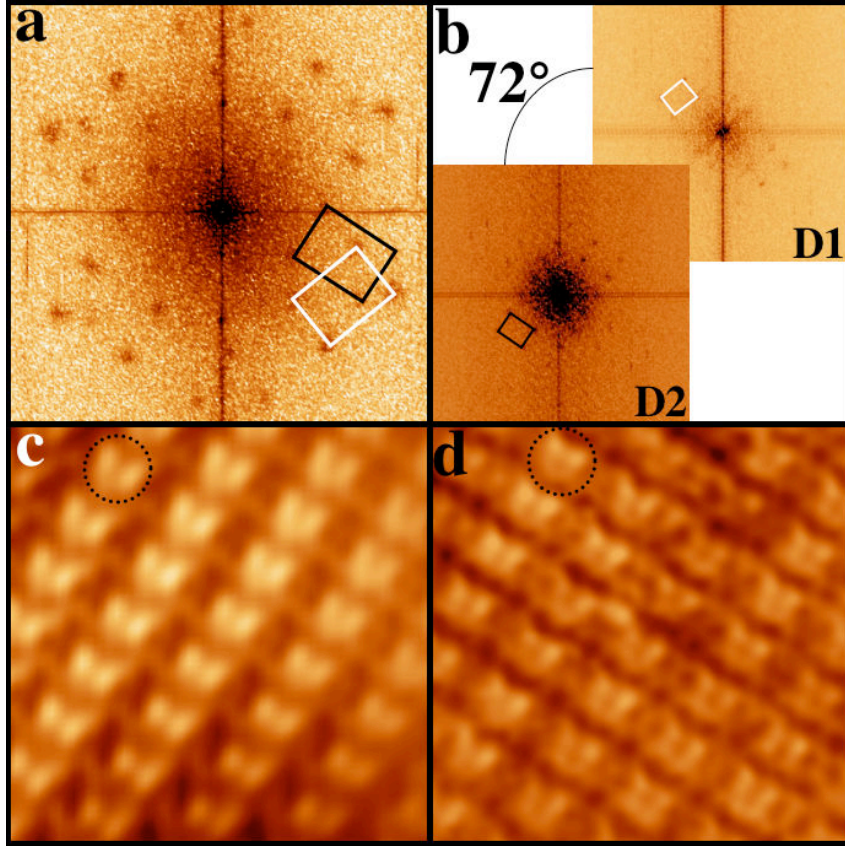


Figure 6.14: (a) FFT calculated from a  $55 \text{ nm} \times 55 \text{ nm}$  STM image showing two domains of  $\gamma\text{-Al}_4\text{Cu}_9$  phase along the  $[110]$  direction. The unit cell of each domain is outlined. (b) Two FFT calculated from two individual domains, each oriented either along the D1 or D2 direction (see Fig. 6.13(h)). The dimensions of the corresponding region of the STM image is  $7 \text{ nm} \times 7 \text{ nm}$ . (c) A Fourier filtered STM image ( $6 \text{ nm} \times 6 \text{ nm}$ ) presents the atomic structure of the  $\gamma\text{-Al}_4\text{Cu}_9$  phase. The common "Y"-like motif is outlined by a circle. (d) STM image recorded on the  $(110)$  surface of the  $\gamma\text{-Al}_4\text{Cu}_9$  single crystal.

been successfully achieved. Among the possible surface terminations, one type of terraces exhibits features comparable to those presented on Fig. 6.14(c) [245]. In this Al/Cu study, a good agreement is obtained between the experimental STM images and the simulated STM images based on the relaxed  $\gamma\text{-Al}_4\text{Cu}_9$  structure terminated by a puckered layer as the topmost surface plane. From a comparison with other works and using LEED and STM measurements, we believe that the surface alloy formed, upon adsorption of 10 ML Cu adatoms on the  $\text{Al}_{13}\text{Co}_4$  surface held at  $473 \text{ K}$ , is of  $\gamma\text{-Al}_4\text{Cu}_9$  type.

### 6.4.3.2 X-ray photoelectron diffraction measurements

Figure 6.15 corresponds to XPD patterns recorded for the Al 2s, Co 2p, and Cu 2p core levels as a function of Cu adsorption on the (100) surface of Al<sub>13</sub>Co<sub>4</sub> surface held at 573 K. All XPD pattern have been measured from normal emission (center) to a polar emission angle of 70°, i.e. almost parallel to the crystal surface. The rings around the stereographically projected patterns show 90° polar emission. The bright and dark contrasts indicate high and low intensities, respectively.

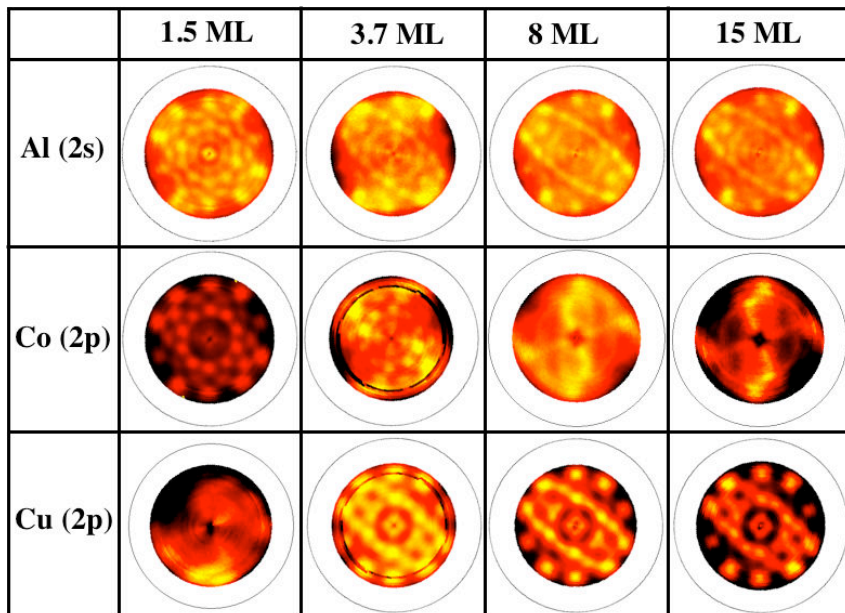


Figure 6.15: *Experimental XPD patterns of Al 2s ( $E_{Kin} = 1135.6$  eV), Co 2p<sub>3/2</sub> ( $E_{Kin} = 475$  eV) and Cu 2p<sub>3/2</sub> ( $E_{Kin} = 320$  eV) core levels as a function of Cu coverage. The different depositions ( $\theta \approx 1.5$  ML, 3.7 ML, 8 ML and 15 ML) of Cu adatoms are performed with the Al<sub>13</sub>Co<sub>4</sub>(100) surface held at 573 K.*

For 1.5 ML coverage, the XPD patterns appear very similar to those recorded for the clean surface. At this stage, the photoelectron intensity map for Cu emitters remains featureless. At 3.7 ML Cu coverage and above, the XPD patterns of Al 2s and Cu 2p core levels are now sharp and 2-fold symmetric. The quality of the diffraction image associated with the Co 2p core level degrades drastically above 2 ML to finally vanish around 8 ML. The local real space environment around Al and Cu emitters stays almost unchanged above 8 ML coverage. For the Al 2s pattern, decagonal rings are situated at characteristic polar angles (36°, 50° and 60°) with 10 maximas separated by an azimuthal angle of 36°. For the Cu 2p patterns, the central and outer rings are situated at polar angle of 36° and 60° respectively. In agreement with the STM and LEED measurements, the analysis of both diffraction images (Al 2s and Cu 2p) suggests the presence of two domains rotated by 72° from each.

Interestingly, similar XPD patterns can be obtained by depositing 15.0 ML of Cu at 300 K followed by subsequent annealing to 573 K for 30 min.

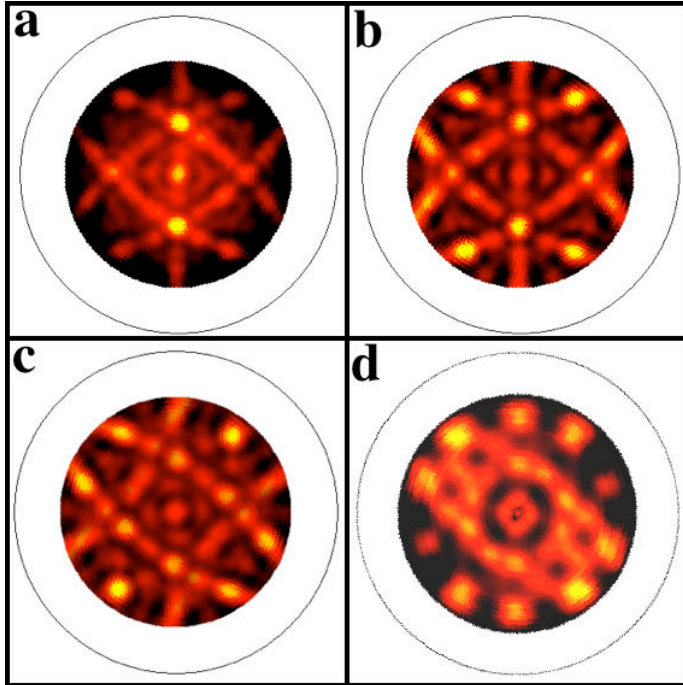


Figure 6.16: *SSC simulations for (a) the Al 2s ( $E_{Kin} = 1370$  eV) and (b) the Cu 2p ( $E_{Kin} = 1166$  eV) core levels. (c) SSC pattern generated by additive superposition of the SCC simulation displayed in (b) with itself rotated by 72°. (d) XPD pattern obtained for the Cu 2p core level after 15 ML coverage.*

To ascertain the conclusions drawn from the LEED and the STM analysis, SSC simulations for the Al 2s and Cu 2p emissions (Fig.6.16(a),(b)) have been performed based on the  $\gamma\text{-Al}_4\text{Cu}_9$  phase. The cluster used to carry out the calculations consists of 464 atoms (136 Al + 328 Cu) with 21 Al and 48 Cu as emitters. The model is established such as the two topmost surface terminations are two puckered layers orientated with their [110] axis normal to the surface plane. The termination is then labelled as a  $P_P$  layer. Fig.6.16(c) exhibits the additive superposition of the SSC simulations shown in (b) with itself rotated then by 72°. The highest intensity spots present in the simulations are present in the XPD images recorded for 8 to 15 ML coverage. The excellent agreement between experimental and simulated patterns (comparing for instance Fig.6.16(c) and (d)) confirms the formation of two (110) domains of the  $\gamma\text{-Al}_4\text{Cu}_9$  phase as surface alloy.

#### 6.4.3.3 X-ray photoelectron spectroscopy measurements

XPS measurements have been carried out at each stage of the Cu deposition on the  $\text{Al}_{13}\text{Co}_4(100)$  surface. The evolution of the area under the peak ratio

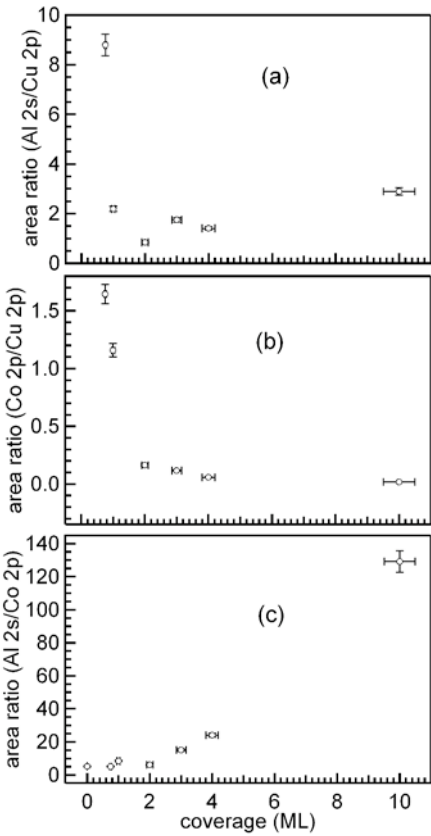


Figure 6.17: The ratio of area under the peak for (a) Al 2s to Cu 2p, (b) Co 2p to Cu 2p, and (c) Al 2s to Co 2p core levels are shown for Cu deposition at 473 K.

of the substrate (Al 2s, Co 2p) to adlayer (Cu 2p) core levels and Al 2s to Co 2p are plotted on Fig.6.17 as a function of Cu coverage deposited at 473 K. Up to 2 ML Cu coverage, the substrate signal (Al 2s and Co 2p) decreases continuously as evident from Al 2s to Cu 2p (Fig.6.17(a)) and Co 2p to Cu2p area ratio (Fig.6.17(b)). For coverages greater than 2 ML, the area ratio of Co 2p/Cu 2p remains extremely small while the area ratio of Al 2s/Cu 2p increases slowly to finally stabilise at 10 ML coverage. This indicates that the extent of intermixing of the deposited layer with the substrate at lower coverages is smaller compared to coverages  $\geq 3$  ML. More interestingly, the Al 2s/Co 2p ratio is significantly increasing with increasing Cu coverage. This evolution suggest the occurrence of demixing of the two substrate elements and an Al enrichment in the surface region probed by XPS. These observations indicate that the near surface region is mainly composed of Al and Cu atoms with almost no traces of Co atoms.

Figures 6.18 shows the substrate and adlayer core levels spectra as a function of Cu coverages. For each element, the spectra have been again normalised

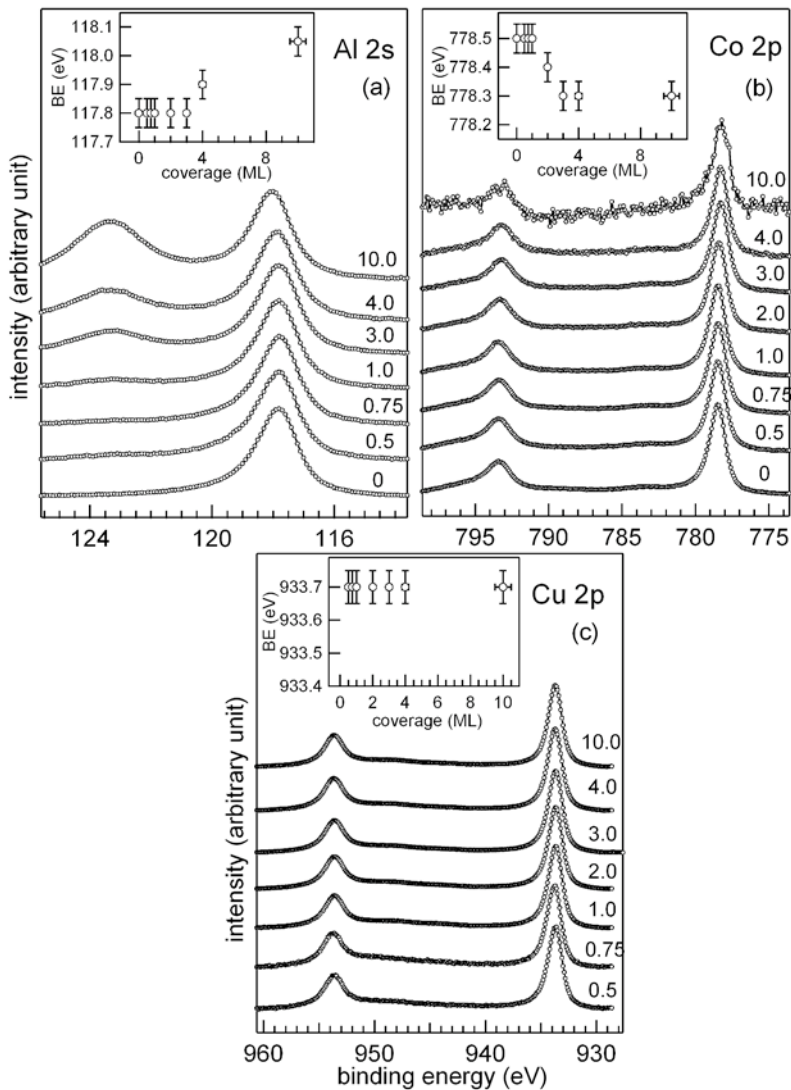


Figure 6.18: *Al 2s, Co 2p, and Cu 2p* core level spectra as a function of Cu coverage deposited at 473 K. The peaks are normalized to the highest peak height and staggered along the vertical axis. Cu coverages are indicated in terms of equivalent ML at the right hand side of the spectra. Insets show the binding energy variation of each core level as a function of Cu coverage.

to the height of the dominant peak. We have not observed any changes in the core level lineshapes (broadening) with increasing deposition. Insets show the evolution of the binding energy of Al 2s, Cu 2p, and Co 2p core levels as a function of Cu coverage. Regarding the Al 2s core level, the peak shifts towards higher BE above 3 ML to finally reach 118.05 eV for 10 ML coverage. This value is in agreement with the BE measured for Al 2s (118.10 eV) on the (110) surface of the  $\gamma\text{-Al}_4\text{Cu}_9$  single crystal. The BE position of Cu 2p is

unchanged from low to high coverage. The measured value of 933.70 eV is in good agreement with the Cu  $2p$  BE measured from the  $\gamma\text{-Al}_4\text{Cu}_9$  crystal [257]. There is a continuous shift in the BE of Co  $2p$  towards lower BE side for Cu coverage  $\geq 0.75$  ML. There is total shift of 0.2 eV between the BE of Co  $2p$  in the  $\text{Al}_{13}\text{Co}_4$  sample and after 10 ML Cu dosage, BE being then equal to 778.3 eV. With the apparent demixing of Al and Co atoms upon dosing, Co atoms should be surrounded by alike atoms. The shift in the BE of Co  $2p$  is consistent with the BE measure on a Co single crystal (778.15 eV). These measurements combined with the STM, LEED and XPD analysis confirm the formation of the  $\gamma\text{-Al}_4\text{Cu}_9$  phase for high Cu coverage deposited between 473 K and 573 K.

## 6.5 Discussion

We have investigated the growth mode of Cu thin films on the  $p\text{-}10f$  surface of the  $\text{Al}_{13}\text{Co}_4$  complex metallic alloy system. Using several techniques including STM, LEED, XPS and XPD, we have characterized Cu adsorption from submonolayer to 10 ML coverage and from 300 K up to 573 K. Prior to dosing, the  $\text{Al}_{13}\text{Co}_4$  (100) surface has been analysed by STM and LEED. As previously reported [70], the clean surface exhibits atomically flat terraces separated by a step height equal to half of the unit cell parameter ( $a/2$ ). Due to the high annealing temperature used in this study, only one surface termination has been observed on the terraces. It corresponds to the  $T1$  termination, as labelled by Addou *et al.* [70], formed by bipentagonal motifs. While only incomplete puckered layers are exposed at the topmost surface, several point defects appear within each terrace. The latter correspond to partial desorption of the bipentagonal motifs. Hence, the temperature window required to select one surface termination without the formation of defects appears to be rather narrow. However, the LEED and the XPD patterns still exhibit the  $p\text{-}10f$  symmetry of the sample surface.

The adsorption of Cu adatoms at room temperature leads to the formation of two surface structures. Up to 1 ML, we observed the formation of a pseudomorphic overlayer. The LEED pattern and the STM images confirm the  $p\text{-}10f$  symmetry of the monolayer. At this stage, the evolution of the XPS core level intensities displayed on Fig.6.8(c) indicates an Al enrichment at the surface compared to Co atoms (demixing). Hence, this monolayer is likely to contain Al and Co atoms in addition to Cu adatoms. Moreover, adatom-substrate intermixing has been reported while depositing Cu adatoms on an Al(111) surface [94]. Although pseudomorphic, the monolayer is therefore not made of a single element in contrast with Cu adsorption on the 5-fold surface of the icosahedral Al-Pd-Mn quasicrystal surface where Cu grows in a layer-by-layer manner with no intermixing [142]. Upon the growth of the second layer, step edges are first decorated (Fig.6.4(c)). This implies a higher mobility of adatoms compared to the submonolayer regime where this preferential nucleation is not observed. Above 2 ML, diffraction measurements suggest the

formation of a new phase with two (110) domains rotated by approximately 72° from each other. The lattice parameters extracted from the LEED pattern ( $a = 2.85 \pm 0.10 \text{ \AA}$ ) are in agreement with the lattice parameters expected for a CsCl type structure of Al(Cu,Co). This  $\beta$ -phase of Al(Cu,Co) is reported with a lattice parameters equal to  $a = 2.875 \text{ \AA}$  [95]. At 8 ML, the almost featureless XPD pattern of Co 2p suggests that this surface alloy is indeed mainly composed of Al and Cu atoms. This is further supported by XPS measurements which show increase in the Al/Co ratio upon deposition. An alternative to this  $\beta$  phase could have been the AlCu<sub>3</sub> phase with a lattice parameter equal to  $a = 2.956 \text{ \AA}$ , i.e. close also to the experimental parameter. This phase is excluded as it is a high temperature phase (1052 K) [95]. A similar  $\beta$ -phase has been reported previously while dosing Cu adatoms at room temperature on the icosahedral Al-Cu-Fe quasicrystal surface. The  $\beta$ -Al(Cu,Fe) was obtained after 2 ML Cu deposition [96]. As the substrate is five-fold symmetric, the LEED pattern exhibits five rotational domains rotated by 72° from each other. Hence, it is quite surprising to grow two domains with an angle of 72° on this orthorhombic substrate. As for the quasicrystal surface, the growth of the  $\beta$ -phase proceeds along the most atomically dense directions of the surface plane, i.e the [6 241 280] and [-6 -241 280] directions. The latter are defined here by the orientation of the two types of bipentagonal motifs (72.7° apart from Grin *et al.* [66]) present within a complete puckered layer.

At higher temperature (473-573 K) and up to 1 ML coverage, Cu grows pseudomorphically on the Al<sub>13</sub>Co<sub>4</sub> sample. The reduced island density (due to coalescence) at submonolayer coverage compared to room temperature deposition combined with the step edge decoration indicate a much higher adatom mobility within this temperature regime. At this temperature, the XPS measurements indicate also an enhanced diffusion of Cu adatoms within the substrate. The scale difference between Fig.6.8(a) and Fig.6.17(a) for the first stages of adsorption is characteristic of a faster Cu adatoms diffusion into the substrate. The  $p\text{-}10f$  patterns observed from XPD and LEED patterns are still present and appear much sharper. The improved quality of the diffraction pattern is explained by a better structural ordering within the monolayer. This is further confirmed using STM where irregular pentagonal-like motifs periodically distributed across the terraces are now well distinguished. Lead adsorption on the Al<sub>13</sub>Co<sub>4</sub> substrate leads to the formation of similar, although more resolved, irregular pentagonal motifs [70]. It is reasonable at this stage to postulate that the Cu pentagonal motifs should be related to the bipentagonal features present on the clean surface. The exact atomic arrangement remains to be determined. Upon additional deposition, the growth mode proceeds in a layer-by-layer manner. The formation of the  $\beta$ -Al(Cu,Co) phase is again observed above 2 ML coverage with, this time, with increased ordering within the film as revealed by the sharp diffraction spots on the LEED patterns. At coverages higher than 7.5 ML, the  $\beta$ -phase is replaced by a  $\gamma$ -Al<sub>4</sub>Cu<sub>9</sub> phase. Both phases ( $\beta$  and  $\gamma$ ) are oriented along the [110] direction and grow with two domains rotated by 72° from each other, i.e. along the bipentagonal motif

directions.

Finally, the formation of the  $\gamma$ -Al<sub>4</sub>Cu<sub>9</sub> phase seems independent of the initial structural complexity of the substrate. It appears also independent of the initial bulk composition as long as the substrate is composed of Al atoms, with the critical Al content still to be determined. A critical thickness of Cu adatoms is obviously required along with optimised deposition parameters. This conclusion is supported by recent studies which demonstrate that Cu adsorption on the icosahedral Al-Pd-Mn and Al-Cu-Fe quasicrystal surfaces leads to the formation in both cases of the  $\gamma$ -Al<sub>4</sub>Cu<sub>9</sub> phase as a surface alloy [96, 97]. In all cases, the (110) planes of the  $\gamma$ -Al<sub>4</sub>Cu<sub>9</sub> phase are exposed at the surface as they correspond to the densest bulk layers.

Although we have successfully formed a pseudomorphic monolayer, the growth of the decagonal Al-Cu-Co quasicrystalline phase has not been achieved. One of the main reasons lies in the depletion of Co in the surface near region as Cu deposition is performed. Additional work will be required, first within a higher temperature range and then with different deposition rates, to fully ascertain the (im)possibility to grow this quasicrystal phase as surface alloy.

## 6.6 Conclusions

We have further investigated the *p*-10*f* surface of the orthorhombic Al<sub>13</sub>Co<sub>4</sub> crystal. The results obtained from the clean surface demonstrate the possibility to prepare an Al<sub>13</sub>Co<sub>4</sub> (100) surface with only one type of surface termination. This surface has been used as a template for the adsorption of Cu thin films. From 300 K to 573 K, Cu adatoms grow pseudomorphically up to one monolayer. At 300 K, the  $\beta$ -Al(Cu,Co) phase appears for coverages greater than one monolayer. For higher temperature deposition, the  $\beta$ -Al(Cu,Co) phase is followed by the formation of the  $\gamma$ -Al<sub>4</sub>Cu<sub>9</sub> phase. Both  $\beta$  and  $\gamma$  phases grow as two (110) domains rotated by 72° from each other. The orientations of the bipentagonal motifs present on the clean Al<sub>13</sub>Co<sub>4</sub> (100) surface dictate the growth orientation of these domains. The initial bulk composition and structural complexity of the substrate have a minor role in the formation of the  $\gamma$ -Al<sub>4</sub>Cu<sub>9</sub> phase as long as the amount of Al and the Cu film thickness reach a critical stoichiometry.

# Chapter 7

## Conclusions and perspectives

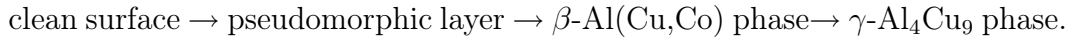
In this work, we have successfully characterised the *pseudo*-10-fold surfaces of the Al<sub>13</sub>Co<sub>4</sub> and T-Al<sub>3</sub>(Mn, Pd) crystals, which are approximants to decagonal quasicrystals. The results obtained on these two samples indicate a common trend with the conclusions drawn on other complex metallic alloys surfaces. The surfaces can be prepared by cycles of sputtering and annealing, leading to a step and terrace morphology. The step heights and the surface terminations are respectively related to the interlayer spacing and planes present within the structural bulk model. As for quasicrystals, the same criteria to select the topmost termination are preserved. Indeed, the surface planes correspond to the densest planes with the highest concentration of Al and the bulk truncation takes place at the largest interlayer gap when such applies. For the Al<sub>13</sub>Co<sub>4</sub> crystal, the incomplete puckered layer is observed at the surface. While it is initially the densest layer (26 atoms), our current model suggests the desorption of 14 atoms upon the preparation of the surface. In the case of the T-Al<sub>3</sub>(Mn, Pd) crystal, the surface termination consists of a combination of the two puckered layers (closely spaced) and the cleavage plane is indeed at the largest interlayer spacing of 1.75 Å. As in the quasicrystalline surface, no chemical segregation and/or lateral reconstruction are observed. The electronic and crystallographic structures determined experimentally are supported by and in agreement with DFT calculations. The experimental STM images are also well reproduced by the simulated images.

Following the investigation of the clean surfaces, single elements have been deposited on both samples. From room to high temperature deposition, both Pb and Cu adsorbates adopt a pseudomorphic structure up to one monolayer. The latter represent intermediate systems between clean surfaces of pure Pb and Cu crystals and the pseudomorphic films formed when adsorbed on quasicrystal surfaces. These results offer the possibility to study the electronic structure and the physical and chemical properties of Pb and Cu thin films of increasing structural complexity. Photoemission and/or scanning tunneling spectroscopy measurements should be carried out to characterize these pseudomorphic layers. These investigations may give some insight, for instance, into why the sticking coefficient of Pb appears different on the Al<sub>13</sub>Co<sub>4</sub> and

the T-Al<sub>3</sub>(Mn, Pd) surfaces above one monolayer.

We have successfully identified an initial nucleation site for Pb adatoms on the Pb/Al<sub>13</sub>Co<sub>4</sub> surface. This work should be shortly completed by a theoretical approach to ascertain the active site observed experimentally on this surface and to generate the resulting simulated STM images. As the Al<sub>13</sub>Co<sub>4</sub> crystal has been reported for its potential use in catalysis, it is crucial to identify additional potential trapped sites and to analyse further its surface reactivity. Hence, our experiments should be soon followed by the adsorption of O<sub>2</sub>, CO and NO on the Al<sub>13</sub>Co<sub>4</sub> (100) surface. Unfortunately, a similar analysis has been limited on the T-Al<sub>3</sub>(Mn, Pd) (010) sample due to the chemical disorder and the structural imperfections present at the surface.

Finally, the initial objective to evaporate Cu adatoms on the Al<sub>13</sub>Co<sub>4</sub> sample was to form the decagonal Al-Cu-Co quasicrystalline phase. Additional work will be required, within a higher temperature range and deposition rate, to fully ascertain the (im)possibility to grow this quasicrystal phase as a surface alloy. In the meantime, one can think of analysing the evolution of the electronic structure (using ARPES for instance) as the growth of the following phases proceeds:



Due to the time constraint, it has not been possible to study the deposition of Cu on the T-Al<sub>3</sub>(Mn, Pd) sample. However, it would be interesting to investigate the different phases that can be formed at the T-Al<sub>3</sub>(Mn, Pd) surface and compare them with the results obtained for the following systems: Cu/Al(111), Cu/Al<sub>13</sub>Co<sub>4</sub>, and Cu/*i*-Al-Pd-Mn.

# Appendix A

## XPD and SSC methods

### A.1 X-ray Photoelectron Diffraction

The principle of XPD is schematically shown on figure A.1(a) [258]. A spherical photoelectron wave originating from an emitter atom is elastically scattered by the neighboring atoms. The scattered parts of the electron wave interfere with the direct unscattered wave thus modulating the photoemission current as a function of the emission direction. This modulation is measured by scanning the single crystalline sample orientation with respect to the analyzer, hence sampling the photoemission intensity for different emission angles. The modulation of the photoemission intensity due to this interference depends on the kinetic energy of the photoelectron, the atomic type and electronic configuration of the scatterer and the scattering angle. At high kinetic energies ( $>500\text{eV}$ ), the so-called “forward-focussing” effect becomes dominant [258–260]. In this energy range, the scattering amplitude exhibits a sharp and pronounced peak along the nearest-neighbour directions. For simple systems (e.g. single crystal metal surfaces) this effect then allows for a direct assignment of peaks in the diffraction pattern with nearest neighbour directions in the sample. It should be noted that in general, the outgoing wave is not only scattered at one atom but is sequentially scattered from several atoms. The photoelectron energies in a photoelectron diffraction experiment typically range from about 20 eV to more than 1 keV. As illustrated on figure A.1(b), the angular dependence of the scattering amplitude is strongly influenced by the kinetic energy of the photoelectron. Below about 200 eV, the scattering amplitude has strong contributions from first and higher order interference occurring at large scattering angles. At energies above 500 eV, the atomic scattering factor strongly peaks at zero scattering angle, leading to a forward focusing of the electron flux along directions pointing from the photoemitter towards the scattering atoms. In this regime, the angular emission patterns thus allow a straightforward identification of bond directions. Most XPD experiments have been performed in the higher kinetic energy, or forward focusing, regime. The particular advantage of this kind of experiment is that prominent intensity maxima can often be identified with bond directions, and one finds that the photoelectron angular distribution is to first approximation a forward-projected image of the local

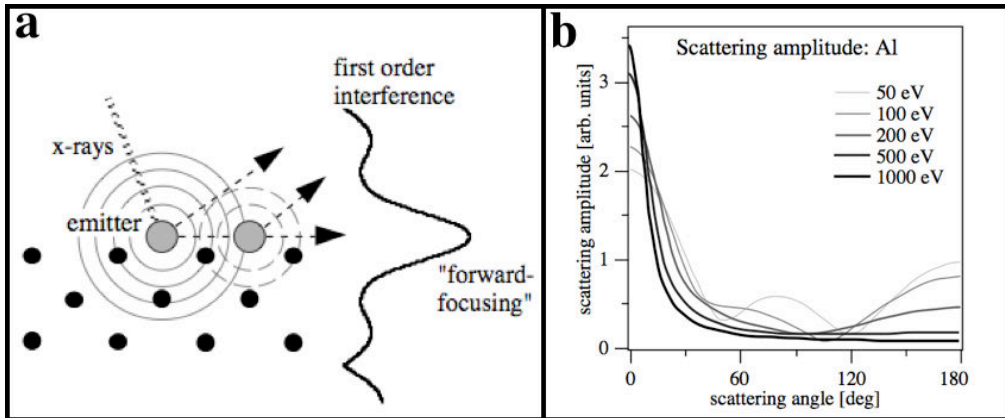


Figure A.1: (a) A schematic illustration of the principle of XPD. The photoelectron source wave emanating from the emitter-atom is diffracted by the neighbouring atoms (scatter-atoms). For each emitter-scatterer direction, a forward-focusing (FF) component and true interference related intensity modulations are present. The FF presents a dominant elastic scattering processes associated with photoelectron diffraction, which are relevant for adsorbate systems. (b) Scattering amplitude calculated for an electron plane wave incident on an Al atom at different kinetic energies. Reprinted from [261].

atomic structure around the photoemitter.

In a XPD experiment, the sample is irradiated by X-rays of sufficient energy to emit electrons from the core levels of atoms within the sample. The intensity of the photoelectrons for a certain, element characteristic peak is determined as a function of azimuthal or/and polar angle for one or a few photoelectron energies. The intensity of the photoelectron peak can also be measured as a function of electron kinetic energy by changing the incident photon energy in synchrotron radiation experiments. XPD directly probes the local geometric atomic order around an emitter and is hence sensitive to the surface and sub-surface crystallographic structure which is not accessible using the STM. The diffraction pattern will be specific to a single element corresponding to the element which emitted the photoelectron. Therefore, the structural nature of the surroundings of each element in a sample can be investigated individually. However, without theoretical simulations it is often difficult to understand the different structures appearing in XPD data and to link them to specific atomic positions of the crystal structure.

## A.2 Single Scattering Cluster Simulations

The correct interpretation of XPD patterns requires a complete theoretical approach to link a model structure to its corresponding XPD pattern. In the present work, diffraction patterns have been simulated within the framework of single scattering cluster (SSC) theory [105, 106, 259, 261]. Modelling of the ph-

toelectron diffraction process involves the following steps [262], schematically represented on figure A.2:

1. Excitation process (photon polarization vector  $\epsilon$ ); a photon impinging on an atom creates a spherical photoelectron source wave  $\exp(ikr)/r$  with quantum numbers  $(l, m)$  i.e. with given angular momentum symmetry.
2. Elastic scattering processes; the outgoing source wave is scattered off the neighbouring atoms, including single and multiple elastic scattering (complex scattering factors  $f_j(\theta_j)$ ).
3. Inelastic scattering; the outgoing wave is scattered inelastically leading to an attenuation of the wave amplitude (inelastic mean free path  $\Lambda_e$ ).
4. Incoherence due to thermal vibrations; the coherent contribution to the elastic scattering processes in a Debye-Waller type fashion (mean square atomic displacements  $\langle u_j^2 \rangle$ ) is reduced.
5. Refraction; the surface potential step leads to a refraction of the outgoing wave ( $V_0$ ).
6. Summation; different paths within the sample can lead to contributions along the same orientation in vacuum. These different contributions have to be added together for the final intensity along a given direction.

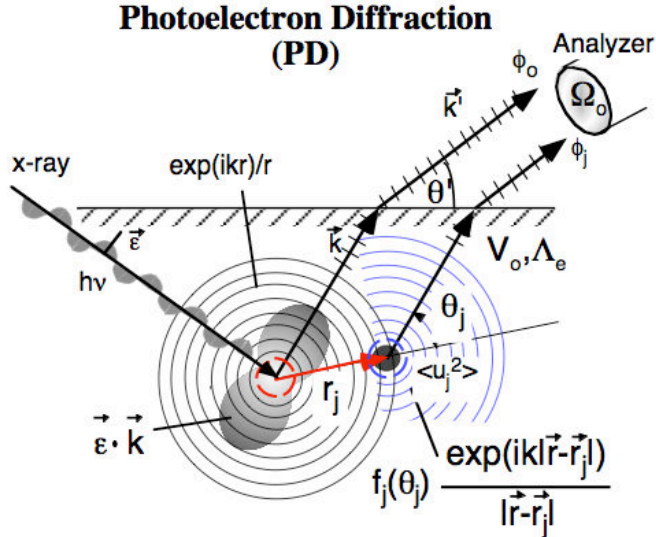


Figure A.2: A schematic illustration of the processes involved in a theoretical description of photoelectron diffraction [261].

Within this SSC approach, the intensity from a particular emitter is calculated as the square of the coherent sum of the unscattered photoelectron wave

$(\phi_0)$  and all singly scattered amplitudes  $(\phi_j)$  from neighbouring atoms  $(j)$  in a cluster representing the crystalline atomic structure of the sample. The SSC simulation has been widely used due to its simplicity and ability to correctly reproduce experimental patterns in a wide variety of cases. More involved modelling based on multiple scattering cluster (MSC) is being used increasingly in recent years [263]<sup>1</sup>. MSC overcomes some of the problems of SSC. It is used to analyze more complex diffraction features away from the FF directions that also contain useful fine structural information. For our experiments, the geometrical environment of each chemical species can be carried out using SSC calculations producing an excellent agreement between the experimental patterns and SSC simulations.

---

<sup>1</sup>entitled: “Multiple scattering of electrons in solids and molecules: A cluster-model approach”

# Bibliography

- [1] N.W. Ashcroft and N.D. Mermin, *Solid State Physics* (Fort Worth, Saunders, 1976).
- [2] D. Shechtman, I. Blech, D. Gratias, and J.W. Cahn, Phys. Rev. Lett **53**, 1951 (1984).
- [3] International Union of Crystallography, Acta Cryst. A **48**, 928 (1992).
- [4] *Basics of Thermodynamics and phase transitions in complex intermetallics* (eds. E. Belin-Ferré, World Scientific Singapore, 2008).
- [5] J.M. Dubois, *Useful Quasicrystals* (World Scientific, Singapore, 2005).
- [6] E. Belin-Ferré and A. Traverse, J. Phys.: Cond. Matter **3**, 2157 (1991).
- [7] E. Belin-Ferré, Z. Dankhazi, A. Sadoc, Y. Calvayrac, T. Klein, and J.M. Dubois, J. Phys.: Cond. Matter **4**, 4459 (1992).
- [8] E. Belin-Ferré, Z. Dankhazi, and A. Sadoc, Matter. Sci. Eng. A **181/182**, 717 (1994).
- [9] E. Belin-Ferré, Z. Dankhazi, A. Sadoc, and J.M. Dubois, J. Phys.: Cond. Matter **6**, 8771 (1994).
- [10] G. Trambly de Laissardiere, D. Nguyen-Manh, L. Magaud, J.P. Julien, F. Cyrot-Lackmann, and D. Mayou, Phys. Rev. B **52**, 7920 (1995).
- [11] E. Belin-Ferré and J.M. Dubois, J. Phys.: Cond. Matter **8**, L717 (1996).
- [12] W. Hume-Rothery, J. Inst. Met. **35**, 295 (1926).
- [13] R. Asahi, H. Sato, T. Takeuchi, and U. Mizutani, Phys. Rev. B **71**, 165103 (2005).
- [14] E. Belin-Ferré, M. Klansek, Z. Jaclic, J. Dolinsek, and J.M. Dubois, J. Phys.: Cond. Matter **17**, 6911 (2005).
- [15] T. Klein, C. Berger, D. Mayou, and F. Cyrot-Lackmann, Phys. Rev. Lett. **66**, 2907 (1991).

- [16] S.J. Poon, F. Zavaliche, and C. Beeli, *in Quasicrystals, Preparation, Properties and Applications Current Topics*, (Eds. J.M. Dubois, P.A. Thiel, A.P. Tsai and K. Urban, Materials Research Society, Pittsburgh, 1999), p. 365.
- [17] J.M. Dubois and P. Weinland, Eur. Patent 0356287 A1 and U. S. Patent 5,204,191, April 20 (1993).
- [18] Metals Handbook, *Desk Edition* (American Society for Metals International, Materials Park, Ohio, 1984).
- [19] R. Penrose, Bull. Inst. Math. Appl. **10**, 266 (1974).
- [20] C. Janot and M. de Boissieu, Phys. Rev. Lett. **72**, 1674 (1994).
- [21] C. Janot and M. de Boissieu, Phys. Rev. B **53**, 181 (1996).
- [22] D. Gratias, F. Puyraimond, M. Quiquandon, and A. Katz, Phys. Rev. B **63**, 024202 (2000).
- [23] G. Bergman, L. T. Waugh, and L. Pauling, Acta Cryst. **10**, 254 (1957).
- [24] A.R. Kortan, R.S. Becker, F.A. Thiel, and H.S. Chen, Phys. Rev. Lett. **64**, 200 (1990).
- [25] L. Barbier, D. Le Floc'h, Y. Calvayrac, and D. Gratias, Phys. Rev. Lett. **88**, 85506 (2002).
- [26] T.M. Schaub, D.E. Bürgler, H.-J. Güntherodt, and J.-B. Suck, Phys. Rev. Lett. **73**, 1255 (1994).
- [27] Z. Papadopolos, G. Kasner, J. Ledieu, E.J. Cox, N.V. Richardson, Q. Chen, R.D. Diehl, T.A. Lograsso, A.R. Ross, and R. McGrath, Phys. Rev. B **66**, 184207 (2002).
- [28] B. Unal, T.A. Lograsso, A. Rossand, C.J. Jenks, and P.A. Thiel, Phys. Rev. B **71**, 165411 (2005).
- [29] Z. Shen, C.R. Stoldt, C.J. Jenks, T.A. Lograsso, and P.A. Thiel, Phys. Rev. B **60**, 14688 (1999).
- [30] Z. Shen, M.J. Kramer, C.J. Jenks, A.I. Goldman, T.A. Lograsso, D.W. Delaney, M. Heinzig, W. Raberg, and P.A. Thiel, Phys. Rev. B **58**, 9961 (1998).
- [31] M. Krajcí, J. Hafner, J. Ledieu, and R. McGrath, Phys. Rev. B **73**, 024202 (2006).
- [32] M. Gierer, M.A. Van Hove, A.I. Goldman, Z. Shen, S.-L. Chang, C.J. Jenks, C.-M. Zhang, and P.A. Thiel, Phys. Rev. Lett. **78**, 467 (1997).

- [33] M. Gierer, M.A. Van Hove, A.I. Goldman, Z. Shen, S.-L. Chang, P.J. Pinhero, C.J. Jenks, J.W. Anderegg, C.-M. Zhang, and P.A. Thiel, Phys. Rev. B **57**, 7628 (1998).
- [34] D. Naumović, P. Aebi, L. Schlapbach, C. Beeli, T.A. Lograsso, and D.W. Delaney, *Proceedings of the 6th International on Quasicrystals (ICQ-6, Yamada Conference XLVII)* (eds. S. Takeuchi and T. Fujiwara (World Scientific), Singapore, 1998).
- [35] H.R. Sharma, K.J. Franke, W. Theis, P. Gille, Ph. Ebert, and K.H. Rieder, Phys. Rev. B **68**, 542105 (2003).
- [36] B. Bolliger, M. Erbudak, A. Hensch, and D.D. Vvedensky, Mater. Sci. Eng. A **859**, 294 (2000).
- [37] J.C. Zheng, C.H.A. Huan, A.T.S. Wee, M.A. Van Hove, C.S. Fadley, F.J. Shi, E. Rotenberg, S.R. Barman, J.J. Paggel, K. Horn, Ph. Ebert, and K. Urban, Phys. Rev. B **69**, 134107 (2004).
- [38] V. Fournée, T.C. Cai, A.R. Ross, T.A. Lograsso, J.W. Evans, and P.A. Thiel, Phys. Rev. B **67**, 033406 (2003).
- [39] O. Gröning, R. Widmer, P. Ruffieux, and P. Gröning, Phil. Mag. **86**, 773 (2006).
- [40] Z. Shen, C.J. Jenks, J. Anderegg, D.W. Delaney, T.A. Lograsso, P.A. Thiel, and A.I. Goldman, Phys. Rev. Lett **78**, 1050 (1997).
- [41] D. Rouxel, T.H. Cai, C.J. Jenks, T.A. Lograsso, A. Ross, and P. Thiel, Surf. Sci. **461**, L521 (2000).
- [42] H.R. Sharma, V. Fournée, M. Shimoda, A.R. Ross, T.A. Lograsso, A.P. Tsai, and A. Yamamoto, Phys. Rev. Lett. **93**, 165502 (2004).
- [43] T. Cai, F. Shi, Z. Shen, M. Gierer, A.I. Goldman, M.J. Kramer, C.J. Jenks, T.A. Lograsso, D.W. Delaney, P.A. Thiel, and M.A. Van Hove, Surf. Sci. **495**, 19 (2001).
- [44] T. Cai, V. Fournée, T. Lograsso, A. Ross, and P.A. Thiel, Phys. Rev. B **65**, 140202(R) (2002).
- [45] F. Shi, Z. Shen, D.W. Delaney, A.I. Goldman, C.J. Jenks, M.J. Kramer, T.A. Lograsso, P.A. Thiel, and M.A. Van Hove, Surf. Sci. **86**, 411 (1998).
- [46] J.A. Barrow, V. Fournée, A.R. Ross, P.A. Thiel, M. Shimoda, and A.P. Tsai, Surf. Sci. **539**, 54 (2003).
- [47] M. Shimoda, H.R. Sharma, and A.P. Tsai, Surf. Sci. **598**, 88 (2005).
- [48] H.R. Sharma, V. Fournée, M. Shimoda, A.R. Ross, T.A. Lograsso, P. Gille, and A.P. Tsai, Phys. Rev. B **78**, 155416 (2008).

- [49] H.R. Sharma, W. Theis, P. Gille, and K.H. Rieder, Surf. Sci. **511**, 387 (2002).
- [50] M. Kishida, T. Kamimura, R. Tamura, K. Edagawa, S. Takeuchi, T. Sato, Y. Yokoyama, J.Q. Guo, and A.P. Tsai, Phys. Rev. B **65**, 94208 (2002).
- [51] H.R. Sharma, K.J. Franke, W. Theis, A. Riemann, S. Fölsch, P. Gille, and K.H. Rieder, Surf. Sci. **561**, 121 (2004).
- [52] J. Y. Park, D. F. Ogletree, M. Salmeron, R. A. Ribeiro, P. C. Canfield, C. J. Jenks, and P. A. Thiel, Science **309**, 1354 (2005).
- [53] R. McGrath, J. Ledieu, E.J. Cox, and R.D. Diehl, J. Phys.: Condens. Matter **14**, R119 (2002).
- [54] N. Ferralis, R.D. Diehl, K. Pussi, M. Lindroos, I. Fisher, and C.J. Jenks, Phys. Rev. B **69**, 75410 (2004).
- [55] H.R. Sharma, K.J. Franke, W. Theis, A. Riemann, S. Fölsch, P. Gille, and K.H. Rieder, Phys. Rev. B **70**, 235409 (2004).
- [56] J. Yuhara, J. Kilkovits, M. Schmid, P. Varga, T. Shishido Y. Yokoyama, and K. Soda, Phys. Rev. B **70**, 24203 (2004).
- [57] M. Gierer, A. Mikkelsen, M. Gräber, P. Gille, and W. Moritz, Surf. Sci. **463**, L654 (2000).
- [58] K.J. Franke, *PhD thesis* (Free University, Berlin, Germany, 2003).
- [59] M. Shimoda, Prog. Surf. Sci. **75**, 87 (2004).
- [60] M. Shimoda, J.Q. Guo, T.J. Sato, and A.P. Tsai, Surf. Sci. **454**, 11 (2000).
- [61] V. Fournée, A.R. Ross, T.A. Lograsso, J.W. Anderegg, C. Dong, M. Kramer, I.R. Fisher, P.C. Canfield, and P.A. Thiel, Phys. Rev. B **66**, 165423 (2002).
- [62] H.R. Sharma, M. Shimoda, V. Fournée, A.R. Ross, T.A. Lograsso, and A.P. Tsai, Phys. Rev. B **71**, 224201 (2005).
- [63] R. Mäder, R. Widmer, B. Bauer, P. Gille, P. Gröning, W. Steurer, and O. Gröning, Phys. Rev. B **81**, 064201 (2010).
- [64] R. Widmer, R. Mäder, C. Pignedoli, M. Heggen, M. Feuerbacher, and O. Gröning, **to be published**, (2010).
- [65] J. Ledieu, private communication, 2009.

- [66] J. Grin, U. Burkhardt, M. Ellner, and K. Peters, *J. Alloys Comp.* **206**, 243 (1994).
- [67] M. Mihalkovič and M. Widom, *Physical Review B* **75**, 014207 (2007).
- [68] H. Klein, M. Boudard, M. Audier, M. de Boissieu, H. Vincent, L. Beraha, and M. Duneau, *Phil. Mag. Lett.* **75**, 197 (1997).
- [69] K. Hiraga, M. Kaneko, Y. Matsuo, and S. Hashimoto, *Phil. Mag. B* **67**, 193 (1993).
- [70] R. Addou, E. Gaudry, Th. Deniozou, M. Heggen, M. Feuerbacher, P. Gille, Yu. Grin, R. Widmer, O. Gröning, V. Fournée, J.M. Dubois, and J. Ledieu, *Phys. Rev. B* **80**, 014203 (2009).
- [71] Th. Deniozou, R. Addou, A. Shukla, , M. Heggen, M. Feuerbacher, R. Widmer, O. Gröning, M. Krajcí, J. Hafner, V. Fournée, J.M. Dubois, and J. Ledieu, submitted to *Phys. Rev. B* (2010).
- [72] X.Z. Li and K. Hiraga, *J. Alloy comp.* **269**, L13 (1998).
- [73] E. Cockayne and M. Widom, *Philos. Mag. A* **77**, 593 (1998).
- [74] T. Goedecke, *Z. Metallkd.* **62**, 842 (1971).
- [75] J. Grin, U. Burkhardt, M. Ellner, and K. Peters, *Z. Kristallogr.* **209**, 479 (1994).
- [76] P.J. Black, *Acta Crystallographica* **8**, 43 (1955).
- [77] R.C. Hudd and W.H. Taylor, *Acta Cryst. A* **15**, 441 (1962).
- [78] K. Saito, K. Sugiyama, and K. Hiraga, *Mat. Sci. Engineering* **294**, 279 (2000).
- [79] C.L. Henley, *J. Non-Cryst. Solids* **153-154**, 172 (1993).
- [80] Y. Matsuo, M. Kaneko, T. Yamanoi, N. Kaji, K. Sugiyama, and K. Hiraga, *Phys. Mag. Lett.* **76**, 357 (1997).
- [81] M.A. Taylor, *Acta Cryst.* **14**, 84 (1961).
- [82] J. Ledieu, E.J. Cox, R. McGrath, N.V. Richardson, Q. Chen, V. Fournée, T.A. Lograsso, A.R. Ross, K.J. Caspersen, B. Unal, J.W. Evans, and P.A. Thiel, *Surf. Sci.* **583**, 4 (2005).
- [83] V. Fournée, P.J. Pinhero, J.W. Anderegg, T.A. Lograsso, A.R. Ross, P.C. Canfield, I.R. Fisher, and P.A. Thiel, *Phys. Rev. B* **62**, 14049 (2000).
- [84] B. Unal, C.J. Jenks, and P.A. Thiel, *Phys. Rev. B* **77**, 195419 (2008).
- [85] D.C. Langreth, *Phys. Rev. B* **1**, 471 (1970).

- [86] A.K. Shukla, P. Krüger, R.S. Dhaka, D.I. Sayago, K. Horn, and S.R. Barman, Phys. Rev. B **75**, 235419 (2007).
- [87] E. Bauer and J.H. van der Merwe, Phys. Rev. B **33**, 3657 (1986).
- [88] J. Ledieu, L. Leung, L.H. Wearing, R. McGrath, T.A. Lograsso, D. Wu, and V. Fournée, Phys. Rev. B **77**, 073409 (2008).
- [89] Th. Deniozou, J. Ledieu, V. Fournée, D. M. Wu, T. A. Lograsso, H. I. Li, and R. D. Diehl, Phys. Rev. B **79**, 245405 (2009).
- [90] E. Johnson, A. Johansen, U. Dahmen, S. Chen, and T. Fujii, Mat. Sci. Eng. A **304-306**, 187 (2001).
- [91] V. Matolín, I. Matolínová, N. Tsud, S. Fabík, J. Libra, V. Dudr, V. Cháb, and K.C. Prince, Phys. Rev. B **74**, 075416 (2006).
- [92] J.A Smerdon, L. Leung, J.K. Parle, C.J. Jenks, R. McGrath, V. Fournée, and J. Ledieu, Surf. Sci. **602**, 2496 (2008).
- [93] J. Ledieu, M. Krajčí, J. Hafner, L. Leung, L.H. Wearing, R. McGrath, T.A. Lograsso, D. Wu, and V. Fournée, Phys. Rev. B **79**, 245405 (2009).
- [94] C.J. Barnes, H. Asonen, A. Salokatve, and M. Pessa, Surf. Sci. **184**, 163 (1987).
- [95] P. Villars and L. D. Calvert, *Pearson's Handbook of Crystallographic Data for Intermetallic Phases* (American Society for Metals International, Materials Park, Ohio, 1998).
- [96] T. Duguet, E. Gaudry, T. Deniozou, J. Ledieu, M.C. de Weerd, T. Belmonte, J.M. Dubois, and V. Fournée, Phys. Rev. B **80**, 205412 (2009).
- [97] M. Bielmann, A. Barranco, P. Ruffieux, O. Gröning, R. Fasel, R. Widmer, and P. Gröning, Adv. Eng. Mat. **7**, 392 (2005).
- [98] C. Janot, *Quasicrystals: A Primer*. (2nd ed. Oxford University Press, Oxford, 1994).
- [99] A. P. Tsai and M. Yoshimura, Applied Catalysis (2001).
- [100] M. Audier, M. Durand-Charre, and M. De Boissieu, Phil. Mag. B **68**, 607 (1993).
- [101] M. Krajčí and J. Hafner, Phys. Rev. B **71**, 054202 (2005).
- [102] X.Z. Li and K.H. Kuo, Phil. Mag. B **65**, 525 (1992).
- [103] G. Binning, H. Rohrer, Ch. Gerber, and E. Weibel, Phys. Rev. Lett **49**, 57 (1982).

- [104] C. Davisson and L.H. Germer, Phys. Rev. **30**, 705 (1927).
- [105] P.A. Lee, Phys. Rev. B **13**, 5261 (1976).
- [106] S. Kono, S.M. Goldberg, N.F.T. Hall, and C.S. Fadley, Phys. Rev. B **22**, 6085 (1980).
- [107] C. Dong, Q.H. Zhang, D.H. Wang, and Y.M. Wang, Euro. Phys. J. B **6**, 25 (1998).
- [108] C. Dong, J. Phys. (Paris) **5**, 1625 (1995).
- [109] L. Bindi, P.J. Steinhardt, N. Yao, and P.J. Lu, Science **324**, 1306 (2009).
- [110] L. Pauling, Am. Scientist **43**, 215 (1955).
- [111] S. Samson, Nature **195**, 259 (1962).
- [112] S. Samson, Acta Crystallogr. **19**, 401 (1965).
- [113] S. Samson, Acta Crystallogr. **23**, 586 (1967).
- [114] S. Samson, Acta Crystallogr. **17**, 491 (1964).
- [115] M. Cooper, K. Robinson, and L. Pauling, Acta Cryst. **20**, 614 (1966).
- [116] M. Boudard, M. de Boissieu, C. Janot, G. Heger, C. Beeli, H.-U. Nissen, H. Vincent, R. Ibberson, M. Audier, and J.M. Dubois, J. Phys.: Cond. Matter **4**, 10149 (1992).
- [117] A.P. Blandin, *Phase stability in metals and alloys* (eds. P.S. Rudman, J. Stringer, R.I. Jaffee, McGraw Hill, New York, 1965), p. 115.
- [118] A.P. Tsai, J. Non-Cryst. Sol. **334-335**, 317 (2004).
- [119] H. Jones, Proc. Phus. Soc. **49**, 250 (1937).
- [120] G. Trambly de Laissardiere, D. Nguyen-Manh, and D. Mayou, Progress in Materials Science **50**, 679 (2005).
- [121] M. Krajčí, J. Hafner, and M. Mihalkovič, Phys. Rev. B **55**, 119 (1997).
- [122] J.M. Dubois, *New Horizons in Quasicrystals: Research and Applications* (eds. A.I. Goldman and D.J. Sordelet and P.A. Thiel and J.M. Dubois (World Scientific), Singapore, 1997).
- [123] J.M. Dubois, Physica Scripta **T49 A**, 17 (1993).
- [124] J.M. Dubois, P. Plaindoux, E. Bellin-Ferré, N. Tamura, and D. J. Sordelet, *Proc. 6th. Int. Conf. on Quasicrystals* (eds. S. Takeuchi and T. Fujiwara (World Scientific), Singapore, 1998).

- [125] N. Rivier and D. Boose, *Proc. 5th. Int. Conf. on Quasicrystals* (eds. C. Janot and R. Mosseri (World Scientific), Singapore, 1995).
- [126] W. Steurer, T. Haibach, B. Zhang, S. Kek, and R. Luck, *Acta. Crystallogr., Sect. B: Struct. Sci.* **49**, 661 (1993).
- [127] A. Yamamoto, *Acta Cryst.* **52**, 508 (1996).
- [128] A. Yamamoto and S. Weber, *Phys. Rev. Lett.* **78**, 4430 (1997).
- [129] W. Steurer and T. Haibach, *In Physical Properties of Quasicrystals* (Eds. Z.M. Stadnik (Springer), Berlin, 1999), p. 86.
- [130] N. Ferralis, K. Pussi, E.J. Cox, M. Gierer, J. Ledieu, I.R. Fisher, C.J. Jenks, M. Lindroos, R. McGrath, and R.D. Diehl, *Phys. Rev. B* **69**, 153404 (2004).
- [131] J. Y. Park, D. F. Ogletree, M. Salmeron, R. A. Ribeiro, P. C. Canfield, C. J. Jenks, and P. A. Thiel, *Phys. Rev. B* **72**, 220201 (2005).
- [132] M. Krajčí, J. Hafner, and M. Mihalkovič, *Phys. Rev. B* **73**, 134203 (2006).
- [133] M. Feuerbacher, C. Thomas, and K. Urban, *in Quasicrystals, Structure and Physical Properties* (eds. H.-R. Trebin, (Wiley-VCH, Weinheim), 2003).
- [134] J. Ledieu, C.A. Muryn, G. Thornton, R.D. Diehl, T.A. Lograsso, D.W. Delaney, and R. McGrath, *Surf. Sci. Lett.* **472**, 89 (2001).
- [135] J. Ledieu, R. McGrath, R.D. Diehl, T.A. Lograsso, A.R. Ross, Z. Papadopolos, and G. Kasner, *Surf. Sci. Lett.* **492**, L729 (2001).
- [136] R. McGrath, J. Ledieu, and R.D. Diehl, *Progress in Surface Science* **75**, 131 (2004).
- [137] S. Ohhashi, J. Hasegawa, and S. Takeuchi, *Phil. Mag.* **87**, 3089 (2007).
- [138] H.R. Sharma, M. Shimoda, K. Sagisaka, H. Takakura, J. A. Smerdon, P.J. Nugent, R. McGrath, D. Fujita, S. Ohhashi, and A.P.Tsai, *Phys. Rev. B* **80**, 121401(R) (2009).
- [139] V. Fournée, J.A. Barrow, M. Shimoda, A.R. Ross, T.A. Lograsso, P.A. Thiel, and A.P. Tsai, *Surf. Sci.* **541**, 147 (2003).
- [140] M. Boudard, H. Klein, M. de Boissieu, M. Audier, and H. Vincent, *Phil. Mag. A* **74**, 939 (1996).
- [141] T. Cai, J. Ledieu, R. McGrath, V. Fournée, T.A. Lograsso, A.R. Ross, and P.A. Thiel, *Surf. Sci.* **526**, 115 (2003).

- [142] J. Ledieu, J.-T. Hoeft, D.E. Reid, J.A. Smerdon, R.D. Diehl, T.A. Lograsso, A.R. Ross, and R. McGrath, Phys. Rev. Lett. **92**, 135507 (2004).
- [143] J. Ledieu, J.-T. Hoeft, D.E. Reid, J.A. Smerdon, R.D. Diehl, N. Ferralis, T.A. Lograsso, A.R. Ross, and R. McGrath, Phys. Rev. B **72**, 35420 (2005).
- [144] H.R. Sharma, M. Shimoda, A.R. Ross, T.A. Lograsso, and A.P. Tsai, Phys. Rev. B **72**, 45428 (2005).
- [145] J. Ledieu, P. Unsworth, T.A. Lograsso, A.R. Ross, and R. McGrath, Phys. Rev. B **73**, 012204 (2006).
- [146] H.R. Sharma, M. Shimoda, and A.P. Tsai, Advances in Physics **56**, 403 (2007).
- [147] L. Leung, J. Ledieu, L. Unsworth, T.A. Lograsso, A.R. Ross, and R. McGrath, Surf. Sci. **600**, 4752 (2006).
- [148] M. Shimoda, J.Q. Guo, T.J. Sato, and A.P. Tsai, Phys. Rev. B **62**, 11288 (2000).
- [149] M. Shimoda, J.Q. Guo, T.J. Sato, and A.P. Tsai, Surf. Sci. **507-510**, 276 (2000).
- [150] M. Shimoda, J.Q. Guo, T.J. Sato, and A.P. Tsai, Jpn. J. Appl. Phys. **40**, 6073 (2001).
- [151] M. Shimoda, T.J. Sato, A.P. Tsai, and J.Q. Guo, J. Alloys Compd. **342**, 441 (2002).
- [152] V. Fournée, A.R. Ross, T.A. Lograsso, and P.A. Thiel, Mat. Res. Soc. Symp. Proc. **805**, LL8.3.1 (2004).
- [153] S. Curtarolo, W. Setyawan, N. Ferralis, R.D. Diehl, and M.W. Cole, Phys. Rev. Lett. **95**, 136104 (2005).
- [154] R. Luescher, T. Fluckiger, M. Erbudak, and A.R. Kortan, Phys. Rev. B **68**, 212203 (2003).
- [155] R. Luescher, M. Erbudak, and Y. Weisskopf, Surf. Sci. **569**, 163 (2004).
- [156] B. Bolliger, V.E. Dmitrienko, M. Erbudak, R. Lüscher, H.-U. Nissen, and A.R. Kortan, Phys. Rev. B **63**, 052203 (2001).
- [157] Y. Weisskopf, R. Luescher, and M. Erbudak, Surf. Sci. **578**, 35 (2005).
- [158] V. Fournée, M. Shimoda, A.R. Ross, T.A. Lograsso, J.W. Lograsso, and P.A. Thiel, Surf. Sci. **537**, 5 (2003).

- [159] K.J. Franke, H.R. Sharma, W. Theis, P. Gille, P. Ebert, and K.H. Rieder, Phys. Rev. Lett. **89**, 156104 (2002).
- [160] W. Theis, H.R. Sharma, K.J. Franke, and K.H. Rieder, in *Quasi Crystals-Structure and Physical Properties* (eds. J. Trebin, (Wiley-VCH, GmbH, Germany), 2003).
- [161] V. Fournée, H.R. Sharma, M. Shimoda, A.P. Tsai, B. Unal, A.R. Ross, T.A. Lograsso, and P.A. Thiel, Phys. Rev. Lett. **95**, 155504 (2005).
- [162] L. Huang, S. J. Chey, and J. H. Weaver, Surf. Sci. **416**, L1101 (1998).
- [163] V. YehL. Berbil-Bautista, C.Z. Wang, K.M. Ho, and M.C. Tringides, Phys. Rev. Lett. **85**, 5158 (2000).
- [164] T. Nagao, J.T. Sadowski, M. Saito, S. Yaginuma, Y. Fujikawa, T. Kogure, T. Ohno, Y. Hasegawa, S. Hasegawa, and T. Sakurai, Phys. Rev. Lett. **93**, 105501 (2004).
- [165] D.A. Evans, M. Alonso, R. Cimino, and K. Horn, Phys. Rev. Lett. **70**, 3483 (1993).
- [166] D.-A. Luh, T. Miller, J.J. Paggel, M. Y. Chou, and T.-C. Chiang, Science **292**, 1131 (2001).
- [167] A. Vasquez de Parga R.Otero and R. Miranda, Phys. Rev. B **66**, 115401 (2002).
- [168] P. Moras, Y. Weisskopf, J.-N. Longchamp, M. Erbudak, P. H.Zhou, L. Ferrari, and C. Carbone, Phys. Rev. B **74**, 121405 (2006).
- [169] P. Gille and B. Bauer, Cryst. Res. Technol. **43**, 1161 (2008).
- [170] N. Shramchenko and F. Dénoyer, Eur. Phys. J. B **29**, 51 (2002).
- [171] T. Goedecke and M. Ellner, Z. Metallkd. **87**, 854 (1996).
- [172] B. Grushko and T. Velikanova, CALPHAD **31**, 217 (2007).
- [173] D. Naumović, P. Aebi, L. Schlapbach, C. Beeli, K. Kunze, T.A. Lograsso, and D.W. Delaney, Phys. Rev. Lett. **87**, 195506 (2001).
- [174] G. Kresse and J. Furthmüller, Phys. Rev. B **54**, 11169 (1996).
- [175] G. Kresse and J. Furthmüller, Computational Materials Science **6**, 15 (1996).
- [176] S. Baroni, A. Dal Corso, S. de Gironcoli, P. Giannozzi, C. Cavazzoni, G. Ballabio, S. Scandolo, G. Chiaroyyi, P. Focher, A. Pasquarello, K. Laasonen, A. Trave, R. Car, N. Marzari, and A. Kokalj, <http://www.pwscf.org>.

- [177] J. P. Perdew, K. Burke, and M. Ernzerhof, Phys. Rev. Lett. **77**, 3865 (1996).
- [178] D. Vanderbilt, Physical Review B **41**, 7892 (1990).
- [179] N. Troullier and J. L. Martins, Physical Review B **43**, 1993 (1991).
- [180] J. Tersoff and D. R. Hamann, Physical Review B **31**, 805 (1985).
- [181] F. Jona, D. Sondericker, and T.M. Marcus, J. Phys. C **9**, 1405 (1976).
- [182] H.B. Nielsen and D.L. Adams, J. Phys. C **15**, 615 (1982).
- [183] J.R. Noonan and H.L. Davis, J. Vac. Sci. Technol. A **8**, 2671 (1990).
- [184] C. Stampfl, M. Scheffler, H. Over, J. Burchhardt, M. Nielsen, D.L. Adams, and W. Moritz, Phys. Rev. B **49**, 4959 (1994).
- [185] J. L. F. Da Silva, C. Stampfl, and M. Scheffler, Surface Science **600**, 703 (2006).
- [186] A. Kiejna and B.I. Lundqvist, Phys. Rev. B **63**, 085405 (2001).
- [187] J. Stewart, O. Pohland, and J.M. Gibson, Phys. Rev. B **49**, 13848 (1994).
- [188] M. Polak and L. Rubinovich, *Surface alloys and alloy surfaces* (Eds. D.P. Woodruff (Elsevier), Amsterdam, 2002), p. 86.
- [189] M. Widom and E. Cockayne, Physica A **232**, 713 (1996).
- [190] Yu. Grin, B. Bauer, U. Burkhardt, R. Cardoso-Gil, J. Dolinský, M. Feuerbacher, P. Gille, F. Haarmann, M. Heggen, P. Jeglič, M. Müller, S. Paschen, W. Schnelle, and S. Vrtník, EUROMAT 2007: European Congress on Advanced Materials and Processes, Nürnberg, Germany, 2007.
- [191] P. Jeglič, M. Heggen, M. Feuerbacher, B. Bauer, P. Gille, and F. Haarmann, Journal of Alloy and Compounds **480**, 141 (2009).
- [192] H. Klein, M. Durand-Charre, and M. Audier, J. Alloys Compd. **296**, 128 (2000).
- [193] K. Robinson, Acta Cryst. **7**, 494 (1954).
- [194] M. Krajcí, M. Windisch, J. Hafner, G. Kresse, and M. Mihalkovič, Phys. Rev. B **51**, 17355 (1995).
- [195] J. Ledieu, C.A. Muryn, G. Thornton, G. Cappello, J. Chevrier, R.D. Diehl, T.A. Lograsso, D.W. Delaney, and R. McGrath, Mater. Sci. Eng. A. **294**, 871 (2000).

- [196] G. Neuhold, S.R. Barman, K. Horn, W. Theis, Ph. Ebert, and K. Urban, J. Phys. Cond. Matt **58**, 734 (1998).
- [197] V. Fournée, J.W. Anderegg, A.R. Ross, T.A. Lograsso, , and P.A. Thiel, J. Phys. Cond. Matt **14**, 2691 (2002).
- [198] K. Horn, W. Theis, J.J. Paggel, S.R. Barman, E. Rotenberg, Ph. Ebert, and K. Urban, J. Phys. Cond. Matt **18**, 435 (2006).
- [199] G. Kresse and D. Joubert, Phys. Rev. B **59**, 1758 (1999).
- [200] J.P. Perdew and Y. Wang, Phys. Rev. B **45**, 13244 (1992).
- [201] P.E. Blöchl, Phys. Rev. B **50**, 17953 (1994).
- [202] M. Mihalkovič and M. Widom, alloy database at <http://alloy.phys.cmu.edu/46> .
- [203] J. Ledieu and R. McGrath, J. Phys.: Condens. Matter **15**, S3113 (2003).
- [204] W. Steurer, private communication, 2009.
- [205] Z.M. Stadnik, D. Purdie, M. Garnier, Y. Baer, A.-P. Tsai, A. Inoue, K. Edagawa, , and S. Takeuchi, Phys. Rev. Lett. **77**, 1777 (1996).
- [206] Z.M. Stadnik, D. Purdie, M. Garnier, Y. Baer, A.-P. Tsai, A. Inoue, K. Edagawa, S. Takeuchi, and K.H.J. Buschow, Phys. Rev. B **55**, 10938 (1997).
- [207] A.K. Shukla, C. Biswas, R.S. Dhaka, S.C. Das, P. Krüger, and S.R. Barman, Phys. Rev. B **77**, 195103 (2008).
- [208] M. Mori, S. Matsuo, T. Ishimasa, T. Matsuura, K. Kamiya, H. Inokuchi, and T. Matsukawa, J. Phys: Cond. Matter **3**, 767 (1991).
- [209] M. Krajcí and J. Hafner, Phys. Rev. B **80**, 214419 (2009).
- [210] C.J. Jenks, S.-L. Chang, J.W. Anderegg, P.A. Thiel, and D.W. Lynch, Phys. Rev. B **54**, 6301 (1996).
- [211] M. Krajcí, J. Hafner, and M. Mihalkovič, Phys. Rev. B **55**, 843 (1997).
- [212] V. Fournée, E. Belin-Ferré, P. Pêcheur, J. Tobola, Z. Dankhazi, A. Sadoc, and H. Müller, J. Phys. Cond. Matt **14**, 87 (2002).
- [213] A.P. Tsai, J.Q. Guo, E. Abe, H. Takakura, and T.J. Sato, Nature **408**, 537 (2000).
- [214] H. Takakura, C.P. Gómez, A. Yamamoto, M. De Boissieu, and A.P. Tsai, Nature Materials **6**, 58 (2007).
- [215] M. Krajcí and J. Hafner, Phys. Rev. B **71**, 184207 (2005).

- [216] M. Krajčí and J. Hafner, Phys. Rev. B **75**, 224205 (2007).
- [217] M. Krajčí and J. Hafner, Phys. Rev. B **77**, 134202 (2008).
- [218] J.A Smerdon, J.K. Parle, L.H. Wearing, T.A. Lograsso, A.R. Ross, and R. McGrath, Phys. Rev. B **78**, 075407 (2008).
- [219] W. Setyawan, R.D. Diehl, and S. Curtarolo, Physical Review Letters **102**, 055501 (2009).
- [220] J. H. Dil, J. W. Kim, S. Gokhale, M. Tallarida, and K. Horn, Physical Review B **4**, 045405 (2004).
- [221] E. Ogando, N. Zabala, E. V. Chulkov, and M. J. Puska, Physical Review B **15**, 153410 (2004).
- [222] F. Calleja, M. C. Passeggi, J. J. Hinarejos, A. L. de Parga, and R. Miranda, Physical Review Letters **97**, 186104 (2006).
- [223] Y. Guo, Y.-F. Zhang, X.-Y. Bao, T.-Z. Han, Z. Tang, L.-X. Zhang, W.-G. Zhu, E.G. Wang, Q. Niu, Z.Q. Qiu, J.-F. Jia, Z.-X. Zhao, and Q.-K. Xue, Science **306**, 1915 (2004).
- [224] M.M. Özer, C.-Z. Wang, Z. Zhang, and H.H. Weitering, Journal of Low Temperature Physics **157**, 221 (2009).
- [225] M.P. Seah and W.A. Dench, Surface and Interface Analysis **1**, 2 (1979).
- [226] D. Briggs and M. P. Seah, *Practical Surface Analysis by Auger and X-ray Photoelectron Spectroscopy* (John Wiley and Sons Ltd., New York, YEAR).
- [227] S. Tougaard, Surface Science **216**, 343 (1989).
- [228] A.K. Shukla, S. Banik, R.S. Dhaka, C. Biswas, S.R. Barman, and H. Haak, Review of Scientific Instruments **75**, 4467 (2004).
- [229] J.J. Yeh and I. Lindau, Atomic Data and Nuclear Data Tables **32**, 1 (1985).
- [230] A. K. Shukla, R. S. Dhaka, S. W. D'Souza, Sanjay Singh, D. Wu, T. A. Lograsso, M. Krajčí, J. Hafner, K. Horn, and S. R. Barman, Phys. Rev. B **79**, 134206 (2009).
- [231] A.K. Shukla, R.S. Dhaka, S.W. D'Souza, M. Maniraj, S.R. Barman, K. Horn, Ph. Ebert, K. Urban, D. Wu, and T.A. Lograsso, J. Phys.: Condens. Matter **21**, 405005 (2009).
- [232] A.K. Shukla, R.S. Dhaka, C. Biswas, S. Banik, S.R. Barman, K. Horn, Ph. Ebert, and K. Urban, Phys. Rev. B **73**, 054432 (2006).

- [233] U. Mizutani, J. Phys.:Condens. Matter **10**, 4609 (1998).
- [234] U. Mizutani, T. Takeuchi, and H. Sato, Progress in Materials Science **49**, 227 (2004).
- [235] E. Belin-Ferré and J.M. Dubois, Int. J. Mat. Res. **97-7**, 985 (2006).
- [236] J.M. Dubois, P. Brunet, and E. Belin-Ferré, in *Quasicrystals: Current Topics* (eds. edited by E. Belin-Ferre, C. Berger, M. Quiquandon and A. Sadoc (World Scientific,, Singapore, 2000).
- [237] J. Y. Park and P. A. Thiel, J. Phys.: Condens. Matter **20**, 314012 (2008).
- [238] R. McGrath, J. Smerdon, H.R. Sharma, W. Theis, and J. Ledieu, J. Phys.: Cond. Matter (2009).
- [239] W. Setyawan, R.D. Diehl, N. Ferralis, M.W. Cole, and S. Curtarolo, J. Phys.: Cond. Matter **19**, 016007 (2007).
- [240] J.A Smerdon, L. Leung, J.K. Parle, C.J. Jenks, R. McGrath, V. Fournée, and J. Ledieu, Phys. Rev. B **78**, 075407 (2008).
- [241] J.A Smerdon, J. Ledieu, J.T. Hoeft, D.E. Reid, L.H. Wearing, R.D. Diehl, T.A. Lograsso, A.R. Ross, and R. McGrath, Phil. Mag. **86**, 841 (2006).
- [242] D. Reid, J.A Smerdon, J. Ledieu, and R. McGrath, Surf. Sci. **600**, 4132 (2006).
- [243] H.R. Sharma, M. Shimoda, V. Fournée, A.R. Ross, T.A. Lograsso, and A.P. Tsai, Applied Surface Science **241**, 256 (2005).
- [244] T. Duguet, Ledieu, J., J.M. Dubois, and V. Fournée, Journal of Physics Condensed Matter **20**, 314009 (2008).
- [245] T. Duguet, E. Gaudry, T. Deniozou, J. Ledieu, M.C. de Weerd, T. Belmonte, J.M. Dubois, and V. Fournée, to be published **111**, 111 (2009).
- [246] T. Grenet, F. Giroud, J. L. Joulaud, and M. Capitan, Phil. Mag. A **82**, 2909 (2002).
- [247] C. Dong, J.M. Dubois, S.S. Kang, and M. Audier, Phil. Mag. B **65**, 107 (1992).
- [248] C. Dong and J.M. Dubois, J. Non-Cryst. Solids **159**, 107 (1993).
- [249] S. Andersson and B.G. Hyde, J. Solid State Chem. **9**, 92 (1974).
- [250] A.J. Bradley, Nature **168**, 661 (1951).
- [251] C. Dong, Phil. Mag. A **73**, 1519 (1996).

- [252] W. Steurer, J. Phys.: Condens. Matter **3**, 3397 (1991).
- [253] J. D. R. Buchanan, T. P. A. Hase, B. K. Taner, P. J. Chen, L. Gan, C. J. Powell, and W. F. Eglhoff, Phys. Rev. B **66**, 104427 (2002).
- [254] M. Čekada, P. Panjan, J. Dolinšek, A. Zalar, Z. Medunić, M. Jakšić, and N. Radič, Thin Solid Films **515**, 7135 (2007).
- [255] J.M. Vandenberg and R.A. Hamm, Thin Solid Films **97**, 313 (1982).
- [256] H.G. Jiang, J.Y. Dai, H.Y. Tong, B.Z. Ding, Q.H. Song, and Z.Q. Hu, J. Appl. Phys. **74**, 6165 (1993).
- [257] E. Gaudry A. Shukla, M.C. de Weerd, T. Duguet, J.M. Dubois, J. Ledieu, and V. Fournée, in preparation (2009).
- [258] C.S. Fadley and S.A.L. Bergström, Phys. Lett. A. **19**, 375 (1971).
- [259] C.S. Fadley, in *Synchrotron Radiation Research: Advances in Surface Science* (eds. R. Z. Bachrach, Plenum, New York, 1990).
- [260] W.F. Egelhoff, Crit. Rev. Solid. State Mat. Sci. **16**, 213 (1990).
- [261] R. Fasel, *Adsorbed monolayers and submonolayers studied by angle-scanned photoemission*, PhD thesis (Fribourg University, Fribourg (Schweiz), 1996).
- [262] C.S. Fadley, in *Progress in Surface Science* (eds. S. G. Davison, Pergamon, New York, 1990), Vol. 16.
- [263] F.J. Garcia de Abajo, M.A. Van Hove, and C.S. Fadley, Phys. Rev. B **63**, 075404 (2001).

# Curriculum Vitae

Name Rafik ADDOU  
Date of Birth 19/03/1981  
Nationality Moroccan/French

## Education

- Mars 2010 Doctorate in Science and Engineering of Materials and Metallurgy at the “Institut National Polytechnique de Lorraine”, Nancy (France).
- 2005/2006 Université d’Aix-Marseille II (France).  
2nd year Master Physics of Materials and Nanosciences.
- 2004/2005 Université d’Aix-Marseille II.  
1st year Master Physics and Sciences of Materials.
- 2003/2004 Université Mohamed Premier, Oujda (Morocco).  
Mastery: Physical Sciences, mention: Electronic.
- 2002/2003 Université Mohamed Premier, Oujda.  
Bachelor: Physical Sciences, mention: Physics.

## Communications

### Oral talks:

\* 27-28 April 2009: 3rd workshop of the European Network of Excellence Complex Metallic Alloys, Berlin.

“Growth of Cu thin films on the (100) surface of the orthorhombic  $Al_{13}Co_4$  crystal”

\* 06-11 July 2008: 10th International Conference on Quasicrystals, Zürich.  
“Surface Structure Investigations of the Orthorhombic  $Al_{13}Co_4$  and T- $Al_3(Mn, Pd)$  Approximants”

\* 27 June 2008: Ecole Nationale des Mines, Nancy.  
“Complex Metallic Alloys Surfaces:  $Al_{13}Co_4$  and T- $Al_3(Mn, Pd)$ ”

\* 02 October 2007: Empa, Swiss Federal Laboratories for Materials Testing and Research, “nanotech@surfaces” Laboratory, Thun (Switzerland).  
“Surface Structures of the Orthorhombic T- $Al_3(Mn, Pd)$  and  $Al_{13}Co_4$  Approximants”

\* 21 November 2007: “Empa PhD Symposium”, Dübendorf (Switzerland).  
“*The Surface Structure of the T-Al<sub>3</sub>(Mn,Pd) Complex Metallic Alloy*”

**Posters:**

- 04-07 Octobre 2009, 1st International Conference on Complex Metallic Alloys and their Complexity C-MAC1, Nancy (France).

“*Lead Adsorption on the Pseudo-10-fold Surface of the Orthorhombic Al<sub>13</sub>Co<sub>4</sub>*”

- 30 August - 04 Septembre 2009, European conference on surface science ECOSS26, Parma (Italy).

“*Lead Adsorption on the Pseudo-10-fold Surface of the Orthorhombic Al<sub>13</sub>Co<sub>4</sub>*”

- 27-29 January 2009, Surface and Interface Day, Nancy.

“*Surface Structure Investigation of the Orthorhombic Al<sub>13</sub>Co<sub>4</sub>*”

- 25-31 May 2008, 3rd European School in Materials Sciences, Ljubljana (Slovenia). **First Prize for this poster presentation.**

First Prize for Poster presentation “*Surface Structure Investigation of the Orthorhombic Al<sub>13</sub>Co<sub>4</sub>*”

- 21-23 May 2008, International WorkShop SPLDS (Statistical Physics and Low Dimensional Systems), Nancy.

“*Surface Structure Investigation of the Orthorhombic Al<sub>13</sub>Co<sub>4</sub>*”

- 15 May 2007, Ecole Doctorale EMMA 2008, Nancy.

“*Surface Structure Investigation of the Orthorhombic Al<sub>13</sub>Co<sub>4</sub>*”

- 10 May 2007, Ecole Doctorale EMMA, Nancy.

“*Study of the (010) surface of the T-Al<sub>3</sub>(Mn, Pd) Complex Metallic Alloy*”

- 26-29 March 2007, Forum de Microscopies à Sonde Locale, Troyes (France).

“*Study of the (010) surface of the T-Al<sub>3</sub>(Mn, Pd) Complex Metallic Alloy*”

## **Additional Professional Experience**

- February - March 2009: Work experience for 2 months at the Empa, Swiss Federal Laboratories for Materials Testing and Research, “nanotech@surfaces” Laboratory, Thun (Switzerland).
- First Prize for Poster presentation at the 3rd European School in Materials Sciences, Ljubljana (Slovenia).

- 25-31 May 2008: 3rd European School in Materials Sciences, Ljubljana.
- 22-31 January 2008: Work experience at the “Berliner Elektronenspeicher-ring - Gesellschaft für Synchrotronstrahlung”, Berlin (Germany).
- August 2007 - March 2008: Work experience for 8 months at the Empa, Swiss Federal Laboratories for Materials Testing and Research, “nanotech@surfaces” Laboratory, Thun.
- 24-29 June 2007: Intensive training course in English, Dijon (France).
- 20-27 May 2007: 2nd European School in Materials Sciences, Ljubljana.
- March-June 2006: Training course in CINaM “Centre Interdisciplinaire de Nanoscience de Marseille” (France). Topic: “*Local measure of the low energy electron transmission through ultra-thin films auto-supported*”.
- April-June 2005: Training course in CINaM. Topic: “*Study of the phase transition and measure of the diffusion coefficient on the phospholipids bi-layer using FRAP*”.

## List of publications

◊ R. Addou, E. Gaudry, Th. Deniozou, M. Heggen, M. Feuerbacher, P. Gille, Yu. Grin, R. Widmer, O. Gröning, V. Fournée, J.M. Dubois and J. Ledieu.

“*Investigation of the (100) surface of the orthorhombic Al<sub>13</sub>Co<sub>4</sub> crystal*”, Physical Review B **80**, 014203 (2009).

◊ Th. Deniozou, R. Addou, A. Shukla, M. Heggen, M. Feuerbacher, M. Krajčí, J. Hafner, R. Widmer, O. Gröning, V. Fournée, J.-M. Dubois and J. Ledieu. “*Structural investigation of the (010) surface of the orthorhombic T-Al<sub>3</sub>(Mn,Pd) crystal*”, Physical Review B **81**, 125418 (2010).

◊ R. Addou, A. Shukla, M.C. Deweerdt, P. Gille, V. Fournée, O. Gröning, J.M. Dubois and J. Ledieu.

“*Growth of Cu thin films on the pseudo-ten-fold surface of the orthorhombic Al<sub>13</sub>Co<sub>4</sub> crystal*” (in preparation).

◊ R. Addou, M. Heggen, M. Feuerbacher, V. Fournée, J.M. Dubois and J. Ledieu.

“*Growth of Pb thin films on the pseudo-decagonal surface of the orthorhombic Al<sub>13</sub>Co<sub>4</sub> and T-Al<sub>3</sub>(Mn,Pd)) approximants*” (in preparation).

◊ Th. Deniozou, R. Widmer, K. Emtsev, Th. Seyller, R. Addou, J. Ledieu, V. Fournée, M. Heggen, M. Feuerbacher and K. Horn

“*The electronic structure of the orthorhombic Al<sub>13</sub>Co<sub>4</sub> complex metallic alloy*” (in preparation).

AUTORISATION DE SOUTENANCE DE THESE  
DU DOCTORAT DE L'INSTITUT NATIONAL  
POLYTECHNIQUE DE LORRAINE

000

VU LES RAPPORTS ETABLIS PAR :

**Madame Marie-Geneviève BARTHÈS-LABROUSSE, Directeur de Recherche, ICMMO-LEMHE,  
Université Paris-Sud, Orsay**

**Monsieur Marc DE BOISSIEU, Directeur de Recherche, SIMAP, St Martin d'Hères**

Le Président de l'Institut National Polytechnique de Lorraine, autorise :

**Monsieur ADDOU Rafik**

à soutenir devant un jury de l'INSTITUT NATIONAL POLYTECHNIQUE DE LORRAINE,  
une thèse intitulée :

**« Surfaces d'alliages métalliques complexes : structure, propriétés nanostructuration »**

en vue de l'obtention du titre de :

**DOCTEUR DE L'INSTITUT NATIONAL POLYTECHNIQUE DE LORRAINE**

en « **Sciences des Matériaux** » Spécialité : « **Science et Ingénierie des Matériaux et  
Métallurgie** »

Fait à Vandoeuvre, le 16 mars 2010

Le Président de l'I.N.P.L.

F. LAURENT



## Surfaces d'Alliages Métalliques Complexes: structure, propriétés et nanostructuration

Ce travail a permis de déterminer les structures atomique et électronique de deux surfaces d'alliages métalliques complexes à l'aide d'une approche multi-techniques supportée par des calculs *ab initio* de structure électronique. Les surfaces de ces cristaux ont pu être corrélées à certains plans présents dans les modèles structuraux disponibles. La terminaison dominante de la surface (100) d' $\text{Al}_{13}\text{Co}_4$  est identifiée comme un plan corrugé incomplet du volume. La surface (010) de T- $\text{Al}_3(\text{Mn}, \text{Pd})$  présente un nombre conséquent d'imperfections structurales. A l'exception de certains sites lacunaires, elle est identique au plan corrugé complet du massif. Dans une seconde étape, ces échantillons ont été utilisés comme substrat pour la croissance de films minces métalliques. Les atomes de Pb déposés sur ces deux surfaces suivent un mode de croissance pseudomorphique jusqu'à la formation de la monocouche. Dans le cas de l' $\text{Al}_{13}\text{Co}_4$ , le coefficient de collage du Pb s'annule une fois cette monocouche formée. Sur la surface T- $\text{Al}_3(\text{Mn}, \text{Pd})$ , la croissance de couches additionnelles de Pb est observée. L'adsorption du Cu sur  $\text{Al}_{13}\text{Co}_4$  mène de nouveau à un mode de croissance pseudomorphique jusqu'à la monocouche. Au-delà de ce dépôt, la phase  $\beta\text{-Al}(\text{Cu}, \text{Co})$  apparaît en surface. Pour des dépôts à des températures plus élevées, la phase- $\beta$  est suivie par la formation de la phase  $\gamma\text{-Al}_4\text{Cu}_9$ . Les phases  $\beta$  et  $\gamma$  croissent suivant deux domaines (110) orientés l'un par rapport à l'autre avec un angle de  $72^\circ$ .

**Mots-clés:** *alliages métalliques complexes, surface d'approximants, structure atomique de surface, structure électronique, adsorption, nanostructuration, STM, LEED, XPS, UPS, XPD, SSC, Calculs DFT,  $\text{Al}_{13}\text{Co}_4$ , T- $\text{Al}_3(\text{Mn}, \text{Pd})$ ,  $\text{Al}_4\text{Cu}_9$ .*

## Complex Metallic Alloy Surfaces: structure, properties and nanostructured surface

We report the investigation of *pseudo*-ten-fold surfaces on two complex metallic alloys considered as approximants to the decagonal quasicrystal. The atomic and electronic structure of the both samples is investigated by means of a multi-technique approach supported by *ab initio* electronic structure calculations. The main termination of the (100) surface of  $\text{Al}_{13}\text{Co}_4$  is attributed to an incomplete puckered layer. The (010) surface of T- $\text{Al}_3(\text{Mn}, \text{Pd})$  exhibits an important amount of structural imperfections. With the exception of several vacancies, this surface is identical to the complete puckered layer. In a second stage, both surfaces have been used as templates for the growth of metallic thin films. On both surfaces, Pb adatoms adopt a pseudomorphic growth mode up to one monolayer. For the  $\text{Al}_{13}\text{Co}_4$  surface, the sticking coefficient of Pb vanishes upon the completion of the monolayer. However, it remains sufficient for the growth of additional layers on the T- $\text{Al}_3(\text{Mn}, \text{Pd})$  (010) surface. The adsorption of Cu on the  $\text{Al}_{13}\text{Co}_4$  surface follows also a pseudomorphic growth mode up to one monolayer. The  $\beta\text{-Al}(\text{Cu}, \text{Co})$  phase appears for coverages greater than one monolayer. For higher temperature deposition, the  $\beta$ -phase is followed by the formation of the  $\gamma\text{-Al}_4\text{Cu}_9$  phase. Both  $\beta$  and  $\gamma$  phases grow as two (110) domains rotated by  $72^\circ$  from each other.

**Key words:** *complex metallic alloys, approximant surfaces, atomic structure of surfaces, electronic structure, adsorption, nanostructured surface, STM, LEED, XPS, UPS, XPD, SSC, DFT calculations,  $\text{Al}_{13}\text{Co}_4$ , T- $\text{Al}_3(\text{Mn}, \text{Pd})$ ,  $\text{Al}_4\text{Cu}_9$ .*

